La dynamique structurale de l'acétylcholinestérase: étude réalisée par cristallographie aux rayons X et une méthode spectroscopique complémentaire.

Benoît Sanson

UNIVERSITÉ JOSEPH FOURIER – GRENOBLE I

École Doctorale de Physique

THÈSE

pour obtenir le grade de

DOCTEUR DE L'UNIVERSITÉ JOSEPH FOURIER
Spécialité : Physique pour les sciences du vivant

Soutenue publiquement par

Benoît SANSON

le 12 octobre 2009

Dynamique structurale de l'acétylcholinestérase étudiée par cristallographie aux rayons X et par une méthode spectroscopique complémentaire

---

Composition du Jury :

Président	**Prof. Patrick MASSON**
Rapporteurs	**Prof. Éric CHABRIÈRE**
	Prof. Maurice GOELDNER
Examinateurs	**Dr. Dominique BOURGEOIS**
	Prof. Israel SILMAN
Directeur de thèse	**Dr. Martin WEIK**

Thèse préparée à l'Institut de Biologie Structurale (CEA-CNRS-UJF)

Remerciements

Je tiens avant tout à remercier chaleureusement **Martin Weik**, mon directeur de thèse, pour la confiance et le soutien qu'il m'a accordés tout au long de ces quatre années. Ses conseils, ses encouragements, sa patience et sa gentillesse ont beaucoup compté dans l'accomplissement de cette thèse. Pour m'avoir offert l'opportunité d'intégrer son équipe, je lui adresse toute ma gratitude.

Je remercie particulièrement **Jacques-Philippe Colletier** pour son amitié et sa disponibilité. C'est essentiellement lui qui m'a initié au monde des cholinestérases et formé à la cristallographie. Je lui suis également reconnaissant de m'avoir impliqué dans ses propres travaux de thèse et d'avoir favorablement contribué aux miens. Je rends hommage à sa passion pour la science et à son éloquence.

Je souhaite remercier les membres du jury, et plus spécialement **Eric Chabrière** et **Maurice Goeldner** de m'avoir fait l'honneur d'être les rapporteurs de cette thèse.

J'adresse mes remerciements sincères à **Israel Silman** et **Joel Sussman** pour leur gentillesse au cours de notre fructueuse collaboration, ainsi qu'au cours de mon séjour en Israël. Je souhaite aussi remercier, au sein de leurs laboratoires respectifs : **Yaacov Ashani, Harry M. Greenblatt Mihal Harel**, **Lilly Toker**, **Tzviya Zeev-Ben-Mordehai**, **Boris Brumshtein**, **Eran Hodis**, **Aviv Paz** et **Moshe Ben-David**.

Pour sa sympathie et ses précieux conseils, je souhaite vivement remercier **Patrick Masson**. Un grand merci aussi à **Florian Nachon**, pour son affabilité et sa disponibilité. Pour sa gentillesse et pour avoir bravé le froid aussi souvent à mes côtés, j'aimerais spécialement remercier **Marie-Thérèse Froment**.

Je voudrais sincèrement remercier **Dominique Bourgeois**, **Philippe Carpentier** et **Antoine Royant**. Leur aide et leur disponibilité m'ont été particulièrement précieuses.

Je remercie **Joanne McCarthy**, **Elspeth Garman**, **Raimond Ravelli**, **Virgile Adam** et toutes les personnes de l'ESRF qui m'ont apporté leur aide.

J'adresse mes remerciements à tous les collaborateurs des travaux décrits dans ce manuscrit, et plus particulièrement à **Didier Fournier** et à **Giuseppe Campiani**.

J’aimerais remercier tous les membres (partis ou présents) du Laboratoire de Biophysique Moléculaire. Merci à **Christine Ebel**, la directrice du laboratoire, pour m’avoir accueilli dans le laboratoire. Je remercie **Fred Vellieux** et **Colin Jackson**, pour leur aide et leur amabilité. Je remercie **Nicolas Coquelle**, **Marion Jasnin**, **Eva Rosenbaum**, **Katy Wood**, **Asun Durá**, **Emanuela Fioravanti**, **Mylène Ferruit**, **Aline Appourchaux**, **Renata Grzela**, **Antonina Naskalska** et **Izabela Wojtal**, pour le plaisir que j’ai eu à travailler en leur compagnie et pour les soirées agréables passées ensemble.

Je tiens à remercier tous ceux de l’IBS qui m’ont apporté leur aide, leur soutien et leur sympathie : **Richard Kahn**, **Gaël Goret**, **Sergey Tcherniuk**, **Pauline Macheboeuf**, **Charles Calmettes**, **Bastien Hermant**, **Robert van Liis** et **Benjamin Fould**.

Merci à mes amis, et en particulier à **Mathieu**, **Gautier**, **Helga**, **Mihai**, **François** et **Magalie.**

Je suis profondément reconnaissant envers **toute ma famille :** je sais que je peux toujours compter sur leur soutien.

Mille mercis à **Andreea**, mon plus grand soutien au cours de cette thèse. Je ne saurais lui montrer toute la gratitude qu’elle mérite. Mulțumesc mult !

Table des matières

INTRODUCTION GÉNÉRALE 2

1. LA DYNAMIQUE STRUCTURALE DES PROTÉINES 6

1.1 Le paysage conformationnel 6

1.2 Mouvements, échelles de temps et méthodes associées 8

1.3 Relations dynamico-structurales entre une protéine et son solvant 11

1.4 Transition vitreuse du solvant et transition dynamique d'une protéine 13

2. L'ACÉTYLCHOLINESTÉRASE (AChE) 16

2.1 Découverte 16

2.2 Rôle classique 17

2.3 Une enzyme très rapide 19

2.4 Structure tridimensionnelle 19

2.4.1 Le site actif 21

2.4.2 La gorge aromatique 23

2.4.3 Le site périphérique 24

2.5 Fonctionnement : mécanisme catalytique et paradoxe 26

2.6 Rôles non-classiques 28

3. L'AChE, CIBLE D'UN VASTE RÉPERTOIRE DE LIGANDS 32

3.1 Les organophosphorés 32

3.1.1 Origine et utilisation des organophosphorés 33

3.1.2 Mécanisme d'inhibition de l'AChE par les OP 34

3.1.3 Réactivation de l'AChE inhibée par un OP 37

3.2 Toxines 41

3.2.1 La fasciculine 2 41

3.2.2 L'aflatoxine 42

3.3 Les médicaments anti-Alzheimer 43
4. OBJECTIFS DE LA THÈSE 46
5. MÉTHODOLOGIE 50
5.1 La cristallographie des protéines 50
5.1.1 Introduction 50
5.1.2 Les principes de la cristallographie des protéines 51
5.1.3 La cristallogenèse 56
5.1.4 Le montage des cristaux sur le diffractomètre 59
5.1.5 La collecte de données 60
5.1.6 Traitement des données cristallographiques 66
5.1.7 Résolution d'une structure 68
5.1.8 Affinement de la structure 70
5.1.9 La cristallographie cinétique 72
5.2 Microspectrophotométrie 76
5.2.1 Luminescence et spectroscopie 76
5.2.2 Le cryobench 78
5.2.3 Temps de vie de phosphorescence en fonction de la température 80
6. RÉSULTATS 84
6.1 Acétylcholinestérase en complexe avec de putatives molécules anti-Alzheimer 84
6.1.1 Présentation de l'article 84
6.1.2 Article 84
6.1.3 Bilan 102
6.2 Instantanés de l'acétylcholinestérase avec le soman et le 2-PAM 102
6.2.1 Présentation de l'article 102
6.2.2 Article 103
6.2.3 Bilan 134
6.3 L'acétylcholinestérase en complexe avec l'aflatoxine, un inhibiteur du PAS 134
6.3.1 Présentation de l'article 134

6.3.2 Article 135
6.3.3 Bilan 159
6.4 L'aflatoxine : un inhibiteur phosphorescent qui suggère un nouveau moyen d'étudier la dynamique des protéines 159
6.4.1 Présentation de l'article 159
6.4.2 Article 160
6.4.3 Bilan 180
7. DISCUSSION GÉNÉRALE, CONCLUSION & PERSPECTIVES 182
BIBLIOGRAPHIE 189
ANNEXES 211

INTRODUCTION

GÉNÉRALE

INTRODUCTION GÉNÉRALE

Les protéines sont essentielles à la vie. Elles sont à la base de tous les processus biologiques, du métabolisme aux mécanismes complexes qui sous-tendent la pensée. Comprendre leur fonctionnement est crucial pour approfondir nos connaissances dans le domaine de la biologie, et développer les thérapeutiques et les biotechnologies. On peut comparer ces macromolécules à des machines de taille nanométrique. Les outils permettant la visualisation de leur structure ont été conçus et améliorés au cours du XX^{e} siècle. La cristallographie aux rayons X, en particulier, a considérablement contribué à la résolution de nombreuses structures protéiques. Pourtant, la photographie d'une machine ne suffit pas à en comprendre le fonctionnement; les relations structure-fonction ne fournissent pas d'explications suffisantes et satisfaisantes. Bien que les structures des protéines permettent parfois la visualisation des atomes d'hydrogène, les détails structuraux ne suffisent pas à appréhender pleinement le fonctionnement d'une protéine. Ainsi, on pourra toujours mettre en pièces une machine, la clef de son mécanisme n'en émergera pas spontanément pour autant. Pour répondre à cette attente, on aimerait plutôt regarder cette machine en train de fonctionner. C'est exactement le but ultime des études de dynamique structurale des protéines : regarder les protéines fonctionner. La diffraction de Laue et les méthodes rapides en RMN atteignent ce but dans le cas de certaines protéines.

L'acétylcholinestérase (AChE) représente un véritable défi dans le cadre de la dynamique structurale. Elle figure parmi les enzymes les plus rapides de la nature. En hydrolysant le neurotransmetteur acétylcholine, elle assure la terminaison de la transmission de l'influx nerveux au sein des synapses cholinergiques et des jonctions neuromusculaires. Malgré un site actif enfoui au fond d'une gorge étroite, elle est capable d'hydrolyser plus de mille fois par seconde son substrat. Pour parvenir à une telle efficacité catalytique, cette enzyme doit posséder une machinerie aux mécanismes subtils. On connaît à présent bien sa structure. Des études d'ordre dynamique ont aussi permis d'étoffer la connaissance de ses propriétés. Pourtant, l'essence de son efficience nous échappe encore. Des expériences de cristallographie cinétique ont permis de confirmer et de visualiser les étapes de la réaction catalytique. Cette approche suggère qu'une compréhension plus

profonde de la fonction de cette enzyme émergera d'une étude combinant structure et dynamique ; les deux aspects ne doivent pas être séparés. En ce sens, l'AChE constitue un paradigme de la dynamique structurale.

De par son rôle essentiel au parcours de l'influx nerveux, l'AChE est la cible d'une panoplie très large de molécules capables de l'inhiber. On compte parmi ces dernières des molécules naturelles, telles des toxines de serpents ou certaines mycotoxines. De nombreuses molécules synthétiques peuvent également être répertoriées, parmi lesquelles les toxiques de guerre organophosphorés et la majorité des médicaments visant à lutter contre les signes de la maladie d'Alzheimer. La compréhension de son fonctionnement dépasse par conséquent le cadre de la recherche fondamentale. La mise au point des futurs médicaments anti-Alzheimer et des antidotes contre les intoxications aux organophosphorés (OP) bénéficiera d'une compréhension approfondie de la dynamique structurale de l'AChE.

Au cours de cette thèse, nous avons mis à profit la diversité des molécules pouvant se lier à l'AChE pour obtenir des informations dynamico-structurales cruciales pour mieux comprendre son fonctionnement. Des ligands spécifiques des deux sites de fixation privilégiés de l'enzyme, ses sites actif et périphérique, ont été soigneusement choisis et employés pour sonder spécifiquement ces régions. Cette stratégie nous a permis d'explorer une partie du paysage conformationnel de l'AChE, d'améliorer la compréhension de la machinerie catalytique de l'enzyme et de fournir une base nouvelle au développement de drogues anti-Alzheimer et d'antidotes contre les intoxications aux OP. Nous proposons en outre une nouvelle méthode pour sonder la dynamique des protéines, sur la base d'un complexe de l'AChE avec un inhibiteur phosphorescent. Les travaux menés au cours de cette thèse s'intègrent au domaine de la cristallographie cinétique.

Afin de mieux appréhender l'intérêt de nos travaux, nous détaillerons le contexte dans lequel ils ont été menés, l'objet étudié (l'AChE), et les outils mis en œuvre. Ainsi, nous dresserons dans un premier temps un portrait rapide de la dynamique structurale. Dans une deuxième partie consacrée à l'AChE, nous mettrons en lumière les éléments structuraux qui nous ont intéressés dans nos expériences. Nous insisterons ensuite sur les relations entre l'AChE et les ligands que nous avons employés. La cristallographie aux rayons X et les principes de la spectroscopie seront ensuite sommairement exposés. Nous

présenterons et discuterons alors nos résultats. Enfin, des perspectives de ces travaux seront proposées.

1. LA DYNAMIQUE STRUCTURALE DES PROTÉINES

1. LA DYNAMIQUE STRUCTURALE DES PROTÉINES

Les processus dynamiques des protéines sont essentiels au fonctionnement cellulaire, et par conséquent à la vie. La diversité des fonctions portées par les protéines ne peut être uniquement expliquée par leurs structures. Pourtant, ce sont les relations structure-fonction seules qui ont été extensivement étudiées. On explique encore parfois aux étudiants de premier cycle universitaire que les protéines interagissent avec un substrat ou un inhibiteur à la manière d'une serrure avec une clef. Cette vision occulte l'aspect dynamique, qui est pourtant essentiel à une compréhension plus complète, et plus exacte, du fonctionnement d'une protéine. Néanmoins, au cours des dernières années, une prise de conscience s'est opérée ; les relations structure-dynamique-fonction sont devenues le nouveau paradigme de l'étude des protéines. On reconnaît aujourd'hui que c'est la synergie entre la structure et la dynamique qui assure leur fonction biologique aux protéines.

Les protéines possèdent parfois un rôle catalytique ; on les nomme alors également enzymes. Pour remplir ce rôle biocatalytique, les enzymes fournissent un environnement optimisé à la réaction en vue d'accélérer son avancement. Cet environnement est atteint à travers l'échantillonnage de très nombreuses conformations. L'étude de la dynamique structurale d'une protéine a pour objet d'identifier ces conformations afin d'élucider le fonctionnement de ladite protéine [Henzler-Wildman & Kern 2007a; Henzler-Wildman 2007c; Henzler-Wildman 2007b; Parak 2003b; Parak 2003a; Russel 2009].

1.1 Le paysage conformationnel

La notion de paysage conformationnel (Fig. 1) a été proposée par Frauenfelder et coll. en 1975 [Austin 1975]. En étudiant la re-liaison, après rupture préalable par photolyse, du monoxide de carbone et de l'oxygène dans la myoglobine, les auteurs ont observé des barrières énergétiques multiples et une cinétique non exponentielle du processus en dessous de 230 K. Le concept de paysage conformationnel a été développé par la suite [Frauenfelder 1991].

Une protéine peut exister dans un grand nombre de sous-états conformationnels (SC). L'ensemble des SC peut être décrit par le paysage conformationnel. En pratique, une protéine échantillonne un large ensemble de SC autour d'une structure moyenne. Même en état de repos apparent, la conformation d'une protéine fluctue au sein du paysage conformationnel.

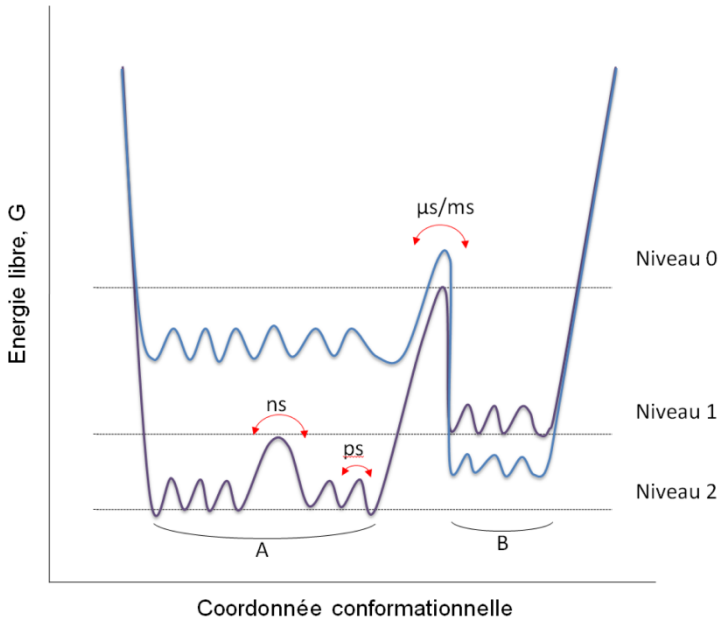

Figure 1. Représentation schématique du paysage conformationnel d'une protéine. Les processus dynamiques de la protéine sont hiérarchisés en niveaux. Chaque niveau correspond à l'échelle de temps du changement conformationnel associé. La hauteur des barrières énergétiques définit la probabilité de passage d'un niveau à l'autre : elle traduit ainsi la cinétique du changement conformationnel. D'après [Henzler-Wildman 2007a].

Le paysage conformationnel permet de définir la hiérarchie et l'amplitude des mouvements qui se produisent dans une protéine [Henzler-Wildman 2007a; Henzler-Wildman 2007c]. En effet, les processus dynamiques qui régissent le fonctionnement d'une protéine sont soumis à la thermodynamique. Ainsi, à chaque SC est associée une probabilité relative. La conformation d'une protéine fluctue parmi les différents SC rendus accessibles par son énergie thermique. Ces fluctuations ont lieu à différentes échelles temporelles : de la picoseconde à la minute (et parfois même au-delà). Alors que les fluctuations lentes correspondent aux niveaux les plus élevés du paysage conformationnel, les fluctuations les plus rapides correspondent à des niveaux plus bas.

Les différents SC sont séparés par des barrières énergétiques plus ou moins hautes. Par exemple, les SC du niveau 0 correspondent à des changements conformationnels lents, tels que ceux qui se produisent au cours de la réaction catalytique. La probabilité de passer d'un SC à un autre à ce niveau est faible, comme l'indique la hauteur des barrières qui les séparent. Au contraire, les SC des niveaux ultérieurs correspondent à des mouvements de plus en plus rapides. Les niveaux les plus élevés correspondent à des mouvements atomiques à l'échelle de la picoseconde.

Pour permettre son efficacité en tant que biocatalyseur, une enzyme doit non seulement conserver sa structure tridimensionnelle, mais également être capable de mouvements. Les fluctuations rapides, à l'échelle atomique, facilitent les mouvements à plus grande échelle (à la fois spatiale et temporelle) en agissant un peu à la manière d'un lubrifiant. [Parak 2003b] Les fluctuations fonctionnellement importantes ont probablement été sélectionnées par l'évolution, ce qui explique la surprenante efficacité catalytique de certaines enzymes, telles que l'acétylcholinestérase (cf. partie 2 : L'acétylcholinestérase).

Nous tenons à préciser que la représentation de la figure 1 est extrêmement simplifiée. Le paysage conformationnel est en réalité hautement multidimensionnel. Pour une protéine composée de N atomes, le nombre de dimensions s'élève à 3N – 6. En outre, il faut garder à l'esprit que le paysage conformationnel dépend de la température, de la pression et des conditions de solvant. C'est notamment en jouant sur la température que la cristallographie cinétique peut piéger certains sous-états conformationnels (cf. partie 5.1.9 : La cristallographie cinétique).

1.2 Mouvements, échelles de temps et méthodes associées

L'étude dynamico-structurale d'une protéine passe par l'exploration de son paysage conformationnel. Pour y parvenir, les changements conformationnels de l'enzyme doivent être caractérisés à toutes les échelles de temps. Comme nous l'avons mentionné plus, à chaque échelle de temps correspond un ensemble de mouvements et une échelle spatiale (Fig. 2).

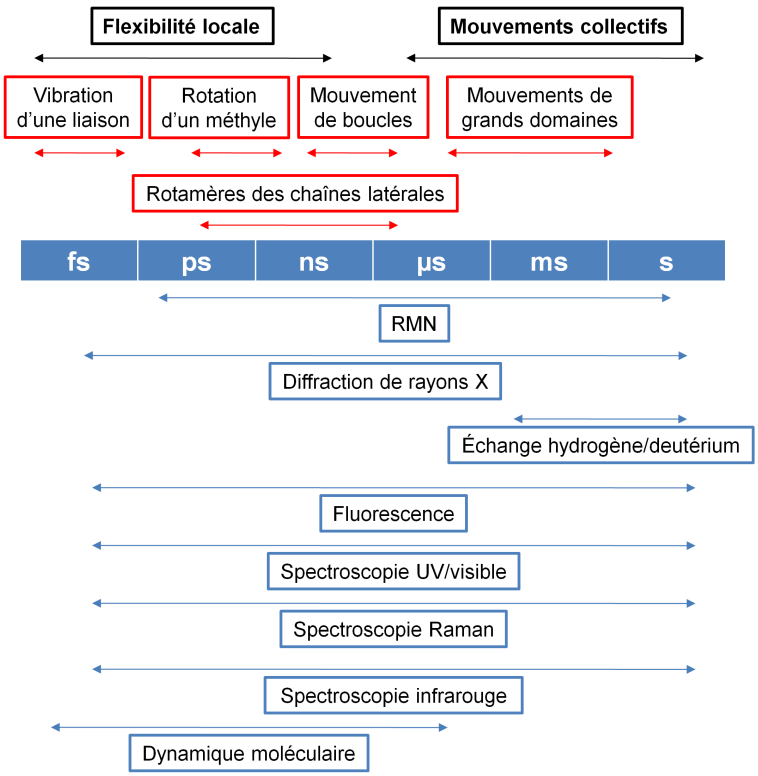

Figure 2. Mouvements se produisant dans une enzyme. Les échelles de temps associées et les méthodes adaptées à leur mesure sont reportées. D'après [Henzler-Wildman 2007a].

Les mouvements rapides (de la picoseconde à la microseconde) :

Parmi les mouvements les plus rapides se produisant au sein des protéines, on compte essentiellement ceux des chaînes latérales. La flexibilité de ces dernières varie en fonction de leur nature (la chaîne latérale d'une lysine est plus flexible que celle d'une alanine), de leur environnement (un résidu de surface est plus mobile qu'un résidu enfoui, lequel fait alors partie d'un réseau d'interactions multiples avec ses voisins) et des conditions de température et de pression. Le mouvement des chaînes latérales se fait sur l'ensemble de la gamme de temps « rapide ».

Les mouvements les plus lents de cette gamme sont les mouvements de boucles. Au contraire, la rotation de groupements tels que les méthyles se fait à l'échelle de la picoseconde.

Tous ces mouvements concernent les niveaux les plus élevés du paysage conformationnel (niveaux 1 et 2). Il existe des mouvements encore plus rapides, à des niveaux plus élevés. Par exemple, la vibration des liaisons interatomiques se fait à l'échelle de la femtoseconde.

Les mouvements « lents » (de la milliseconde à la seconde et plus) :

Ce sont des mouvements collectifs de grande amplitude impliquant de larges domaines de l'enzyme. C'est l'interconversion entre les niveaux 0 du paysage conformationnel qui est en jeu à cette échelle temporelle. Ces évènements sont donc rares par comparaison aux mouvements rapides, mais la plupart des processus biologiques (catalyse, transduction d'un signal, interactions protéine-protéine) ont lieu à cette échelle.

La longue durée de vie des états de niveau 0 rend leur caractérisation structurale aisée. Il est en effet parfois possible de les observer directement. Alternativement, le piégeage des états intermédiaires de la réaction catalytique est envisagé (cf. partie 5.1.9 : La cristallographie cinétique).

Les méthodes pour caractériser la dynamique structurale

Aucune méthode ne permet de couvrir toute la gamme des échelles spatiale et temporelle pertinentes pour les études de dynamique structurale des protéines. La figure 2 montre le domaine d'application temporel de diverses techniques actuellement utilisées, détaillées ci-dessous.

_ La Résonance Magnétique Nucléaire (RMN). Elle exploite le moment magnétique des atomes de spin nucléaire non nul, qui peut interagir avec un champ magnétique. La mesure de la relaxation des spins après une impulsion radio-fréquence constitue le cœur de la méthode. La RMN permet d'explorer une grande partie des échelles temporelles pertinentes dans le cadre de la dynamique d'une protéine (de la ps à la s, et plus). Elle est cependant limitée par la taille de l'objet étudié : en moyenne, les échantillons dépassent rarement les 30 kDa.

_ La dynamique moléculaire (DM) n'est pas une technique expérimentale, mais entre dans le cadre des simulations numériques. A l'aide des équations de la mécanique newtonienne et de la mécanique quantique, la trajectoire du système est échantillonnée par pas à l'échelle de la femtoseconde. Les simulations les plus longues atteignent l'échelle de la milliseconde. La DM requiert des temps de calcul très longs. Les simulations gros-grain, par exemple, permettent de contourner cette limite. En combinant plusieurs atomes en une seule particule, les simulations peuvent alors atteindre l'échelle de la milliseconde.

_ La diffusion de rayons X aux petits angles (SAXS) résolue en temps. Comme son nom l'indique, cette méthode exploite la diffusion des rayons X par la protéine. Cette technique est limitée en termes de résolution spatiale et temporelle.

_ La cristallographe aux rayons X monochromatique. Cette méthode est la méthode de choix lorsque l'on souhaite avoir accès à la structure d'une protéine à l'échelle atomique (cf. partie 2.1 : La cristallographie aux rayons X). Cependant elle ne permet, en principe, que l'étude de la structure d'une protéine au repos. Nous verrons plus loin comment on peut tirer parti de la connaissance du paysage conformationnel d'une protéine pour transformer la cristallographie aux rayons X en une méthode cinétique (cf. partie 5.1.9 : La cristallographie cinétique).

_ La diffusion neutronique permet d'atteindre des échelles spatiale et temporelle de l'ordre de l'angström et de la ns, respectivement.

1.3 Relations dynamico-structurales entre une protéine et son solvant

Dans son environnement physiologique, une protéine est entourée par des molécules de natures très diverses : de l'eau, des ions, des petites molécules et d'autres macromolécules. Le solvant dans lequel baignent les protéines est toutefois essentiellement composé de molécules d'eau. On distingue deux types d'eau : la couche d'hydratation (Fig. 3) et l'eau volumique ou *bulk* [Otting 1991]. La couche d'hydratation concerne les molécules les plus proches de l'enzyme ; on considère qu'une couche est nécessaire au fonctionnement d'une protéine [Rupley & Careri 1991]. Parmi les molécules d'eau de la couche d'hydratation, certaines sont en interaction directe avec la protéine. Ce sont des molécules d'eau dites structurales qui peuvent être présentes dans les « poudres sèches » de protéines (que l'on prépare pour une expérience de diffusion de neutrons, par exemple). Cette eau est suffisamment stabilisée pour pouvoir être modélisée dans une structure cristallographique. Elle est considérée par certains comme faisant partie intégrante de la structure d'une protéine [Ball 2007]. L'eau *bulk* est celle située au-delà de la couche d'hydratation.

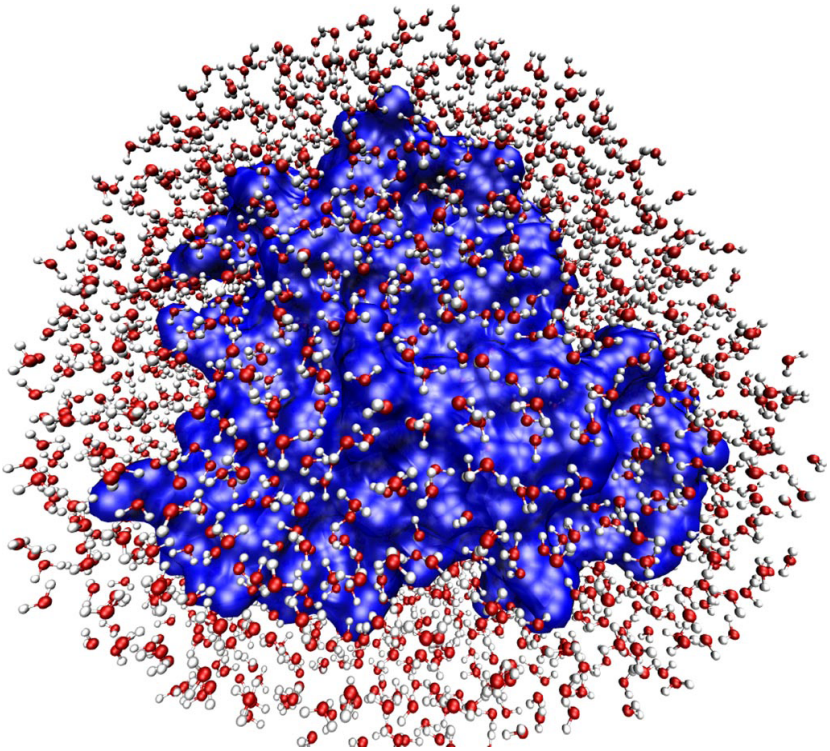

Figure 3. La couche d'hydratation de la myoglobine. La surface de la protéine est représentée en bleu. Reproduit de [Frauenfelder 2009].

Le cytoplasme est un milieu très encombré : la distance moyenne entre deux macromolécules y est de 10–20 Å [Ball 2007]. Ainsi, comme l'influence sur l'eau de la macromolécule peut s'étendre jusqu'à 20 Å [Ebbinghaus 2007], l'eau cellulaire serait majoritairement différente de la forme *bulk* [Brovchenko & Oleinikova 2008]. Le sujet est, toutefois, encore controversé.

On estime aujourd'hui que les mouvements des protéines sont couplés aux fluctuations du solvant [Fenimore 2002; Fenimore 2004; Frauenfelder 2009; Wood 2008]. Fenimore écrit : « Le solvant est un participant actif, pas un badaud innocent ». En d'autres termes, les protéines ne sont pas des objets rigides mais sont en partie contrôlées par les mouvements du solvant. Des expériences de spectroscopie Mössbauer et de diffusion de neutrons ont permis de montrer les relations qui existent entre une protéine et son solvant. On peut ainsi distinguer deux types de mouvements associés aux protéines :

_ les mouvements asservis au solvant *bulk*. Cela concerne les mouvements de grande amplitude, en particulier l'entrée et la sortie de ligands ;

_ les mouvements vibrationnels qui sont propres à la protéine.

On distingue également parfois les mouvements couplés à la couche d'hydratation. Les chaînes latérales des résidus d'une protéine, en particulier, sont sensibles aux fluctuations rapides de la couche d'hydratation. Toutefois, aucun consensus n'existe à ce sujet.

1.4 Transition vitreuse du solvant et transition dynamique d'une protéine

L'importance du solvant a été soulignée plus haut. Que ce soit en solution ou dans un cristal, une protéine baigne dans son solvant. La nature très diverse des solutés pouvant exister dans ce solvant rend très difficile la connaissance de ses propriétés, notamment son comportement aux basses températures couramment utilisées en cryo-cristallographie autour de 100 K.

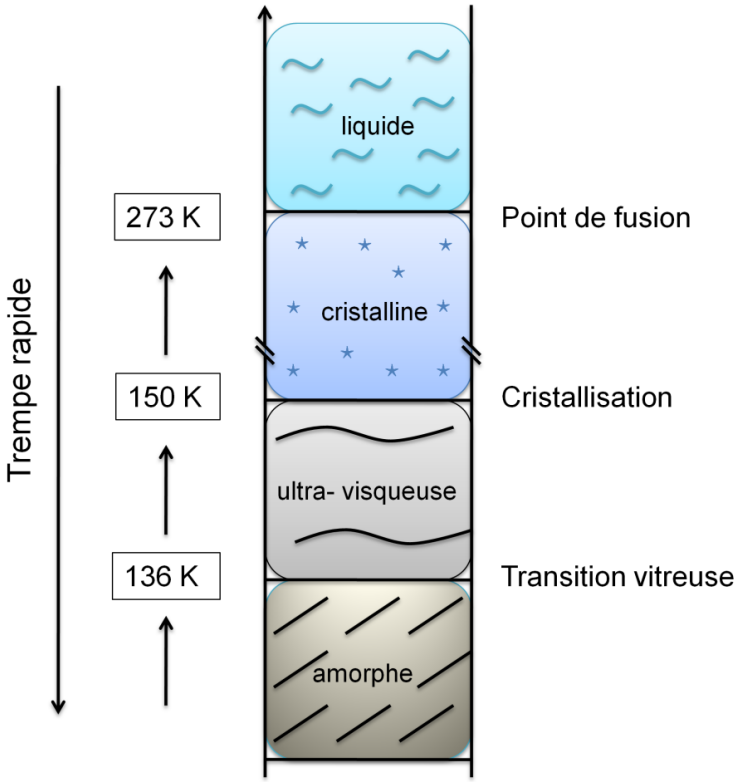

Figure 4. Les différents états de l'eau refroidie ultra-rapidement. Reproduit de [Mishima & Stanley 1998].

On peut toutefois considérer le cas de l'eau pure pour se faire une idée du comportement du solvant lors du processus de refroidissement ultra-rapide (Fig. 4). Lorsque l'eau est

refroidie très rapidement, en dessous de sa température de transition vitreuse T_g, elle ne forme pas de glace cristalline, mais un solide amorphe [Mishima 1998]. On dit également que l'eau est vitrifiée ; sa structure conserve l'arrangement désordonné caractéristique d'un liquide. Ce n'est qu'en la réchauffant que la glace cristalline se forme, vers 150 K (T_x). Il existe entre T_g et T_x une phase où l'eau est ultra-visqueuse. Concrètement, le réarrangement des molécules d'eau en un réseau cristallin confère une mobilité transitoire aux molécules d'eau [Kim 2009; Weik 2005].

On peut raisonnablement s'attendre à ce que le solvant entourant une protéine se comporte d'une manière similaire, mais avec une température de transition vitreuse différente. Alors que la présence de sel dans l'eau abaisse son point de fusion, la présence de solutés augmente la température de transition vitreuse.

Les mouvements des protéines peuvent être rangés dans deux classes distinctes : des mouvements asservis à ceux du solvant et des mouvements non-asservis [Fenimore 2002]. Les processus dynamiques des protéines asservis sont couplés aux fluctuations du solvant : par exemple, l'ouverture ou la fermeture d'un canal à travers la protéine. Au contraire, la formation d'une liaison est un processus non asservi. Selon Fenimore et coll., le solvant est responsable de l'enthalpie d'activation, alors que la protéine et sa couche d'hydratation contrôlent l'entropie d'activation [Fenimore 2002].
Les protéines peuvent subir, à l'instar des milieux désorganisés tels que les verres, une transition dynamique à des températures voisines de 200 K [Doster 1989; Parak 1982]. Le paysage conformationnel des protéines ressemble, en effet, à celui d'un verre [Angell 1995]. Le refroidissement d'une protéine au-dessous de sa température de transition dynamique (T_d) aboutit à des mouvements moins rapides et de moindre amplitude. La mobilité du solvant joue un rôle essentiel dans la dynamique des protéines uniquement au-dessus de T_d [Vitkup 2000]. En-dessous de T_d, alors que le solvant est pratiquement figé, la dynamique intrinsèque de la protéine peut être mise en évidence.

2. L'ACÉTYLCHOLINESTÉRASE

2. L'ACÉTYLCHOLINESTÉRASE (AChE)

Dans cette partie, nous détaillerons le rôle et les caractéristiques structurales de l'AChE. Nous justifierons le choix de cette enzyme dans le cadre de l'étude de dynamique structurale menée au cours de cette thèse. Nous montrerons également la place importante qu'elle occupe au sein des préoccupations actuelles de santé publique.

L'AChE est une protéine exprimée chez les eucaryotes supérieurs. Dans le cadre de nos expériences, nous avons utilisé l'AChE de *Torpedo californica (Tc)*, une raie du pacifique (cf. section Résultats). Les différents projets menés au cours de cette thèse nécessitaient la cristallisation de l'AChE. Parce qu'elle cristallise uniquement en présence de fasciculine, une toxine de serpent, l'enzyme humaine n'aurait pu être utilisée dans le cadre de nos expériences. Sauf indication contraire, les considérations qui suivent concernent l'AChE de cette espèce.

L'AChE (EC 3.1.1.7) appartient à la famille des cholinestérases, les enzymes capables d'hydrolyser les esters de choline (cholinesters) dont fait partie l'acétylcholine (ACh). Sa découverte a motivé de nombreux efforts pour comprendre son fonctionnement. La résolution de la structure de la *Tc*AChE a permis d'identifier son site actif au fond d'une gorge profonde de 20 Å [Sussman 1991]. Cette découverte a immédiatement suscité des interrogations concernant le trafic des substrats et des produits enzymatiques dans l'AChE. Comment concilier l'enfouissement du site actif à la rapidité requise (et mesurée) de cette enzyme pour remplir son rôle ?

2.1 Découverte

En 1914, alors qu'il isolait l'ACh, Henry Dale suspectait déjà une enzyme d'être responsable de son élimination dans le système circulatoire [Dale 1914]. Il devait recevoir, conjointement à Otto Loewi, le prix Nobel de médecine en 1936 pour ses « découvertes relatives à la transmission chimique de l'impulsion nerveuse ».

En 1932, une enzyme capable d'hydrolyser à la fois l'ACh et la butyrylcholine (BCh) fut isolée dans le sérum de cheval [Stedman 1932]. Elle fut nommée choline-estérase (ChE). Il fut alors proposé pour la première fois qu'une enzyme soit responsable de l'hydrolyse spécifique de l'ACh. En 1940, Alles et Hawes [Alles & Hawes 1940] furent les premiers à décrire les différences entre les cholinestérases du sérum et celles des érythrocytes. Richter et Croft montrèrent en 1942 que les ChE érythrocytaires hydrolysent spécifiquement l'ACh [Richter & Croft 1942]. L'AChE fut isolée dans le cerveau des mammifères en 1935 [Stedman & Stedman 1935]. Dix ans plus tard, il fut montré que la ChE présente dans le cerveau des vertébrés était du même type que la ChE érythrocytaire [Nachmansohn & Rothenberg 1945; Zeller & Bissegger 1943]. En s'appuyant sur sa spécificité pour l'ACh, Augustinsson et Nachmannsohn baptisèrent définitivement l'AChE en 1949 [Augustinsson & Nachmansohn 1949]. L'autre représentante de la famille des ChEs fut longtemps appelée pseudo-cholinestérase en raison de la méconnaissance de son rôle physiologique. Le terme de butyrylcholinestérase (BuChE, EC 3.1.1.8) a depuis été retenu. Bien que sa structure ait été résolue [Nicolet 2003], son rôle précis n'a toujours pas été élucidé [Masson 2009]. Elle pourrait cependant agir comme détoxifiant du système circulatoire.

A partir des années 50, la quête de la compréhension du fonctionnement de l'AChE a suscité beaucoup d'efforts. Des études biochimiques et de biologie moléculaire ont permis d'élaborer des modèles de plus en plus précis de sa structure et de sa cinétique.

2.2 Rôle classique

L'AChE est exprimée dans de nombreux tissus. Mais c'est à la jonction neuromusculaire ou dans les synapses reliant certains neurones qu'elle remplit son rôle le mieux connu.

Une synapse cholinergique fonctionne schématiquement en quatre temps. Le neurotransmetteur, l'ACh, est d'abord libéré, diffuse à travers la fente synaptique, se lie réversiblement au récepteur nicotinique et est finalement hydrolysé (Fig. 5). C'est lors de cette dernière étape qu'intervient l'AChE. Elle remplit sa fonction cholinergique en assurant la terminaison de la transmission de l'influx nerveux au sein des jonctions neuromusculaires et des synapses cholinergiques [Silman & Sussman 2005]. Cette action

est réalisée par l'hydrolyse de son substrat, l'acétylcholine (ACh), en acétate et choline (Schéma 1).

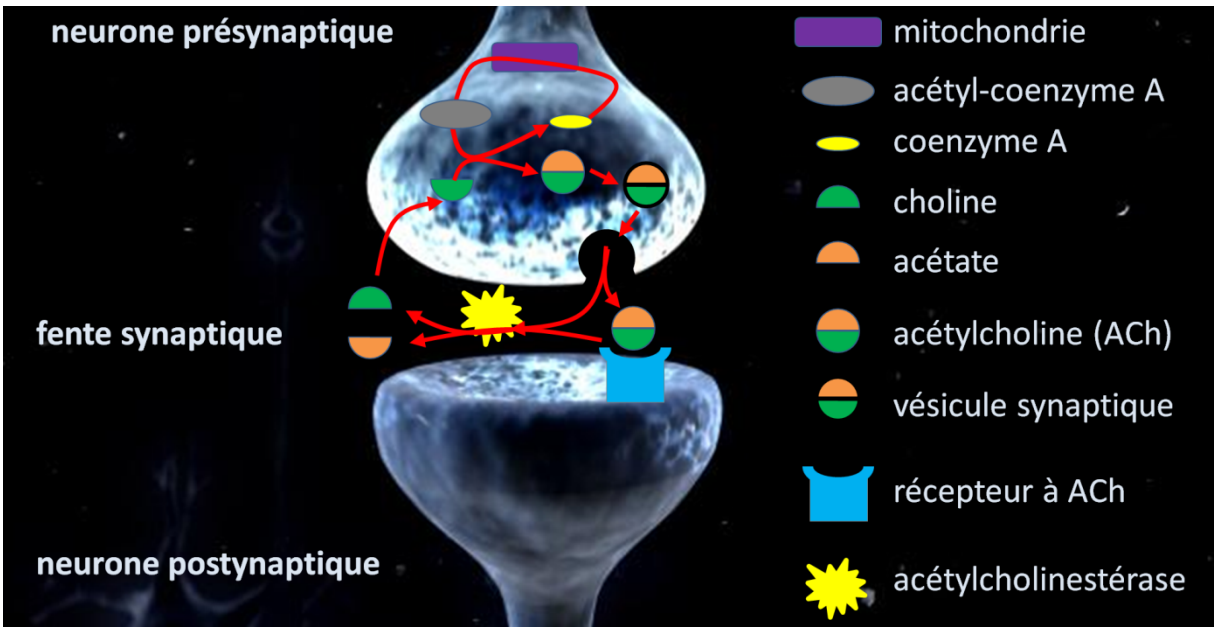

Figure 5. Représentation schématique d'une synapse cholinergique. L'acétylcholine (ACh) est produite dans le neurone présynaptique et est ensuite libérée par exocytose dans la fente synaptique où elle diffuse. Elle peut alors se lier au récepteur à ACh situé sur la membrane postsynaptique. L'acétylcholinestérase est responsable de la dégradation de l'ACh en acétate et choline.

Le rôle de l'AChE requiert une grande efficacité. L'ensemble des évènements que constitue la transmission de l'influx nerveux au sein d'une synapse dure à peine quelques millisecondes. Il faut donc que l'AChE, qui termine cette suite d'évènements soit suffisamment rapide pour restaurer les conditions nécessaires à la transmission d'un nouvel influx.

2.3 Une enzyme très rapide

L'AChE est une enzyme extrêmement rapide : selon l'espèce, elle est capable d'hydrolyser son substrat entre 1000 et 20000 fois par seconde. Cela fait d'elle une des enzymes les plus rapides de la nature. Avec une efficacité catalytique estimée à environ 1.5 x 10^8 $M^{-1}.s^{-1}$, la diffusion des substrats et des produits, vers et à partir de son site actif, constitue pratiquement l'étape limitante de la réaction catalytique [Hasinoff 1982; Quinn 1987; Rosenberry 1975]. Le temps de vie du complexe enzyme/substrat est alors négligeable en comparaison du temps moyen nécessaire à la rencontre des deux entités.

L'efficacité catalytique maximale atteignable par une enzyme se situe quelque part entre 10^7 $M^{-1}.s^{-1}$ et 10^{10} $M^{-1}.s^{-1}$, selon les contraintes d'orientation imposées par la structure de l'enzyme lors de sa rencontre avec son substrat [Stroppolo 2001]. L'AChE peut donc être considérée de ce point de vue comme cinétiquement, ou catalytiquement, parfaite. Il a été proposé que la propension d'une enzyme à se rapprocher de son efficacité catalytique maximale reflète son degré d'évolution. On peut cependant remarquer que de ce point de vue, une enzyme ne peut jamais réellement atteindre son efficacité maximale. En effet, une plus grande efficacité enzymatique n'accélérerait pas la réaction, n'apporterait aucun avantage à l'organisme hôte et ne serait donc tout simplement pas sélectionnée lors de l'évolution.

2.4 Structure tridimensionnelle

La première structure tridimensionnelle d'une AChE à être résolue fut celle d'une raie du pacifique, *Torpedo californica (Tc)* (Fig. 6) [Sussman 1991]. Ce poisson torpille fut choisi pour son organe électrique, lequel lui permet d'assommer ses proies (ou ses prédateurs) en leur délivrant des décharges électriques puissantes (~100 V et ~30 A). Les électrocytes de l'organe électrique fonctionnent un peu à la manière d'une jonction neuromusculaire; l'AChE, qui y joue un rôle prépondérant, y est présente en grande quantités.

La *Tc*AChE est exprimée sous forme d'un dimère lié à la membrane par un lien glyco-phosphatidyl-inositol. C'est ce dimère qui a été purifié puis cristallisé.

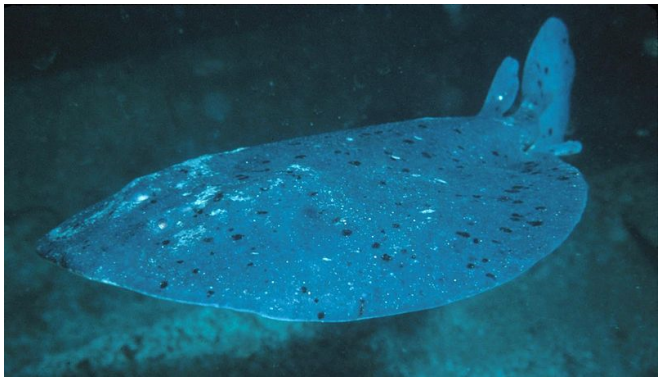

Figure 6. Photographie d'une raie Torpedo californica. Reproduit de [1].

Un monomère d'AChE présente un repliement de type α/β hydrolase [Ollis 1992], alternant 15 hélices α et 11 feuillets β. L'extrémité N-terminale présente une portion de feuillet β qui n'interagit pas avec le reste de la structure. Deux hélices α de chaque monomère, dont l'hélice α C-terminale, s'associent pour former le dimère. Le paquet de 4 hélices α (4-helix bundle) ainsi formé assure la cohésion des deux monomères en un dimère très stable.

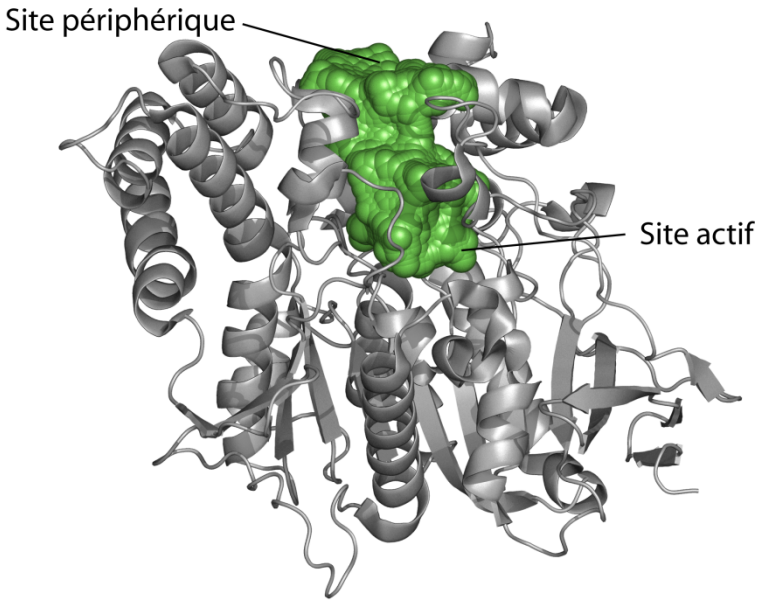

Figure 7. Vue d'ensemble de la TcAChE. La structure secondaire de l'enzyme est représentée par des « cartoons » gris. La surface de la gorge, qui plonge pratiquement jusqu'au centre de l'enzyme, apparaît en vert.

La structure atomique de l'AChE a permis de mettre en évidence deux régions essentielles à l'enzyme, situées de part et d'autre de la gorge (Fig.7) qui pénètre l'enzyme jusqu'à son centre : le site actif au fond, et le site périphérique à l'entrée.

2.4.1 Le site actif

Le site actif (Fig. 8), au sein duquel se trouve la machinerie catalytique, se subdivise en un sous-site estérasique et un sous-site « anionique ».

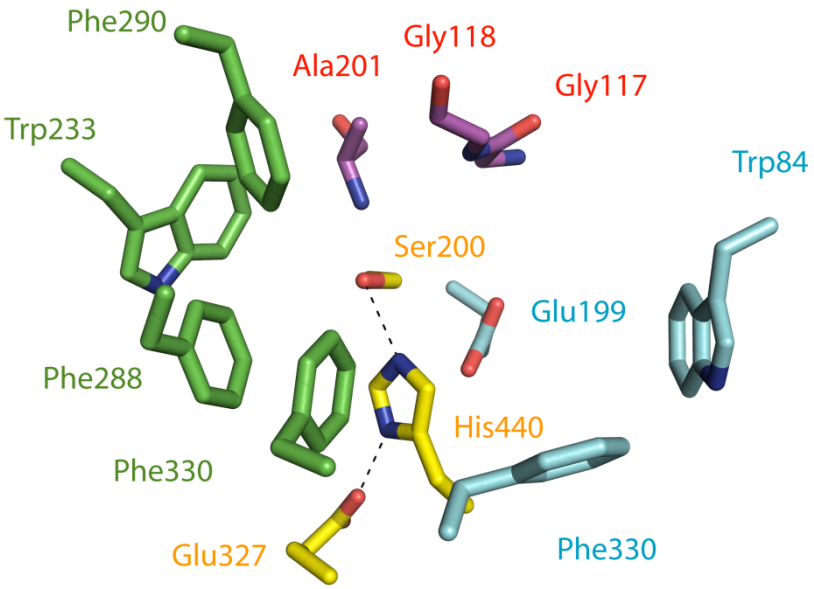

Figure 8. Le site actif de la TcAChE. Les résidus de la triade catalytique, du trou oxyanion, du site anionique et de la poche acyle sont représentés par des bâtonnets jaunes, orange, cyan et vert, respectivement. Les liaisons hydrogène qui assurent le maintien de la triade catalytique sont représentées par des tirets noirs.

Le site estérasique abrite la triade catalytique. Comme toutes les enzymes de la famille des protéases à sérine, l'AChE possède une telle triade. Les résidus qui la composent, Ser200, His440 et Glu327 ont été identifiés par mutagenèse dirigée [Gibney 1990; Shafferman 1992a]. La Ser200 est au cœur des deux étapes essentielles de la réaction catalytique. En effet, dans un premier temps, le groupement acétyle d'une molécule d'ACh se lie à la Ser200 pour former l'intermédiaire tétraédrique ; c'est l'étape d'acétylation. L'ACh est ensuite clivée, et la portion choline est expulsée. Enfin, l'AChE est régénérée au cours de l'étape de déacétylation, et l'acétate est expulsé. L'His440 permet le transfert de proton nécessaire aux deux étapes sus-mentionnées. Le Glu327

permet à la fois de polariser l'His440 et de la maintenir dans une orientation favorable à ce transfert.

L'efficacité catalytique remarquable de l'AChE ne provient pas uniquement de sa triade catalytique. Le fond de la gorge, à sa proximité, est en réalité tapissé de résidus utiles à l'optimisation de le la réaction catalytique. Ainsi, la charge négative qui se forme sur l'oxygène du carbonyle de l'ACh au cours de l'acétylation est stabilisée dans une poche nommée trou « oxyanion ». Cette poche est constituée des résidus Gly117, Gly118 et Ala201. De manière analogue, le groupement méthyle du carbonyle de l'ACh (puis de la sérine acétylée) est stabilisé par un ensemble de résidus aromatiques. Il s'agit des résidus Trp233, Phe288, Phe290 et Phe331 qui forment la « poche acyle ». Cette poche assure un rôle essentiel dans a sélectivité de l'AChE pour ses substrats [Harel 1992].

En face du site estérasique, au fond de la gorge, se situe le site anionique. L'origine de sa dénomination est historique : avant la publication de la structure de la *Tc*AChE, on imaginait qu'un ensemble de résidus chargés négativement permettait la stabilisation de la charge positive portée par la portion choline de l'ACh. En réalité, le site anionique est constitué des résidus Trp84, Glu199 et Phe330. Bien que le Glu199 contribue de manière électrostatique à la stabilisation de la charge positive de l'ACh, celle-ci est essentiellement assurée par les électrons π du Trp84, ainsi que ceux de la Phe330 dans une moindre mesure. Ainsi, le groupement choline de l'ACh peut établir des interactions de type cation-π avec les résidus aromatiques du site anionique. Le sous-site anionique est également impliqué dans la liaison à des inhibiteurs du site actif de l'AChE. Les structures des complexes de la *Tc*AChE avec les inhibiteurs edrophonium et tacrine [Harel 1993] montrent des interactions de type cation-π, et des empilements π (π-stackings), respectivement, avec le noyau indole du Trp84. On estime que près de la moitié de l'énergie libre de stabilisation de l'ACh est fournie par le site anionique [Harel 1996]. En outre, ce site permet des affinités beaucoup plus élevées que celles de l'ACh : l'affinité de l'analogue de substrat *m*-(*N*,*N*,*N*-trimethylammonio)-2,2,2-trifluoroacetophenone (TMTFA) est 10^{10} fois plus élevée que celle de l'ACh [Harel 1996]. Enfin, ce site joue également un grand rôle dans la spécificité de l'AChE.

2.4.2 La gorge aromatique

La gorge qui mène au site actif de l'AChE (Fig. 7) est à l'origine de débats récurrents concernant le fonctionnement de l'enzyme. Sa profondeur est de 20 Å, et les 14 résidus qui la tapissent sont essentiellement de nature aromatique. A mi-hauteur, elle présente un resserrement (*bottleneck*) au niveau des résidus Tyr121, Phe330 et Phe331. Dans la structure native, l'espace accessible au solvant est d'environ 3 Å. Si la structure était statique, seules des molécules d'eau pourraient traverser la gorge. La flexibilité conformationnelle est donc essentielle au fonctionnement de l'enzyme, en permettant le passage des substrats et des produits, vers et à partir du site actif.

Cette observation a été le point de départ d'une interrogation à laquelle aucune réponse définitive n'a encore été apportée. Comment une enzyme dont le site actif est si profondément enfoui peut-elle être aussi rapide ?

Diverses hypothèses ont été émises quant à l'origine de ce paradoxe apparent. L'existence d'une porte de sortie alternative (*backdoor*) a été proposée à la lumière de trajectoires calculées par Dynamique Moléculaire [Gilson 1994] montrant l'ouverture d'un passage par rotation de la chaîne latérale du Trp84.

La gorge de l'AChE guide et oriente les substrats [Ripoll 1993; Sussman 1991]. Bien que le mécanisme n'ait pas été confirmé, l'hypothèse d'un guidage électrostatique a toutefois été retenue. Puisque la charge électrique nette de l'enzyme est négative (-11e) [Nolte 1980], et compte tenu de la forte dépendance de l'activité de l'AChE à la force ionique [Changeux 1966], il a été imaginé que la répartition des charges puisse jouer un rôle dans le fonctionnement de l'enzyme. Il a ainsi pu être mis en évidence que l'AChE possède un champ électrostatique parallèle à l'axe de la gorge [Ripoll 1993]. Bien que la mutation de 7 des résidus acides à l'origine du champ électrostatique (situés près de l'entrée de la gorge) n'ait pas révélé une influence du potentiel électrostatique [Shafferman 1994], des simulations de mouvements browniens ont conforté l'idée d'un guidage électrostatique par la gorge des substrats [Antosiewicz 1995c; Antosiewicz & McCammon 1995b; Antosiewicz 1995a].

2.4.3 Le site périphérique

Le site périphérique (PAS pour « Peripheral Anionic Site » ; Fig. 9) est un site de liaison aux substrats et ligands situé à l'entrée de la gorge qui mène au site actif (Fig. 8). Son existence a été postulée dès les années 60 [Changeux 1966]. L'origine de son nom est historique, à l'instar de son homologue du site actif, le sous-site anionique. En effet, le PAS a d'abord été caractérisé par sa capacité à lier des ligands cationiques. Cette dénomination a été en quelque sorte légitimée lorsque fut identifié son résidu le plus important, le Trp279 [Harel 1993; Schalk 1994], bien que celui-ci soit absent dans l'AChE du poulet [Eichler 1994] et dans la BChE [Nicolet 2003].

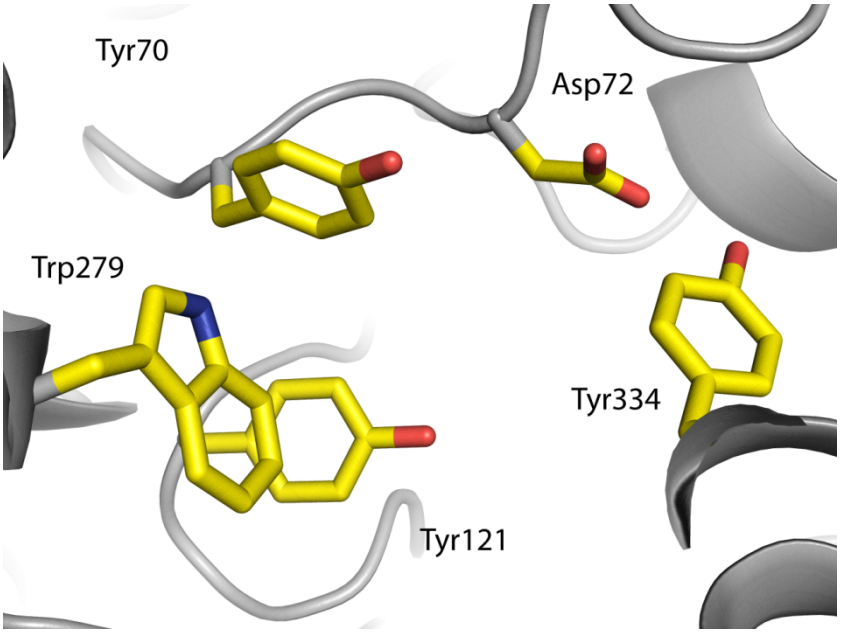

Figure 9. Le site périphérique de la Tc*AChE. Les résidus qui le composent sont représentés par des bâtonnets jaunes. La structure secondaire de l'enzyme apparaît en gris.*

Le PAS est essentiellement constitué de résidus aromatiques. Par des mesures de cinétique enzymatique combinées à l'utilisation de mutants et de ligands spécifiques du PAS, on a pu identifier en sus du Trp279, les résidus Tyr70 et Tyr121 [Schalk 1995], l'Asp72 et la Tyr334 [Barak 1994; Shafferman 1992b]. La caractérisation du PAS a été

confirmée par les structures des complexes de l'AChE avec le décaméthonium [Harel 1993], la fasciculine [Bourne 1995; Harel 1995; Kryger 2000], le propidium et d'autres inhibiteurs spécifiques du PAS [Bourne 2003; Bourne 2004], ainsi que par dynamique moléculaire [Cavalli 2004].

Le rôle du PAS n'a pas encore été complètement élucidé. Toutefois, il joue un rôle dans les phénomène d'inhibition par le substrat dans le cas de l'AChE [Bergmann 1950; Radic 1991], et d'activation par excès de substrat dans les cas de l'AChE de drosophile [Stojan 1998] et de la BChE [Masson 1996; Masson 1997]. Les structures de la mAChE et de la *Tc*AChE en présence d'une haute concentration de substrat (ou de produit) ont confirmé la fixation de ce dernier au PAS [Bourne 2006; Colletier 2006a]. A l'opposé, il a été proposé que la liaison de l'ACh à l'Asp72 soit la première étape de la catalyse [Mallender 2000]. Le PAS pourrait permettre l'accélération de la réaction catalytique aux basses concentrations de substrat [Brochier 2001; Nachmansohn 1945]. Il pourrait donc agir comme un régulateur de l'activité catalytique, en adaptant l'efficacité de l'AChE à la concentration d'ACh. Il est alors tentant de transposer cette observation au contexte physiologique. Lors de la libération de l'ACh, sa concentration pourrait inhiber l'AChE suffisamment longtemps pour lui permettre de se fixer au récepteur nicotinique et de transmettre l'influx nerveux. La concentration en ACh libre serait alors propice à une activation de l'AChE, et celle-ci pourrait remplir son rôle cholinergique.

Le rôle du PAS pourrait ne pas être uniquement d'ordre stérique. Très tôt, il lui fut associé un rôle de régulateur allostérique de l'activité de l'AChE [Changeux 1966 ; Rosenberry 1975]. La liaison de ligands spécifiques au PAS module l'activité catalytique [Barak 1994; Eastman 1995; Radic 1995; Rosenberry 1996]. Il fut observé que le mutant W84A était réfractaire à l'inhibition par le propidium [Ordentlich 1993a], ce qui suggéra aux auteurs la possibilité d'un « dialogue » (*cross-talk*) entre les deux sites. La mutagenèse de résidus clés du PAS et de la gorge avait déjà permis de suggérer la possibilité qu'un signal transite du PAS au site actif [Shafferman 1992b]. La liaison de substrats dans le site actif provoque le *quenching* de la fluorescence de sondes pécifiques du PAS telles que le propidium [Taylor & Lappi 1975] et la thioflavine T [De Ferrari 2001a; Harel 2008].

2.5 Fonctionnement : mécanisme catalytique et paradoxe

L'AChE est une enzyme extrêmement rapide. Pourtant, son site actif est enfoui au fond d'une gorge étroite et profonde. Un paradoxe apparent naît de cette double constatation : comment une enzyme dont le site actif est si difficile d'accès au substrat peut-elle être aussi rapide ?

Dans la partie précédente, nous avons vu qu'une partie de la réponse résidait dans le PAS. Celui-ci permet d'accélérer la catalyse aux basses concentrations. En outre, le potentiel électrostatique de l'AChE permet d'attirer l'ACh, chargée positivement, vers la gorge.

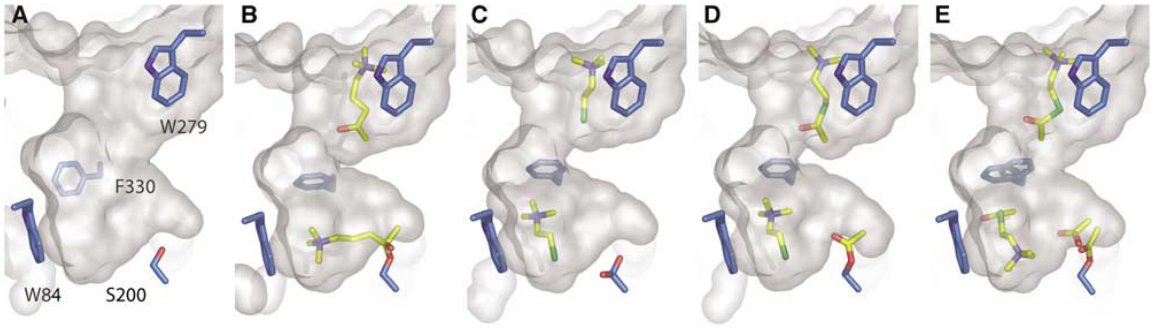

Figure 10. Le trafic des produits et des substrats dans la gorge de la TcAChE. La surface de la gorge apparaît en gris A/ dans sa forme native, et en présence B/ d'OTMA, un analogue de substrat non hydrolysable, C/ de 20 mM TCh, D/ de 20 mM ATCh et E/ 500 mM ATCh. Les résidus Ser200, Trp84, Phe330 et Trp279 sont représentés par des bâtonnets bleus. Les ligands apparaissent sous forme de bâtonnets jaunes. Reproduit de [Colletier 2006a].

Les cinétiques de l'AChE mesurées à haute concentration en substrat [Stojan 2004] ont permis de mettre en évidence deux causes d'inhibition par le substrat : a) la présence de la choline après dissociation de l'ACh gêne l'expulsion de l'acétate et b) la liaison d'un substrat au PAS gêne l'étape de déacétylation. Sur cette base, et en employant une méthode s'apparentant à la cristallographie cinétique, il a été possible d'obtenir des instantanés du trafic des substrats et produits au sein de la gorge de l'AChE [Bourne 2006; Colletier 2006a] qui illustrent parfaitement le phénomène d'inhibition par le substrat (Figure 10). Ainsi, une concentration modérée en substrat ou en produit (20mM) aboutit à la fixation de l'un ou l'autre au niveau du PAS et d'un produit au niveau du CAS (Fig. 10C/D). Une concentration plus élevée révèle (Fig. 10E), elle, la présence d'une molécule de substrat à la fois sur le PAS et sur le CAS. Le trempage de cristaux

d'AChE dans une solution contenant un analogue non-hydrolysable (Fig. 10B) de substrat a permis de capturer l'intermédiaire tétraédrique qui suit l'étape d'acétylation. On peut noter que dans tous les cas, la Phe330 agit comme un clapet qui se referme sur le site actif, l'isolant ainsi de l'extérieur. Si cet isolement peut permettre d'accélérer l'hydrolyse en favorisant l'attaque par une molécule d'eau sur la liaison à cliver, il explique également en partie la perturbation du trafic.

Les considérations qui précèdent montrent les limites du fonctionnement de l'AChE à haute concentration de substrat. Toutefois, l'efficacité catalytique de l'AChE implique l'entrée et la sortie de 1000 à 20000 molécules de substrats, et donc de produits, chaque seconde. Compte tenu de l'enfouissement du site actif et de l'étroitesse de la gorge, cette efficacité reste difficile à concevoir, même à des concentrations plus faibles en substrats. Il est évident qu'une flexibilité conformationnelle de l'enzyme, et en particulier de sa gorge, sont nécessaires à l'accomplissement de son rôle.

Des simulations de dynamique moléculaire ont étayé l'hypothèse de l'existence d'une porte de sortie annexe (*backdoor*) au niveau du Trp84 [Axelsen 1994; Gilson 1994; Tai 2001; Tai 2002]. Bien que la mutagenèse de résidus clés dans l'ouverture de la *backdoo*r n'ait pas pu confirmer son existence [Faerman 1996; Kronman 1994; Velan 1996], une activité résiduelle de l'AChE a pu être mesurée en présence de facsiculine [Eastman 1995; Marchot 1993; Radic 1994; Radic 1995], un peptide qui obstrue l'ouverture de la gorge en se liant au PAS [Bourne 1995; Harel 1995; Kryger 2000]. Il est donc probable que des mouvements de la boucle Ω, mis en évidence par dynamique moléculaire [Bui & McCammon 2005; Bui & Andrew McCammon 2008; Shi 2003; Xu 2008c], soient responsables de l'ouverture d'un canal suffisamment large pour laisser sortir la choline. Toutefois, le temps de vie de la *backdoor* serait alors trop court pour pouvoir être caractérisé structuralement par des méthodes conventionnelles.

On peut également noter que la boucle acyle est suspectée de permettre l'ouverture d'un canal similaire pour permettre l'expulsion de l'acétate [Kovach 1994]. La mobilité de cette boucle a été mise en évidence dans le complexe de l'AChE avec la galanthamine [Greenblatt 2004].

2.6 Rôles non-classiques

L'AChE joue également des rôles autres que celui de la terminaison de la transmission de l'influx nerveux au sein des synapses cholinergiques [Silman 2005]. Il semble que tous ces rôles non-classiques impliquent spécifiquement le PAS.

Un épissage alternatif induit par un stress produit une AChE dont l'extrémité C-terminale est impliquée dans la différentiation hématopoïétique. L'AChE pourrait agir comme une protéine d'adhésion lors du développement et du maintien des synapses. Puisque l'AChE possède une grande homologie avec la neuroligin, une protéine d'adhésion neuronale, elle pourrait comme cette dernière jouer un rôle dans l'autisme et certains retards mentaux. On suspecte par ailleurs l'AChE de jouer un rôle dans la croissance des neurites (les prolongements cellulaires des neurones, c'est-à-dire les axones et les dendrites).

Le rôle non-classique qui suscite le plus d'intérêt est l'implication de l'AChE dans la maladie d'Alzheimer (MA). Elle se caractérise par la perte progressive des facultés cognitives (mémoire, raisonnement, orientation, langage). La MA représente près de 70% des causes de démence sénile. Bien que la MA soit sous-diagnostiquée, des études épidémiologiques permettent néanmoins d'estimer sa prévalence [Lobo 2000; Ramaroson 2003]. Elle touche environ 1% des personnes entre 65 et 69 ans, et plus de 40% des personnes entre 90 et 95 ans. En France, 850000 personnes étaient atteintes par la MA en 2007, et on compte l'apparition de 165000 nouveaux cas chaque année. La MA est une maladie directement liée à l'âge : le vieillissement actuel de la population entraînera inévitablement une forte augmentation de la prévalence. On peut d'ores et déjà anticiper que l'impact sur la société sera considérable, non seulement sur le plan financier, mais également social et humain. C'est dans ce contexte qu'a été lancé en Fance en 2007 le Plan Alzheimer : il prévoit un budget de 1,6 milliards d'euros sur 5 ans (2008-2012) consacrés à la recherche de traitements et à l'amélioration de la prise en charge des patients.

La MA se caractérise notamment par une perte neuronale et une diminution de la production d'ACh, essentiellement au niveau du cortex cérébral et de l'hippocampe, régions impliquées dans les processus cognitifs [Davies & Maloney 1976; Whitehouse 1982]. Sur le plan anatomique, les signes neuropathologiques de la MA se manifestent par la présence de plaques amyloïdes (dites séniles) et d'enchevêtrement de neurofibrilles qui finissent par tuer les neurones. Il a été montré que l'AChE promeut l'assemblage du

peptide Aβ en fibres à l'origine des plaques séniles [Bartolini 2003; Inestrosa 1996], probablement au travers d'interactions au niveau du PAS. Bien que la pertinence physiologique de cette observation n'ait pas été clairement établie, on sait que les ChEs sont associées, dans le cerveau des sujets atteints, aux plaques amyloides [Carson 1991; Moran 1993] et aux enchevêtrements de neurofibrilles [Mesulam 1992].

En conclusion, les rôles non-classiques de l'AChE sont généralement associés à des pathologies neurologiques et semblent converger vers une implication de son PAS. Ce site est donc une cible à privilégier dans la recherche de traitements contre la MA et les autres maladies neurodégénératives associées à l'AChE. La plupart des médicaments anti-Alzheimer sont actuellement des inhibiteurs de l'AChE qui agissent au niveau de son site actif en vue de restaurer la fonction cholinergique, et donc d'améliorer les fonctions cognitives des personnes touchées. Les molécules de la future génération (cf partie 3) prennent en compte le rôle du PAS dans l'apparition des plaques séniles. Ces inhibiteurs à vocation double, qui agissent à la fois au niveau du site actif et du PAS, devraient non seulement restaurer la fonction cholinergique, mais également retarder le développement des plaques. Bien évidemment, ces traitements ne peuvent, au mieux, que stopper l'évolution de la maladie, et doivent donc être prescrits le plus tôt possible. Mais en attendant d'être en mesure de détruire les plaques séniles et de remplacer les neurones perdus, cette solution semble la plus prometteuse.

3. L'AChE, CIBLE D'UN VASTE

RÉPERTOIRE DE LIGANDS

3. L'AChE, CIBLE D'UN VASTE RÉPERTOIRE DE LIGANDS

Dans cette partie, nous présentons les ligands utilisés en complexe avec l'AChE au cours de cette thèse. Chacune de ces différentes classes de molécules se lie spécifiquement au site actif, au site périphérique ou pontent les deux sites. En présentant sommairement leur origine et leurs interactions avec l'AChE, nous soulignerons l'importance de mieux connaître leur mécanisme d'inhibition. Nous justifierons également leur emploi en tant que sondes spécifiques de leurs sites de fixation à l'AChE.

3.1 Les organophosphorés

D'un point de vue général, les composés organophosphorés (OP) sont une classe de molécules organiques qui possèdent au moins un atome de phosphore (l'ADN, per exemple). Par abus de langage, on emploie le terme d'OP pour désigner les insecticides, les pesticides et les toxiques de guerre neurotoxiques qui répondent à cette définition. Ces molécules sont issues de la course à l'armement au cours des deux guerres mondiales. La première guerre mondiale avait toutefois été le théâtre de l'utilisation de composés similaires, les organochlorés tels que le gaz moutarde.

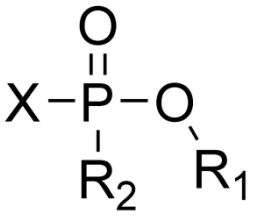

Schéma 2. Structure générale des OP.

Les OP possèdent la structure générale suivante (Schéma 2). L'atome de phosphore, pentavalent, est lié par une double liaison à un atome d'oxygène (ou de soufre), à un groupement partant (X) et à deux substituants (R_1, lié par un atome d'oxygène, et R_2).

3.1.1 Origine et utilisation des organophosphorés

Bien que la synthèse des premiers OP remonte au XIX^{e} siècle, leur développement en temps qu'insecticides a démarré dans les années 30 [Costa 2006]. Un chimiste allemand, Gerhard Schrader, est à l'origine du tout premier insecticide commercialisé (Bladan), et de l'un des plus connus, le parathion (1944). Depuis, des centaines d'autres OP de ce type ont été synthétisés.

Alors qu'il était employé par le conglomérat allemand IG Farben, Gerhard Schrader découvrit « accidentellement » le premier agent neurotoxique, le tabun (GA, 1936). Le contexte de la seconde guerre mondiale l'amena à développer trois autres composés : le sarin, (GB, 1938), le soman (GD, 1944) et le cyclosarin (GF, 1949). Ces OP constituent la famille des agents G (German) (Schéma 3).

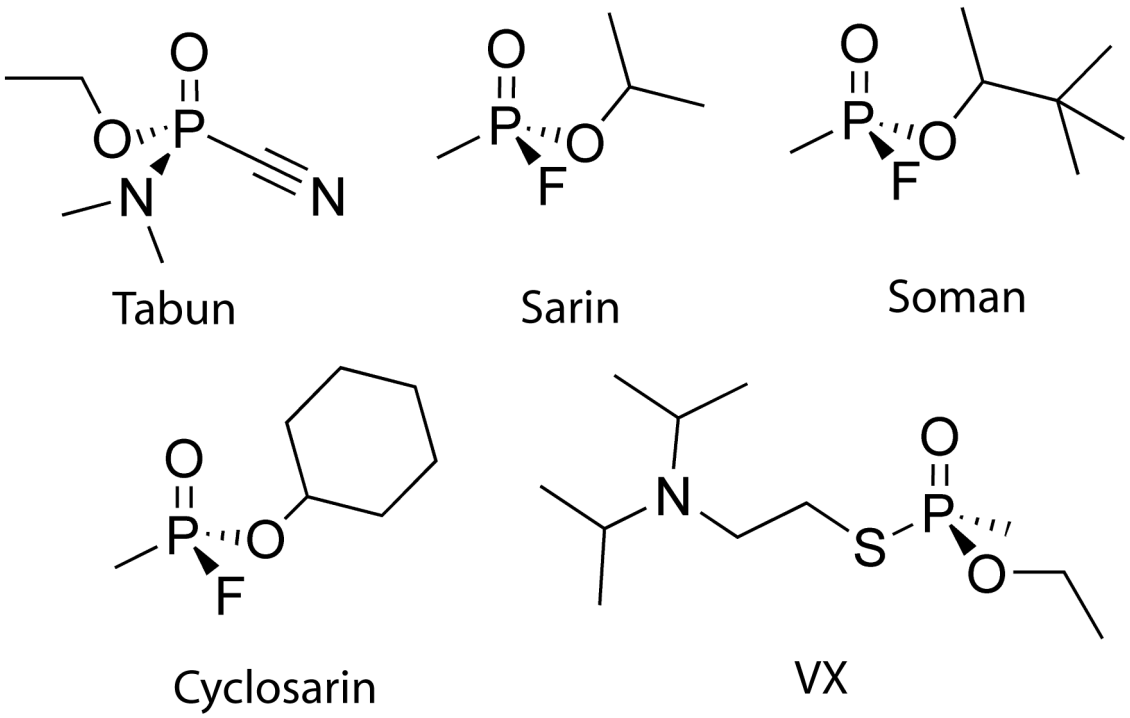

Schéma 3. Structure desOP de la série G et du VX.

D'autres OP ont été développés par la suite. Les britanniques ont mis au jour, dans les années 50, la famille des agents V, parmi lesquels le VX est certainement le plus connu. Les russes ont complété la gamme plus tardivement (entre les années 70 et 90), avec les agents Novichok (nouveau venu en russe) [Bagjar 2006].


MASSACRE BY POISON GAS

Many die, 1,200 collapse in Tokyo Tube attack

SIX people died today and more than 1,200 panic-stricken commuters collapsed as clouds of Nazi nerve gas swept through Tokyo's rush-hour subway system.

Figure 11. L'attaque du métro de Tokyo au gaz sarin.

Les OP ont été utilisés à plusieurs reprises de manière avérée. L'armée irakienne en a fait usage contre des civils kurdes en 1988 [Macilwain 1993]. L'usage de sarin et de VX, par la secte Aum Shinrikyō, dans des attentats et assassinats perpétrés entre 1994 et 1995, a fait émerger une menace terroriste chimique : les agents neurotoxiques ne sont plus limités aux champs de bataille. Le plus tristement célèbre de ces attentats est celui de l'attaque au sarin d'une rame bondée du métro de Tokyo le 20 mars 1995, qui a fait douze morts et plus de 5000 blessés (Figure 11) [Nagao 1997].

On recense chaque année plus de 3 millions de cas d'intoxication par des OP, dont 200000 sont mortels (suicides, majoritairement) [Eddleston 2008]. Des séquelles musculaires et cognitives sont souvent constatées chez les survivants.

3.1.2 Mécanisme d'inhibition de l'AChE par les OP

Les agents neurotoxiques sont en général propagés sous forme d'aérosols, et pénètrent ensuite par voie cutanée. L'une des cibles primaires des OP est alors l'AChE, et plus précisément l'AChE du système cholinergique lorsque les toxiques ont franchi la barrière

hémato-encéphalique (BHE). L'inhibition de l'AChE se fait en deux étapes. Dans un premier temps, l'OP se fixe à la sérine catalytique, en résultat d'une attaque nucléophile de type SN2, avec départ concomitant du groupement partant, et inversion de la stéréochimie de l'OP. L'intermédiaire tétraédrique alors formé ressemble à celui qui existe lors de la liaison de l'ACh à la sérine catalytique lors de la réaction catalytique. Dans un second temps, l'un des substituants de l'OP est clivé (cela correspond en général à une déalkylation). Cette seconde réaction aboutit à une enzyme « vieillie » : l'AChE est alors irréversiblement inhibée. La létalité des OP provient de la ressemblance entre la réaction catalytique et la réaction d'inhibition par les OP : en quelque sorte, cette dernière est une hydrolyse incomplète. Aucune molécule connue ne permet de réactiver une AChE vieillie. L'AChE peut toutefois être réactivée avant le vieillissement. Une famille de molécules appartenant à la classe des oximes peut remplir ce rôle plus ou moins efficacement selon le couple OP/oxime considéré (cf. partie 3.1.3).

En pratique, l'inhibition de l'AChE par les OP aboutit à l'accumulation d'ACh dans les synapses cholinergiques et les jonctions neuromusculaires, et provoque en conséquence la réponse exagérée des récepteurs cholinergiques (nicotiniques et muscariniques). Trois syndromes sont associés à l'intoxication aigüe par les OP. Le syndrome muscarinique aboutit essentiellement à une hypersécrétion (salivaire, bronchique…), un relâchement des muscles lisses et des troubles cardiaques. Le syndrome nicotinique, lié à une dépolarisation persistante des muscles striés, conduit à des troubles musculaires (jusqu'à la paralysie) et une stimulation du système sympathique (tachycardie, hypertension…). Le syndrome central se traduit par une excitation (tremblements, convulsions, céphalées…) puis une dépression (somnolence voire coma) du système nerveux central (SNC).

Des modèles du mécanisme d'inhibition ont été construits peu à peu, essentiellement par mutagenèse dirigée combinée à la cinétique enzymatique [Saxena 1993; Saxena 1998; Shafferman 1996; Viragh 1997]. L'obtention des structures de l'AChE conjuguée à plusieurs des OP susmentionnés a permis de conforter et d'améliorer ces modèles (Tableau 1).

OP	Espèce	Etat de l'enzyme	Code PDB	Référence
soman	*Tc*	vieillie	1som	[Millard 1999b]
sarin	*Tc*	vieillie	1cfj	[Millard 1999b]
VX	*Tc*	non-vieillie	1vxr	[Millard 1999a]
VX	*Tc*	vieillie	1vxo	[Millard 1999a]
sarin	m	non-vieillie	2jgg	[Hornberg 2007b]
sarin	m	vieillie	2jgl[1]	[Hornberg 2007b]
VX	m	non-vieillie	2jgh	[Hornberg 2007b]
VX	m	vieillie	2jgl[1]	[Hornberg 2007b]
tabun	m	non-vieillie	3dl4	[Carletti 2008b; Ekström 2006b]
tabun	m	vieillie	3dl7	[Carletti 2008b; Ekström 2006b]

Tableau 1. Structures des conjugués d'AChE et d'OP résolues.

Au cours de cette thèse, nous nous sommes intéressés au cas du soman. Parmi les OP les plus « courants », il restait le seul duquel la forme non-vieillie de son conjugué à une AChE n'avait pas été caractérisée. L'explication repose sur le temps de demi-vie ($t_{1/2}$) particulièrement court du conjugué AChE/soman non-vieilli (le $t_{1/2}$ est directement lié à la vitesse de vieillissement). Dans le cas de la huAChE, le $t_{1/2}$ de l'enzyme inhibée par le soman est d'environ 3 min, alors qu'il est compris entre 3 h et 231 h pour les autres OP [Worek 2002]. Cette propriété contribue à faire du soman l'un des agents neurotoxiques les plus dangereux. Puisque les antidotes existants ne sont pas efficaces à réactiver l'AChE après son vieillissement, il est crucial de disposer d'un composé suffisamment efficace pour agir dans un délai aussi court.

[1] Les structures des formes vieillies des conjugués mAChE/VX et mAChE/sarin sont identiques [Hornberg 2007b].

C'est dans ce contexte que nous avons cherché à caractériser structuralement les différentes étapes de l'inhibition de la *Tc*AChE par le soman. Les structures obtenues devraient permettre d'élaborer des réactivateurs à l'efficacité accrue (cf. partie 6.2) [Sanson 2009].

3.1.3 Réactivation de l'AChE inhibée par un OP

Les traitements

Le traitement prophylactique actuel (recommandé par les armées de l'OTAN) repose sur l'injection préalable de bromure de pyridostigmine, un composé appartenant à la classe des carbamates [R-N-(C=O)O-R]. La pyridostigmine vise à inhiber transitoirement l'AChE. Ce traitement est loin d'être parfait puisque ce composé ne franchit pas la BHE. Il a toutefois été utilisé au cours de la première guerre du Golfe en 1991 pour protéger les soldats en cas d'attaque chimique [Soreq & Seidman 2001]. La pyridostigmine est suspectée d'être, au moins partiellement, à l'origine des troubles cognitifs et physiologiques rapportés par les vétérans de cette guerre, et connus aujourd'hui sous le nom de syndrome de la guerre du Golfe. Le stress auquel étaient soumis les soldats aurait permis à la pyridostigmine de franchir la BHE. L'origine du syndrome a probablement, toutefois, des causes multifonctionnelles.

En cas d'intoxication par les OP, le traitement repose sur l'injection de trois composés pour pallier les défaillances vitales qui en résultent, en sus des procédures classiques de réanimation. Un anticonvulsivant (benzodiazépines telle que le diazépam) réduit l'excitabilité du neurone post-synaptique. L'atropine, un antagoniste cholinergique (antimuscarinique), permet le blocage des récepteurs cholinergiques muscariniques au niveau du SNC et du système nerveux autonome, mais pas au niveau des jonctions neuromusculaires. Une oxime, enfin, doit permettre la réactivation de l'AChE non encore vieillie.

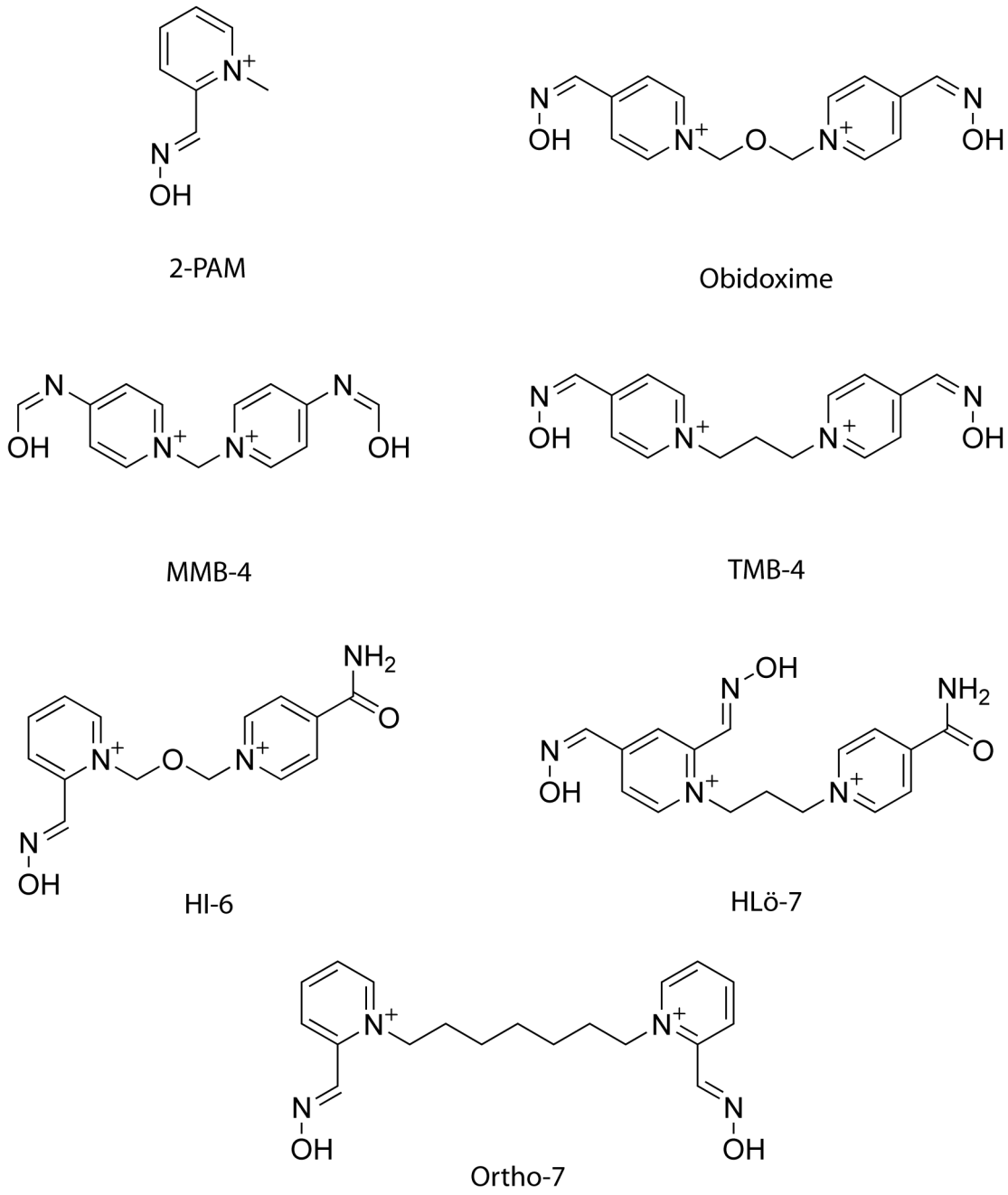

Schéma 4. Structures de sept oximes parmi les plus étudiées.

C'est l'inefficacité des antimuscariniques à restaurer la fonction cholinergique au niveau des jonctions neuro-musculaires qui à conduit au développement des oximes quaternaires dans les années 50. Le 2-PAM (pralidoxime, 2-pyridine aldoxime) est la première oxime à avoir été synthétisée [Wilson & Ginsburg 1955]. Le TMB-4 (trimedoxime), un composé bispyridinium, s'avéra plus efficace que le 2-PAM, notamment en cas d'empoisonnement au tabun [Hobbiger & Sadler 1959; Poziomek 1958]. Des milliers d'autres oximes ont été synthétisées depuis (Schéma 4). L'obidoxime (toxogonine), synthétisée par l'équipe de

Hagedorn, reste à ce jour l'un des meilleurs réactivateurs d'AChE inhibée par des pesticides OP. La même équipe est également à l'origine de la synthèse de deux réactivateurs, le HI-6 [Oldiges & Schoene 1970] et le H-Lö7 [Eyer 1992], surclassant toutes les oximes susmentionnées dans leur efficacité à réactiver l'AChE inhibée par des agents neurotoxiques.

Seuls la pralidoxime et l'obidoxime ont été commercialisées à ce jour, malgré une efficacité médiocre à réactiver l'AChE inhibée notamment par le soman et le cyclosarin [Worek 2005]. Le HI-6 et le TMB-4 sont également employés par l'armée américaine.

Bases structurales du mécanisme de réactivation

La réactivation par les oximes repose sur l'attaque nucléophile de l'atome de phosphore de l'OP lié à la sérine catalytique par la fonction oximate (NO^-) de l'oxime. Dans un premier temps, l'oxime se lie à l'adduit OP, formant un conjugué oxime-phosphyle-AChE réversible (état de transition penta-coordonné). La sérine catalytique est ensuite libérée par le départ de l'oxime phosphylée. L'état de protonation de l'oximate est crucial pour la réactivation : l'efficacité des oximes dépend donc du pH.

L'efficacité des oximes à réactiver l'AChE a été testée pour de nombreux couples OP/oximes [Aurbek 2006; Worek 2002; Worek 2004]. Malgré l'accumulation de nombreuses données, aucune relation claire reliant l'efficacité et la structure de l'oxime n'a pu être établie. En conséquence, l'efficacité d'une oxime est difficile à prévoir. La modélisation [Kovarik 2004; Kovarik 2006; Luo 2003; Wong 2000] puis la caractérisation par cristallographie aux rayons X [Ekström 2006a; Ekström 2007] de structures d'AChEs en complexe avec des oximes a permis de confirmer et de révéler les sites d'interaction entre AChE et oximes. Ainsi, le 2-PAM se fixe dans le site actif de la *Tc*AChE via des interactions de type cation-π avec le Trp84 (code PDB 2vq6). Il a été mis en évidence que les oximes bis-pyridinium HI-6, obidoxime, ortho-7 et HLö-7 [Ekström 2007] se lient au niveau du PAS de la mAChE [Ekström 2006a] via des interactions de type cation-π impliquant un noyau pyridinium, pris en sandwich entre le Trp286(279) (la numérotation est celle de la mAChE ; les nombres entre parenthèses réfèrent à la *Tc*AChE) et la Tyr124(121) (HI-6 et HLö-7) ou le Trp286(279) et la Tyr72(70) (obidoxime et ortho-7). Les changements conformationnels des résidus du PAS impliqués dans la liaison aux oximes dans les complexes susmentionnés suggèrent

qu'une flexibilité de l'enzyme est nécessaire pour accommoder ces oximes. En outre, en se liant au niveau du PAS, la fonction oximate de ces oximes pointe vers le fond de la gorge. Il a été montré que la réactivation nécessite l'alignement de l'oximate, du phosphore de l'OP et de l'oxygène de la sérine catalytique [Ashani 1995]. La liaison d'une oxime au niveau du PAS permet non seulement une meilleure stabilisation de l'oxime dans l'AChE, mais aussi une orientation plus favorable à la réactivation. L'encombrement stérique du site actif de l'AChE joue également un rôle dans l'efficacité des réactivateurs.

Obtenir la structure de complexes ternaires AChE-OP-oxime représente une des pistes les plus prometteuses en vue de concevoir des réactivateurs à spectre d'OP plus larges et plus efficaces que les oximes synthétisés jusqu'à ce jour. L'obtention de ces structures par cristallographie aux rayons X est un défi pour plusieurs raisons. D'une part, les oximes bispyridinium sont des molécules flexibles. D'autre part, la liaison de l'oxime à l'AChE phosphorylée conduit à la réactivation. Cependant, les structures de la mAChE non-vieillie inhibée par le tabun et en complexe avec le HLö-7 ou l'ortho-7 [Ekström 2007] (codes PDB 2jez et 2jf0) et de la mAChE non-vieillie ou vieillie inhibée par le sarin en complexe avec le HI-6 ont été obtenues [Ekstrom 2009] (code PDB 2whp et 2whq). Pour y parvenir, les cristaux ont été trempés successivement dans des solutions contenant l'OP et l'oxime pendant des durées appropriées (de l'ordre de la minute). Ces structures ont permis de préciser les mécanismes de la réactivation.

Les oximes présentent un inconvénient majeur. Après la réactivation, la phosphyloxime formée peut inhiber à nouveau l'AChE [Ashani 2003; Luo 1999]. Toutefois, dans le cas de la réactivation de l'AChE inhibée par le soman, les phosphyloximes sont instables si la fonction oxime est portée par le pyridinium en position 2 (c'est le cas du 2-PAM, du HI-6 et du HLö-7). L'inhibition par la phosphyloxime est alors moins probable en comparaison à une réactivation par des oximes de type 4-pyridinium comme le TMB-4.

Les données concernant l'efficacité des réactivateurs doivent être nuancées. Pour des raisons éthiques évidentes, les essais sont pratiqués *in vitro* ou sur des animaux, puis sont extrapolés à l'homme. En outre, les oximes ne représentent pas l'unique stratégie de lutte contre l'empoisonnement aux OP. Deux types de bioépurateurs sont également en développement.

Les piégeurs catalytiques

Les enzymes à l'essai pour ce rôle sont les carboxylestérases [Maxwell & Brecht 2001] et les ChEs [Masson 2008]. La huBChE devrait remplacer la pyridostigmine au sein de l'armée américaine, et être commercialisée à la fin de l'année 2009 (Protexia®).

Les piégeurs catalytiques, injectés dans le sang de manière préventive, peuvent inactiver les OP en les liant de manière irréversible avant qu'ils n'atteignent leur cible, l'AChE, en particulier au niveau du SNC et des jonctions neuromusculaires.

Les bioépurateurs catalytiques

Les bioépurateurs catalytiques ne se contentent pas de piéger l'OP, mais le dégradent également. C'est le cas de la phosphotriestérase (PTE) bactérienne [Dumas 1990] et de la paraoxonase humaine [Rochu 2007] (ces enzymes sont optimisées par évolution dirigée). Des mutants de huBChE ont été développés, parmi lesquels le G117H [Lockridge 1997; Millard 1995], mais ils possèdent une activité beaucoup plus faible que celle de la PTE.

3.2 Toxines

L'AChE est la cible de nombreuses toxines, d'origine animale, végétale et fongique. Nous nous focaliserons sur deux exemples : la fasciculine 2 (FAS2) et l'aflatoxine. L'alkaloïde d-tubocurarine est également connue pour ses propriétés anesthésiques.

3.2.1 La fasciculine 2

Les fasciculines sont des toxines aux propriétés anticholinestérasiques présentes dans le venin de certains serpents. La FAS2 a été isolée à partir du venin du mamba vert. C'est un peptide de 61 résidus qui présente une structure en trois doigts [le Du 1996]. Sa constante d'inhibition est de l'ordre du picomolaire [Marchot 1993]. Elle inhibe l'AChE en se fixant à l'entrée de la gorge au niveau du PAS [Bourne 1995; Harel 1995; Kryger 2000], bloquant ainsi le trafic des substrats et produits (Fig.12). L'étude des complexes

d'AChE et de FAS2 a permis d'obtenir des informations sur la dynamique et le fonctionnement de l'AChE, notamment en ce qui concerne le phénomène d'allostérie et l'ouverture de la *backdoor* [Eastman 1995; Radic 1995; Rosenberry 1996; Shi 2003; Tai 2002].

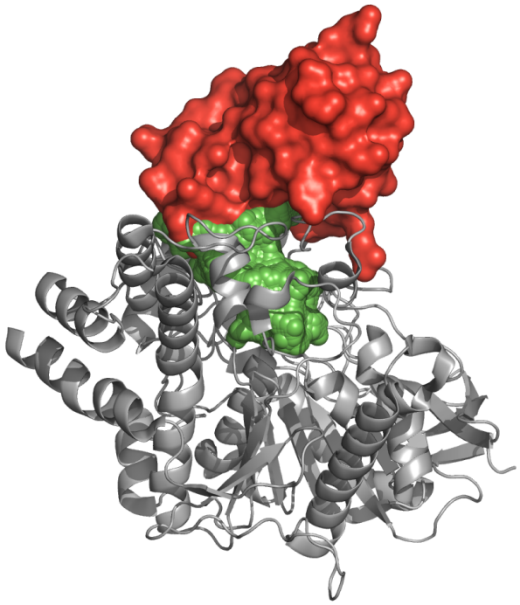

Figure 12. Inhibition de la Tc*AChE par la fasciculine. La structure secondaire de la TcAChE apparaît sous forme de rubans. La gorge de la* Tc*AChE est en vert. La surface de la fasciculine est en rouge.*

3.2.2 L'aflatoxine

L'aflatoxine est une toxine produite par des champignons de la famille des *Aspergillus* (l'espèce *Aspergillus flavus* a donné son nom à la toxine : A-fla). L'aflatoxine B1 (AB1) est un sous-produit métabolique de la toxine produite par le champignon, laquelle est non seulement toxique mais est également considérée comme l'un des cancérogènes les plus puissants recensés à ce jour [1993]. Les champignons *Aspergillus* poussent préférentiellement sur des cultures céréalières, sous des climats chauds et humides : l'AB1 est un enjeu de santé publique, essentiellement dans les pays en voie de développement. Pour éviter l'exposition à cette toxine, la teneur en AB1 doit pouvoir être mesurée.

C'est dans ce contexte que nous avons proposé l'AChE comme biosenseur capable de détecter l'AB1 à de très faibles concentrations [Hansmann, Sanson, Stojan, Weik, Marty & Fournier 2009] (annexe 2). En effet, l'AB1 est également un inhibiteur du PAS de l'AChE, même si ce rôle n'est pas pertinent dans le phénomène de toxicité. Au cours de cette thèse, nous avons ainsi cherché à élucider la structure de l'AChE en complexe avec l'AB1 (cf. partie 6.3). Les propriétés luminescentes de l'AB1 nous ont également permis de mettre au point une méthode pour sonder la dynamique lente de l'AChE aux températures comprises entre 100 et 240K (cf. partie 6.4).

3.3 Les médicaments anti-Alzheimer

Nous avons vu plus haut (partie 2.6) que l'AChE est une cible privilégiée pour les médicaments anti-Alzheimer. A l'exception de la memantine (2003, Ebixa®), qui est un antagoniste des récepteurs nicotiniques, tous les médicaments anti-Alzheimer sont des inhibiteurs des ChEs. La tacrine (1993, Cognex®) a été le premier médicament utilisé pour lutter contre la MA. Au cours de la décennie qui a suivi, plusieurs autres molécules ont reçu des autorisations de mise sur le marché : le donépézil (1997, E2020, Aricept®), la rivastigmine (1997, Exelon®) et la galanthamine (2001, Reminyl®). L'huperzine A (HupA) est actuellement la drogue la plus prometteuse [Sabbagh 2009]. C'est un alkaloïde extrait de la plante *Huperzia Serrata*, laquelle est utilisée depuis des siècles dans la médecine chinoise. L'HupA serait actuellement l'inhibiteur de ChE le plus efficace pour traiter la MA : elle franchit plus facilement la BHE, sa biodisponibilité est plus grande et sa durée d'action est plus longue. L'efficacité de toutes ces drogues est toutefois très modérée. En outre, en raison de leurs nombreux effets secondaires, elles sont souvent mal tolérées.

La plupart des médicaments susmentionnés se lient au niveau du site actif de la TcAChE, comme en attestent les structures de la *Tc*AChE avec la tacrine [Harel 1993] (code PDB 1acj ; Fig. 13), le donépézil [Kryger 1998] (code PDB 1eve), la rivastigmine [Bar-On 2002] (code PDB 1gqr), la galanthamine [Greenblatt 2004] (code PDB 1w6r) et l'HupA [Raves 1997] (code PDB 1vot). Le donépézil se lie également au niveau du PAS.

Les potentielles drogues anti-Alzheimer testées actuellement exploitent le deuxième site de fixation [Colletier 2006b; Rydberg 2006]. En se fixant au PAS, ces nouvelles molécules pourraient en particulier permettre de bloquer la fibrillogenèse d'Aβ. Cette thèse a été l'occasion de caractériser les relations structurales entre l'AChE et de nouvelles molécules supposées anti-Alzheimer (partie 6.1).

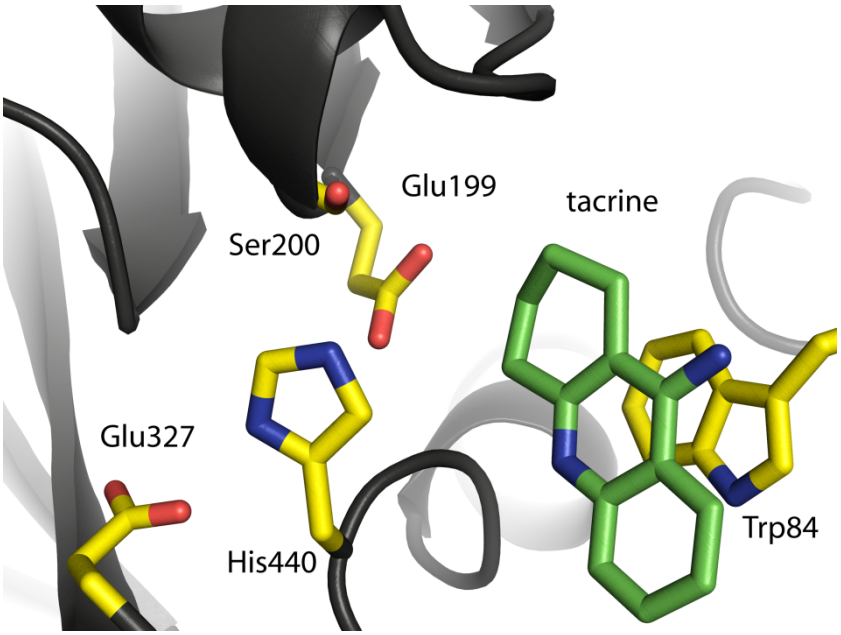

Figure 13. La tacrine dans le site actif de la TcAChE (code PDB 1acj). Les résidus du site actif et la tacrine sont représentés par des bâtonnets jaunes et verts, respectivement.

4. OBJECTIFS DE LA THÈSE

4. OBJECTIFS DE LA THÈSE

Nous avons montré que l'AChE est une enzyme adaptée à une étude de dynamique structurale des protéines. Nous avons également souligné la place qu'occupe l'AChE au sein de préoccupations de santé publique majeures. Ainsi, mieux comprendre le fonctionnement de l'AChE en établissant les relations qui existent entre sa structure, sa dynamique et son activité biologique pourrait non seulement ouvrir de nouvelles perspectives quant à l'étude de la dynamique structurale d'autres protéines, mais pourrait également contribuer à élaborer les traitements que nécessitent les troubles liés à l'inhibition de cette enzyme, qu'ils soient d'ordre pathologique ou accidentel.

La grande diversité des molécules pouvant se lier à l'AChE représente pour nous un avantage de taille dans le cadre d'une étude de dynamique structurale. Nous avons ainsi pu, indépendamment, nous intéresser à différentes questions biologiques ou pharmacologiques. En outre, la diversité des molécules utilisées nous a permis de nous focaliser sur différentes régions de l'enzyme.

Les objectifs de cette thèse étaient doubles. D'une part, nous souhaitions améliorer la compréhension des mécanismes de fonctionnement de l'AChE, notamment lorsqu'elle est inhibée par des OP, des toxines, ou des molécules potentiellement anti-Alzheimer. Les molécules que nous avons choisies appartiennent à ces trois catégories. Sur le plan pharmacologique, ce travail vise à permettre l'élaboration d'antidotes plus efficaces contre les intoxications aux OP et à aider à la conception de nouveaux médicaments utiles à la lutte contre la MA. Sur le plan biologique, nous avons également cherché à mettre en évidence la communication allostérique suspectée entre le CAS et le PAS. D'autre part, nos travaux ont visé à développer de nouvelles méthodes pour étudier la dynamique de l'AChE. Nous avons ainsi participé à deux projets de cristallographie et initié la mise en place d'une méthode permettant la caractérisation de la dynamique lente de l'AChE. L'approche structurale a été réalisée par cristallographie des protéines aux rayons X (cf. partie 5.1). L'approche dynamique a été rendue possible par des techniques spectroscopiques, notamment la mesure du temps de vie de phosphorescence d'un ligand luminescent de l'AChE.

La cristallographie aux rayons X nous a permis de résoudre la structure de la *Tc*AChE en complexe avec deux molécules potentiellement anti-Alzheimer synthétisées par des chimistes de l'université de Sienne, le NF766 et le NF1056. Les anti-Alzheimer de seconde génération se liaient jusqu'alors uniquement au niveau des résidus du CAS ou du PAS. Nos résultats révèlent l'importance de nouveaux points d'ancrage propres à augmenter le potentiel de ces molécules dans leur rôle double d'inhibiteur de l'activité cholinestérasique et d'inhibiteur de la promotion de la fibrillation d'Aβ (partie 6.1). Ces travaux font suite à un projet auquel nous avons participé : la résolution de la structure d'un complexe de la *Tc*AChE avec un anti-Alzheimer de seconde génération, le NF595 [Colletier, Sanson, Nachon, Gabellieri, Fattorusso, Campiani & Weik 2006a] (annexe 1). La structure, qui révèle un changement conformationnel de grande amplitude du Trp279, le résidu principal du PAS au niveau duquel se lie le NF595, suggère de prendre en compte les conformations minoritaires d'une enzyme dans la conception d'un médicament pour en optimiser l'action.

L'AB1, extrêmement cancérigène, dérive d'une mycotoxine présente dans certaines cultures des régions chaudes et humides. En outre, l'AB1 se lie spécifiquement au niveau du PAS : nous avons participé à une étude visant à mettre au point un biosenseur, basé sur l'inhibition de l'AChE par l'AB1, capable de détecter les traces d'AB1 dans une culture [Hansmann, Sanson, Stojan, Weik, Marty & Fournier 2009] (annexe 2). A cette occasion nous avons obtenu les structures de la *Tc*AChE en complexe avec l'AB1 (partie 6.3). Nous montrons ici les seules structures disponibles de la *Tc*AChE en complexe avec un ligand du PAS dans les deux groupes d'espace les plus fréquemment rencontrés dans le cas de structures de *Tc*AChE ($P3_121$ et $P2_12_12_1$). Ces structures ont été l'occasion de mettre en lumière des artéfacts que l'on peut rencontrer en cristallographie des protéines, et qui peuvent biaiser l'interprétation des données. Nos travaux décrivent la procédure suivie pour éviter ce problème.

Nous avons tiré profit de la phosphorescence de l'AB1 : nous avons utilisé celle-ci comme marqueur phosphorescent spécifique du PAS (partie 6.4). Nous avons ainsi pu avoir accès à la dynamique lente du PAS de la *Tc*AChE dans une gamme de températures cryogéniques comprises entre 100 et 240 K. Nous pouvons alors préciser, ou du moins confirmer, la température la plus propice à une expérience de cristallographie cinétique contrôlée par la température. Nous avons en effet pu participer à deux projets de ce type, l'un basé sur l'utilisation de produits en cage [Colletier, Royant, Specht, Sanson, Nachon,

Masson, Zaccai, Sussman, Goeldner, Silman, Bourgeois & Weik 2007] (annexe 3) et l'autre sur la radiolyse d'un analogue de substrat [Colletier, Bourgeois, Sanson, Fournier, Sussman, Silman & Weik 2008] (annexe 4).

Enfin, nous avons résolu les structures des conjugués de *Tc*AChE avec le soman dans les étapes principales de l'inhibition (partie 6.2). Contrairement à l'AB1 et aux anti-Alzheimer, le soman se lie spécifiquement au niveau du CAS. C'est un OP qui aboutit à un vieillissement rapide de l'AChE et contre lequel tous les antidotes disponibles sont inefficaces. Alors que la forme vieillie du conjugué avait été résolue par co-cristallisation de *Tc*AChE et de soman [Millard 1999b], nous avons été en mesure d'obtenir la structure des formes non-vieillie et vieillie par trempage de cristaux de *Tc*AChE dans une solution de soman. Nous avons également cherché à expliquer le manque d'efficacité du réactivateur le plus utilisé, le 2-PAM, dans le cas d'une inhibition de l'AChE par le soman. La structure d'un complexe ternaire *Tc*AChE vieillie/soman/2-PAM a ainsi été résolue. Elle montre que l'orientation du 2-PAM n'est pas favorable à la réactivation.

Dans la suite (partie 5), nous décrirons les méthodes et les outils mis en œuvre pour mener à bien nos travaux. La cristallographie des protéines aux rayons X sera présentée dans les grandes lignes. La cristallographie cinétique sera abordée à cette occasion. Nous décrirons ensuite la technique spectroscopique mise en oeuvre au cours de cette thèse.

Les résultats (partie 6) sont présentés sous la forme de quatre articles (parus, soumis ou en préparation) rédigés en anglais. Nous discuterons alors l'ensemble des résultats obtenus au cours de cette thèse et dégagerons des perspectives de nos travaux avant de conclure (partie 7).

5. METHODOLOGIE

5. MÉTHODOLOGIE

Dans cette partie, nous décrirons les principales méthodes expérimentales mises en œuvre dans notre étude : la cristallographie aux rayons X (CRX) et la microspectrophotométrie (MSP).

5.1 La cristallographie des protéines

5.1.1 Introduction

La caractérisation structurale des macromolécules biologiques à l'échelle atomique (c'est-à-dire à une résolution de l'ordre de l'angström ; 1 Å = 10^{-10} m) est essentiellement réalisée au moyen de deux techniques très populaires : la cristallographie aux rayons X (CRX) et la résonance magnétique nucléaire (RMN). C'est au moyen de la CRX que John Kendrew et Max Perutz purent résoudre les structures de l'hémoglobine et de la myoglobine, les toutes premières structures tridimensionnelles de macromolécules, il y a cinquante ans. Ces travaux leur ont permis de recevoir conjointement le prix Nobel en 1962.

A ce jour, la CRX a permis la résolution de 6 fois plus de structures macromoléculaires que la RMN : près de 50000 structures obtenues par CRX ont été déposées dans la Protein Data Bank (PDB) contre environ 6000 par RMN. Une telle différence s'explique par la jeunesse relative de la RMN (moins de 30 ans), mais surtout par la limitation de cette dernière dans la taille des échantillons (entre 20 kDA et 30 kDa en moyenne). La CRX ne possède pas une telle contrainte : la structure du ribosome, quoiqu'à seulement 5.5 Å, a pu être résolue par cette technique [Yusupov 2001]. Toutefois, la RMN est applicable à des protéines en solution et fournit également des informations dynamiques.

La nature même des structures obtenues est également déterminante dans le choix de la méthode. En effet, la CRX aboutit à une structure unique alors que la RMN fournit un ensemble de structures (duquel découle le caractère dynamique). Bien que l'unicité de la structure obtenue par CRX soit essentiellement artéfactuelle (sélection des conformations

de plus basse énergie, influence de l'empilement cristallin, *etc.*), les coordonnées atomiques obtenues par CRX sont plus précises et offrent une base de travail plus adéquate à la conception de drogues (*stucture-based drug design*).

On ne saurait être tout à fait complet sans mentionner la microscopie électronique structurale. Toutefois, les résolutions atteintes par la ME sont généralement de l'ordre de la dizaine d'angströms, ce qui en fait une méthode plus adaptée à la caractérisation structurale de très gros assemblages moléculaires tels que les virus et les ribosomes.

La CRX a été la principale méthode expérimentale utilisée au cours de cette thèse. Dans la partie qui suit, les principes de la CRX sont exposés. Nous nous sommes ensuite attachés à détailler, d'un point de vue chronologique, les étapes qui mènent à la résolution d'une structure par CRX. La fin de cette section est consacrée à une brève présentation de la cristallographie cinétique.

5.1.2 Les principes de la cristallographie des protéines

Seuls les principes fondamentaux nécessaires à une compréhension globale de la CRX sont exposés dans cette partie. Des informations plus détaillées peuvent être trouvées dans des ouvrages de référence [Drenth & Mesters 2007; McPherson 2002]. Nous nous sommes en particulier limités à la CRX monochromatique.

5.1.2.1 Pourquoi utiliser les rayons X en cristallographie des protéines ?

Les rayons X sont des ondes électromagnétiques (OEM) d'énergie comprise entre 0.1 keV et 100 keV. Leur longueur d'onde est donc comprise entre 0.1 Å et 900 Å, approximativement. Puisque les distances interatomiques au sein d'une protéine sont de l'ordre d'1.5 Å, les rayons X de longueur d'onde comparable sont adaptés à la résolution d'une structure à résolution atomique. Puisqu'il n'existe pas de lentille capable de focaliser les rayons X, on a recours à une méthode indirecte.

La CRX repose en premier lieu sur l'interaction des rayons X, considérés ici comme des OEM, avec les électrons de la protéine. L'OEM incidente fait osciller les électrons qui

réémettent ensuite un rayonnement de même fréquence (ce qui est uniquement vrai dans le cas d'une interaction élastique, on parle alors de diffusion Thomson). L'onde résultante émise par le cristal est la somme des ondes émises par tous les électrons de la protéine. Cependant, l'échantillon étant sous forme cristalline, cette onde est également la somme de toutes les ondes de chaque protéine qui compose le cristal. L'agencement régulier et périodique des protéines dans le cristal est à l'origine de phénomènes d'interférences, constructives et destructives, entre les OEM. La nature du réseau cristallin impose des conditions à la diffusion : on parle alors de diffraction. Sur l'écran d'observation, des tâches forment un cliché de diffraction. La position des tâches sur le cliché de diffraction renseigne sur la géométrie du réseau cristallin. L'intensité des tâches est beaucoup plus riche en information : elle dépend de la structure de la protéine. Une expression permettant de calculer l'onde diffractée par un cristal à la distribution de la densité électronique d'une protéine peut être aisément établie. Le but d'une expérience de cristallographie sera alors d'inverser cette relation, et de calculer la distribution de la densité électronique à partir de l'onde diffractée.

5.1.2.2 Le réseau cristallin

Le phénomène de diffraction naît de l'agencement périodique, dans les trois dimensions de l'espace, des molécules qui composent un cristal. La régularité de cette organisation est telle qu'elle se reflète à l'échelle macroscopique sous formes de faces planes. Dans cet empilement régulier, on peut identifier la répétition d'un motif, la maille élémentaire, caractérisée par trois vecteurs ($\vec{a}, \vec{b}$ et $\vec{c}$) et trois angles (α, β et γ) ; la maille élémentaire est la plus petite unité d'espace qui permet de reconstruire le motif cristallin par translation (selon les vecteurs susmentionnés). De ce point de vue, et indépendamment du contenu de la maille élémentaire, le cristal peut être vu comme un réseau. Nous verrons par la suite que la diffraction des rayons X (RX) peut alors être considérée comme une réflexion sur les plans du réseau cristallin.

5.1.2.3 La symétrie cristalline

Le contenu de la maille élémentaire peut présenter des symétries internes. La maille élémentaire peut alors être reconstruite par l'application des opérateurs de symétrie correspondants à l'unité asymétrique, c'est-à-dire la plus petite unité d'espace qui ne

possède pas d'élément de symétrie. Les opérateurs de symétrie possibles sont des axes de rotation (simples ou hélicoïdaux) d'ordre 2, 3, 4 ou 6, des centres d'inversion et certaines combinaisons de ces opérateurs. Si l'unité asymétrique contient plusieurs copies de la protéine cristallisée, celles-ci peuvent être liées par des opérateurs de symétrie non-cristallographique.

Il existe 230 manières de combiner ces opérateurs de symétrie : ce sont les 230 groupes d'espace. Seuls 64 groupes d'espace sont autorisés dans les cristaux des protéines. En effet, l'application des symétries miroirs et des centres d'inversion sur les protéines conduirait à transformer des acides aminés de type L en acides aminés de type D, lesquels ne rentrent pas dans la composition des protéines.

5.1.2.4 La loi de Bragg

Lors d'une expérience de CRX, le cristal est placé sur le trajet d'un faisceau de RX de longueur d'onde λ. Comme les ondes des RX diffusés n'ont pas tous la même phase, les interférences entre elles sont pour la plupart destructives. En effet, chaque atome du cristal participe à la diffraction, et la distribution des phases des RX est homogène dans l'espace des phases ( ]0-2π]). L'amplitude de l'onde résultante en un point (du détecteur, par exemple) doit donc être statistiquement nulle. Toutefois, il existe un nombre discret de conditions pour lesquelles les interférences sont constructives. Tout se passe comme si les RX étaient réfléchis par les plans du réseau cristallin (Fig. 14). Ainsi si les RX réfléchis par un ensemble de plans parallèles du cristal sont en phase, ils donneront lieu à des interférences constructives. Cette condition est exprimée par la loi de Bragg :

$$2d\sin\theta = n\lambda$$

d correspond à l'espacement entre deux plans, θ est l'angle entre la direction du RX incident et la surface d'un plan, λ la longueur d'onde des RX et n un entier. La différence de marche entre deux RX parallèles est égale à 2d sinθ. L'interférence constructive se produit lorsque la différence de marche est un multiple de la longueur d'onde des RX (nλ).

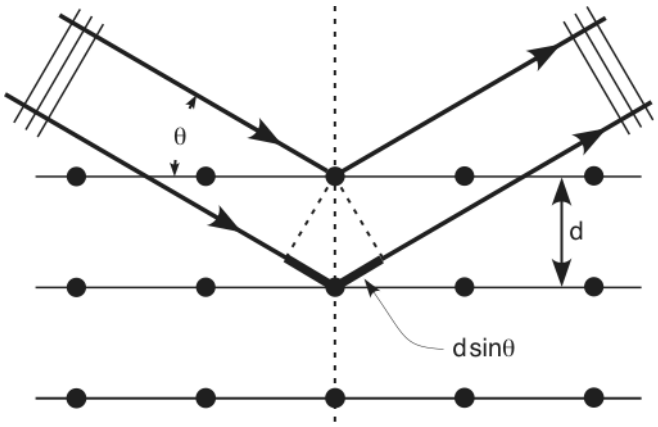

Figure 14. Représentation schématique de la loi de Bragg.

5.1.2.5 Réseau réciproque et résolution

Afin de pouvoir mesurer leur intensité, les RX sont interceptés sur un écran (le détecteur), et dessinent ainsi des clichés de diffraction (voir plus loin). L'ensemble des taches de diffraction, obtenues par rotation du cristal dans le faisceau de RX, est une projection du réseau réciproque du cristal. Le réseau réciproque, purement imaginaire, est la transformée de Fourier (TF) du réseau réel. Les vecteurs qui définissent la maille du réseau réciproque sont les inverses des vecteurs de la maille du réseau réel. En conséquence, si les plans du réseau réciproque sont identifiés par leurs indices de Miller (h, k et l), les distances d_{hkl} entre les plans du réseau réciproque seront égales à 1/d. Or :

$$\frac{1}{d} = \frac{2\sin\theta}{\lambda}$$

représente l'inverse de la résolution d'une réflexion. Sur le cliché de diffraction, plus les taches sont éloignées du centre, plus l'angle θ entre les RX et le plan du réseau dans l'espace réel est grand, et donc plus haute est la résolution de la réflexion correspondante. On pourra alors définir la résolution d'un jeu de données comme étant la résolution de la réflexion la plus éloignée du centre du détecteur.

5.1.2.6 La sphère d'Ewald

La construction d'Ewald (Figure 16) permet de prédire la direction des RX diffractés, et donc le contenu des clichés de diffraction. Considérons un faisceau de RX parallèle et de longueur d'onde λ : alors la longueur d'onde dans l'espace réciproque sera égale à 1/λ.

Les RX sont représentés par une sphère de rayon 1/λ (la sphère d'Ewald). Le cristal et son réseau réciproque sont centrés en O. La diffraction se produit lorsqu'un nœud du réseau réciproque (défini par ses indices hkl) entre en contact avec la surface de la sphère d'Ewald (en P). La direction de l'onde diffractée est celle de l'axe MP sur la figure 15. Les RX incident et diffracté font un angle de 2θ. La position de la réflexion correspondante peut alors être déterminée sur la base de la valeur de 2 θ et de la distance cristal-détecteur.

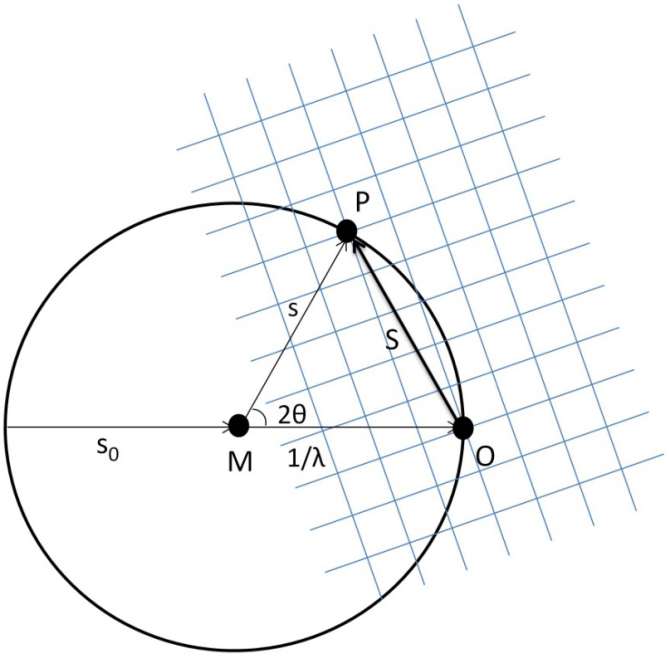

Figure 15. La sphère d'Ewald.

5.1.2.7 La transformée de Fourier

Les clichés de diffraction peuvent être vus comme le résultat d'une TF du réseau cristallin dans l'espace réel. Résoudre la structure d'une protéine par CRX implique donc d'être capable de réaliser l'opération inverse.

Tous les atomes de toutes les protéines d'un cristal participent à chacune des réflexions. Le facteur de structure F(hkl), définit la relation entre la réflexion associée et la distribution de la densité électronique ρ(xyz) de la protéine :

$$F(hkl) = V \int_{x=0}^{1} \int_{y=0}^{1} \int_{z=0}^{1} \rho(xyz) e^{2\pi i(hx+ky+lz)} dxdydz$$

On voit dans cette équation que le facteur de structure F(hkl) est la TF de la densité électronique ρ(xyz). L'intégration est réalisée sur tout le volume V de maille élémentaire[2] (la symétrie cristalline rend équivalents toutes les positions liées par des opérateurs de symétrie). D'un point de vue expérimental, il est important de souligner que l'amplitude du facteur de structure est proportionnelle à l'intensité mesurée sur les clichés de diffraction.

La TF inverse permet de calculer la densité électronique à partir des facteurs de structure :

$$\rho(xyz) = \frac{1}{V}\sum_h\sum_k\sum_l F(hkl)e^{-2\pi i(hx+ky+lz)}$$

Une triple sommation remplace la triple intégration : les indices h, k et l peuvent uniquement prendre des valeurs discrètes et entières. Les cristaux de protéines et les clichés de diffraction étant centrosymétriques (si la loi de Friedel est respectée ; voir plus loin), la relation se simplifie ainsi :

$$\rho(xyz) = \frac{2}{V}\sum_h\sum_k\sum_l |F(hkl)|\cos[2\pi(hx+ky+lz) - \alpha(hkl)]$$

Dans cette dernière relation, la phase α(hkl) apparaît. L'impossibilité de la mesurer directement est à l'origine du problème de phase (voir plus loin).

5.1.3 La cristallogenèse

5.1.3.1 Principe

L'obtention d'un cristal de la protéine d'intérêt convenable à la diffraction par les rayons X est bien évidemment requise en préambule à une expérience de CRX. La cristallogenèse est l'étape la moins comprise de la CRX. Bien qu'il n'existe pas de théorie de la cristallogenèse, certaines règles empiriques ont néanmoins pu être établies.

La cristallisation d'une protéine soluble est un cas très particulier d'agrégation. La solubilité d'une protéine dépend d'un grand nombre de facteurs : sa propre concentration, la température, le pH, la force ionique, la concentration et la nature de l'espèce tampon et

[2] La maille est ici réduite comme en attestent les bornes d'intégration.

d'un éventuel additif, *etc*. Ainsi, les conditions de cristallisation d'une protéine doivent réaliser un compromis entre les différents facteurs thermodynamiques qui déterminent la solubilité d'une protéine. L'ensemble des conditions qui permettent la cristallisation d'une protéine donnée est, en général, trouvé au travers d'un processus d'essai/erreur. Aujourd'hui, la recherche des conditions de cristallisation est réalisée par des robots capables de cribler des milliers de conditions en n'utilisant qu'un petit volume de la solution protéique. L'affinement des conditions favorables, lorsqu'il en existe, sont éventuellement affinées à la main.

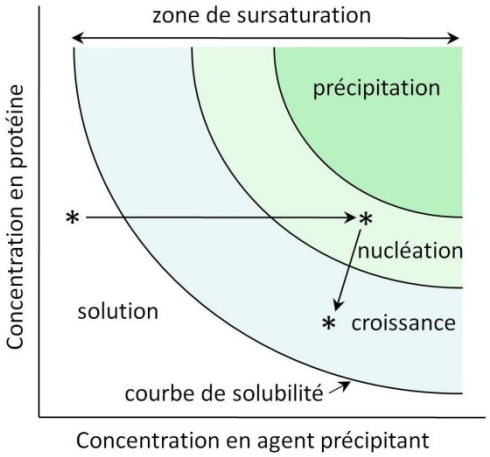

Figure 16. Courbe de solubilité typique d'une protéine en fonction de sa concentration et de la concentration en agent précipitant. La protéine en solution est amenée à sursaturation. Des petits agrégats de la protéine peuvent alors se former (nucléation), qui croîtront jusqu'à devenir des cristaux de taille adéquate pour une expérience de CRX.

On peut comparer la cristallisation d'une protéine à celle du chlorure de sodium dans les marais salants. La protéine (très pure) est solubilisée à une concentration donnée. En pratique, un agent précipitant est ajouté à une concentration telle que la protéine ne précipite pas. L'agent précipitant est en général un sel ; le [(4s)-2-methyl-2,4-pentanediol] (MPD) et les polyethylene glycol (PEG) sont également très utilisés. La solution protéique est ensuite graduellement amenée à sursaturation. De petits agrégats de la protéine peuvent alors se former : c'est le phénomène de nucléation. La croissance du cristal se produit alors. Un diagramme de phase résume le comportement d'une protéine au cours de la cristallisation (Fig. 16). Ce diagramme met en évidence la zone de nucléation, où la sursaturation est favorable à la nucléation, et la zone de croissance (métastable), où la sursaturation est typiquement plus faible.

5.1.3.2 Technique de cristallisation

La technique de cristallisation la plus répandue de nos jours repose sur le contrôle de la diffusion de vapeur [McPherson 1976]. Elle se décline en deux méthodes : la goutte suspendue et la goutte assise. Nous nous focalisons ici sur la technique utilisée au cours de cette thèse, la méthode de la goutte suspendue (Fig. 17). Nous n'avons pas eu recours à un robot de cristallisation.

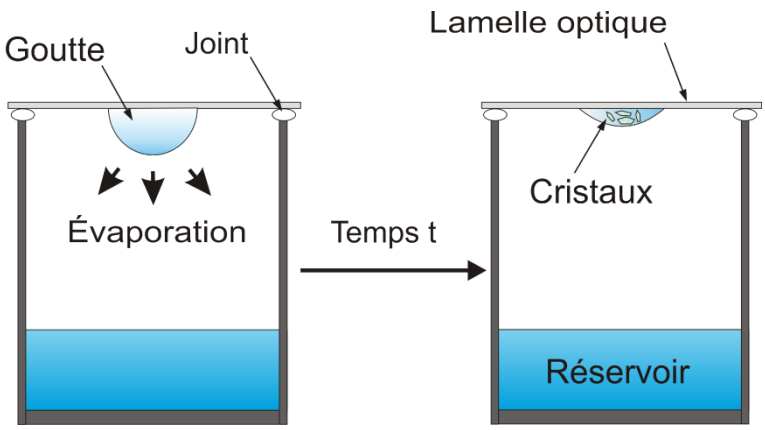

Figure 17. Représentation schématique de la technique cristallisation par diffusion de vapeur en goutte suspendue.

La protéine, en solution aqueuse, est introduite dans une « solution précipitante » contenant les éventuels composés favorisant sa cristallisation (tampon, agent précipitant, *etc.*). Une goutte (1 à 5 µl) de cette solution est déposée sur une lamelle optique siliconée, laquelle est placée hermétiquement en regard d'un puits. Le puits est partiellement rempli (~1 ml) avec la solution précipitante. Comme la goutte et le réservoir n'ont pas la même composition, les espèces volatiles diffusent jusqu'à l'équilibre des pressions de vapeur saturante de chacune des solutions. En général, la goutte est moins concentrée en agents précipitants ; elle se concentre au gré de la diffusion de vapeur vers le réservoir. La protéine, elle, n'est pas volatile et reste donc dans la goutte. Ainsi, l'état de sursaturation

propice à la nucléation peut être atteint et éventuellement conduire à l'apparition de cristaux.

Si la tension de surface de la goutte est trop faible, on peut constater son étalement sur la lamelle. La méthode de la goutte assise est alors plus appropriée. Le principe est le même, mais au lieu d'être suspendue, la goutte est déposée au sommet d'une base surélevée.

5.1.3.3 La technique de micro-ensemencement

Pour favoriser l'apparition des cristaux, nous avons parfois eu recours à la technique de micro-ensemencement. C'est une technique empirique qui consiste à broyer un cristal jusqu'à obtenir une myriade de cristallites, lesquels sont alors dilués à une concentration adéquate. Les cristallites sont alors déposées dans des gouttes de cristallisation fraîchement préparées (nous avons utilisé une moustache de chat) et servent de point de nucléation pour démarrer la croissance cristalline.

5.1.4 Le montage des cristaux sur le diffractomètre

5.1.4.1 La cryo-cristallographie

Historiquement, les données cristallographiques étaient collectées à température ambiante dans des capillaires. Cette pratique, adaptée aux diffractomètres de laboratoire, a été bouleversée par l'apparition des synchrotrons (voir plus loin). Le rayonnement synchrotron est beaucoup plus puissant (d'au moins deux ordres de grandeur) que celui produit par un générateur de rayons X de laboratoire. A température ambiante, il entraîne des dommages d'irradiation (voir plus loin) aboutissant rapidement à la destruction du cristal. La cryo-cristallographie [Garman 1999; Hope 1988; Hope 1990] permet de réduire l'effet délétère des rayons X sur les cristaux ; un cristal peut être exposé 70 fois plus longtemps à température cryogénique qu'à température ambiante [Nave & Garman 2005; Owen 2006]. En pratique, la collecte de données au synchrotron se fait généralement à une température voisine de 100K.

5.1.4.2 La cryo-protection

Le cristal est placé dans un flux d'azote (~100 K) au moyen d'une cryo-boucle (*cryo-loop*) [Teng 1990]. Cet outil permet de pécher le cristal dans la goutte où il se trouve et de le placer sur la tête goniométrique du diffractomètre. Le montage doit être effectué suffisamment rapidement afin que l'eau présente dans le cristal se solidifie dans une forme vitreuse : on parle de congélation ultra-rapide (*flash- cooling*) [Garman & Doublie 2003; Juers & Matthews 2001]. L'expansion qui accompagne la formation de glace cristalline endommagerait la structure du cristal.

Pour éviter la formation de glace cristalline, on transfère généralement le cristal dans une solution cryo-protectrice. Les cryo-protecteurs les plus courants sont le glycérol, le MPD et les PEG de faible poids moléculaire. Des huiles (de paratone ou de paraffine, par exemple) sont également utilisées. Elles ont l'avantage d'éviter l'assèchement du cristal et d'éliminer une grande partie du solvant qui l'entoure, diminuant ainsi la diffusion des rayons X par celui-ci. Les cas les moins favorables sont rencontrés lorsque le cristal a poussé dans une solution contenant un sel : il faut éviter que celui-ci cristallise à l'intérieur des canaux de solvant. Il faut donc remplacer le sel par la solution cryo-protectrice tout en conservant l'intégrité structurale du cristal. Au contraire, certains agents précipitants sont également de bons cryo-protecteurs. C'est le cas du PEG, en particulier. Les cristaux peuvent alors être directement placés dans le flux d'azote. C'était le cas de nos cristaux d'acétylcholinestérase, lesquels ont poussé dans une solution contenant du PEG 200 (voir plus loin).

5.1.5 La collecte de données

5.1.5.1 Les sources de rayons X

Les générateurs à anode tournante

Dans un laboratoire de cristallographie, les rayons X sont le plus souvent produits par un générateur à anode tournante. Dans un tube scellé, sous vide, des électrons sont émis par

un filament de tungstène qui constitue la cathode de l'appareil. Un fort potentiel négatif entre l'anode et la cathode accélère les électrons à grande vitesse. L'énergie des électrons est suffisamment élevée pour provoquer des transitions électroniques entre les orbitales internes des atomes qui constituent l'anode (des couches L ou M à la couche K). Le retour des électrons aux positions inoccupées s'accompagne de l'émission de rayons X. La longueur d'onde du rayonnement dépend de la nature de la transition électronique et du matériau qui constitue l'anode. En général, l'anode est en cuivre et on règle le potentiel entre l'anode et la cathode de sorte à sélectionner la raie Kα du cuivre (qui correspond à une transition L→K) dont la longueur d'onde est d'environ 1.54 Å.

L'essentiel de l'énergie des électrons accélérés est convertie sous forme de chaleur ; la rotation de l'anode permet d'éviter sa destruction prématurée. En outre, ce système autorise la production d'un faisceau de rayons X plus intense que dans un système à anode fixe.

Nous avons restreint notre utilisation de ces générateurs à des tests. Nous avons en effet eu accès régulièrement au European Synchrotron Radiation Facility (ESRF), le synchrotron de Grenoble, la source de rayons X la plus brillante[3] d'Europe.

Le rayonnement synchrotron

Les synchrotrons [Mitchell 1999] sont des structures annulaires dont le diamètre varie entre 10 m et plusieurs centaines de m. Des électrons (ou des positrons) sont accélérés par un accélérateur linéaire, amenés à une vitesse proche de celle de la lumière (environ 3.10^8 $m.s^{-1}$) dans un accélérateur annulaire (*booster)*, avant d'être injectés dans l'anneau de stockage pour une durée de plusieurs heures. Les changements de direction des particules dans l'anneau sont à l'origine de l'émission d'un rayonnement sur une large gamme de longueurs d'onde, des ondes radio aux rayons γ, avec un maximum d'intensité centré sur 1 Å. A chaque cycle, une impulsion radiofréquence permet de compenser la perte d'énergie due à l'émission des rayons X. L'orbite des électrons n'est pas réellement circulaire. Elle est maintenue par la présence d'aimants de courbure (*bending magnets* ; BM) tout au long de l'anneau.

[3] La brillance est définie par le nombre de photons/s/mrad²/mm²/0.1 % de la largeur spectrale.

Pour utiliser les rayons X dans une expérience de CRX, les rayons doivent être captés vers la cabine expérimentale. Une ligne de lumière consiste en l'ensemble des éléments qui se situent entre l'anneau de stockage et la cabine expérimentale. Deux types de lignes de lumière existent :

_ les lignes BM.

_ les lignes ID (*Insertion Device*), plus récemment développées. Les ID sont des éléments insérés entre les sections linéaires de l'anneau qui permettent d'étendre le spectre vers les plus basses longueurs d'onde. Il en existe différents types (*wigglers* et ondulateurs). Leur fonctionnement repose sur une alternance de pôles magnétiques successivement positifs et négatifs qui produisent des courbures transversales le long de la trajectoire de la particule. Le rayonnement résultant est beaucoup plus intense que celui des lignes BM.

A titre de comparaison, une collecte de 3 minutes sur une ligne ID prendrait environ 3 heures sur une ligne BM (et une journée sur un diffractomètre de laboratoire).

L'autre avantage majeur des synchrotrons réside dans la possibilité de sélectionner une longueur d'onde, par le biais d'un monochromateur. Cette propriété permet, en particulier, le phasage d'un jeu de données (voir plus loin) au moyen d'atomes lourds ou de diffuseurs anomaux. La diffraction de Laue exploite plus largement encore le caractère polychromatique du rayonnement synchrotron (voir plus loin).

5.1.5.2 L'enregistrement des clichés de diffraction

Afin de pouvoir identifier et mesurer l'intensité de tâches de diffraction, il faut les enregistrer. En CRX, les données sont enregistrées en interceptant les RX sur un écran (le détecteur). Le cliché de diffraction (Fig. 18) ainsi formé est (idéalement) constellé de taches de diffraction. La nature du réseau cristallin et l'orientation du cristal déterminent la position des taches de Bragg. Leur intensité est liée au contenu de la maille : elle est porteuse de l'information structurale (cette information n'est que partielle puisque l'on ne peut mesurer la phase associée aux taches de Bragg : cf. partie 2.1.7.1). Deux types de détecteurs sont aujourd'hui couramment employés.

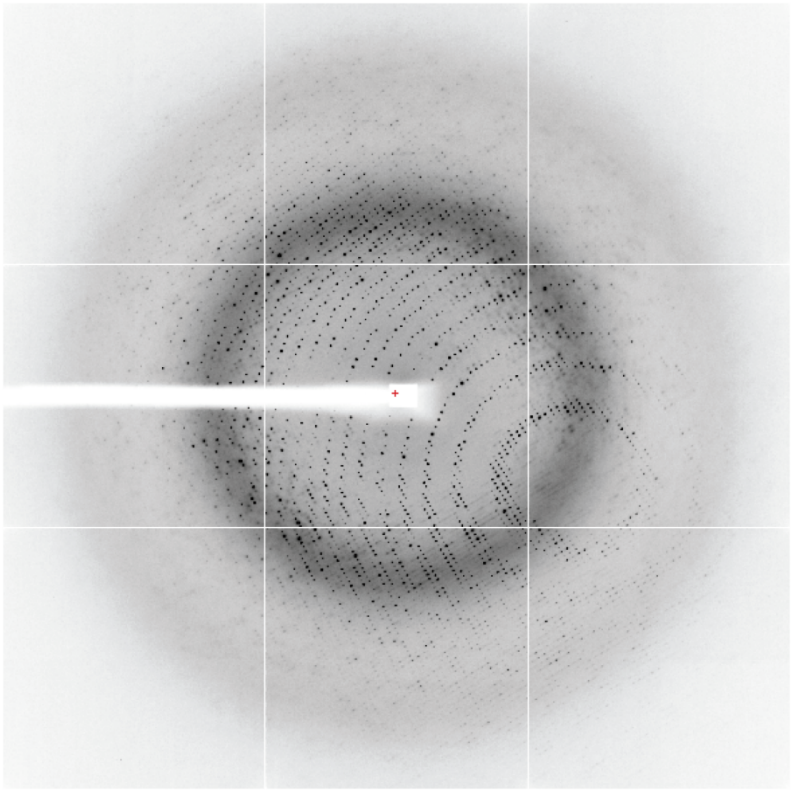

Figure 18. Cliché de diffraction enregistré à partir d'un cristal natif de TcAChE. L'ombre du beamstop, qui protège le détecteur du rayonnement X direct, est visible.

_ Les *Image Plates* (IP) : ce sont des plaques recouvertes d'une fine couche d'un composé inorganique phosphoré capable de retenir une fraction de l'énergie des rayons X. Après exposition aux rayons X, l'IP est lue en éclairant la plaque pixel par pixel : l'énergie stockée est libérée sous forme d'une lumière d'intensité proportionnelle au nombre de photons X absorbés. L'effacement de la plaque, par exposition plus franche à la lumière, nécessite plusieurs minutes. Le temps de lecture est donc un inconvénient majeur des IP. Pour cette raison, ces détecteurs sont aujourd'hui essentiellement réservés aux diffractomètres de laboratoire.

_ Les détecteurs à CCD (Charge-Coupled Device) : c'est le type de détecteur que l'on rencontre typiquement dans les synchrotrons [Westbrook & Naday 1997]. Leur temps de lecture est plus court que celui des IP (approximativement 1 s). Ces détecteurs fonctionnent sur la base de l'effet photoélectrique. Les photons X sont dans un premier temps convertis en lumière visible au travers d'un écran luminescent. Dans chaque pixel, les photons visibles sont ensuite convertis en paires électron/trou dans un matériau semi-conducteur. Des électrons sont ainsi collectés proportionnellement au nombre de photons

X reçus par le CCD. La lecture du détecteur se fait par transfert de charges : une tension proportionnelle au nombre d'électrons collectés est amplifiée et convertie en un signal numérique prêt pour le traitement de données.

Un nouveau type de détecteurs est apparu récemment, le PILATUS [Broennimann 2006]. C'est un détecteur à pixels qui compte chaque photon reçu. Ses caractéristiques permettent l'enregistrement de données en continu sur un cristal en rotation pendant toute la durée de la collecte de données. Un cliché de diffraction peut être enregistré en moins de 10 ms. En conséquence, la collecte d'un jeu de données complet peut être réalisée en quelques secondes. Nous n'avons pas eu accès à ce type de détecteur au cours de cette thèse.

5.1.5.3 Exposition et dommages d'irradiation aux rayons X

L'avantage majeur du synchrotron, la brillance du faisceau de rayons X qu'il produit, est en même temps un inconvénient de taille. Même autour de 100 K, les rayons X causent des dommages irréversibles aux protéines. Le désordre qui en résulte réduit le pouvoir de diffraction du cristal. La limite de Henderson a été définie dans ce contexte : il a été calculé qu' à 77 K, un cristal de macromolécules perd la moitié de son pouvoir de diffraction quand il a reçu une dose (énergie absorbée par unité de mase) de 2.10^7 Gy[4] [Henderson 1990]. Une approche expérimentale suggère une valeur de $4{,}3.10^7$ Gy [Owen 2006]. Toutefois, les auteurs suggèrent une limite de 3.10^7 Gy en-deçà de laquelle l'information biologique n'est pas compromise.

D'un point de vue expérimental, les dommages d'irradiation se traduisent, en sus de la diminution progressive de l'intensité diffractée, par l'augmentation de la mosaïcité, du facteur B de Wilson [Gonzalez & Nave 1994] et du volume de la maille élémentaire [Ravelli 2002]. Les RX induisent également des dommages spécifiques [Burmeister 2000; Leiros 2001; Ravelli & McSweeney 2000; Weik 2000; Weik 2002] : en particulier, la rupture des ponts disulfure et la décarboxylation des acides aminés acides (aspartate et glutamate).

[4] Le Gray est ainsi défini : 1 Gy = 1 $J.kg^{-1}$.

5.1.5.4 Stratégie de collecte

Certains paramètres de collecte doivent être choisis avec soin.

_ Le temps d'exposition : ce doit être un compromis entre le niveau de signal/bruit des réflexions enregistrées et les dommages d'irradiation aux RX. Ce temps est également choisi de sorte à ne pas saturer les pixels du détecteur : les *overloads* ainsi générés conduisent à des réflexions inutilisables.

_ La résolution : le détecteur doit être placé à une distance telle que les réflexions de plus haute résolution puissent être enregistrées, tout en exploitant au maximum sa surface. Sur le cliché de diffraction, les réflexions de basse résolution sont au centre, alors que les réflexions de haute résolution sont au bord. Plus la résolution atteinte est haute, plus l'information structurale est détaillée. Les résolutions typiques atteintes avec les cristaux de protéines (autour de 2 Å) permettent d'affiner 4 paramètres par atome : les coordonnées (x, y, et z) et le facteur d'agitation thermique (B). Idéalement, le rapport nombre d'observations/paramètres affinés doit être au minimum de 1,5. En CRX, une observation est une réflexion indépendante.

_ La plage angulaire : il s'agit d'enregistrer des clichés de diffraction dans un nombre d'orientations du cristal suffisant pour reconstruire le réseau réciproque le plus complètement possible. Selon la symétrie du cristal et l'axe suivant lequel il est monté, un jeu complet nécessite en théorie des plages de 30° à 180° (limite supérieure imposée par la centro-symétrie des cristaux).

_ L'angle d'oscillation : en pratique, le cristal oscille pendant l'enregistrement du cliché. Ainsi les clichés contiennent plus de réflexions et proviennent de domaines angulaires contigus. Plusieurs passes (allers-retours) permettent d'améliorer le rapport signal/bruit de la réflexion. La rapidité des détecteurs permet d'envisager des oscillations inférieures à 1°. En pratique, l'angle d'oscillation est choisi de manière à éviter les overlaps (superposition de plusieurs réflexions sur une même zone du détecteur). Il tient donc être adapté à la mosaïcité du cristal. On cherche également à maximiser le signal/bruit des réflexions et à minimiser l'exposition totale (et donc les dommages d'irradiation). Dans le cas des cristaux d'AChE, nous n'avons pas constaté d'amélioration nette dans l'enregistrement et le traitement des données pour des valeurs inférieures à 1° et avons donc généralement choisi cette valeur lors de la collecte des jeux de données.

5.1.6 Traitement des données cristallographiques

Nous décrivons dans cette partie toutes les étapes qui permettent de calculer les facteurs de structure d'un jeu de données à partir des clichés de diffraction. Le problème de la phase sera abordé dans la partie consacrée à la résolution d'une structure. Dans le cadre des expériences de CRX sur les cristaux d'AChE, nous avons essentiellement utilisé le programme XDS [Kabsch 1993], et dans une moindre mesure MOSFLM [Leslie 2006].

5.1.6.1 Indexation

Au cours de l'indexation, on détermine les paramètres de maille et l'orientation du cristal à partir d'un petit nombre de clichés de diffraction. On en déduit le groupe d'espace vraisemblable auquel le cristal appartient. Chaque nœud du réseau (réciproque) correspondant sera ensuite identifié par des indices de Miller (h k l).

5.1.6.2 Intégration

La position des taches est prédite à partir des réflexions de Bragg issues de l'indexation. L'intensité des taches est alors estimée au travers de la sommation des intensités de tous les pixels qui la constituent. En pratique, le profil moyen des taches est généré (la divergence du faisceau de RX et la mosaïcité du cristal ont tendance à élargir les taches), et l'intégration est réalisée après ajustement de la forme de la tache avec le profil.

Concomitamment, les paramètres de maille, et certains paramètres relatifs au détecteur et au cristal sont également affinés.

5.1.6.3 La mise à l'échelle

La dernière étape est une mise à l'échelle de l'intensité des réflexions basée sur l'intensité des réflexions de mêmes indices (h k l) ou liées par la symétrie. Ces réflexions devraient avoir la même intensité. Toutefois, ce n'est jamais le cas pour différentes raisons : l'intensité du rayonnement synchrotron décroît au cours du temps, selon l'orientation du cristal le chemin traversé par les RX est variable, le dommage d'irradiation augment au cours du temps, *etc*.

Finalement, on dispose d'un jeu d'indices (hkl) associés à une intensité I et son incertitude σ(I). Les facteurs de structure seront calculés sur la base de ces données (voir plus loin).

5.1.6.4 Les indicateurs de la qualité des données

Plusieurs indicateurs permettent de juger de la qualité d'un jeu de données.

_ Le rapport signal/bruit : il est défini par le rapport I/σ(I).

_ La complétude : elle correspond au pourcentage de réflexions mesurées par rapport aux réflexions possibles.

_ La redondance : la mesure répétée d'une même réflexion, pour différentes orientations du cristal, permet d'améliorer le rapport signal/bruit.

_ Le facteur R_{sym} : l'écart type de l'intensité des réflexions identiques (ou liées par la symétrie) est donné par la relation :

$$R_{sym}(I) = \frac{\sum_{hkl}\sum_{i}\left|I_i(hkl) - \overline{I(hkl)}\right|}{\sum_{hkl}\sum_{i}(hkl)}$$

Au cours de cette thèse, les données ont été indexées, intégrées et mises à l'échelle avec le logiciel XDS (X-ray Detector Software) [Kabsch 1993]. Les auteurs d'XDS proposent un indicateur supplémentaire, le R_{meas} :

$$R_{meas}(I) = \frac{\sum_{hkl}\frac{n_h}{n_h - 1}\sum_{i}\left|I_i(hkl) - \overline{I(hkl)}\right|}{\sum_{hkl}\sum_{i}(hkl)}$$

Cet indicateur est défini de manière similaire au R_{sym}, mais il est indépendant de la multiplicité n_h des réflexions [Diederichs & Karplus 1997]. En effet, le R*sym* augmente pour des réflexions mesurées plusieurs fois. Ainsi, pour tenir compte de l'amélioration que représente la moyenne de plusieurs mesures pour une même réflexion, chaque réflexion est pondérée par un facteur qui dépend de sa multiplicité.

_ La résolution (la plus élevée possible). Elle détermine la finesse de la structure que l'on cherche à résoudre. Ce n'est pas réellement un critère de qualité du jeu, mais le niveau de détails de la structure à résoudre en dépend.

5.1.7 Résolution d'une structure

Le problème de la phase

Bien que l'intensité des RX puisse être mesurée avec précision, cette information n'est pas suffisante pour calculer les facteurs de structure, puis la densité électronique, de la protéine d'intérêt. Comme toute OEM, les RX sont caractérisés par leur intensité et leur phase. Or, il n'existe aucun moyen de mesurer la phase dans une expérience de CRX. Différentes méthodes ont ainsi vu le jour pour résoudre le problème.

Le remplacement isomorphe

Deux méthodes de phasage, nommées SIR (Single Isomorphous Replacement) et MIR (Multiple Isomorphous Replacement), reposent sur l'utilisation d'atomes lourds. De par leur grand nombre d'électrons, les atomes lourds ont un pouvoir diffusif largement supérieur aux atomes qui constituent les protéines. Les deux méthodes nécessitent la collecte d'un jeu de données de la protéine native et d'un (SIR) ou plusieurs (MIR) jeux de données d'un dérivé d'atomes lourds de cette même protéine. L'intérêt de la méthode MIR est de lever l'ambiguïté inhérente à la méthode SIR qui offre deux solutions possibles sans avoir à les tester toutes deux. Le dérivé est obtenu par trempage d'un cristal dans une solution contenant l'atome lourd ou par co-cristallisation de la protéine avec celui-ci.

Leur principe repose sur le calcul d'une carte de Patterson pour identifier la position des atomes lourds dans la structure du dérivé. L'astuce d'une carte de Patterson consiste à calculer une pseudo-carte de densité électronique en utilisant l'intensité des réflexions plutôt que leur amplitude et en prenant toutes les phases égales à zéro. On peut montrer que les cartes de Patterson représentent les distances interatomiques plutôt que les positions des atomes. C'est la méthode utilisée pour résoudre la structure des petites molécules. Au-delà de 500 atomes « non-hydrogène », les cartes deviennent

ininterprétables. Toutefois, il est aisé par cette méthode de repérer la position d'un atome lourd dans une protéine et de calculer les phases des facteurs de structure de l'atome lourd. Si les structures native et dérivée sont isomorphes, leurs phases doivent être très proches. Dès lors, les phases de la structure peuvent être calculées par une TF adaptée.

La diffusion anomale

De manière analogue aux méthodes SIR et MIR, il existe deux méthodes de phasage basées sur l'utilisation de diffuseurs anomaux : les méthodes SAD (Single wavelength Anomalous Diffraction) et MAD (Multiple wavelength Anomalous Diffraction), qui diffèrent par le nombre de jeux de données nécessaires à leur mise en œuvre.

Si l'on suppose que les électrons d'une protéine sont libres, la diffusion s'accompagne d'une différence de phase de 180°. Ce n'est plus vrai dans le cas d'un diffuseur anomal à des longueurs d'onde proches de leur seuil d'absorption. La conséquence utile pour le phasage est que les paires de réflexions liées par centro-symétrie, les paires de Friedel, n'ont plus la même intensité. La loi de Friedel est brisée. Comme dans le cas des méthodes SIR et MIR, le calcul d'une carte de Patterson et une TF adaptée permettent de calculer les phases de la protéine.

La méthode MAD est uniquement pratiquée dans un synchrotron : elle nécessite la sélection des longueurs d'onde appropriées au diffuseur anomal employé.

Les nouvelles méthodes

Il existe d'autres méthodes de phasage moins courantes. Par exemple, les méthodes RIP (Radiation-Induced Phasing) exploitent les différences de phase entre deux jeux collectés avant et après une irradiation intense de RX [Nanao 2005; Ravelli 2005] ou d'UV [Nanao & Ravelli 2006]. Cette méthode évite le recours à l'utilisation d'un dérivé mais nécessite une haute résolution.

Les méthodes directes ou *ab initio* telles que Shake-and-Bake [Xu & Weeks 2008a] sont considérées comme les méthodes du futur. Comme leur nom l'indique, elles ne nécessitent qu'un seul jeu de données. L'hypothèse est faite que l'information sur la phase est contenue dans l'intensité des taches de diffraction. Basées sur la théorie des

probabilités, ces méthodes nécessitent beaucoup de temps de calcul, une haute résolution et sont pour le moment limitées par à des molécules ne contenant pas plus de 1000 atomes « non-hydrogène ».

Le Remplacement Moléculaire

Le remplacement moléculaire est la méthode de phasage la plus simple, mais ne peut être mis en œuvre que si l'on dispose du modèle d'une structure que l'on suppose ressembler à la structure à déterminer. Elle consiste à superposer la structure cherchée à la structure de référence en deux étapes [Crowther & Blow 1967; Rossmann & Blow 1962] : la recherche de la meilleure orientation (au travers d'une fonction de rotation) et de la position dans la maille élémentaire (fonction translationnelle).

Un remplacement moléculaire était suffisant pour phaser les données relatives aux structures obtenues au cours de cette thèse, *i.e.* des complexes (et des conjugués) de la *Tc*AChE avec divers ligands. En effet, les structures de la *Tc*AChE, dans les deux formes cristallines employées, étaient déjà connues. En outre, les différences entre les complexes et les structures natives étaient généralement limitées. En pratique, un affinement par corps rigide (Rigid-Body Refinement) ou même un premier cycle d'affinement au moyen des logiciels d'affinement, désormais très robustes, était suffisant pour obtenir un modèle de départ et calculer les cartes de densité électronique initiales (voir plus loin).

5.1.8 Affinement de la structure

Une fois que l'on dispose de facteurs de structure, avec amplitudes et phases, et d'un modèle, on affine ce dernier afin d'obtenir le meilleur accord entre les facteurs de structures expérimentaux (F_{obs}) et ceux du modèle (F_{calc}). Le calcul d'une carte de densité électronique $2F_{obs}$ - F_{calc} (ou $3F_{obs}$ - $2F_{calc}$) par TF permet de visualiser le modèle et les données expérimentales. Les cartes générées par différence de Fourier ($F_{obs} - F_{calc}$) font apparaître des densités électroniques négatives ou positives qui permettent de rendre compte des erreurs du modèle. Une densité positive indique l'absence d'atomes au contraire d'une densité négative qui appelle à retirer les atomes modélisés dans cette zone. En pratique (et ce fut notre stratégie pour toutes les structures obtenues au cours de

cette thèse) le modèle initial (obtenu par remplacement moléculaire ou affinement par corps rigide) contient uniquement les résidus de la protéine. A l'aide des indications des cartes $F_{obs} - F_{calc}$, on peut reconstruire le modèle en déplaçant des résidus et en ajoutant ligands et molécules d'eau.

L'affinement est réalisé par un processus itératif alternant reconstruction du modèle et minimisation des différences entre les facteurs de structure expérimentaux et observés grâce à des logiciels *ad hoc*. La reconstruction est effectuée à l'aide de programmes permettant d'afficher à la fois le modèle et les cartes de densité électronique ; nous avons utilisé Coot [Emsley & Cowtan 2004]. La procédure de minimisation est réalisée sur la base d'une méthode des moindres carrés, ou d'un cas particulier de cette dernière, le maximum de vraisemblance. En outre, l'affinement est pondéré par l'introduction de contraintes géométriques, en particulier sur la longueur des liaisons et les angles qu'elles forment entre elles. Lorsque les paramètres géométriques sont fixés, à l'exception des angles dièdres, on parle d'affinement contraint. Si ces paramètres sont autorisés à évoluer avec une tolérance plus ou moins grande, l'affinement est restreint. Plus la résolution est élevée, plus bas sera ajusté le poids des contraintes géométriques. Nous avons essentiellement utilisé les logiciels CNS [Brunger 2007] et le module REFMAC [Murshudov 1997] de la suite CCP4 [1994].

L'agrément entre les facteurs de structure observés et calculés est estimé par le facteur R :

$$R = \frac{\sum_{hkl} \left\| F_{obs} \right| - k \left| F_{calc} \right\|}{\sum_{hkl} \left| F_{obs} \right|}$$

Le facteur R, exprimé en %, doit être le plus petit possible. Toutefois sa valeur peut artificiellement diminuer en cas de « suraffinement ». Ce phénomène se produit lorsque trop de paramètres sont introduits au cours de l'affinement. Pour pallier à ce problème, on exclut de l'affinement une partie des données (typiquement 5%), qui sera réservée au calcul du facteur R_{free}, homologue du facteur R en utilisant lesdites réflexions [Brunger 1992]. En pratique, on poursuit l'affinement tant que les modifications apportées au modèle font diminuer R et R*free*. Il arrive que le R continue de diminuer alors que le R*free* reste stable ou augmente : c'est là le signe d'un probable suraffinement : les modifications du modèle n'améliorent pas réellement la structure.

Les phases du modèle biaisent fortement les données. Pour effacer cette « mémoire », on a généralement recours à un recuit simulé (*simulated annealing*). C'est une procédure de dynamique moléculaire qui consiste à donner suffisamment d'énergie aux atomes (« chauffage ») pour sortir la structure d'un éventuel puits de potentiel duquel la minimisation n'aurait pu la sortir. La structure est ensuite « refroidie » lentement avant d'être à nouveau minimisée.

Lorsque les facteurs R et R_{free} ont convergé, la structure est validée avant d'être éventuellement déposée dans la PDB.

5.1.9 La cristallographie cinétique

La cristallographie cinétique regroupe un ensemble de techniques basées sur la cristallographie aux RX et des méthodes complémentaires qui sont le plus souvent spectroscopiques. C'est une méthode qui permet de caractériser les différents états conformationnels d'une protéine permis par sa dynamique. Dans le cas d'une enzyme, elle vise à capturer les intermédiaires réactionnels qui existent dans la suite des évènements de la réaction catalytique (chemin réactionnel). L'idée maîtresse est le contrôle de l'évolution de la réaction par la température, la pression, ou l'irradiation par la lumière UV/visible ou les RX. Nous détaillerons ici les principes de ces méthodes ainsi que leurs limitations. Pour de plus amples informations, le lecteur pourra consulter les revues récentes sur le sujet [Bourgeois & Royant 2005; Bourgeois & Weik 2009].

5.1.9.1 Activité dans la forme cristalline

Bien que la plupart des enzymes restent actives sous forme cristalline [Mozzarelli & Rossi 1996], certains écueils doivent être évités dans l'interprétation de données cristallographiques. Les interactions qui maintiennent l'édifice cristallin sont faibles : elles ne concernent en général que quelques résidus de surface. L'énergie associée à un contact cristallin est de l'ordre de grandeur de celle d'une liaison hydrogène (~10 $kcal.mol^{-1}$). Il arrive que l'empilement cristallin concerne des résidus importants pour l'activité catalytique. Plus rarement, ces contacts peuvent gêner le trafic des substrats et produits. Toutefois, les protéines conservent leur flexibilité sous forme cristalline, comme

en attestent l'impossibilité de modéliser certains acides aminés, la dépendance en température des facteurs B [Petsko & Ringe 1984] et l'hétérogénéité structurale qui caractérise les cristaux de protéines [Smith 1986]. Le pH et la nature du solvant sont également des facteurs qui peuvent gêner l'activité ou conduire à l'observation de conformations artéfactuelles. Une expérience de cristallographie cinétique sera donc possible uniquement si les conditions cristallographiques (empilement cristallin, température, pH, force ionique, présence de certains ligands, *etc*) n'entravent pas l'activité de la protéine.

Nous avons mentionné plus haut que le paysage conformationnel d'une enzyme dépend de la température. Il s'ensuit que les SC piégés à basse température peuvent se révéler être des SC minoritaires à température ambiante.

5.1.9.2 Uniformité, synchronisation et stratégies de déclenchement

Parce que les différences entre l'enzyme native et son intermédiaire réactionnel sont souvent subtiles, la population dans la forme « excitée » doit être la plus homogène possible afin d'être résolues par la diffraction aux rayons X (une structure déterminée par CRX est une moyenne de toutes les molécules du cristal ayant participé à la diffraction). Il faut donc synchroniser le déclenchement de la réaction dans les molécules présentes dans le cristal, lequel est composé d'environ 10^{14} protéines. En pratique, la vitesse de déclenchement de la réaction doit être beaucoup plus grande que celle de l'avancement de la réaction catalytique envisagée. Une vitesse de déclenchement lente suffit dans les cas où le piégeage est réalisé à basse température, ou lorsque l'intermédiaire ne peut pas évoluer en raison d'une mutation dirigée ou de l'empilement cristallin. On peut dans ces cas envisager des trempages ou l'initiation de la réaction par exposition à une lumière.

Trois stratégies de déclenchement ont été proposées.

_ La diffusion d'un ligand est la plus simple à mettre en en place. Toutefois, la diffusion est un processus lent. Par exemple, le coefficient de diffusion de la fluorescéine a été mesuré à ~3.10^{18} $m^2.s^{-1}$ dans les canaux de solvant du lysozyme orthorhombique larges de ~2 nm [Cvetkovic 2005]. On peut grossièrement estimer que, dans un cristal de dimension caractéristique de l'ordre de 100 μm, les protéines les plus enfouies seront atteintes au bout d'une milliseconde environ. On notera tout de même que les canaux de

solvant du lysozyme sont particulièrement étroits. L'effet du confinement est, évidemment, moins important dans un cristal dont les canaux sont plus larges.

_ L'activation d'une réaction par application d'une irradiation laser (dans le domaine UV/visible) est beaucoup plus rapide. Elle suppose néanmoins la photosensibilité de la protéine ou l'utilisation d'un composé photosensible externe tel qu'un ligand en cage. L'avantage est que le déclenchement peut être réalisé à n'importe quelle température. La réaction peut ensuite être contrôlée par la température.

_ Le déclenchement par l'irradiation X possède les mêmes avantages que la précédente méthode. Cela concerne des réactions redox initiées par les radicaux libres générés par la radiolyse de l'eau. Des liaisons sensibles aux rayons X permettront également cette approche. Il faut toutefois être capable de déconvoluer les dommages d'irradiations aux RX afin d'être en mesure d'interpréter les données.

5.1.9.3 La diffraction de Laue : cristallographie en temps résolu

La diffraction de Laue est la méthode historique de diffraction des rayons X. C'est pour la découverte de la diffraction de ces derniers par des réseaux cristallins tridimensionnels que Max von Laue reçut le prix Nobel de physique en 1914. Toutefois, cette méthode utilise un faisceau de rayons X polychromatique. Par la suite, la résolution de structures, et en particulier de celles des protéines, s'est faite avec des faisceaux monochromatiques pour la plus grande simplicité de traitement des clichés de diffraction.

Pourtant, la diffraction de Laue connaît un nouvel âge d'or dans le domaine de la cristallographie cinétique depuis l'avènement des synchrotrons. Les faisceaux de rayons X très intenses combinés à l'utilisation de détecteurs et d'obturateurs plus rapides a permis de réaliser l'enregistrement de clichés de diffraction en 100 ps [Schotte 2004].

La méthode de cristallographie cinétique par diffraction de Laue repose le plus souvent sur une stratégie « pompe/sonde ». Une courte impulsion laser est d'abord appliquée à l'échantillon pour l'amener à sa forme excitée, suivie d'une courte impulsion de rayons X. Cette séquence est répétée autant de fois que nécessaire pour parcourir l'ensemble du réseau réciproque et diminuer le rapport signal/bruit. La durée séparant l'impulsion laser de l'impulsion de rayons X peut être variée pour balayer la dimension temporelle, et ainsi permettre *in fine* d'obtenir le film de la réaction catalytique.

La diffraction de Laue n'est toutefois applicable qu'à un nombre limité de protéines. Non seulement l'échantillon doit être le siège d'une réaction photo-déclenchable et réversible, mais il doit également présenter une faible mosaïité et pouvoir supporter une grande dose de RX sans perdre son pouvoir de diffraction. En outre, le traitement des clichés de diffraction Laue s'avère généralement complexe.

5.1.9.4 La cristallographie cinétique par piégeage d'intermédiaires réactionnels

Les méthodes de piégeage sont, elles, plus faciles à mettre en œuvre et s'adressent potentiellement à toutes les protéines qui produisent des cristaux d'une qualité de diffraction suffisante.

Dans la stratégie de piégeage, on cherche à accumuler l'intermédiaire réactionnel avant de le piéger, en général, par refroidissement ultra-rapide. L'utilisation d'un analogue de substrat, d'un mutant ou tout changement dans la nature du solvant (le pH, par exemple) ne permettant pas le prolongement de la réaction au-delà de cet intermédiaire est également possible.

Si le déclenchement ne nécessite pas une synchronisation rapide, on peut amorcer la réaction avant le refroidissement ultra-rapide (stratégie «trigger-freeze »). Lorsque l'intermédiaire est transitoire où qu'il survient rapidement après l'initiation de la réaction, on cherchera plutôt à figer le système avant d'initier la réaction (stratégie « freeze-trigger »). Dans le cas d'une réaction photo-activable, on pourra refroidir le système avant de l'exciter, puis jouer sur la température pour ajuster l'avancement de la température. On peut également artificiellement modifier la hauteur de la barrière énergétique (mutagenèse, pH) de façon à laisser s'accumuler l'intermédiaire qui ne pourra pas évoluer.

Peu importe la stratégie choisie, l'échantillon est amené à une température adaptée à la collecte de données cristallographiques (autour de 100 K).

5.2 Microspectrophotométrie

Au cours de cette thèse, nous avons eu recours à des techniques spectroscopiques pour étudier la dynamique de la *Tc*AChE. La spectroscopie de fluorescence et la fluorescence résolue en temps sont aujourd'hui des outils répandus en biophysique. Nous nous sommes tournés vers une approche similaire, basée sur la phosphorescence. Nous présenterons dans un premier temps les principes physiques qui sous-tendant les techniques spectroscopiques mises en œuvre au cours de cette thèse, en mettant l'accent sur le phénomène de phosphorescence. Nous décrirons ensuite brièvement le laboratoire où ont été effectuées ces mesures, le cryobench. La méthode de mesure du temps de vie de phosphorescence d'un ligand lié à la *Tc*AChE, que nous avons développée, sera rapidement introduite.

5.2.1 Luminescence et spectroscopie

La luminescence consiste en l'émission de lumière par une substance. Elle se produit à partir d'états électroniques excités générés par l'absorption d'un photon. Selon la nature de l'état excité, on distingue deux formes de luminescence : la fluorescence et la phosphorescence. Ces deux phénomènes sont caractérisés en particulier par leur temps de vie. Le temps de vie (τ) d'un fluorophore est la durée moyenne entre l'excitation et le retour à l'état de repos. Comme la fluorescence se produit lorsque des électrons sont excités dans des états singulets, leur retour à l'état fondamental est autorisé par leur spin (opposé à l'électron auquel ils sont appariés dans l'orbitale de repos) et l'émission qui l'accompagne se produit rapidement : le temps de vie de fluorescence typique est de l'ordre de 10 ns. Dans le cas de la phosphorescence, les électrons sont excités dans des états triplets et leur spin est identique à celui de l'électron dans l'orbitale de repos. Ainsi, les transitions électroniques vers l'état de repos sont interdites. En conséquence, la phosphorescence a des temps de vie typiques de l'ordre de la ms à la s, voire plus (comme dans le cas des aiguilles de réveil qui brillent dans le noir pendant plusieurs minutes). En outre, pour un fluorophore donné, la longueur d'onde associée à la phosphorescence est généralement plus grande. La distinction entre la fluorescence et la phosphorescence n'est

pas toujours évidente. Un diagramme de Jablonski permet d'illustrer les phénomènes d'absorption et d'émission (Fig. 19).

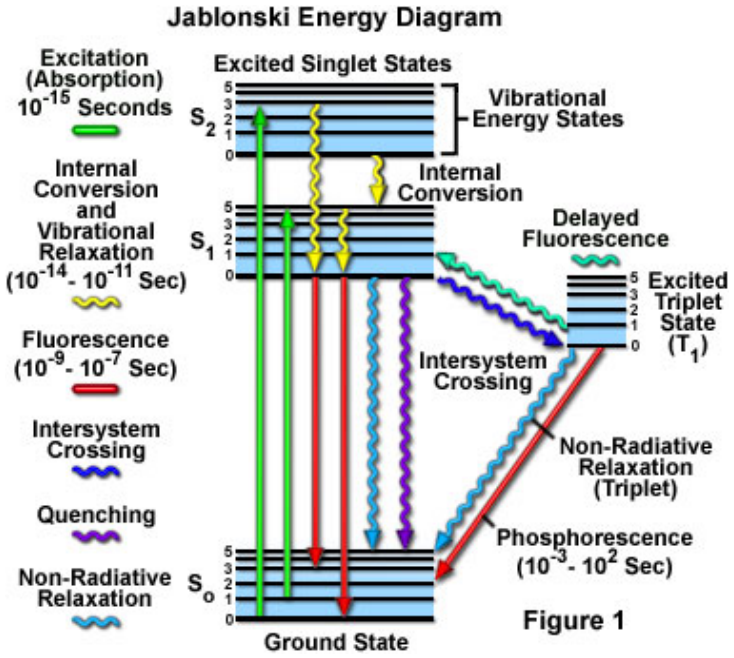

Figure 19. Diagramme de Jablonski. Reproduit de [2].

A température ambiante, la phosphorescence est rarement observée dans des solutions contenant un fluorophore. En effet, certains phénomènes entrent en compétition avec l'émission : la désexcitation non-radiative et le phénomène de *quenching* (ce qui est vrai également pour la fluorescence). Le *quenching* est la diminution de l'intensité de la luminescence induite par différents processus. Le *quenching* collisionnel se produit lorsque des molécules appelées *quenchers* entrent en contact avec le fluorophore, ce qui conduit à une désexcitation sans émission. Le *quenching* statique se produit quand un fluorophore forme un complexe non fluorescent avec le *quencher*. Le *quenching* possède d'autres origines, liées à une atténuation de la lumière incidente (absorption par le fluorophore ou une molécule environnante). Un transfert d'énergie par résonance de fluorescence (Fluorescence Resonance Energy Transfer, FRET) peut également causer une diminution de l'intensité de la fluorescence. Si le spectre d'absorption d'un accepteur et le spectre d'émission d'un donneur (le fluorophore) partagent une même gamme de longueurs d'ondes, un transfert d'énergie entre les deux espèces peut conduire à désexciter le fluorophore.

Un fluorophore est caractérisé par son temps de vie, comme nous l'avons indiqué plus haut, mais également par son rendement quantique. C'est le rapport entre la quantité de photons émis et ceux qui sont absorbés. Ainsi, le rendement quantique est d'autant plus élevé que les phénomènes de désexcitation non-radiative et le *quenching* se produisent peu. Les fluorophores se caractérisent en outre par leurs spectres d'absorption et d'émission.

Les fluorophores sont typiquement des molécules aromatiques, telles que l'AB1. Des protéines intrinsèquement fluorescentes, comme la GFP (Green Fluorescent Protein) sont aujourd'hui très étudiées, notamment pour leurs propriétés en tant que sonde pour l'imagerie cellulaire. Toutes les protéines qui possèdent des tryptophanes sont également des fluorophores.

La mesure de l'absorption et de la luminescence d'un fluorophore peut apporter des informations structurales et dynamiques sur ce dernier. Comme l'absorption se produit sur une échelle de temps très rapide (10^{-15} s), elle est en pratique considérée comme étant instantanée. Ainsi, l'absorption fournit une information moyenne sur une population de fluorophores. Compte-tenu des possibilités offertes par la technologie actuelle, l'intensité et le temps de vie d'un fluorophore peuvent être mesurés. Ceci est bien sûr également vrai pour la phosphorescence. La fluorescence et la phosphorescence permettent donc d'envisager des expériences de spectroscopie résolues en temps. La mesure des temps de vie de fluorescence et de phosphorescence offrent ainsi la possibilité de sonder la dynamique d'un fluorophore sur les échelles de temps associées : la ns et la ms/s. En effet, tout évènement affectant le fluorophore ou son environnement pendant la durée de vie de l'état excité sera susceptible de modifier l'intensité et le temps de vie de la luminescence.

Plus d'informations sur les notions relatives à la luminescence et à la spectroscopie peuvent être trouvées dans ce livre [Lakowicz 2006].

5.2.2 Le cryobench

Nous avons effectué toutes nos expériences spectroscopiques au cryobench [Bourgeois 2002]. Ce laboratoire permet de réaliser des expériences de spectroscopie *in crystallo* dans les conditions d'une expérience de CRX : le cristal est monté avec une boucle sur

une tête goniométrique, et l'échantillon peut être placé sous un flux d'azote gazeux à une température typiquement comprise entre 100 K et la température ambiante. L'élément central du cryobench, le microspectrophotomètre est composé de la tête goniométrique, du système cryogénique qui diffuse de l'azote gazeux *via* une canne, de trois objectifs et d'une caméra qui permet de visualiser l'échantillon (Fig. 20). Tous les éléments sont alignés sur le centre optique de l'appareil. Parmi les trois objectifs, deux se font face et permettent des mesures en transmission alors que le troisième permet des mesures à 90°. Des fibres optiques permettent de relier chacun de ces objectifs à des lasers émettant dans l'UV ou le visible, et à un spectromètre qui enregistre les spectres d'absorption ou d'émission. Il est possible de mesurer le temps de vie de fluorescence grâce à un système de TCSPC (Time-correlated Single Photon Counting) [Royant 2007]. Des spectres Raman peuvent également être enregistrés [Carpentier 2007].

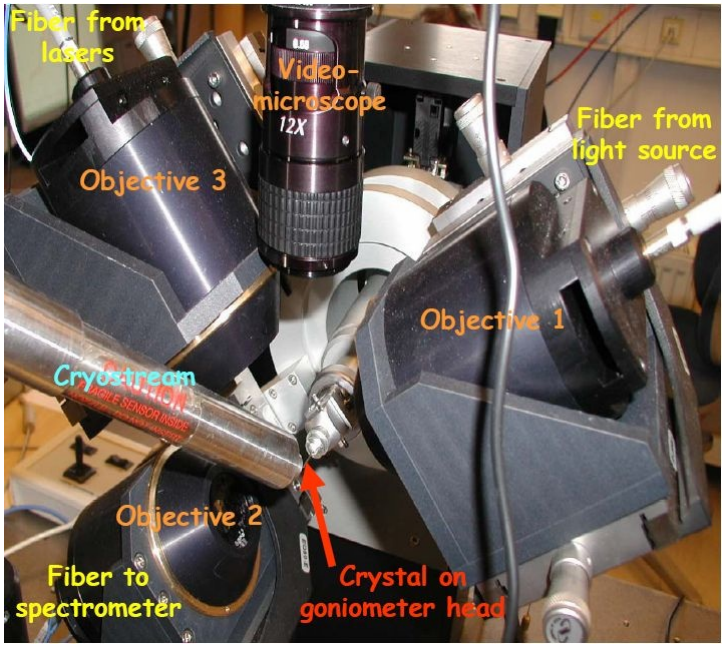

Figure 20. Le microspectrophotomètre du cryobench.

Des expériences de TCSPC ont été réalisées sur des complexes de *Tc*AChE avec le propidium, un inhibiteur fluorescent du PAS. Les résultats que nous avons obtenus sont toutefois difficiles à interpréter. Notamment, deux temps de vie distincts ont été mesurés dans des échantillons cristallins de ces complexes. Plus de mesures sont nécessaires pour pouvoir déterminer sans ambigüité l'origine de chacun de ces temps de vie. En ce qui concerne la spectroscopie Raman, aucun spectre exploitable n'a pu être enregistré sur des

échantillons de *Tc*AChE : le fond du spectre est trop intense pour permettre l'observation de raies suffisamment intenses pour détecter de putatives différences entre deux échantillons. Les expériences de spectroscopie Raman sur la *Tc*AChE devraient toutefois être concluantes à condition de remplacer le solvant par des espèces produisant un fond d'intensité négligeable.

5.2.3 Temps de vie de phosphorescence en fonction de la température

Pour étudier la dynamique de la *Tc*AChE, et en particulier mettre en évidence la transition dynamique de l'enzyme, des expériences de microspectrophotométrie de fluorescence en fonction de la température (TDFM, Temperature-Derivative Fluorescence Microspectrophotometry) ont été conduites récemment [Weik 2004]. Cette méthode repose sur l'utilisation combinée d'un ligand fluorescent et d'une rampe de température. Le centre de masse du spectre d'émission du fluorophore est déterminé pour chaque température. Les résultats n'ont cependant pas permis de sonder la dynamique de la *Tc*AChE : il semble que le signal mesuré provienne du fluorophore (la fluorescéine) présent dans les canaux de solvant. Pour étudier la dynamique de la *Tc*AChE, nous nous sommes tournés vers une nouvelle méthode spectroscopique basée sur la mesure du temps de vie de phosphorescence d'un ligand phosphorescent de l'enzyme, l'AB1.

Nous avons mesuré le temps de vie de phosphorescence de l'AB1 en complexe avec la *Tc*AChE cristalline, et dans la solution de trempage qui a servi à produire les complexes, entre 100 et 240 K. En effet, à ces températures, le temps de vie de phosphorescence est suffisamment long (autour d'1 s) pour pouvoir être mesuré grâce au spectromètre du cryobench. Nous avons initié le développement de cette méthode dans l'idée de disposer d'un moyen simple de mesurer la dynamique lente (à l'échelle de la ms-s) des protéines à des températures cryogéniques. La mesure du temps de vie n'est pas directe. En pratique, l'acquisition de données repose sur l'enregistrement (immédiatement après l'excitation du fluorophore) de l'intensité de la phosphorescence à des intervalles de temps réguliers lors de sa décroissance. Le temps de vie est obtenu après ajustement aux données d'une fonction monoexponentielle. Le traitement de données a été l'occasion de mettre un pied dans le monde de la bioinformatique. En effet, le volume de données à traiter nécessite un traitement automatisé (au moins 6 décroissances ont été enregistrées pour 25 températures

à chaque répétition d'une expérience). Nous avons rédigé à cet effet un script en langage python (annexe 5).

Les détails expérimentaux ainsi que les résultats seront donnés dans la section Résultats (partie 3.4).

6. RÉSULTATS

6. RÉSULTATS

6.1 Acétylcholinestérase en complexe avec de putatives molécules anti-Alzheimer

6.1.1 Présentation de l'article

Le premier article (en préparation) est consacré à l'analyse de structures cristallographiques de la *Tc*AChE en complexe avec des médicaments anti-Alzheimer potentiels. Ces travaux sont le fruit d'une collaboration avec l'équipe du Prof. Giuseppe Campiani, de l'université de Sienne, qui développe, synthétise et caractérise ces molécules.

Les trois molécules utilisées se lient à l'AChE à la fois au niveau du CAS et du PAS, ce qui caractérise la deuxième génération de médicaments anti-Alzheimer. Une première étude, réalisée avec le NF595, a révélé une flexibilité conformationnelle inattendue du PAS [Colletier 2006b] (annexe 1). Les deux molécules utilisées dans les travaux présentés dans l'article qui suit, le NF766 et le NF1056, exploitent chacune un site de fixation additionnel. Un site d'interaction à mi-hauteur a été mis en évidence structuralement grâce au complexe *Tc*AChE/NF766. Le complexe *Tc*AChE/NF1056 montre un site de fixation sur la surface de l'enzyme au pourtour du PAS. Il reste à démontrer que les résidus de l'AChE impliqués dans cette interaction sont ceux qui sont à l'origine de la promotion de la fibrillation d'Aβ. Cette étude structurale ouvre de nouvelles pistes quant à la conception de nouveaux médicaments visant à lutter contre la maladie d'Alzheimer.

6.1.2 Article

Manuscrit en préparation.

Acetylcholinesterase in complex with two putative anti-Alzheimer drugs

Benoît Sanson[†], Jaques-Philippe Colletier[†], Stefania Butini[‖§], Joel L. Sussman[∞], Israel Silman[±], Giuseppe Campiani[‖§] and Martin Weik[†]

[†]Laboratoire de Biophysique Moléculaire, Institut de Biologie Structurale, 38027 Grenoble, France, [‖]European Research Centre for Drug Discovery and Development, Universitá di Siena, Italy, [§]Dipartimento Farmaco Chimico Tecnologico, Via Aldo Moro, Universitá di Siena, 53100 Siena, Italy, [∞]Departments of Structural Biology and [±]Neurobiology, Weizmann Institute, 76100, Rehovot, Israel

Manuscript in preparation.

ABSTRACT

Alzheimer's disease (AD) is becoming a new threat with rapid aging of the population. It has been shown that AD is associated to low levels of acetylcholine and deposition of the β-amyloid peptide (Aβ) into extracellular plaques in the brain. The first generation of anti-Alzheimer drugs has aimed at inhibiting acetylcholinesterase (AChE) in order to restore acetylcholine levels. More recently AChE has been shown to promote the fibrillization of Aβ through its peripheral site (PAS). Second-generation anti-Alzheimer drugs, the so-called bifunctional inhibitors, have then been designed so as to bind at both active site and the PAS, thus inhibiting promotion of Aβ fibrillation. We solved the structures of *Torpedo californica* AChE in complex with two compounds that take advantage of new binding loci. NF766 was shown to bind to AChE through a supplementary mid-gorge interaction. NF1056 features a peptide moiety that binds on the surface close to the PAS. Some of the AChE residues that interact with NF1056 have been shown earlier to interact with Aβ. These structures will be helpful in the design of improved anti-Alzheimer drugs.

INTRODUCTION

Alzheimer's disease (AD) is a progressive and irreversible age-related neurodegenerative disorder. An estimated 10% of the world's population over the age of 65 is afflicted by AD, the prevalence of which rises exponentially with age. With the rapid growth of the oldest age groups in Europe, Asia and North America, the prevalence of AD is expected to increase almost 3-fold by 2050 [Hebert 2003]. The progression of AD therefore represents a major social and economical threat, unless a treatment that slows stops, or cures the disease is designed. The mechanisms leading to the onset of AD remain unclear. The major hallmarks of AD are a loss of cholinergic neurons and deposition of the β-amyloid peptide (Aβ) into extracellular senile plaques in brain regions important for memory and cognition [Holzgrabe 2007]. Intracellular neurofibrillary tangles, stemming from fibers of hyperphosphorylated tau proteins, are also found in the Alzheimer brain [Holzgrabe 2007]. Additionally, the disease is associated to cholinergic dysfunctions of the central nervous system (CNS) [Bartus 1982]. In particular, levels of acetylcholine

(ACh) in the Alzheimer brain are lower than those measured in the healthy brain. Inhibiting acetylcholinesterase (AChE) may restore the level of ACh. AChE thus became the primary target for anti-Alzheimer drugs.

AChE terminates cholinergic transmission at the post-synaptic membrane of both neuromuscular junctions and cholinergic synapses [Silman 2005]. It hydrolyses the neurotransmitter acetylcholine at the bottom of a deep and narrow gorge [Sussman 1991]. At the top of this gorge, a peripheral anionic subsite (PAS) has been described [Sussman 1991; Taylor 1975], which serves as another binding site for substrates and products [Bourne 2003; Colletier 2006a], though its role remains incompletely understood.

Beyond being a target for anti-Alzheimer drugs, AChE is the target of natural toxins or man-made poisons [Soreq 2001]. Organophosphate compounds (OP) and carbamoyls, which are found in either chemical warfare agents such as soman or in insecticides, covalently bind to the active site of AChE and irreversibly inhibit it. Neurotoxins such as the snake venom fasciculin, or the mycotoxin aflatoxin bind to the PAS and hinder substrate and product trafficking through the gorge. Both may modulate the efficiency of catalysis by allosterically modifying the catalytic triad conformation.

The first generation of anti-Alzheimer cholinesterase inhibitors aimed at reversibly inhibiting the catalytic efficiency of AChE so as to compensate for the decreased level in the neurotransmitter acetylcholine (ACh) observed in the Alzheimer's brain. All four molecules that received FDA approval, namely tacrine (Cognex®), E2020 (donepezil, Aricept®) galanthamine (Reminyl®) and rivastigmine (Exelon), as well as (-)-Huperzine A, an alkaloid extracted from the plant *Huperzia serrata* used in China, are reversible inhibitors of AChE, which bind in the active site [Du & Carlier 2004; Greenblatt 2003]. Binding of the anti-Alzheimer drugs was confirmed by the crystallographic structures of the complexes of each inhibitor with AChE [Bar-On 2002; Greenblatt 1999; Harel 1993; Kryger 1998; Raves 1997]. The structural data on AChE in complex with anti-AD drugs was reviewed in 2003 [Greenblatt 2003]. All but rivastigmine bind to Trp84, which is the key residue of the choline-binding pocket of AChE. E2020 binds in the CAS and at the PAS. Rivastigmine covalently binds to Ser200. Geneserine-derived carbamate-based inhibitors are being developed [Bartolucci 2006] in order to improve the binding affinity of anti-AD drugs. They bind covalently to the catalytic serine and disrupt the catalytic triad, which lends

Undesired side-effects and lack of efficiency affect all first generation anti-Alzheimer drugs [Holzgrabe 2007]. Furthermore, AChE was shown to promote Aβ fibrillogenesis

[Inestrosa 1996]. Interests then turned towards new inhibitors acting at the PAS. The structure of *Tc*AChE with the elongated bis-quaternary ligand decamethonium had indeed permitted clear identification of the PAS [Harel 1993]. The second generation of anti-Alzheimer drugs hence aims at dually targeting AChE by inhibiting both its catalytic activity in the active site, and the promotion of Aβ fibrillation by at the PAS [Barak 1995; Du 2004; Ordentlich 1995; Radic 1995]. The 3D structures of *Tc*AChE in complex with bis-tacrines have confirmed that these inhibitors bind both sites through π-π interactions with Trp84 and Trp279 [Colletier 2006b; Rydberg 2006], thereby revealing unanticipated flexibility of the protein, which should be taken into account for designing a potent drug [Butini 2008b; Xu 2008b; Xu 2008c]. Bivalent inhibitors are not based only on tacrine, but e.g. also on HupA [Gemma 2006; Wong 2003]. An enzyme homologous to AChE, butyrylcholinesterase (BuChE), is overexpressed in the AD brain. Though its role is not known, BuChE is able to hydrolyze ACh, making it a valuable target for anti-Alzheimer drugs [Mesulam 2002]. Since AD is also associated with, e.g. neuroinflammation, glutamate-induced neuronal apoptosis and oxidative stress, bivalent inhibitors can be designed, which offer a multi-faceted efficiency against AD [Fang 2008; Li 2005]. It is noteworthy that click chemistry now allows assembling two previously separate moieties in a bivalent inhibitor *in situ* [Bourne 2004].

A midgorge recognition site has been identified in AChE [Savini 2003] and BuChE [Campiani 2005], which is expected to be exploited as a supplementary anchor for an inhibitor in AChE. Bistacrine derivatives bearing peptidic tethers have also been synthesized [Butini 2008a], which aim at increasing the affinity of the drug by increasing its surface of interaction with AChE. Those new compounds represent an additional strategy to design a potent drug through increased affinity and selectivity.

In this study, we solved and analyzed the X-ray structures of *Tc*AChE in complex with two putative new-generation anti-Alzheimer molecules, *viz.* NF766 and NF1056 (scheme 1). The structure of *Tc*AChE in complex with NF595 [Colletier 2006b] was compared to them. Those complex structures push further the basis for a structural approach in the design of efficient and tolerable bivalent anti-Alzheimer drugs. Indeed, flexible structure-based docking of anti-Alzheimer drugs in AChE would benefit from supplementary anchoring sites.

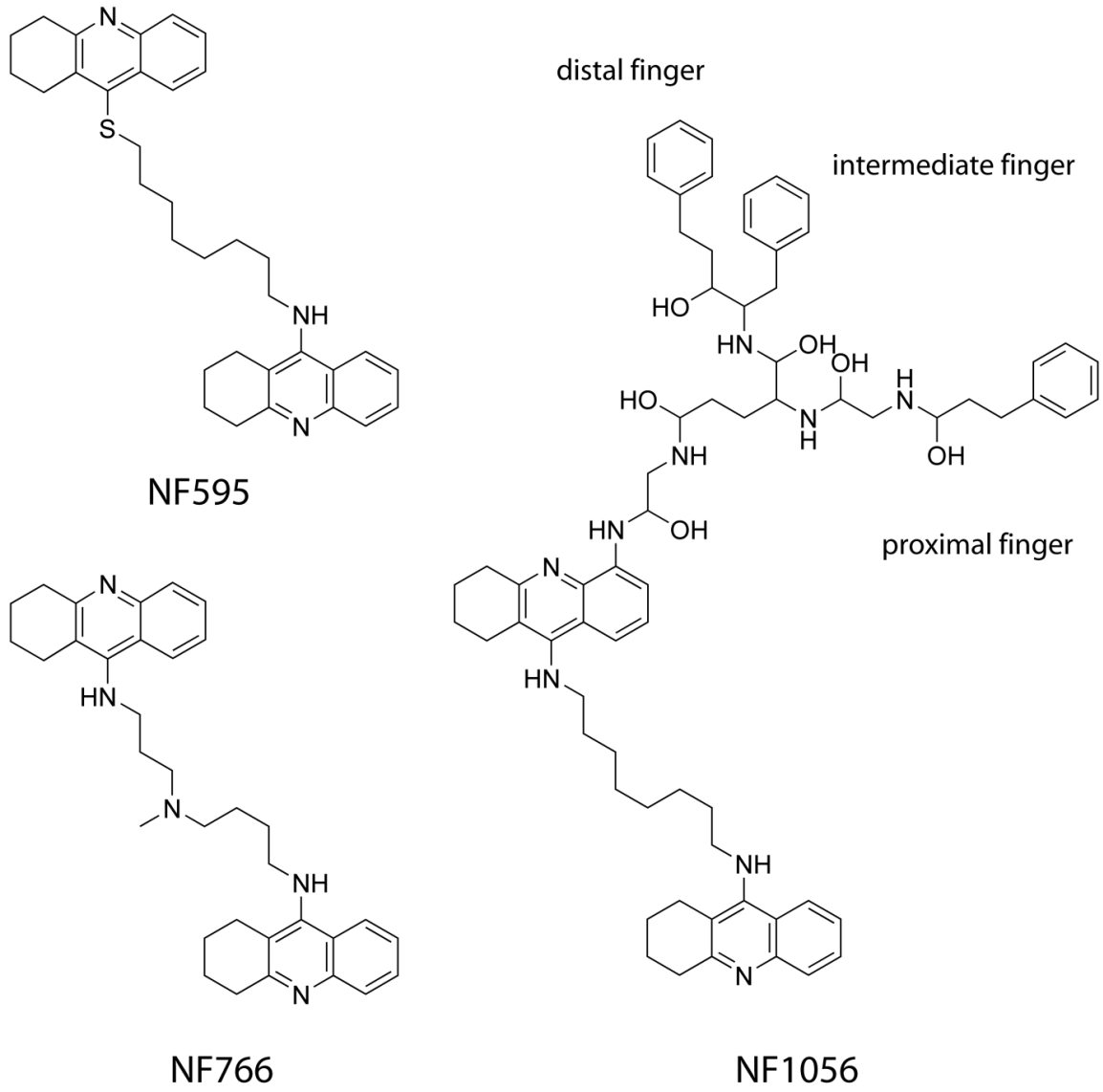

Scheme 1: Chemical structures of NF595, NF766 and NF1056.

MATERIALS AND METHODS

Materials. Polyethyleneglycol (PEG) 200, morpholinoethylsulphonic acid (MES), Sodium acetate (NaAc) and Zinc acetate (ZnAc) were purchased from Sigma Chemical Co. (St Louis, MO, USA). *Tc*AChE was purified as described previously [Sussman 1991]. NF766 and NF1056 (scheme 1) were synthesized at the Università di Siena and solubilized in water and a mixture of 57% methanol (MeOH) and 43% dimethylsulfoxide (DMSO), respectively.

Crystallization and Soaking Procedure. Native trigonal and orthorhombic crystals of *Tc*AChE (space groups $P3_121$ and $P2_12_12_1$, respectively) were obtained at 4°C in hanging drops by the vapor diffusion method in 32-34% PEG 200 and 150mM MES at pH 5.8-6.1. The complexes of both trigonal and orthorhombic *Tc*AChE with NF766 were formed by soaking crystals of the native enzyme into solutions based on 36% PEG200 and 150mM MES (referred to as *the soaking solution*) and 2mM NF766. Trigonal and orthorhombic crystals of *Tc*AChE were soaked in the soaking solution containing 1mM NF1056, yielding a complex with NF1056 only in trigonal crystals. Alternatively, co-crystals of *Tc*AChE and NF1056 were grown, following the conditions described for the structure of the AChE/fasciculine complex (Harel Structure 1995). The reservoir contained 20-25% PEG 200, 0.1 M NaAc, 1mM ZnAc. The drop was a 1:1 ratio of the reservoir containing 200μM NF1056 (and 0.17% MeOH and 0.13% DMSO) and the protein solution (~11 mg/mL). Co-crystallization yielded orthorhombic ($P2_12_12_1$) crystals. Owing to the cryoprotective capacity of PEG 200, no additional cryoprotectant was necessary and crystals was directly loop-mounted and flash-cooled in liquid nitrogen.

Data collection and processing All data collections were performed at the European Synchrotron Radiation Facility (ESRF, Grenoble) on beamlines ID14-2 and -4. The loops containing flash-cooled crystals were transferred on the goniometer head into the cryostream of a cooling device (700 series, Oxford Cryosystems, Oxford, UK) operating at 100 K. For details concerning data collection, see table 1. Reflections were indexed and integrated using XDS [Kabsch 1993]. The intensities of integrated reflections were scaled using XSCALE and structure factors were calculated using XDSCONV. Refinement of

the models was carried out using Refmac5, with the native structures of $P3_121$ and $P2_12_12_1$ *Tc*AChE (PDB entry codes 1EA5 and 1W75, respectively) as the starting models. For calculation of R_{free} the same structure factors were flagged as the ones used for refinement of the starting model (1EA5 or 1W75). For all three structures, a rigid body refinement was first carried out using reflections in the range 20 – 4 Å. All model building and graphic operations were carried out using Coot [Emsley 2004]. In each model, the first set of water molecules was added automatically using the water-picking feature in Coot. Solvent molecules, ligands and sugar molecules, *viz.* N-acetylglucosamine (NAG) and fucose (FUC), were added subsequently. Successive alternation of refinement cycles and manual model building were performed until $R_{cryst.}$ and R_{free} did not decrease any further. Refinement comprised energy minimization and individual isotropic B-factor refinement, using the full range of recorded reflections for each data set. The simulated-annealing omit-maps were calculated using CNS version 1.2 [Brunger 2007] after omitting NF766 or NF1056. Figures were produced with Pymol [DeLano 2002a]. Final models were validated using MOLPROBITY [Davis 2007] and WHATCHECK [Hooft 1996]. Parameters and topologies of PEG, MES, NAG, FUC, NF766 and NF1056 were generated using the PRODRG [Schuttelkopf & van Aalten 2004] server of Dundee University.

RESULTS AND DISCUSSION

Trigonal TcAChE in complex with NF766

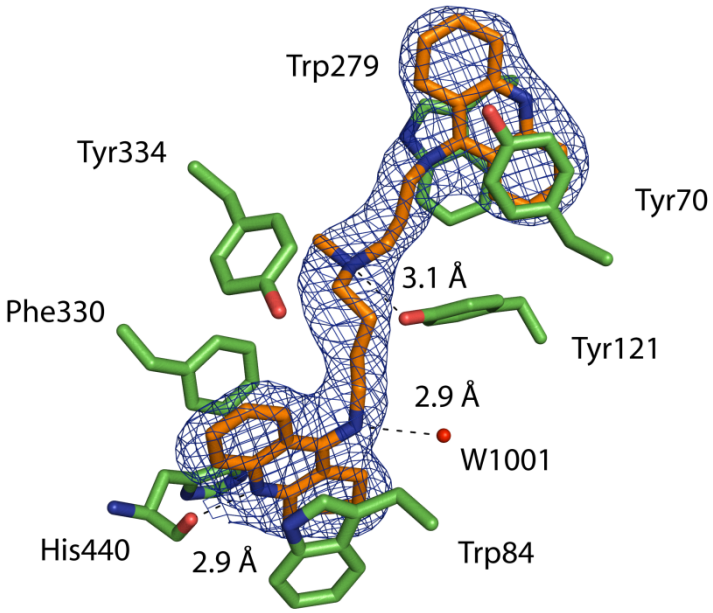

Figure 1. NF766 in complex TcAChE in the trigonal crystal form. The Fo-Fc omit electron density contoured at 3σ is displayed in blue. Residues Tyr70, Trp84, Tyr121, Trp279, Phe330, Tyr334, His440 and NF766 are rendered as sticks. Carbon atoms of amino acids and NF766 are in green and orange, respectively. Nitrogen and oxygen atoms are in blue and red, respectively. A water molecule is represented as a red sphere. Hydrogen bonds are represented as black dashes.

The structure of *Tc*AChE in complex with NF766 (scheme 1) was solved at 2.25 Å resolution in the trigonal ($P3_121$) form. In agreement with each crystallographic structure of *Tc*AChE in complex with a bivalent inhibitor, NF766 adopts a binding mode that spans the gorge (Fig. 1). NF766 is almost identical to NF595 (scheme 1), the structure of which in complex with *Tc*AChE has been solved and published already (PDB entry code: 2CEK) [Colletier 2006b]. As anticipated, inasmuch these two ligands only differ in their linker, NF766 binds in a very similar fashion than NF595 (Fig. 2). One tacrine moiety makes a hydrogen bond with His440 (2.9 Å), as was observed in 2CEK (3.0 Å). Both tacrine moieties participate in π-π interactions with either Trp84 and Phe330 or Trp279 and Tyr70; Phe330 and Trp279 undergo the conformational changes observed in 2CEK with respect to the native structure. It should be noted that the stacking between Tyr70,

the upper tacrine moiety of NF766 and Trp279 is not as parallel as in 2CEK (the long axis of the tacrine is rotated by 15° with respect to the corresponding tacrine of NF595; Fig.1), making NF766 bind slightly deeper into the gorge of AChE. This slight misalignment is not accompanied by a comparable change in the conformation of Trp279 with respect to that in 2CEK, hence supporting the hypothesis that this conformation was selected in the conformational landscape of the enzyme, rather than being induced [Xu 2008b].

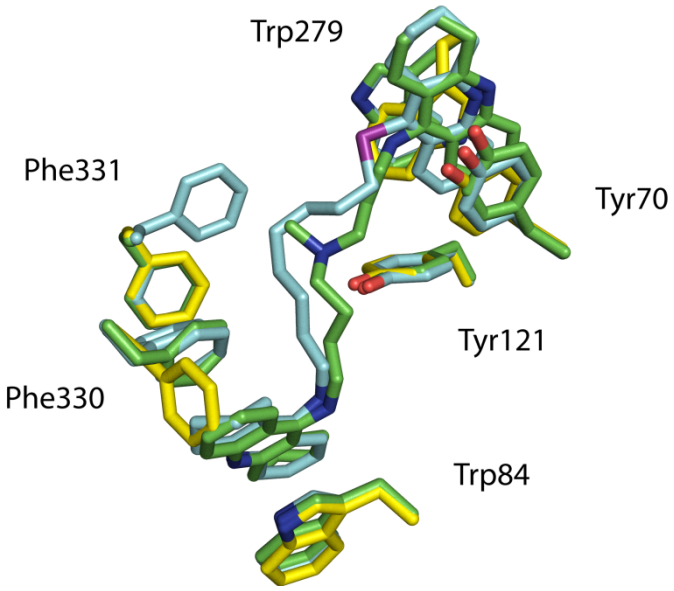

Figure 2. Overlay of the gorge of TcAChE in its native form and in complex with NF595 and NF766. Gorge residues and ligands are rendered as sticks, with carbon atoms in yellow, cyan and green in the native enzyme, the TcAChE/NF595 complex and the TcAChE/NF766 complex, respectively. Nitrogen and oxygen atoms are in blue and red, respectively.

In contrast to 2CEK, the electron density of the linker is clearly defined. Indeed, the B-factor of the linker (50.1 Å²) is significantly smaller than that of the linker of NF595 (60.1 Å²). 2CEK and the *Tc*AChE/NF766 complex have very similar resolution (2.20 and 2.25 Å, respectively) and average overall B-factor (43 and 42 Å², respectively). The B-factors of the corresponding Trp84 and Trp279 in 2CEK are 31 and 45 Å², respectively, and 36 and 41 Å² in the *Tc*AChE/NF766 complex. Hence, the latter shows less structural disorder than 2CEK. We attribute the improved definition of the *Tc*AChE/NF766 complex, with regard to that of 2CEK, to the N-CH3 group of NF766, which replaces a linker C in NF595. The nitrogen atom of this group is engaged in a hydrogen bond with Tyr121 Oη (3.1 Å). The methyl group attached to the nitrogen atom is 3.9 Å from the closest non-hydrogen atom of Tyr334. The linkers of NF595 and NF766 adopt distinct conformations

(Fig. 2). Indeed, in contrast to the rather straight linker of NF595, that of NF766 is markedly bent, and points its convex face towards Tyr334 and Phe330. Yet, NF766 and NF595 are very similar in length: both linkers are constituted of 10 atoms. As a result, the difference observed in the adopted conformations cannot be ascribed to the length of the linkers. The mid-gorge hydrogen bond of the NF766 linker stabilizes its conformation and produces a conformation distinct from that of the NF595 linker.

In 2CEK, Phe330 and Phe331 display two alternate conformations. Comparison with the *Tc*AChE-NF766 complex sheds new light on this observation (Fig. 2). The main interaction between the NF766 linker and the enzyme is the H-bond between the N-CH3 group and Tyr121. On the contrary, the NF595 linker features only hydrophobic interactions with TcAChE (one carbon atom of the linker is 3.8 Å from the closest non-hydrogen atom of Phe331). Thus, hydrophobic interactions are likely to induce the conformational change of Phe331 seen in 2CEK, which leaves room for accommodating Phe330 in a new conformation. Since its electron density is poor, the NF595 linker may have been erroneously attributed a full occupation rate. Thus, it may adopt several conformations not seen in the electron density, which have few effects on the conformations of Phe330 and Phe331.

Surprisingly, the NF766 tacrine moiety that binds in the active site is positioned 180° (around the gorge axis) from the respective tacrine moiety in 2CEK (Fig. 2). The mid-gorge interaction may force that orientation. It should be noted that in 2CEK the orientation may not have been properly modelled. Indeed, the electron was not as clear as in the *Tc*AChE-NF766 complex.

The structure of *Tc*AChE in complex with NF766 was also solved in the orthorhombic ($P2_12_12_1$) form. Though the resolution reached with the orthorhombic structure (1.85 Å) is greater than that of the trigonal structure (2.25 Å), the electron density of the NF766 tacrine moiety that binds at the PAS is not well enough defined to allow for a precise and complete modelling of the ligand (not shown).

Orthorhombic TcAChE in complex with NF1056

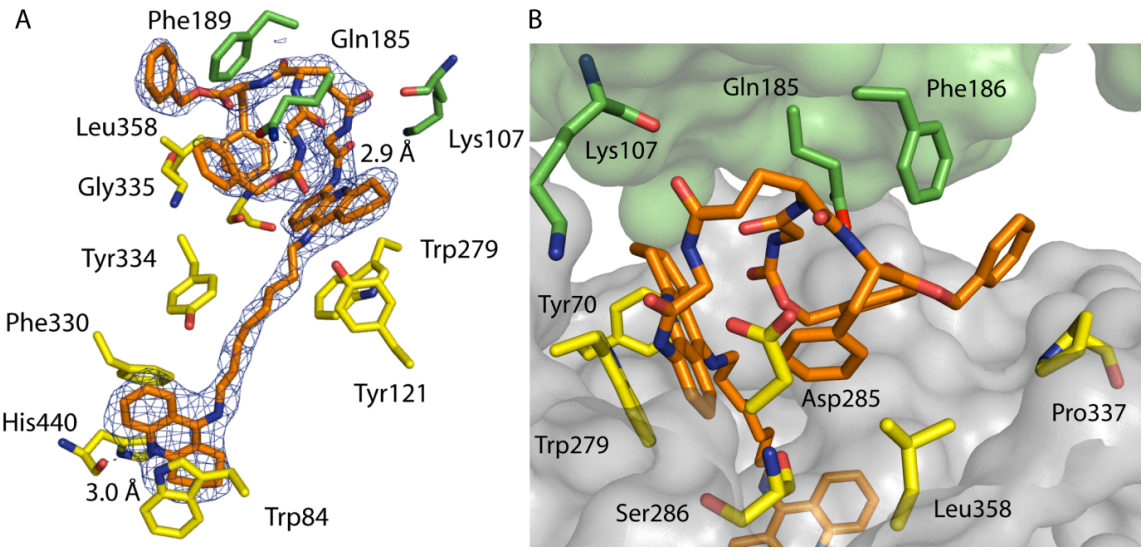

Figure 3. View of the gorge (A) and at the PAS (B) in the NF1056/TcAChE complex in the orthorhombic crystal form. The Fo-Fc omit electron density contoured at 3σ is displayed in blue. Residues Tyr70, Asp285, Ser286, Pro337 and Leu358, residues Lys107, Gln185 and Phe186 of a symmetry-related enzyme and of NF1056 are rendered as sticks with carbon atoms in yellow, green and orange, respectively. In the view of the gorge, residues Trp84, Tyr121, Phe330, Gly335, Tyr334 and His440 are rendered as sticks with carbon atoms in yellow. In the view at the PAS, Pro337 is rendered as sticks using the same color code. Nitrogen and oxygen atoms are in blue and red, respectively. Hydrogen bonds are represented as black dashes. Surfaces of the enzyme and of its symmetry mate are represented in gray and green, respectively.

Co-crystals of *Tc*AChE with NF1056 (scheme 1) were obtained and the structure of the complex was solved at 2.3 Å resolution (Fig. 3A). The crystals proved to belong to the $P2_12_12_1$ space group, i.e. one of the two space groups in which *Tc*AChE commonly crystallizes. Yet, NF1056 is quite a large molecule that was designed on the basis of fasciculin 2 (FAS-2), and the structure of *Tc*AChE in complex with FAS-2 was obtained from $P2_12_12$ crystals in which the gorge is freely accessible[Harel 1995]. Hence, obtaining crystals of the $P2_12_12_1$ space group was not expected since the gorge is close to a crystal contact in that space group (Fig. 3B). Apart from FAS-2, NF1056 is the bulkiest ligand observed in the structure of a ligand-*Tc*AChE complex. The chemical composition of the PAS end of NF1056 greatly differs from that of other previous bis-tacrine inhibitors complexed to *Tc*AChE. Indeed, the tacrine moiety is prolonged by a peptide-like moiety [Butini 2008a], which forms a three-finger motif, each featuring a phenyl group. In the structure of the *Tc*AChE/NF1056 complex, the peptide-like moiety is seen to be extra-enzymatic, with respect to the bis-tacrine moiety that is buried in the gorge of

enzyme. Since the extra-enzymatic moiety does not affect the cystal packing of *Tc*AChE, the observed binding mode of NF1056 is likely to be that in solution.

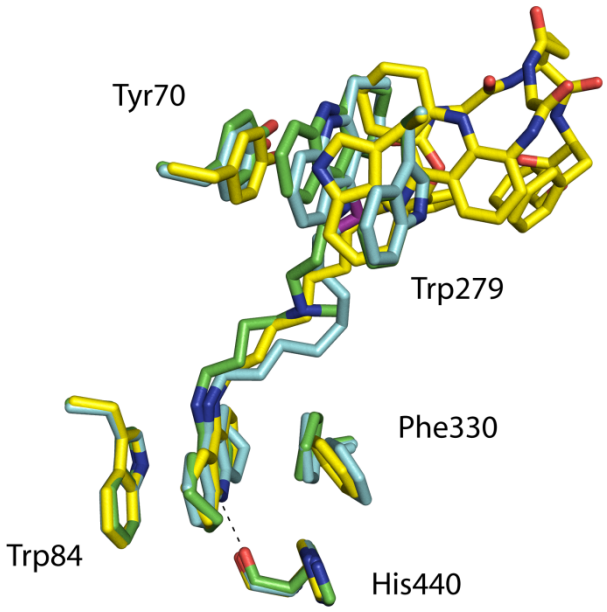

Figure 4. Overlay of the gorge of TcAChE in complex with NF595, NF766 and NF1056. Residues of the enzyme and the ligand of each complex are rendered as sticks, with carbon atoms in cyan, green and orange, respectively. Nitrogen and oxygen atoms are in blue and red, respectively.

Similarly to NF766 and NF595, the terminal tacrine moiety of NF1056 stacks in front of Trp84 (Fig. 3A and 4). Phe330 undergoes a conformational change: its side chain is rotated by ~95° with respect to the structure of the native enzyme. This conformation is very similar to one alternate conformation of Phe330 in 2CEK (Fig. 4). Correspondingly, the Phe331 is rotated by ~65°, which is very close to one alternate conformation of that residue in 2CEK (not shown). A hydrogen bond is established between the distal nitrogen atom of the tacrine moiety and His440O (3.0 Å), which equally exists in the 2CEK and in the *Tc*AChE-NF766 complex (Fig. 3A and 4).

Besides hydrophobic contacts with Phe330, Phe331, Tyr70, Tyr121 and Tyr334, there is no interaction between the linker of NF1056 and the enzyme. It should be mentioned that Tyr334, Tyr121 and Tyr70 also undergo modest conformational changes which bring them closer to the linker. The most prominent movement is the rotation of the Tyr334 carbonyl by ~85° which is accompanied by a global shift of the residue, maximal for Cα (1.1 Å) (not shown).

In contrast with 2CEK and the *Tc*AChE-NF766 complex, Trp279 is not engaged in a π-π stacking interaction with the tacrine moiety that binds at the PAS (Trp279 Cβ is 3.4 Å

from the closest non-hydrogen atom of the tacrine moiety). Indeed, Trp279 undergoes no conformational change (not shown). Thus, the position and orientation of the tacrine moiety that binds at the PAS must be fixed by the binding of the peptide-like moiety, which prevents Trp279 from adopting its conformation seen in the structures of the complexes of *Tc*AChE with NF595 and NF766.

The peptide-like moiety of NF1056 is essentially in hydrophobic interaction with *Tc*AChE, *i.e.* with Tyr70, Trp279, Pro337 and Leu358, and with Phe186 from a symmetry-related enzyme (Fig. 3). Both the enzyme in the asymmetric unit and a symmetry-related enzyme are involved. The proximal finger (scheme 1) is engaged in a hydrogen-bond with the symmetry-related Gln185Oε1 (2.9 Å from the proximal finger nitrogen atom; Fig. 3A), which is also 3.5 Å from the corresponding phenyl moiety. The intermediate finger, on the other hand, does not interact with the symmetry-related enzyme and brings phenyl carbon atoms close to Ser286O (3.1 Å) and Gly335O (3.1 Å; Fig. 3A). The intermediate finger is also 3.4 Å from Asp285Cβ (not shown) and 3.8 Å from Leu358Cδ1 (Fig. 3A). The phenyl moiety of the terminal finger is 3.5 Å from Pro337Cα and 3.8 Å from a symmetry-related Phe189 (their respective ring planes form a ~45° angle). The phenyl ring of the intermediate finger is 3.6 Å and 3.7 Å from those of the proximal and distal fingers, respectively.

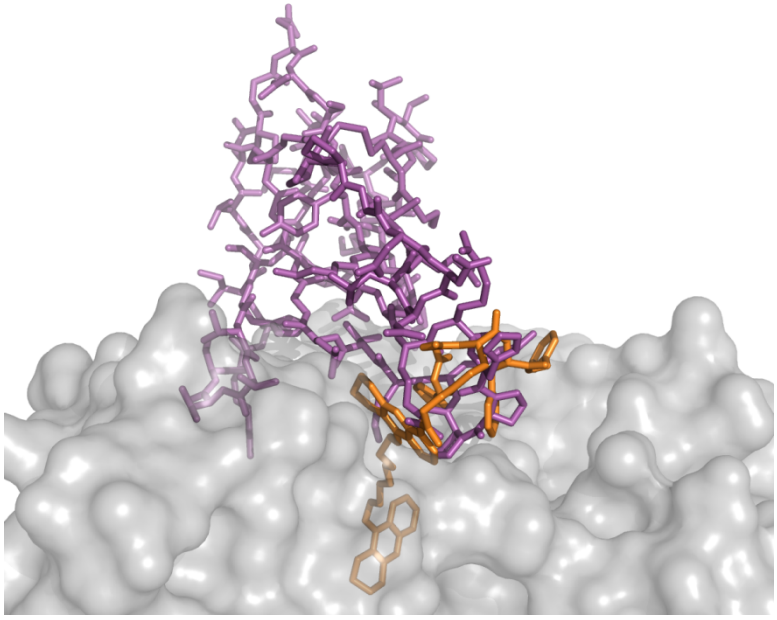

Figure 5. Overlay of TcAChE in complex with NF1056 and FAS-2. NF1056 and FAS-2 are rendered as orange and purple sticks, respectively. The surface of TcAChE is in gray.

NF1056 was designed on the basis of FAS-2 [Butini 2008a]. An overlay of the corresponding complexes with *Tc*AChE shows that the binding locus of NF1056 is almost entirely included in that of FAS-2 (Fig.5) [Harel 1995]. However, it should be reminded that the packing of the crystalline structure of the *Tc*AChE/FAS-2 complex is different from that of the *Tc*AChE/NF1056 complex. Moreover, NF1056 is engaged in interactions with a symmetry-related enzyme. Hence, the binding of NF1056 may not be biologically relevant.

Trigonal TcAChE in complex with NF1056

A soaking procedure allowed to partly solving the structure of NF1056 in complex with $P3_121$ *Tc*AChE, at 2.15 Å resolution. Noteworthy, the same protocol did not yield a complex in $P2_12_12_1$ crystals.

The binding mode of NF1056 in trigonal *Tc*AChE cannot be fully analysed because no clear electron density can be seen above the PAS end of the linker. From the bottom of the gorge to the PAS, NF1056 binds as in the complex obtained from co-crystallisation of orthorhombic crystals. The trigonal packing is not compatible with the conformation of N1056 observed in the structure from orthorhombic crystals. There is not enough room to accommodate the bulky peptide-like moiety of NF1056 at the trigonal PAS in the conformation observed in the orthorhombic complex. It is even surprising that the buried part of the molecule can be fully modeled. This finding suggests that the extra-enzymatic part of NF1056 is disorganized. It is likely that it is oriented towards the solvent channel.

New anti-Alzheimer drugs

Both bivalent inhibitors whose complexes with AChE have been obtained exploit new anchoring points within the structure of the enzyme: NF766 shows supplementary binding at mid-gorge height with regard to bivalent inhibitors studied so far; NF1056 lays on the surface of the enzyme around the PAS.

Supplementary anchoring points certainly explain the nM inhibition constants of NF766 and NF1056. Thus, inhibition of the cholinesterase activity of AChE may be achieved, both via steric blockage and by preventing allosteric control of catalysis. A mid-gorge binding to AChE should hamper breathing motions of the gorge. Furthermore, NF766 and NF1056 show increased stability in the gorge. Hence, the flexibility of the PAS may be hampered, which may help preventing promotion of Aβ fibrillogenesis. The sequence of residues 274-308 was shown to interact with Aβ [De Ferrari 2001b]. Some contacts

that NF1056 makes with *Tc*AChE concern residues in this sequence, *viz*. Trp279, Asp285 and Ser286.

The unique features of the two NF compounds offer a template of choice for designing new anti-Alzheimer drugs. New anti-Alzheimer drugs may also be designed through anchoring points with residues of the gorge in minor conformations [Xu 2008b; Xu 2008c]. Alkyl chains are linkers that do not allow for penetrating the blood-brain barrier [Holzgrabe 2007]. Hence, provided that NF766 and NF1056 prove to be efficient anti-Azheimer drugs *in vitro*, efforts should then be directed towards engineering linkers that do not prevent the drugs to reach their target.

Table 1: Crystallographic and refinement statistics.

	Trigonal NF766/TcAChE	*Orthorhombic NF766/TcAChE*	*Trigonal NF1056/TcAChE*	*Orthorhombic NF1056/TcAChE*
PDB entry code				
ESRF beamline	ID14-2	ID14-2	ID14-4	ID14-2
Temperature (K)	100	100	100	100
Number of frames	100	180	150	180
Exposure time (s/frame)	2 (transmission 37.7%)	3	1 (transmission 10%)	3
Wavelength (Å)	0.933	0.933	0.977	0.933
Space group	$P3_121$	$P2_12_12_1$	$P3_121$	$P2_12_12_1$
Unit cell parameters (Å)				
a	112.5	91.9	111.6	91.6
b	112.5	105.5	111.6	106.2
c	137.9	148.1	137.1	151.0
Resolution range (Å)[1]	20.00-2.25 (2.30-2.25)	20.00-1.85 (1.90-1.85)	20.00-2.15 (2.20-2.15)	20.00-2.30 (2.40-2.30)
Completeness (%)[1]	99.7 (99.8)	98.7 (98.6)	99.3 (98.6)	98.6 (98.9)
R_{sym} (%)[1,2]	5.6 (60.4)	8.0 (44.2)	5.1 (59.1)	6.8 (54.3)
$I/\sigma(I)$[1]	20.90 (2.95)	12.25 (3.31)	28.28 (4.04)	19.26 (3.86)
Unique reflections[1]	48167 (2997)	121619	53821 (3505)	65256 (7730)
Redundancy	6.1	4.1	9.1	7.4
$R_{cryst\ (\%)}$	19.57	20.24	19.48	19.59
$R_{free\ (\%)}$	22.77	24.57	22.31	23.19
R.m.s.d. bond length (Å)	0.010	0.012	0.010	0.013
R.m.s.d. bond angles (degree)	1.38	1.44	1.31	1.44
Number of atoms				
Total	4711	9458	4704	9113
Protein	4298	8423	4303	8389
Water	339	718	368	490
Carbohydrates	28	56	28	56
NF	39	78	39	168

B-factor (Å^2)				
Global	41.6	28.6	37.6	38.5
Protein	40.9	25.3	35.2	39.0
Water	47.0	42.6	45.3	43.3
Carbohydrates	64.5	58.2	60.2	59.1
NF	44.4	48.2	62.6	59.1

[1]: values in brackets refer to the highest resolution shell.

[2]: $$R_{sym} = \frac{\sum_{hkl} \sum_{i} \left| I_i(hkl) - \overline{I(hkl)} \right|}{\sum_{hkl} \sum_{i} I_i(hkl)}$$

6.1.3 Bilan

Les résultats précédents sont d'ordre structural. Ils offrent de nouvelles pistes dans la conception de médicaments basée sur des structures d'AChE. Cette étude possède également un caractère dynamique : les structures présentées sont des instantanés de la *Tc*AChE piégés dans des états conformationnels de l'enzyme imposés par la liaison des ligands.

Les molécules utilisées dans ces travaux ont été conçues dans l'idée d'inhiber l'AChE pour traiter la MA. Dans l'article qui suit, une autre classe d'inhibiteurs de l'AChE nous a intéressés : les OP. Les anti-Alzheimer et les OP font l'objet de préoccupations de santé publique pour des raisons opposées.

6.2 Instantanés de l'acétylcholinestérase avec le soman et le 2-PAM

6.2.1 Présentation de l'article

Dans l'article suivant [Sanson 2009], nous nous sommes intéressés à un ligand spécifique du CAS, le soman. Alors que dans l'article précédent, les ligands étaient de potentiels médicaments, le soman est un agent neurotoxique appartenant à la classe des OP. Notre objectif était d'illustrer et de mieux comprendre le mécanisme de vieillissement de l'AChE inhibée par un OP, avec en perspective l'amélioration des réactivateurs (antidotes) existants. Le vieillissement de l'AChE inhibée par le soman est particulièrement rapide : il faut environ 3 minutes, à température ambiante, pour que la moitié des molécules d'AChE inhibées soit vieillie. Nous avons obtenu les structures de la *Tc*AChE inhibée par le soman avant et après vieillissement de l'enzyme. Caractériser structuralement la forme non-vieillie représentait un défi au vu de la rapidité du vieillissement. Un pH alcalin, combiné à un abaissement de la température (4 °C) ont permis de piéger la forme non-vieillie en ralentissant le vieillissement. L'analyse des

structures a permis de nuancer le modèle *push-pull* [Viragh 1997] proposé pour expliquer le mécanisme biochimique qui sous-tend la réaction de vieillissement.

Nous avons également résolu la structure de la *Tc*AChE inhibée par le soman dans sa forme vieillie en complexe avec le 2-PAM. Cette structure apporte un éclairage structural à la faible efficacité du 2-PAM à réactiver l'AChE inhibée par le soman dans sa forme vieillie. En effet, il est apparu que la fonction oxime du 2-PAM ne pointe pas vers l'atome de phosphore du soman, ce qui est requis pour permettre l'attaque nucléophile qui permet la libération de la sérine catalytique.

6.2.2 Article

Sanson *et al.*, J Med Chem 2009, publié en ligne.

Crystallographic snapshots of non-aged and aged conjugates of soman with acetylcholinesterase, and of a ternary complex of the aged conjugate with pralidoxime[‖]

Benoît Sanson[§], Florian Nachon[‡], Jacques-Philippe Colletier[§], Marie-Thérèse Froment[‡], Lilly Toker[#], Harry M. Greenblatt[†], Joel L. Sussman[†], Yaacov Ashani[#], Patrick Masson[‡§], Israel Silman[#], and Martin Weik[§]

[§]Laboratoire de Biophysique Moléculaire, Institut de Biologie Structurale Jean-Pierre Ebel, Commissariat à l'Énergie Atomique, Centre National de la Recherche Scientifique, Université Joseph Fourier, 41 rue Jules Horowitz, 38027 Grenoble, France; [‡]Département de Toxicologie, Centre de Recherches du Service de Santé des Armées, 24 avenue des Maquis du Grésivaudan, 38700 La Tronche, France; [†]Departments of Structural Biology and [#]Neurobiology, Weizmann Institute of Science, Rehovot 76100, Israel

[‖]The authors wish to acknowledge the 100th anniversary of the Division of Medicinal Chemistry of the American Chemical Society.

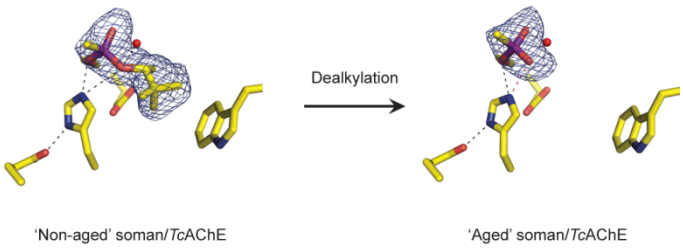

[a] **Abbreviations.** AChE, acetylcholinesterase; OP, organophosphorous; *Tc*, *Torpedo californica*; 2-PAM, pralidoxime, *N*-methylpyridin-1-ium 2-aldoxime methiodide; ACh, acetylcholine; CAS, catalytic anionic subsite; PAS, peripheral anionic site; BChE, butyrylcholinesterase; TMB-4, trimedoxime bromide; CE1, carboxylesterase 1; polyethyleneglycol, PEG; morpholinoethylsulphonic acid, MES; NAG, N-acetylglucosamine; FUC, fucose.

[∞] The atomic coordinates and structure factors (codes 2wfz, 2wg0 and 2wg1) have been deposited in the RCSB Protein Data Bank, www.rcsb.org.

ABSTRACT. Organophosphate compounds (OP) are potent inhibitors of acetylcholinesterases (AChEs[a]) and can cause lethal poisoning in humans. Inhibition of AChEs by the OP soman involves phosphonylation of the catalytic serine, and subsequent dealkylation produces a form known as the 'aged' enzyme. The non-aged form can be reactivated to a certain extent by nucleophiles, such as pralidoxime (2-PAM), whereas aged forms of OP-inhibited AChEs are totally resistant to reactivation. Here, we solved the X-ray crystal structures of AChE from *Torpedo californica* (*Tc*AChE) conjugated with soman before and after aging. The absolute configuration of the soman stereoisomer adduct in the non-aged conjugate is P_SC_R. A structural reorientation of the catalytic His440 side chain was observed during the aging process. Furthermore, the crystal structure of the ternary complex of the aged conjugate with 2-PAM revealed that the orientation of the oxime function does not permit nucleophilic attack on the phosphorus atom, thus providing a plausible explanation for its failure to reactivate the aged soman/AChE conjugate. Together, these three crystal structures provide an experimental basis for the design of new reactivators.

KEYWORDS: Acetylcholinesterase, organophosphate, soman, reactivator, oxime, X-ray crystallography.

INTRODUCTION

The principal role of acetylcholinesterase (AChE, EC 3.1.1.7) is termination of nerve impulse transmission at cholinergic synapses by rapid hydrolysis of the neurotransmitter acetylcholine (ACh) [Silman 2005]. In keeping with its biological role, AChE is a very rapid enzyme, with a turnover number of 10^3–10^4 s^{-1}, depending on the species. The first X-ray structure of an AChE, that from *Torpedo californica* (*Tc*AChE), revealed that its active site is buried at the bottom of a deep and narrow gorge [Sussman 1991]. It features a catalytic triad (Ser200, His440, Glu327) typical of serine hydrolases, and a catalytic anionic subsite (CAS), in which the choline moiety of ACh is stabilized *via* cation-π interactions with Trp84 and Phe330, and by an electrostatic interaction with Glu199 [Colletier 2006a; Sussman 1991]. Stabilization of ACh in the active site also involves interactions of its carbonyl oxygen within the oxyanion hole (Gly118, Gly119, Ala201) and of the methyl moiety of its acetyl group in the acyl pocket (Trp233, Phe288, Phe290, Phe331) [Harel 1996]. At the rim of the gorge, Trp279 is the main component of a so-called 'peripheral' anionic site (PAS) that interacts allosterically with the active site [Rosenberry 2005], and mediates trapping of the substrate *en route* to the active site [Bourne 2006; Colletier 2006a].

AChE is the target of numerous inhibitors, both covalent (irreversible) and non-covalent (reversible), including most approved anti-Alzheimer drugs, and neurotoxins such as the fasciculins, carbamates and organophosphorous (OP) compounds [Silman 2005]. OPs include both insecticides and chemical warfare agents that lead to irreversible inhibition of AChE. Intoxication by OP-based insecticides is a serious public health problem, causing the death of some 200,000 people per year throughout the world [Eddleston 2008]. The lethality of OP nerve agents was evident both when they were employed by Iraqi troops against Iranian troops and Kurd civilians in 1988 [1984; 1986; 1987; Macilwain 1993], and in the Tokyo subway terrorist attack in 1995 [Nagao 1997]. Detailed understanding of the mechanism of AChE inhibition by OPs is thus of major importance in a toxicological context, inasmuch as it may provide crucial information for the rational design of new antidotes.

Soman, *O*-(1,2,2-trimethylpropyl) methylphosphonofluoridate, is one of the most toxic OPs. Inhibition of AChE by soman involves covalent modification of Ser200 (*Tc*AChE

residue numbering throughout the manuscript unless stated otherwise), by a mechanism that implicates nucleophilic attack of the latter on the phosphorus atom of soman, with concomitant departure of its fluoride atom (Scheme 1). Subsequently, AChE catalyzes the dealkylation of the OP adduct at a rate *ca.* 10^{10} higher than that at which non-enzymatic dealkylation would occur [Viragh 1997]. This second step has been termed 'aging', and transforms the 'non-aged' soman/AChE conjugate into an 'aged' conjugate that can no longer be rescued by the available reactivators [Michel 1967]. Among all OPs known to date, with the exception of CH_3POF_2 and CH_3POCl_2 [Segall 1993; Wins & Wilson 1974], soman is the one that produces an aged enzyme most rapidly. Extrapolated half-lives of aging of soman/AChE conjugates range from seconds to several minutes under near physiological conditions [Saxena 1993; Saxena 1998; Shafferman 1996; Viragh 1997]. For the soman/*Tc*AChE conjugate, half-lives for aging of 1.9 and 3.9 min were reported at pH 6.5 and 7.5, respectively, at room temperature [Saxena 1993].

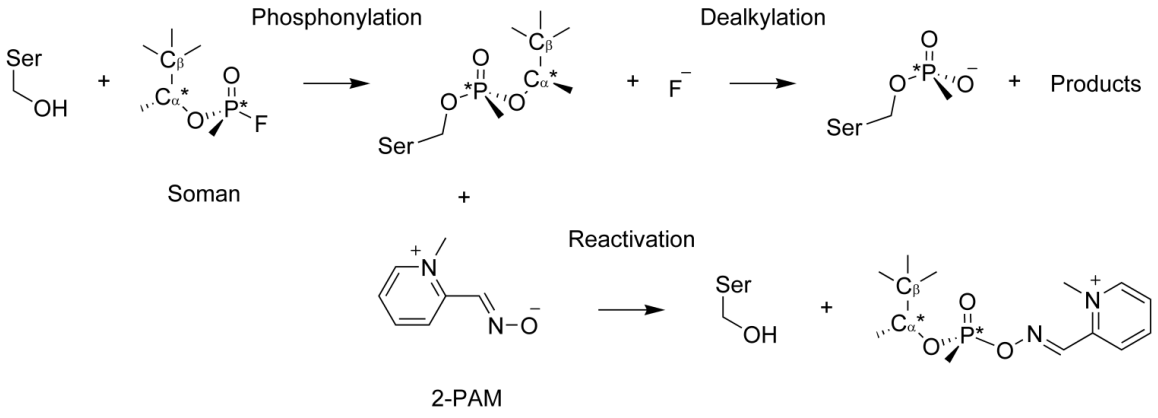

Scheme 1. Irreversible inhibition of AChE by soman (upper panel) and reactivation of the non-aged enzyme with 2-PAM (lower panel). The catalytic Ser200 first performs a nucleophilic attack on the phosphorous atom. Then, the enzyme catalyzes departure of the pinacolyl group ('aging'). Prior to 'aging', reactivation of AChE can occur via nucleophilic attack of the oxime group of 2-PAM on the phosphorus atom of the phosphonyl adduct, resulting in its cleavage from Ser 200 Oγ. Asterisks denote chiral centers.

The mechanism of enzyme-induced aging is not fully understood, and the chemical basis for the unusually fast rate of dealkylation of soman/AChE conjugates requires further clarification. Two pathways were considered, in which either protonation of the pinacolyl oxygen [Michel 1967; Shafferman 1996] or methyl migration from Cβ to Cα of the pinacolyl group [Kovach 2004; Saxena 1993; Viragh 1997] were proposed to be rate-

determining. Regardless of the mechanistic details, it is agreed that dealkylation is accompanied by O-C scission of the P-O-$CH(CH_3)C(CH_3)_3$ chain (Scheme 1), and that Glu199, Phe331, Glu443, His440 and, in particular, Trp84, play important roles in the aging process [Kovach 2004; Saxena 1993; Shafferman 1996; Viragh 1997]. It is of interest that the 'aged' soman/AChE conjugate is analogous to the deacylation tetrahedral intermediate of acetylated AChE [Ashani & Green 1982; Bencsura 1995; Millard 1999b].

Soman contains two chiral centers, the P and Cα atoms, and thus occurs as four stereoisomers. AChEs react preferentially with the P_S enantiomers, with phosphylation rates ~5×10^4 higher for the P_S than for the P_R enantiomers [Benschop & De Jong 1988; Ordentlich 1999]. An in-line displacement of fluoride by Ser200 has been proposed [Berman & Decker 1989], implying that the stereochemistry of the phosphorus atom is reversed following conjugation to the enzyme. The P_R configuration in the crystal structure of the non-aged phosphonylated *Tc*AChE conjugate obtained by use of the *O*-ethyl methylphosphonyl OP, VX, is indeed consistent with inversion at the P atom [Millard 1999a]. As for the preference of AChE for the configuration at the Cα atom, the rates of inhibition of human (hu) AChE [Ordentlich 1999], bovine AChE [Benschop 1984], eel AChE [Benschop 1984], equine butyrylcholinesterase (BChE ; EC 3.1.1.8) [Ordentlich 1999] and huBChE [Millard 1998; Saxena 1998] by the P_SC_S stereoisomer are consistently (though only slightly) higher than by the P_SC_R stereoisomer.

Oximes are capable of reactivating non-aged OP/AChE conjugates [Kewitz & Wilson 1956; Wilson 1955] by nucleophilic attack of the oxime group (R_1R_2C=NOH) on the phosphorus atom [Wilson & Froede 1971; Worek 2005]. So far, only a few oximes have been included in therapeutic regimens for treatment of OP intoxication, *viz.* N-methylpyridin-1-ium 2-aldoxime methiodide (pralidoxime, 2-PAM), trimedoxime bromide (TMB-4) and toxogonin [Marrs 1993]. The *bis*-quaternary oximes, HI-6 and HLö7 have, so far, been the most effective in reactivation of most non-aged OP/huAChE conjugates [Antonijevic & Stojiljkovic 2007]. The non-aged soman/huAChE conjugate obtained by use of the P_SC_S isomer has been reported to be significantly more amenable to reactivation by HI-6 than the P_SC_R adduct [de Jong & Wolring 1985]. Although great efforts are being made to produce more potent reactivators [Yang 2007], no single broad-spectrum reactivator has, so far, been described that is capable of reactivating all non-aged nerve agent/AChE conjugates [Worek 2004]. Furthermore, it has been observed that

phosphonylated oximes, which are formed during reactivation, are capable of re-inhibiting AChE [Ashani 2003; Herkenhoff 2004].

The X-ray structures of several non-aged and aged OP/AChE conjugates have been solved in recent years. Those of the non-aged VX/*Tc*AChE conjugate [Millard 1999a] and of the non-aged tabun conjugate of murine AChE [Ekstrom 2006a] (mAChE) both showed that a reorientation of the side-chain of the catalytic histidine is necessary to accommodate the ethoxy group common to the two inhibitors. Upon aging, these structural changes are reversed, and the catalytic histidine in the aged OP/AChE conjugate reverts to its native conformation. The structure of the aged soman/*Tc*AChE was determined by crystallizing the inhibited enzyme, and here, too, the side-chain of the catalytic His residue was seen to be in its native orientation [Millard 1999b]. However, due to the experimental difficulties imposed by the rapidity of the aging process, the crystal structure of the non-aged soman/AChE conjugate had not been reported.

Here, we present the crystal structures of non-aged and *in crystallo* aged soman/*Tc*AChE conjugates and of a ternary complex of the aged conjugate with the oxime reactivator, 2-PAM. These structures provide important information that can be utilized in clarifying: (a) the role of the architecture of the catalytic site and of water molecules within the gorge on the rate and mechanism of the aging reaction; (b) the resistance of aged OP-AChE conjugates to reactivation. Hopefully, such clarifications will facilitate the quest for new reactivators of OP-inhibited AChE.

RESULTS

Non-aged soman/TcAChE conjugate.

Trapping of the non-aged soman/*Tc*AChE was achieved by reducing the soaking time to 6 min, and raising the pH to 8.2, a pH value at which aging is significantly retarded [Michel 1967; Viragh 1997].

The structure, solved at 1.95 Å resolution, is displayed in Figure 1. The initial F_o-F_c electron density map featured a 12σ peak at covalent bonding distance from Ser200 Oγ, clearly revealing the position of the phosphorus atom of the phosphonyl group. At lower σ levels, the pinacolyl group is clearly defined (Figure 2A). It is stabilized by hydrophobic interaction with Trp84; thus, one of the methyl groups of the pinacolyl Cβ atom (scheme 1) is 3.6 Å from the nearest non-hydrogen atom of Trp84.

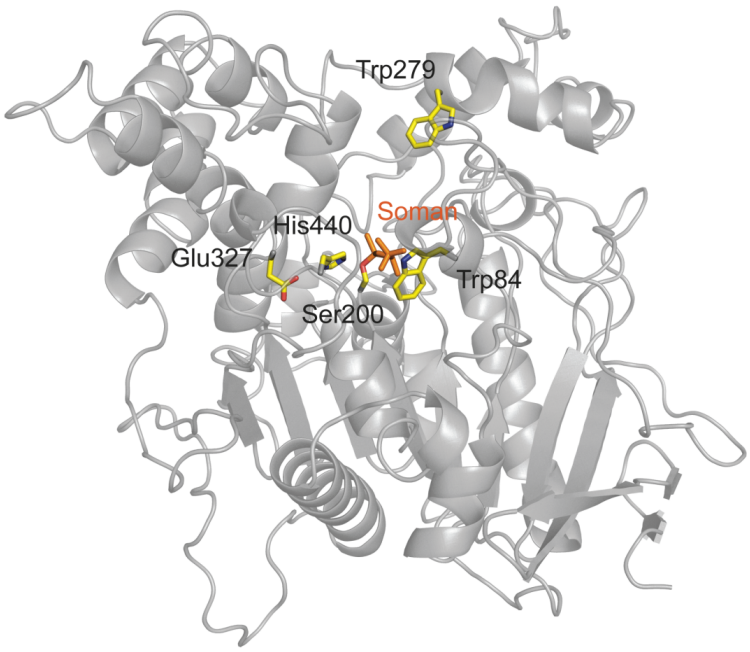

Figure 1. Overall view of the non-aged soman/TcAChE conjugate. The backbone of the enzyme is displayed as a grey ribbon, with the entrance to the active-site gorge at the top. The catalytic triad residues (Ser200, His440 and Glu327), as well as the main residues of the CAS and PAS, Trp84 and Trp279, respectively, are represented as yellow sticks, and the OP moiety as orange sticks.

The catalytic His440 is H-bonded to both Ser200 Oγ (2.7 Å) and Glu327 Oε1 (2.6 Å) through its Nε2 and Nδ1 nitrogens, respectively. The soman O2 atom is within H-bonding distance (3.2 Å) of His440 Nε2, although the bond-angle is unfavorable. Thus, the proton on His440 Nε2 is preferentially oriented towards Ser200 Oγ (Nε2-H-Oγ angle 142°, H-Oγ distance 1.8 Å), rather than towards soman O2 (Nε2-H-02 angle 118°, H-O2 distance 2.6 Å). Mimicking the carbonyl oxygen of the natural substrate, ACh, soman O1 establishes three H-bonds within the oxyanion hole, i.e. Gly118 N (2.7 Å), Gly119 N (2.6 Å) and Ala201 N (3.0 Å; not shown in Figure 2A). Noteworthy, also, is a weak H-bond between soman O2 and water 1001, located up the gorge (3.3 Å), which is also within H-bonding distance (3.3 Å) of Tyr121 Oζ. Glu199 Oε1 is 3.1 Å from the methyl group on the Cα atom, and 4.0 Å from the closest methyl group on the Cβ atom of soman (not shown). Glu199 itself is stabilized by Glu443 through hydrogen bonds with the bridging water 1002, just as was observed for native *Tc*AChE [Koellner 2000; Sussman 1991].

The pinacolyl moiety in the non-aged conjugate perturbs the position of the imidazole ring of His440; consequently, its Nε2 nitrogen is shifted by 0.5 Å relative to its position in the native structure. This is in contrast to the total disruption of the catalytic triad observed in the non-aged VX/*Tc*AChE conjugate [Millard 1999a]. Several other residues in the vicinity of the active site are slightly affected by phosphonylation of Ser200. These include Trp84, Trp233, Phe330, Tyr334, and Tyr442, all located in the bottom half of the gorge. Their movements result in a small (6%) decrease in the volume of the active-site gorge relative to native *Tc*AChE.

The soman soaked into the crystals was a mixture of the four stereoisomers, $P_{R/S}C_{R/S}$. As mentioned above [Millard 1999b], in aqueous solution, AChE reacts preferentially with the P_S enantiomers of soman (Figure 2A). The crystal structure permits assignment of the absolute configuration of the phosphorus atom as P_S, and the fact that the pinacolyl group is retained in the non-aged conjugate permits assignment of the absolute configuration of the Cα carbon to be C_R. It should be noted that the methyl group on the Cα carbon hinders its direct interaction with the carboxyl group of Glu199 (distance Cα-Oε1 4.2 Å; Figure 2A).

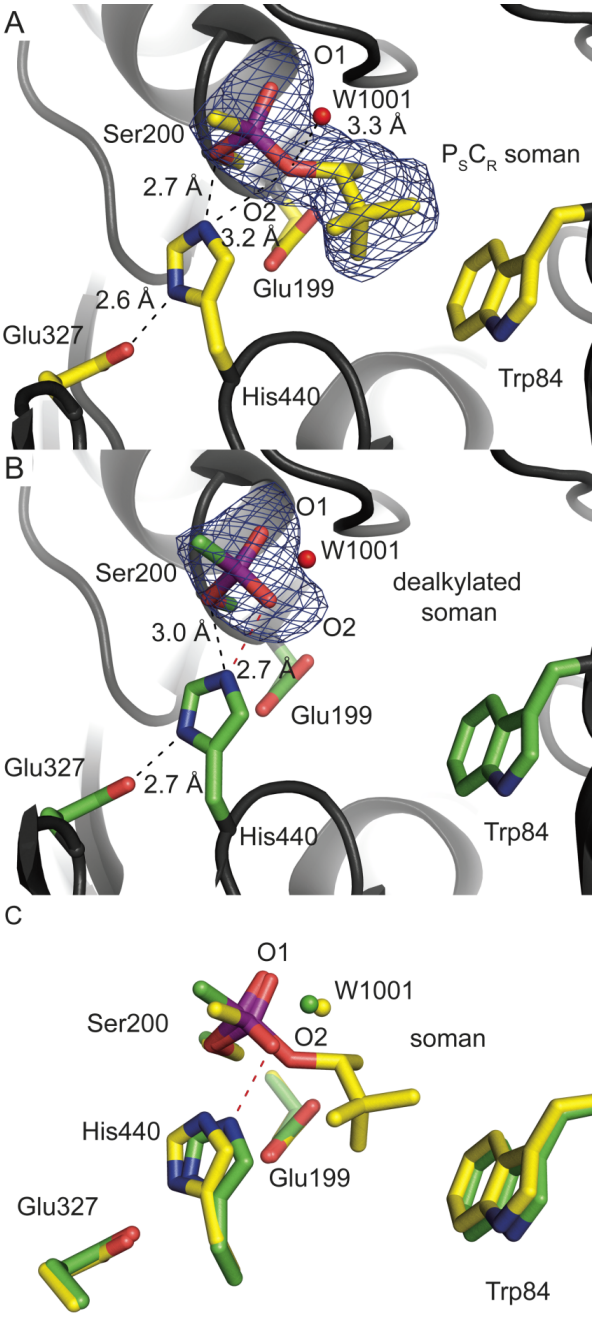

Figure 2. Active sites of the non-aged (A) and aged (B) soman/TcAChE conjugates, and their superposition (C). The F_o-F_c omit maps are contoured at 3σ. The catalytic triad residues (Ser200, His440 and Glu327), Trp84 and the OP adducts are displayed as sticks, with oxygen atoms in red, nitrogen atoms in blue and the phosphorus atom in purple. Carbon atoms of the non-aged conjugate are shown in yellow and those of the aged conjugate in green. A water molecule (1001) interacting with soman O2 is represented as a red ball in (A) and (B), and as yellow and green balls in the non-aged and aged structures, respectively, in (C). Hydrogen bonds and a salt bridge are represented as black and red dashed lines, respectively. The apical nitrogen atom of His440 forms a salt bridge (dashed line) with the negatively charged O2 atom of the soman adduct in the aged conjugate.

Aged soman/TcAChE conjugate.

In order to favor the dealkylation reaction [Michel 1967; Viragh 1997], the pH of the soaking solution was decreased relative to that used to obtain the non-aged conjugate, and the time of soaking was increased. The structure of the aged conjugate was solved at 2.2 Å resolution (Figure 2B). No electron density is observed for the pinacolyl group, demonstrating that the *in crystallo* dealkylation of soman, *viz.,* aging of the conjugate, had indeed occurred. The phosphorus atom adopts a tetrahedral conformation, being linked to Ser200 Oγ, to the methyl carbon, and to the two oxygens. As observed in the non-aged conjugate, the O1 atom of the phosphonyl moiety is stabilized by H-bonds with the three components of the oxyanion hole, *viz.* Gly118 N (2.7 Å), Gly119 N (2.6 Å) and Ala201 N (2.8 Å; not shown in Figure 2B). The negatively charged O2 atom points towards Trp84, and establishes a salt bridge [Klebe 2008; Petsko & Ringe 2004] with His440 Nε2 (2.7 Å). This interaction distance value is in agreement with that reported by Shafferman *et al.* (2.8 Å) [Shafferman 1996], and with that previously observed in the crystal structure of the aged soman/*Tc*AChE conjugate (2.6 Å) [Millard 1999b]. His440 is also hydrogen-bonded to Ser200 Oγ through its Nε2 nitrogen (3.0 Å), and to Glu327 through its Nδ1 nitrogen (2.7 Å). The methyl group of the phosphonyl moiety points towards the acyl pocket (distance of 3.6 Å between closest non-hydrogen atoms). The limited conformational changes reduce the volume of the gorge by 3% compared to the volume of the gorge of the native enzyme.

No significant difference was observed between our crystal structure and that reported earlier after crystallization of the aged conjugate [Millard 1999b], showing that aging in solution and *in crystallo* produce the same final state.

Superposition of the structures of the non-aged and aged conjugates reveals a small, yet crucial, movement within the active site (Figure 2C): the imidazole ring of His440 is tilted back (Nε2 shifts by 0.8 Å) to its native conformation after aging. The resulting proximity between soman O2, which is negatively charged, and His440 Nε2, results in formation of a salt bridge (2.7 Å) (Figure 2B). It should be noted that water molecule 1001, which interacts with soman O2 in the non-aged crystal structure (Figure 2A), is not within H-bonding distance (3.7 Å) of O2 in the aged crystal structure (Figure 2B).

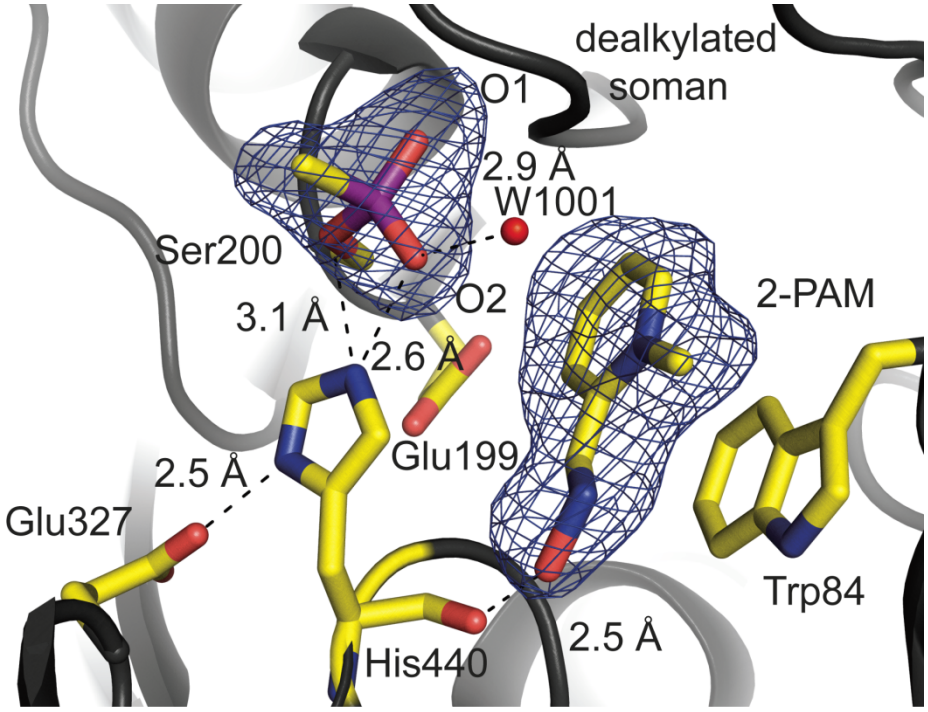

Figure 3. Ternary complex of 2-PAM with the aged soman/TcAChE conjugate. The F_o-F_c omit map is contoured at 3σ. The catalytic triad residues (Ser200, His440 and Glu327) and Trp84 are represented as sticks, and color-coding of these residues, of the OP adduct and of 2-PAM are as in Figure 2A. A water molecule (1001) interacting with O2 of soman and with the nitrogen atom of 2-PAM is represented as a red ball. Hydrogen bonds are shown as dashed lines.

Ternary complex of 2-PAM with the aged soman/TcAChE conjugate.

The structure of the ternary complex of the aged conjugate with the oxime reactivator, 2-PAM, was solved at 2.2 Å resolution. A molecule of 2-PAM is seen at the CAS, but not at the PAS. 2-PAM interacts *via* parallel π-stacking with the indole moiety of Trp84 (distance of 3.5 Å between closest non-hydrogen atoms) (Figure 3). The oxime oxygen is 2.5 Å from His440 O. The conformation of the phosphonyl adduct on Ser200 is not affected by the presence of 2-PAM, and the oxime oxygen is 6.8 Å from the phosphorus atom. This distance precludes nucleophilic attack at the soman phosphorus atom by the oxime, which would be essential for displacing it from Ser200 Oγ. Water molecule 1001 (Figure 3) bridges 2-PAM and the phosphonyl adduct; it is H-bonded to soman O2 (2.8 Å), and interacts electrostatically with 2-PAM N1 (3.4 Å). Noteworthy is the rotation of Phe330 χ1 and χ2 angles, both by ~50°, which brings the residue across the gorge. It should be noted that a PEG molecule spans the gorge (not shown), from the vicinity of Tyr70/Trp279, down to residues Tyr334/Phe330/Phe331, in the middle of the gorge; yet

it does not interact with 2-PAM (distance of 5.9 Å between closest non-hydrogen atoms). The crystal structure presented was solved after soaking crystals of the aged conjugate with 2-PAM at pH 5.6. A structure solved after soaking in 2-PAM at pH 8.2 reproduced all the structural details shown in Figure 3 (data not shown). Thus, the ionization state of the oxime group in solution (pK_a = 7.8) [Wang & Braid 1967] does not appear to influence the mode of 2-PAM binding, which is likely to be governed principally by the hydrophobic interaction with Trp84.

DISCUSSION

This study presents, for the first time, the crystal structure of a 'non-aged' soman/AChE conjugate that was obtained by rapid flash-cooling of crystals of *Tc*AChE soaked with soman at high pH and low temperature, so as to preclude significant 'aging'. The corresponding 'aged' conjugate was generated *in crystallo* by a longer incubation of the soman-soaked crystals at a lower pH. The 'aged' conjugate was further used to obtain a tertiary complex with the oxime reactivator, 2-PAM. These structures provide valuable information for understanding: a) the molecular details of the rapid phosphonylation of AChE by soman and of the 'aging' process; b) the resistance of the 'aged' enzyme to the theoretically possible reactivation. These, in turn, may provide a basis for designing more efficient antidotes against by nerve agent intoxication.

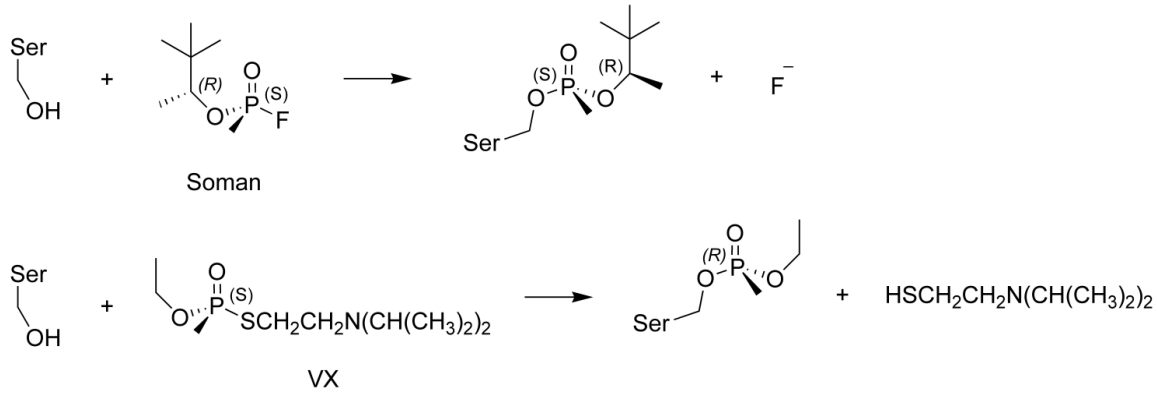

Scheme 2. Phosphylation reaction scheme of AChE with either soman (upper panel) or VX (lower panel).

Soman inhibition of TcAChE.

It is well established that the P_SC_S stereoisomer of soman is the one that interacts preferentially with AChE [Benschop 1984; Ordentlich 1999]. Examination of the 3D structure of the 'non-aged' soman/*Tc*AChE conjugate permits unequivocal assignment of the chirality of the covalently bound OP moiety. This is seen to be P_SC_R. The observation that the same absolute configuration (*viz.,* P_S) is retained at the P atom in the 'non-aged' adduct is attributed to stereo-inversion at the P atom and to replacement of the fluoride leaving group by Ser200 Oγ, which has lower priority order than the fluorine atom in

assignment of the absolute configuration (Scheme 2). Similar inversion and retention of the absolute configuration of the P atom was reported by Cygler *et al.* [Cygler 1994], who determined the crystal structure of a lipase conjugated to a menthyl hexylphosphonate transition state analog. Stereo-inversion at the P atom was also observed for the VX-*Tc*AChE adduct [Millard 1999a], as well as for the VX/mAChE adduct [Hornberg 2007a] ; however, in these cases the P_R configuration was assigned, since the O-CH_2CH_3 moiety has lower priority order than Ser 200 in determining the absolute configuration (Figure 4; Scheme 2). Recently, inversion of the configuration at the P atom was reported for reaction of tabun with mAChE and huBChE [Carletti 2008a]. Thus, an in-line displacement is envisaged in all the cases reported for ChEs, regardless of the nature of the leaving group or the size of the O-alkyl substituent on the OP. This mode of nucleophilic attack is due to the steric constraints within the catalytic site that enforce the approach of the catalytic serine from the face opposite to the leaving group (Figure 4).

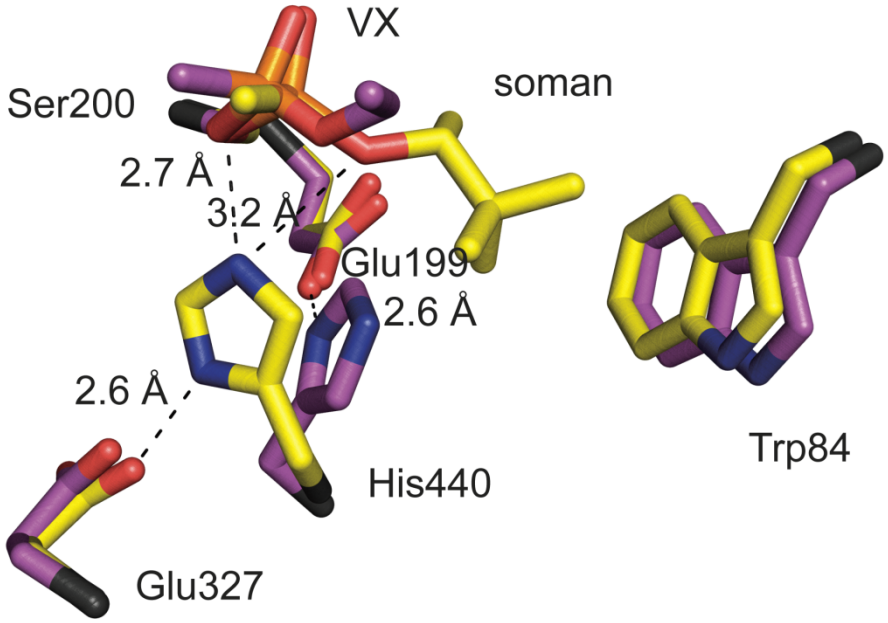

Figure 4. Superposition of the active sites of the non-aged soman/TcAChE and non-aged VX/TcAChE conjugates. Carbon atoms of the soman/TcAChE conjugate are shown in yellow, and those of the VX/TcAChE conjugate in purple. Oxygen and nitrogen atoms are in red and blue, respectively, for the two structures, and phosphorus atoms in orange. Hydrogen bonds are represented as dashed lines.

The P_S configuration of the soman/*Tc*AChE adduct was anticipated on the assumption that phosphonylation proceeds via an in-line displacement mechanism. However, the C_R

stereochemistry of the pinacolyl Cα atom seen in the crystal structure is at odds with the kinetic measurements performed on various AChEs and BChEs, all of which slightly favor the P_SC_S diastereoisomer [Benschop 1984; Ordentlich 1999]. Two possible explanations may be provided: a) Even though the P_SC_S isomer can be docked computationally into the active site without its distortion (not shown), steric constraints produced by crystal packing could change the chiral preference at Cα; b) A second possibility is that inhibition of *Tc*AChE by the P_SC_S isomer is followed by a rapid rearrangement at the Cα atom, resulting from formation of a planar pinacolyl carbenium ion species that realkylates the oxygen of the OP moiety. This would preferentially generate the more stable P_SC_R adduct under the experimental conditions employed. Furthermore, we cannot rule out the possibility that *Tc*AChE preferentially selects the P_SC_R epimer. It would, therefore, be of interest, not only to compare the 3D crystal structures of soman/*Tc*AChE conjugates obtained from the individual P_SC_S and P_SC_R epimers, but also to investigate the kinetics of their reaction with soluble *Tc*AChE. We note that similar rates of aging were observed for various AChEs inhibited with either the P_SC_R or the P_SC_S diastereoisomer [Ordentlich 1999; Saxena 1998; Viragh 1997].

Comparison of the inhibition of TcAChE and of human carboxylesterase by soman.

It is of interest to compare the non-aged soman/*Tc*AChE crystal structure with that of the corresponding non-aged conjugate of human carboxylesterase 1 (huCE1; EC 3.1.1.1). It should be noted that the soman/huCE1 crystals were obtained by crystallization of the soman/huCE1 conjugate produced with soman (stereoisomeric mixture $P_{R/S}C_{R/S}$), which thus displayed no tendency to age over a period of 1-4 weeks [Fleming 2007], as already reported for the rat CE1 conjugate [Maxwell 2001]. huCE1 is a cholinesterase-like α/β hydrolase that contains a catalytic triad, an oxyanion hole and a glutamate equivalent to Glu199. Figure 5 shows that all these residues can be superposed on the homologous residues in *Tc*AChE. However, the substrate specificity pockets in the two enzymes differ in size. Whereas the acyl-binding pocket in *Tc*AChE is too small to accommodate the bulky pinacolyl goup of soman, the analogous pocket in huCE1 is large enough to do so. In contrast, the pocket in huCE1 that is homologous to the large choline-binding pocket in *Tc*AChE is much smaller. Thus, the two enzymatic active sites bear a ‘mirror-image’ relation. This explains the difference in enantioselectivity between *Tc*AChE and huCE1 with respect to their reaction with soman. It was indeed recently shown that huCE1 reacts

preferentially with the P_R isomer of soman in aqueous solution (Matthew Redinbo, personal communication), and it is the P_R configuration that is observed in the crystal structure of the soman/huCE1 conjugate [Fleming 2007]. This suggests that phosphonylation of huCE1 proceeds by a mechanism similar to the standard in-line displacement proposed for ChEs and lipases [Cygler 1994].

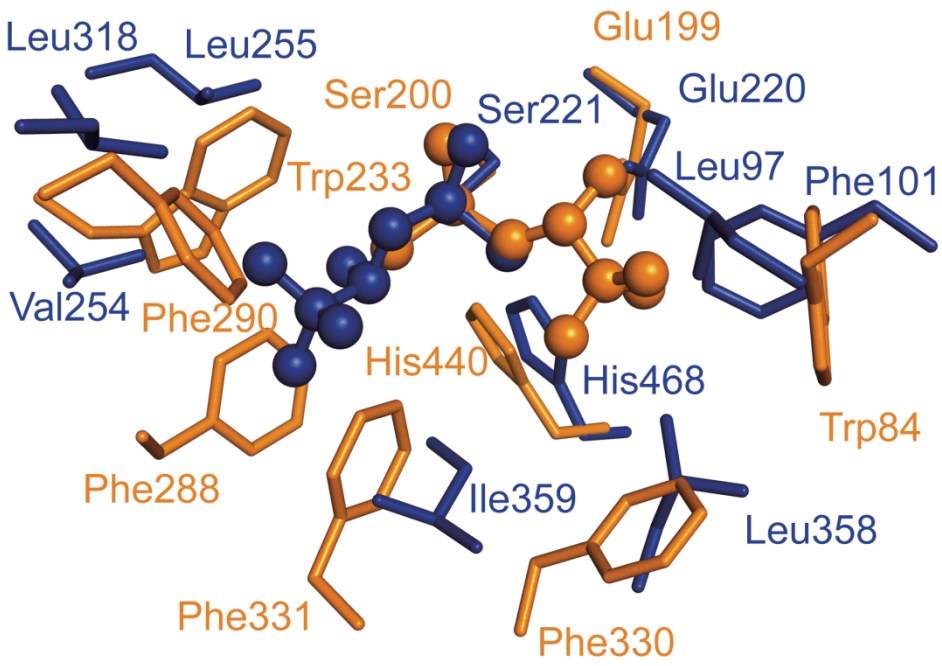

Figure 5. Superposition of the active sites of non-aged soman/TcAChE (orange) and soman/huCE1 (blue) conjugates. The residues and the OP moieties are represented as ball-and-stick models. Labels for TcAChE and huCE1 residues are in orange and blue, respectively.

Structural comparison of the non-aged conjugates of AChEs with soman, VX and tabun.

Comparison of the crystal structure of the non-aged soman/*Tc*AChE conjugate with those of the non-aged VX/*Tc*AChE conjugate [Millard 1999a] and of the non-aged tabun/mAChE conjugate [Carletti 2008a] reveals an interesting difference. In the VX/*Tc*AChE conjugate, there is a disruption of the catalytic triad, resulting in H440 Nε2 forming an H-bond with Glu199 instead of with Glu327, while in the tabun/mAChE conjugate catalytic His447 and Phe338 shift in concert to avoid unfavorable contacts with the phosphoramidate group. In contrast, inhibition of *Tc*AChE by soman results in only a slight reorientation of the imidazole ring of His440, without disruption of the catalytic triad. A movement similar to that occurring upon phosphonylation with VX is precluded

by the presence of the pinacolyl moiety, which is much more bulky than the ethoxy group of VX (Figure 4). Indeed, His440 Nε2 would be only 2.3 Å from the nearest methyl carbon of the pinacolyl moiety if it adopted the same conformation as in the non-aged VX/*Tc*AChE conjugate. The absence of a major conformational change of the catalytic histidine during aging of the soman/*Tc*AChE conjugate could explain partially its accelerated rate of aging relative to the VX/TcAChE conjugate. By contrast, in the non-aged tabun/huBChE conjugate catalytic His438 is restrained by Phe398, a residue which is absent in the AChEs [Carletti 2008a] .

Mechanism of aging of the soman/TcAChE conjugate.

The mechanism of aging (*viz.*, dealkylation of the OP moiety) of conjugates of OP nerve agents with ChEs has been the topic of intense investigation and debate over the past 50 years. Aging of the soman/AChE conjugate has been a particular focus since its rapid rate presents a paramount toxicological challenge. The availability of a high-resolution crystal structure of the non-aged soman/*Tc*AChE conjugate, together with that of the homologous aged conjugate, at last permits a critical examination of the proposed mechanisms at the atomic level.

The proposed mechanisms were generated on the basis of kinetic data [Keijer & Wolring 1969] and product analysis [Michel 1967]. After the 3D structures of *Tc*AChE [Sussman 1991], and subsequently of mAChE [Bourne 1995] and huAChE [Kryger 2000], became available, dynamic modeling was attempted [Shafferman 1996], and various mechanistic proposals were tested by site-directed mutagenesis [Shafferman 1996]. Based on the pH-rate profile of aging [Saxena 1998; Viragh 1997], and the increased resistance of certain mutants to aging [Ordentlich 1993b; Saxena 1993], the following residues have been implicated in the aging of soman/AChE conjugates (*Tc*AChE numbering, with huAChE numbering in brackets): His440 (447); Trp84 (86); Glu199(202); Glu443(450); Phe331(338) [Ordentlich 1993b; Saxena 1993; Shafferman 1996].

Comparison of the crystal structures of the non-aged and aged soman/*Tc*AChE conjugates reveals a small, yet significant, movement of the imidazole ring of His440 (displacement of Nε2 by ~0.8 Å) that results in formation of a salt bridge with soman O2 in the aged conjugate (Figure 2C). In the case of the VX/*Tc*AChE conjugate there is a much larger movement, which involves reformation of the catalytic triad, and concomitant

establishment of a salt bridge homologous to that seen in both the aged soman and aged sarin conjugates [Millard 1999b]. In the case of the tabun/mAChE conjugate, inspection of the crystal structure of the aged conjugate revealed a continuum of conformations that was ascribed, at least in part, to incomplete aging [Carletti 2008a].

The pH/rate profile of aging provides evidence that His440 is involved in the process. In the non-aged soman/*Tc*AChE conjugate, Nε2 of its imidazole ring is within H-bonding distance of both Ser 200 Oγ (2.7 Å) and O2 of the pinacolyl moiety (3.2 Å). The unfavorable bond angle for the H-bond with the pinacolyl O2, taken together with the restricted movement of the imidazole ring imposed by the bulky pinacolyl group, render it unlikely that His440 is directly involved in the aging process by protonation of O2. However, the proximity of the protonated Nε2 may confer a stabilizing electrostatic effect that could contribute to the observed pH-dependence.

Mutation of Glu199 (huAChE 202) to Gln slows the aging of soman-inhibited *Tc*AChE and huAChE to a similar extent [Saxena 1993; Shafferman 1996]. In the electrostatic push-pull mechanism for dealkylation proposed by Viragh et *al.* [Viragh 1997], Glu199 is proposed to play the 'pusher' role, in conjunction with Trp84, triggering methyl migration from Cβ to Cα, with concomitant transformation of Cβ into a positively charged carbenium atom, resulting in Cα-O2 bond breakage. Since Cβ is near Trp84 in the crystal structure of non-aged soman/*Tc*AChE (4.6 Å; Figure 2A), the carbenium ion may indeed be stabilized by a cation-π interaction as proposed [Viragh 1997]. Once the carbenium ion is formed, it undergoes rapid rearrangement that could explain the composition of the low molecular weight products of 'aging' as identified by Michel *et al.* [Michel 1967]. Since Glu199 is actually closer to Cα than to Cβ in the crystal structure, it seems unlikely that it would indeed play a 'pushing' role. It may, however, stabilize the developing carbenium ion. Such an electrostatic stabilization is supported by the effect of mutagenesis of Glu199 to Gln (see above), and also by mutation of Glu443 (Glu450 in hAChE) to Ala; this latter residue is linked to Glu199 via a conserved water molecule (numbered 1002), and may thus be expected to stabilize its position [Koellner 2000; Sussman 1991]. Arguing against the push-pull mechanism as proposed by Viragh et *al.* [Viragh 1997] is the contention that methyl migration prior to carbenium ion formation would be most unfavored in energetic terms. We were unable to find an example in the literature in which methyl migration preceded carbenium ion formation. But methyl migration following carbenium ion formation is an accepted mechanism [Anslyn & Dougherty

2006]. Indeed, in studies on the dealkylation of model OP compounds [Cadogan 1969], the composition of the observed olefin products was in line with the initial formation of a pinacolyl ion. The crystal structure of the non-aged conjugate described in the present paper provides a plausible mechanism for enhancement of carbenium ion formation as follows. The conserved water molecule 1001, which is hydrogen-bonded to Tyr121 Oζ, may enhance cleavage of the O2-Cα bond, by increasing its polarity through hydrogen bonding to O2 (Figure 2A), while His440 would stabilize the partial charge on O2, thus releasing the unstable pinacolyl carbenium ion. This species immediately rearranges by methyl migration from Cβ to Cα to form the 2,3-dimethylbutyl carbenium ion that accounts for the principal olefin isolated. Trp84 may contribute to acceleration of dealkylation by stabilizing the developing positive charge on the pinacolyl moiety In this context, it is interesting to note that the pinacolyl O2-Cα bond is elongated by 0.3 Å and thus weakened, if geometric restraints of this bond are down weighted in an alternate refinement of the non-aged soman/*Tc*AChE conjugate (see Supporting Information). The role of water 1001 in dealkylation could be checked experimentally by mutagenesis of Tyr121 (Tyr124 in huAChE). This mutation does not significantly affect the rate of phosphonylation [Kaplan 2001] but the aging rate of an OP conjugate of the mutant enzyme has not been compared to that of the corresponding conjugate of the wild-type enzyme.

In huAChE mutation to Ala of Phe338 (Phe331 in *Tc*AChE) decreased the rate of aging of the soman conjugate by 160-fold [Shafferman 1996], whereas no effect was observed upon similar mutation of Phe337 (Phe330 in *Tc*AChE). Visual inspection of the 3D structure of the non-aged conjugate suggests that this mutation opens up a cavity into which the imidazole ring of the catalytic His residue can move. This in turn, could weaken the electrostatic stabilization of the developing carbocationic charge on the pinacolyl moiety.

Finally, it should be noted that the solvent-accessible volume of the gorge in the non-aged conjugate is decreased (6%) compared to the native structure. This decrease in gorge volume may generate a more suitably tuned vessel for catalyzing the dealkylation reaction by relevant enzyme residues. After dealkylation, a slight volume increase of 3% is observed, but the volume of the gorge of the aged enzyme is still 3% less than that of the native form. Osmotic vs. hydrostatic pressure, differential scanning calorimetry, and neutron scattering studies indicate that the thermodynamic stability of aged ChEs is

strongly increased and that enzyme dynamics is altered compared to native enzymes [Gabel 2009; Masson 1994; Masson 1999]. Increased thermodynamic stability of aged ChEs was explained by dehydration at the bottom of the gorge, so that the salt bridge between His440 and the phosphonyl moiety is in a low dielectric environment.

Non-functional orientation of 2-PAM in the ternary complex with the aged soman/TcAChE conjugate.

The crystal structure of the ternary complex of 2-PAM with the aged soman/*Tc*AChE conjugate clearly reveals how 2-PAM binds within the CAS of the aged enzyme. The aromatic ring of 2-PAM stacks against the side chain of Trp84, in such a way that the oxime group points towards His440 O (the main-chain oxygen), at a distance of 2.5 Å; not only does it point away from the soman phosphorus atom, with its oxygen atom at a distance of 6.8 Å, but it is also on the wrong side for direct nucleophilic attack on the P-Ser200Oγ bond. The orientation of 2-PAM differs from that seen in the complex of 2-PAM with native *Tc*AChE (Harel, Silman & Sussman, unpublished; PDB code 2VQ6). In this structure, too, the 2-PAM moiety is stacked against Trp84, but in a reversed orientation, so that its oxygen atom is 4.8 Å from Ser200 Oγ, and could be substantially closer to the P atom in a putative OP conjugate.

Attempts were made to trap and solve the 3D structure of the ternary complex of 2-PAM with the non-aged soman/*Tc*AChE conjugate. To this end, crystallographic data were collected on a *Tc*AChE crystal that had been soaked for 5 min in a solution containing soman, at pH 8.2, followed by 5 min soaking in a 10 mM solution of 2-PAM at the same pH. No electron density was found that could account for the presence of 2-PAM, whereas the pinacolyl moiety of non-dealkylated soman was observed at the same position as in the non-aged soman/*Tc*AChE conjugate, *viz.,* in proximity to Trp84, which would preclude binding of 2-PAM at that position as observed for the native enzyme and for the aged soman/*Tc*AChE conjugate (data not shown).

2-PAM thus binds poorly to the non-aged phosphonylated enzyme, and binds in an unfavorable conformation after aging. Apart from 2-PAM, the oximes in use or under consideration for treatment of OP intoxication are elongated molecules, and it was tacitly assumed that they span the active-site gorge, linking the PAS and the CAS, just like such potent bivalent AChE inhibitors as decamethonium [Felder 2002; Harel 1993] and

heptylene-linked bistacrine [Colletier 2006b; Rydberg 2006]. Indeed, such an assumption was made in the design of an effective heptylene-linked bis-pyridinium aldoxime reactivator, Ortho-7 [Pang 2003]. However, the crystal structures of the complexes of three bis-quaternary oximes with mAChE, including Ortho-7 [Ekstrom 2006b], provide strong evidence that their oximate groups attack OP/AChE conjugates from a position up the gorge axis, remote from the Trp residue in the CAS, and it is plausible that 2-PAM also acts on phosphylated conjugates from a similar angle, and not as might be inferred from the crystal structures of the 2-PAM/*Tc*AChE complex or of its ternary complex with the aged soman/*Tc*AChE conjugate.

These findings should stimulate new approaches for improvement in the design of reactivators with better affinity for the non-aged conjugate or that could bind in the proper orientation after aging. Furthermore, since a nucleophilic attack is not prevented by the negative charge on the phosphonyl group [Behrman 1970b; Behrman 1970a], reactivation of aged enzymes should in principle be made possible.

Template for designing novel reactivators.

A large number of putative reactivators have already been synthesized, some of which are currently being tested [Ekstrom 2006b; Ekstrom 2007]. As already mentioned, they are mostly elongated molecules designed to bind simultaneously at the CAS and PAS of AChE. However, no molecule able to reactivate an aged OP/ChE conjugate has yet been found. Furthermore, there is scope for improving the potency of reactivators such as 2-PAM, HI-6, H-Lö7 and MMB-4.

2-PAM, and its bisquarternary analog, HI-6, are both 2-pyridinium mono-aldoximes and yet, as mentioned above, display substantially different potencies in the reactivation of soman/AChE adducts [Luo 2007]. Bimolecular rate constants of the reactivation for soman-inhibited AChEs by various oximes showed that in the case of human AChE HI-6 is $4x10^5$-fold more potent than its mono-quaternary parent analog, 2-PAM. Furthermore, HI-6 was shown to reactivate the conjugate of mAChE obtained with the P_SC_S isomer significantly faster than that generated with the P_SC_R isomer [de Jong 1985] Similar results were reported for electric eel AChE inhibited with the same two potent soman epimers [Benschop 1984]. In this context, the crystal structure of the non-aged soman/*Tc*AChE conjugate presented here provides a valuable template for designing

more potent reactivators. In particular, we propose to conduct molecular dynamics (MD) simulations of the non-aged soman/*Tc*AChE conjugate and take minor conformations accessed during the simulation into account in the design process. Indeed, a recent study showed that side-chain conformations of gorge residues in crystallographic AChE-ligand complexes, which differ from those observed in native AChE, are already accessed in a MD simulation of native AChE [Xu 2008b; Xu 2008c]. Conformational changes upon ligand-binding in AChE thus involve pre-existing equilibrium dynamics, rather than an induced fit, and can be predicted to a certain extent. In the light of the considerations referred to above, it should also be of value to conduct docking experiments for 2-PAM and suitable bi-functionnal reactivators utilizing the crystal structures of native *Torpedo* and mammalian AChEs, as well as of the non-aged and aged soman/*Tc*AChE conjugates.

EXPERIMENTAL SECTION

Materials. Polyethyleneglycol (PEG) 200 and morpholinoethylsulphonic acid (MES) were from Sigma Chemical Co. (St Louis, MO, USA). O-(1,2,2-trimethylpropyl) methylphosphonofluoridate (soman) was obtained from the CEB (Centre d'Étude du Bouchet, Vert-le-Petit, France) and pralidoxime (N-methylpyridin-1-ium 2-aldoxime methiodide, 2-PAM) from EGA-Chemie (Steinheim, Germany). *Tc*AChE was purified as described previously [Sussman 1991].

Crystallization and Soaking Procedures. Trigonal crystals of *Tc*AChE (space group $P3_121$) were obtained by the vapor diffusion method at 4 °C in hanging drops in 32-34% PEG 200 and 150 mM MES, at pH 5.8-6.1. Conjugates and complexes were formed by soaking crystals of the native enzyme at 4 °C into solutions based on either 36% PEG 200/150 mM MES, pH 5.8 (referred to as *soaking solution A*) or 36% PEG 200/150 mM Tris/HCl, pH 8.2 (referred to as *the soaking solution B*). In order to obtain the non-aged soman/*Tc*AChE conjugate, crystals were soaked for 6 min in *soaking solution B* containing 1.3 mM soman (mixture of the four stereoisomers $P_{R/S}C_{R/S}$). Due to the cryoprotective capacity of PEG 200 itself, no additional cryoprotectant was necessary, and the crystal was directly loop-mounted and flash-cooled in liquid nitrogen. The aged soman/*Tc*AChE conjugate was obtained by soaking crystals for 2 h in *soaking solution A* containing 1.3 mM soman. Crystals of the ternary complex of the aged soman/*Tc*AChE conjugate with 2-PAM were obtained in two stages: first, crystals of the aged conjugate were obtained as described above; these crystals were then transferred for 12 h into *soaking solution A* or *B* containing 10 mM 2-PAM (solubilized initially at 100 mM in 150 mM Tris/HCl, pH 8). All soaking and flash-cooling operations were performed at the Centre de Recherches du Service de Santé des Armées (La Tronche).

Data collection and processing. All data collection was performed at the European Synchrotron Radiation Facility (ESRF, Grenoble) on beamlines ID14-2 and ID14-4. The loops containing flash-cooled crystals were transferred on the goniometer head into the cryostream of a cooling device (700 series, Oxford Cryosystems, Oxford, UK) operating at 100 K. For details concerning data collection, see table 1. Reflections were indexed and integrated using XDS [Kabsch 1993]. The intensities of integrated reflections were scaled using XSCALE, and structure factors were calculated using XDSCONV. Refinement of

the models was carried out using Refmac5 [1994], with the native structure of *Tc*AChE (PDB entry code 1EA5) as the starting model. For calculation of R_{free} the same structure factors as the ones used for refinement of the starting model (1EA5) were flagged. For all three structures (*viz.*, the non-aged soman/*Tc*AChE conjugate, the aged conjugate, and the ternary complex of the aged conjugate with 2-PAM), a rigid-body refinement was first carried out using reflections in the range of 20–4 Å. All model building and graphic operations were carried out using Coot [Emsley 2004]. In each model, the first set of water molecules was added automatically using the water-picking feature in Coot. Solvent molecules, ligands and sugar residues of the covalently attached glycan chains, *viz.,* N-acetylglucosamine (NAG) and fucose (FUC), were added subsequently. The occupancies of the soman adduct in the non-aged and in the aged conjugates were estimated to be 90 and 100%, respectively. 2-PAM and soman in the ternary complex were estimated to display full occupancy. Successive alternation of refinement cycles and manual model building were performed until R_{cryst} and R_{free} did not decrease any further. Refinement comprised energy minimization and individual isotropic B-factor refinement, using the full range of recorded reflections for each data set. The simulated-annealing omit-maps shown in Figures 2 and 3 were calculated using CNS version 1.2 [Brunger 2007], after omitting soman adducts and/or 2-PAM. Figures were produced with Pymol [DeLano 2002a]. Active-site gorge volumes were calculated using the CASTP server [Dundas 2006], after removal of ligands and water molecules from the models. Alignment of huCE1 and *Tc*AChE structures was achieved with Theseus [Theobald & Wuttke 2006]. Final models were validated using MOLPROBITY [Davis 2007] and WHATCHECK [Hooft 1996]. Parameters and topologies of PEG, MES, NAG, FUC, 2-PAM, and of non-dealkylated and dealkylated soman adducts, were generated using the PRODRG server at Dundee University [Schuttelkopf 2004].

Acknowledgements. We gratefully acknowledge the ESRF for beam-time under long-term projects MX498, MX609 and MX722 (IBS BAG) and MX551 and MX 666 (radiation-damage BAG), and the ESRF staff for providing efficient help during data collection. Financial support by the CEA, the CNRS and the UJF is acknowledged, as well as a grant to MW from the Agence Nationale de la Recherche (ANR) (project number JC05_45685), a grant to FN from the ANR (ANR-06-BLAN-0163) and from the DGA (08co501), and a DGA grant (03co10-05/PEA 010807) to PM. This study was

supported by the European Commission Sixth Framework Research and Technological Development Program 'SPINE2-COMPLEXES' Project, under contract No. 031220, a research grant from Erwin Pearl, the Benoziyo Center for Neurosciences, the Divadol Foundation, the Nalvyco Foundation, the Bruce Rosen Foundation, the Neuman Foundation. J.L.S. is the Morton and Gladys Pickman Professor of Structural Biology. We thank Dr Matthew Redinbo (Department of Chemistry, University of North Carolina at Chapel Hill) for permission to quote his unpublished data, and Prof David Milstein (Department of Organic Chemistry, Weizmann Institute of Science), for valuable discussions.

Supporting Information Available: Alternate refinement of the non-aged soman/*Tc*AChE conjugate. This material is available free of charge via the Internet at http//pubs.acs.org.

Table 1: Crystallographic and refinement statistics.

	Non-aged soman/TcAChE	*Aged soman/TcAChE*	*Ternary 2-PAM/Aged soman/TcAChE complex*
PDB entry code	2wfz	2wg0	2wg1
ESRF beamline	ID14-4	ID14-2	ID14-2
Temperature (K)	100	100	100
Number of frames	120	100	90
Exposure time (s/frame)	1 (transmission 20%)	2	4
Wavelength (Å)	0.939	0.933	0.933
Space group	$P3_121$	$P3_121$	$P3_121$
Unit cell parameters (Å)			
a=b	111.4	111.6	111.9
c	137.4	136.8	137.2
Resolution range (Å)[1]	20.00-1.95 (2.00-1.95)	20.00-2.20 (2.30-2.20)	20.00-2.20 (2.30-2.20)
Completeness (%)[1]	99.3 (98.8)	99.4 (99.9)	99.5 (99.4)
R_{sym} (%)[1,2]	7.3 (59.8)	13.7 (48.8)	8.0 (49.5)
$I/\sigma(I)$[1]	17.64 (3.12)	10.02 (3.25)	16.12 (3.30)
Unique reflections[1]	71726 (5103)	50212 (6216)	50657 (6244)
Redundancy	7.1	5.6	5.5
R_{cryst} (%)	16.62	17.72	16.58
R_{free} (%)	19.56	22.89	21.18
R.m.s.d. bond length (Å)	0.012	0.014	0.013
R.m.s.d. bond angles (degree)	1.3	1.5	1.4
No. of atoms in ASU			
Total	5206	5113	5221
Protein	4395	4297	4449
Water	660	620	555
Ligands	151	196	217
Carbohydrates	52	56	38
Soman	10	4	4

2-PAM	.	.	10
B-factor (Å^2)			
Overall	31.4	25.4	31.2
Protein	28.3	22.4	28.2
Water	45.7	37.1	42.7
Ligands	57.7	54.0	64.3
Carbohydrates	61.2	56.6	64.6
Soman	32.6	20.8	21.1
2-PAM	.	.	33.3

[1]: values in brackets refer to the highest resolution shell.

[2]: $$R_{sym} = \frac{\sum_{hkl} \sum_{i} \left| I_i(hkl) - \overline{I(hkl)} \right|}{\sum_{hkl} \sum_{i} I_i(hkl)}$$

SUPPORTING INFORMATION

Alternative refinement of soman in the non-aged soman/TcAChE conjugate.

Refinement of the non-aged soman/*Tc*AChE conjugate was carried out using commonly accepted geometrical restraints of bond lengths (estimated standard deviation (ESD) of 0.025 Å for the O2-Cα bond and ESDs of 2.727° for the Cβ-Cα-O2, Cβ-Cα-C3 and C3-Cα-O2 angles, and 3.158° for the Cα-O2-P angle) as calculated by PRODRG [Schuttelkopf 2004] and set by default in Refmac 5 [1994]. This let to the model described in the main text and displayed in figure 2A. An F_o-F_c map showed a strong peak (6σ) of residual density next to the pinacolyl group of soman (figure S1). In an alternative refinement procedure, the geometric restraints on the soman O2-Cα bond were down-weighted by both increasing the allowed standard deviations of its bond length from 0.025 to 1 Å, and omitting those on the angles involving Cα, in the CIF file used by Refmac5 for describing the geometric restraints of ligands. Subsequent refinement with Refmac5 led to an increase in the O2-Cα bond length of the OP moiety of ~ 0.3 Å (1.74 Å instead of 1.48 Å, the ideal value) and to a decrease in the residual density in the F_o-F_c map (4σ) (figure S1). One-by-one down-weighting the geometric restraints of any other bond of the OP moiety did not result in a similar increase in bond lengths (not shown). It is noteworthy that the B-factor of the methyl on Cα is abnormally low (23 Å² vs. 36 Å² for Cα), suggesting strong stabilization by Glu199. This alternative model of the non-aged soman/*Tc*AChE conjugate structure has also been deposited in the PDB (access code 2wg2). It is also worth noting that such elongated bonds have previously been observed [Chabriere 2001; Nicolet 2003]. Hence, the alternative model suggests that the O2-Cα bond is stretched due to the transient formation of a carbenium at Cα, which is highly favored by the electrostatic environment provided by Glu199-, the water molecule 1001 and His440+. This state may be predicted to precede methyl migration from Cβ that would result in definitive breakage of the O2-Cα bond.

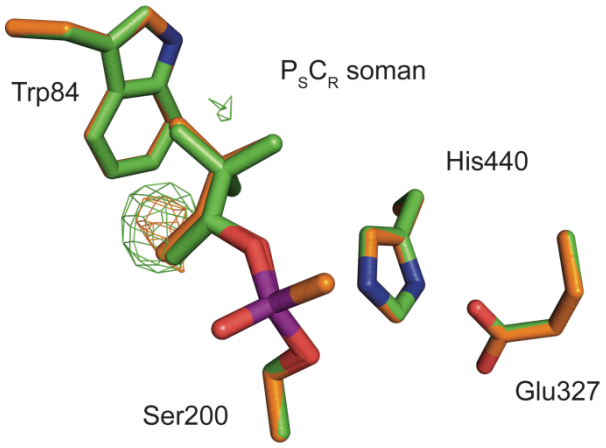

Figure S1: Active site of the non-aged soman/TcAChE conjugate after refinement with common geometrical restraints and down-weighted restraints on the O2-Cα bond. The F_o-F_c maps are contoured at 3σ and are in green and orange for the common and the down-weighted restrained refinements, respectively. The catalytic triad residues (Ser200, His440 and Glu327), Trp84 and the OP moiety are displayed as sticks, oxygen atoms in red, nitrogen atoms in blue and the phosphorus atom in purple. Carbon atoms are in yellow and green for the common and the down-weighted restrained refinements, respectively.

6.2.3 Bilan

Dans l'étude qui précède, les états réactionnels de l'inhibition de l'AChE par le soman ont été caractérisés structuralement. En quelque sorte, nous avons obtenu des instantanés de la réaction de vieillissement.

La mise en relation des résultats des deux articles précédents suggère une approche nouvelle pour la conception de nouveaux réactivateurs. Il a été montré que les réactivateurs qui se lient au PAS (HI-6 et HLö-7, par exemple) sont plus efficaces [Worek 2007]. Pour amener la fonction oxime dans une position favorable à l'attaque nucléophile, celle-ci doit pointer du haut de la gorge vers le bas. Pour y parvenir, il serait intéressant d'exploiter tous les sites de fixation connus de l'AChE, ainsi que les conformations minoritaires associées à sa flexibilité, notamment celle du Trp279, résidu principal du PAS. Une bonne connaissance de la structure et de la dynamique du PAS sont des atouts essentiels dans cette tâche. C'est précisément l'objet des deux études présentées ci-après. Le premier des deux articles suivants est consacré à l'analyse structurale d'un complexe de la *Tc*AChE avec un inhibiteur du PAS. Le second article est une étude dynamique menée avec ce même inhibiteur.

6.3 L'acétylcholinestérase en complexe avec l'aflatoxine, un inhibiteur du PAS

6.3.1 Présentation de l'article

Dans l'article qui suit (soumis), des structures de la *Tc*AChE en complexe avec l'AB1 sont présentées. L'AB1 est une mycotoxine cancérigène qui contamine certaines cultures, représentant ainsi un risque pour la santé. Comme l'AB1 est un inhibiteur du PAS, un biosenseur basé sur l'utilisation de l'AChE pourrait permettre de détecter les traces d'AB1 dans les cultures contaminées. Nous avons pris part à des études cinétiques visant à mettre au point un tel biosenseur [Hansmann Sanson Stojan Weik Marty & Fournier 2009] (annexe 2).

Pour mieux comprendre le mécanisme d'inhibition de l'AB1, nous avons résolu la structure du complexe *Tc*AChE/AB1. Le mode de liaison de l'AB1 est différent selon le groupe d'espace auquel appartiennent les cristaux de *Tc*AChE utilisés dans la procédure de trempage. Afin de déterminer le mode de liaison biologiquement pertinent, nous avons évalué les effets des solvants utilisés pour solubiliser l'AB1 (le DMSO et l'éthanol). Cette étude a mis en évidence des artéfacts de la cristallographie qui peuvent biaiser l'interprétation de données cristallographiques.

6.3.2 Article

Manuscrit soumis.

Torpedo californica Acetylcholinesterase in Complex with the Peripheral Site Ligand Aflatoxin: Influence of Crystallization Conditions and Crystal Packing on the Binding Mode

Benoît Sanson[1], Didier Fournier[2], Joel L. Sussman[3], Israel Silman[4] and Martin Weik[1]

[1]Laboratoire de Biophysique Moléculaire, Institut de Biologie Structurale (CEA/CNRS/UJF), 41 rue Jules Horowitz, 38027 Grenoble Cedex, France; [2]IPBS, 205 route de Narbonne, 31077 Toulouse, France; Departments of [3]Structural Biology and [4]Neurobiology, Weizmann Institute of Science, Rehovot 76100, Israel.

Running title: Aflatoxin binding to acetylcholinesterase

SUMMARY: Acetylcholinesterase catalyzes the neurotransmitter acetylcholine in an active site at the bottom of a deep and narrow gorge. A peripheral binding site at the gorge entrance guides substrates and ligands *en route* to the active site, allosterically modulates catalysis and has been proposed to promote amyloid-plaque formation in Alzheimer disease. Structural information on ligand binding to the peripheral binding site, however, is scarce. Here, we report X-ray crystal structures of *Torpedo californica* acetylcholinesterase in complex with the strongly carcinogenic mycotoxin aflatoxin bound at the peripheral binding site. Acetylcholinesterase in two different crystal forms and aflatoxin solubilized in different organic solvents had to be employed in order to determine unequivocally the functionally relevant ligand binding mode and to identify an observed disruption of the catalytic triad as originating from the presence of ethanol. Besides providing information on ligand binding to the peripheral site, our study identified and eliminated several crystallographically-related artefacts that can impede correct biological information.

KEYWORDS: Acetylcholinesterase, aflatoxin, crystal packing, solvent, ethanol, DMSO, allostery, error-scaled distance-difference matrix

INTRODUCTION

The principal role of acetylcholinesterase (AChE, EC 3.1.1.7) is termination of transmission at cholinergic synapses by rapid hydrolysis of the neurotransmitter, acetylcholine (ACh) [Silman 2005]. In accordance with its biological role, it has unusually high catalytic activity, acting at speeds approaching diffusion control [Quinn 1987], and hydrolyzing ACh with turnover numbers in the range of 10^3-10^4 s^{-1}, depending on the species [Vigny 1978]. Solution of the 3D structure of *Torpedo californica* (*Tc*) AChE revealed that, unexpectedly for such a rapid enzyme, its active site is buried at the bottom of a deep and narrow gorge, ~ 20 Å long, lined by 14 highly conserved aromatic residues [Sussman 1991]. The active site features a catalytic triad, Ser200, His440 and Glu327 (*Tc*AChE numbering), characteristic of serine hydrolases. A catalytic 'anionic' subsite (CAS), constituted primarily of Trp84 and Phe330 makes a π-cation interaction with the positively charged choline moiety of the substrate during the acylation step of catalysis [Colletier 2006a; Sussman 1991], and the oxyanion hole (Gly117N, Gly118N and Ala201N), again characteristic of serine hydrolases, stabilizes the developing

negative charge during catalysis. The binding of ACh is also stabilized by interaction of its acetyl moiety with the 'acyl pocket' composed of Phe288, Trp233, Phe290 and Phe331 [Harel 1996]. Through either cation-π or π–π interactions [Sussman 1991], Trp84, in the CAS, stabilizes the binding of a variety of ligands, including the product of enzymatic hydrolysis, choline [Bourne 2006; Colletier 2006a], tertiary and quaternary aromatic ligands, such as tacrine and edrophonium, respectively [Harel 1993], and a variety of elongated bifunctional gorge-spanning ligands [Colletier 2006b; Felder 2002; Harel 1993; Rydberg 2006].

At the mouth of the gorge, a so-called 'peripheral' anionic subsite (PAS) contributed to by Trp279, Tyr70, Tyr121, Tyr334 and Asp72 [Barak 1994; Radic 1994], serves as a second binding locus for substrates and products, as well as for so-called peripheral site ligands [Taylor 1975] and gorge-spanning ligands [Du 2004]. Binding of ligands to the PAS results in a competitive inhibition by steric blockade, since both substrate entrance to the active site and product clearance are affected [Rosenberry 1999; Szegletes 1998]. However, the kinetic data are not strictly competitive, and have been interpreted in terms of an allosteric interaction between the PAS and the CAS [Changeux 1966; Kitz 1970] that has been confirmed by site-directed mutagenesis [Shafferman 1992b]. Moreover, the activation of substrate hydrolysis observed for AChE from certain species has been attributed to an increase in the rate of deacetylation by a substrate molecule bound at the PAS [Brochier 2001; Colletier 2006a; Stojan 2004]. Kinetic measurements made on the complex of mouse AChE (mAChE) with the snake venom toxin fasciculin 2 (FAS) also confirmed an allosteric effect on the CAS of binding of a ligand to the PAS [Radic & Taylor 2001]. Molecular dynamics simulations also indicated that disruption of the catalytic triad could occur upon binding of FAS at the PAS [Tai 2002]. Furthermore, mutagenesis of Trp86 in mAChE (equivalent to Trp84 in *Tc*AChE) revealed that FAS can allosterically activate the hydrolysis of neutral substrates [Radic 1995], and either enhance [Radic & Taylor 1999] or decrease [Radic 1999; Rosenberry 1999] the rate of phosphylation by neutral and cationic organophosphorus compounds, respectively. Conformational changes induced by binding of ligands at the PAS have also been studied by biophysical techniques, including fluorescence spectroscopy, circular dichroism [Berman 1981] and electron paramagnetic resonance [Grubic 1995].

A route via which an allosteric signal could be transmitted from the PAS to the CAS has been proposed to involve the hAChE residues Asp74(70)-Tyr341(334)-Tyr337(330)

(hAChE numbering with TcAChE numbering in brackets) [Shafferman 1992b]**.** It was subsequently suggested that the putative allosteric effect occurred through the Cys69(67)-Cys96(94) Ω loop (hAChE numbering, with *Tc*AChE numbering in brackets) [Barak 1995], involving also Tyr133(131) and Trp86(84) (hAChE numbering, with *Tc*AChE numbering in brackets) [Barak 1995; Ordentlich 1995]. Cysteine substitution mutagenesis showed that the Ω loop may close upon ligand binding at the PAS, following a lid-like movement gating substrate access to the active site[Shi 2001]. In addition, molecular dynamics simulations of the AChE/FAS complex suggested that enhanced conformational fluctuations of this loop are correlated with the opening of alternative routes for traffic of substrates and products when the inhibitor is bound at the PAS [Bui 2004; Bui 2008].

Only limited structural information is available with respect to binding of ligands at the PAS. This is mainly a consequence of the PAS being at the enzyme surface and thus within zones of contact between adjacent copies of AChE within the crystal; such contacts can impose strong steric constraints on binding of ligands at the PAS. Complexes FAS with mAChE [Bourne 1995], *Tc*AChE [Harel 1995] and hAChE [Kryger 2000], all obtained by cocrystallization, provided the first experimental insight into ligand binding at the PAS. Subsequently, the crystal structures were reported of complexes of mAChE with decidium, propidium and gallamine [Bourne 2003], and with choline and with a non-hydrolysable substrate analogue [Bourne 2006], and of complexes of *Tc*AChE with thiocholine, acetylthiocholine and a non-hydrolysable substrate analogue [Colletier 2006a], and with thioflavin T (ThT) [Harel 2008]. None of these complexes revealed any significant structural changes that might produce an allosteric effect at the active site due to binding of a ligand at the PAS.

Evidence has been presented that the PAS enhances the rate of assembly of the Aβ peptide to amyloid fibrils [Inestrosa 1996], a process that is one of the hallmarks of Alzheimer's disease. Gorge-spanning bifunctional inhibitors, binding at both the PAS and in the CAS, may thus serve as a new category of AD drugs that both inhibit AChE activity by binding in the CAS, and retard amyloid plaque formation by binding at the PAS [Recanatini & Valenti 2004; Silman 2005]. Numerous crystal structures of complexes of AChE with such gorge-spanning bifunctional inhibitors have been reported. These include complexes with decamethonium [Harel 1993], the anti-Alzheimer drug E2020 [Kryger 1998], BW284C51 [Felder 2002], inhibitors produced by 'click-chemistry'

[Bourne 2004], bis-tacrines [Colletier 2006b; Rydberg 2006], the anti-cancer prodrug CPT-11 [Harel 2005], and gorge-spanning oxime reactivators of conjugates of AChE with organophosphate nerve agents [Ekstrom 2006b]. Again, none of these crystal structures showed structural changes that might provide insight into allosteric regulation of catalytic activity by binding of a ligand at the PAS.

Aflatoxin B1 (AB1, scheme 1) is a powerful hepatotoxic and carcinogenic mycotoxin [Richard 2007]. It presents a serious health treat, since it contaminates crops in wet and hot climate zones. AB1 was shown to be an AChE inhibitor, and it was proposed that it does so by binding at the PAS [Hansmann 2009]. Consequently, AChE has been proposed as a probe for measuring concentrations of this mycotoxin in food [Hansmann 2009]. It is of interest that evidence has been presented that another mycotoxin, territrem, also inhibits AChE by blocking the active-site gorge [Chen 1999].

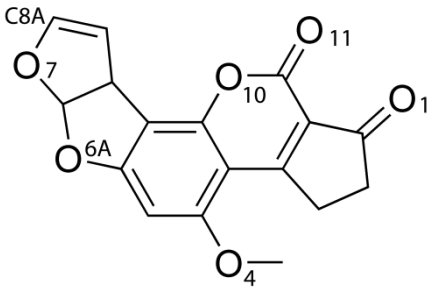

Scheme 1. Chemical formula of aflatoxin B1.

In the present study, binding of AB1 to *Tc*AChE was addressed structurally by X-ray crystallography, using crystals of two different space groups. AB1 indeed binds exclusively at the PAS, in both the orthorhombic ($P2_12_12_1$) and trigonal ($P3_121$) crystal forms employed, yet in different orientations. These different orientations can be ascribed to differences in crystallization conditions and in crystal packing. Structural changes are observed that may hint at allosteric effects on the CAS of inhibitor binding at the PAS. A disruption of the catalytic triad was observed in the *Tc*AChE/AB1 complex in the orthorhombic form and was identified as being due to the presence of 10% ethanol. The study illustrates the necessity of careful control experiments addressing the influence of solvent and crystal packing before the physiological relevance of observed ligand target complexes can be ascertained.

MATERIALS AND METHODS

Chemicals. Aflatoxin B1 (AB1), polyethyleneglycol (PEG) 200, morpholinoethylsulfonic acid (MES), ethanol (EtOH) and dimethysulfoxide (DMSO) were purchased from Sigma Chemical Co. (St Louis, MO, USA). Saturated solutions of AB1 made up in EtOH and DMSO had estimated concentrations of ~1 and 80 mM, respectively.

*Crystallization and soaking procedure. Tc*AChE was purified as described previously [Sussman 1991]. Trigonal (space group $P3_121$) and orthorhombic (space group $P2_12_12_1$) crystals were grown at 4°C in hanging drops, using the vapor diffusion method, in 32-34% PEG200/150mM MES, pH 5.6-6.0. A micro-seeding procedure was employed in order to favor the growth of trigonal crystals. Complexes were obtained by soaking crystals of *Tc*AChE into solutions based on 36% PEG200/150mM MES, pH 5.8 (referred to as the *soaking solution*). Regardless of the space group, complexes of *Tc*AChE with EtOH-solubilized AB1 (AET and AEO) were obtained using soaking solution containing 10% of the saturated solution of AB1 in EtOH, thus having a final AB1 concentration of ~100μM. Orthorhombic crystals of the AB1/*Tc*AChE complex of *Tc*AChE (ADO) were obtained using soaking solution containing 10% of the saturated solution of AB1 in DMSO, thus having a final AB1 concentration of ~8mM. The structures of trigonal *Tc*AChE in EtOH, and of orthorhombic *Tc*AChE in EtOH or in DMSO were obtained by replacing the neat soaking solution with soaking solution containing 10% of the appropriate solvent. The structures shown were obtained without EtOH or DMSO in the well solution.

Data collection and processing. All data collection was performed at the European Synchrotron Radiation Facility (ESRF, Grenoble), on beamlines ID14-1, ID14-2, ID14-4 and ID29). The cryoprotective properties of PEG200 precluded the use of a supplementary cryoprotectant. The crystals were directly loop-mounted on the goniometer head and concomitantly flash-cooled in a stream of gaseous nitrogen at 100K. Details of data collection are shown in Table1.

The data were indexed and integrated using XDS [Kabsch 1993], the intensities of integrated reflections were scaled using XSCALE, and structure factors were calculated using XDSCONV. Refinement was carried out using Refmac5 [Murshudov 1997], with the native structures of trigonal (space group $P3_121$) and orthorhombic ($P2_12_12_1$) *Tc*AChE

(PDB entry codes 1EA5 and 1W75, respectively) as the starting models, which contain one and two molecules in the asymmetric unit, respectively. For calculation of R_{free}, the same structure factors were flagged as were used for refinement of the starting model. All model building and graphic operations were carried out using Coot [Emsley 2004]. In each model, the first set of water molecules was added automatically, using the water-picking feature in Coot. Ligands were added, and N-acetylglucosamine (NAG) and fucose (FUC) were modeled at glycosylation sites. Successive alternation of refinement cycles and manual model building were performed until $R_{cryst.}$ and R_{free} did not decrease any further. Refinement comprised energy minimization and individual isotropic B-factor refinement, using the full range of recorded reflections for each data set. The refinement was improved using two TLS groups per monomer (sets of residues 4-305 and 306-535) [Painter & Merritt 2006]. The simulated-annealing omit-maps shown in figures 2A and 2B were calculated using CNS version 1.2 [Brunger 2007], after omitting AB1 coordinates. Figures were produced with Pymol [DeLano 2002b]. Final models were validated using MOLPROBITY [Davis 2007] and WHATCHECK [Hooft 1996]. Parameters and topologies of PEG, MES, NAG, FUC, ethanol, DMSO and AB1 were generated using the PRODRG server of Dundee University [Schuttelkopf 2004].

Error-scaled difference-distance matrices. Calculation of the error-scaled difference-distance matrices (ESDDM) was performed using ESCET [Schneider 2000; Schneider 2002]. The genetic algorithm of ESCET offers an unbiased way of detecting small conformational differences between two related structures.

RESULTS

The structure of *Tc*AChE complexed with AB1 was determined in two space groups, one trigonal ($P3_121$), and the other orthorhombic ($P2_12_12_1$). A total of six categories of data sets were required to determine the modes of binding of the ligand to the enzyme, and to provide a description of the related conformational changes. The corresponding structures are abbreviated as follows: 1. AET: that of an AB1/*Tc*AChE complex obtained by soaking into trigonal *Tc*AChE crystals AB1 in a soaking solution having a final EtOH concentration of 10%; 2. ET: that of native trigonal *Tc*AChE crystals exposed to the same soaking solution, but devoid of AB1; 3. AEO: that of an AB1/*Tc*AChE complex obtained by soaking into orthorhombic *Tc*AChE crystals AB1 in a soaking solution having a final EtOH concentration of 10% ; 4. EO: that of native orthorhombic *Tc*AChE crystals exposed to the same soaking solution, but devoid of AB1; 5. ADO: that of an AB1/*Tc*AChE complex obtained by soaking into orthorhombic *Tc*AChE crystals AB1 in a soaking solution containing a final DMSO concentration of 10%; 6. DO: that of native orthorhombic *Tc*AChE crystals exposed to the same soaking solution containing 10% DMSO, but devoid of AB1.

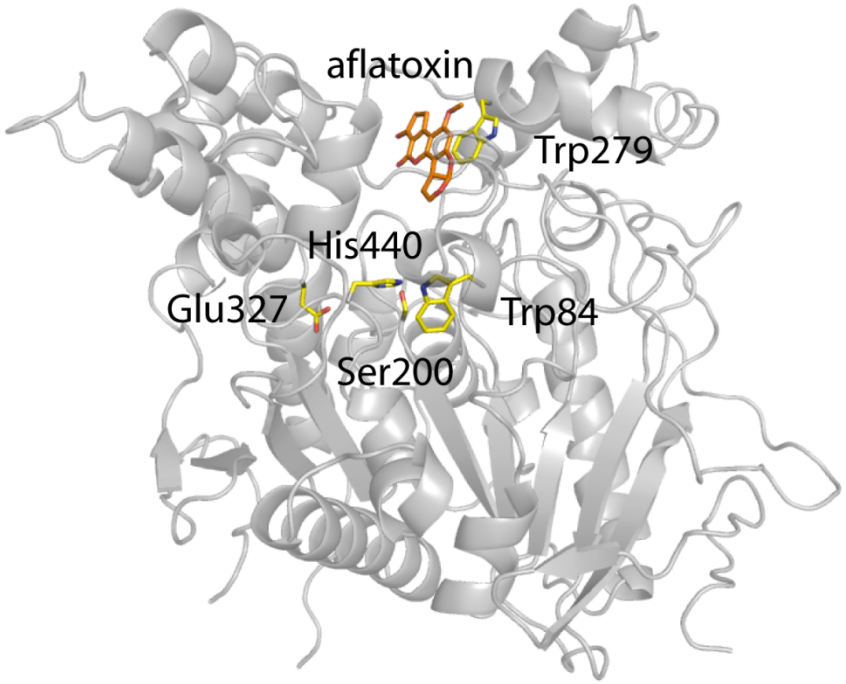

Figure 1. Overview of the structure of the AB1/TcAChE complex in the orthorhombic crystals. TcAChE is represented as a ribbon diagram. Residues of the catalytic triad (Ser200-Glu327-His440) and the PAS residue Trp279 are represented as yellow sticks. AB1, bound at the PAS, is represented as orange sticks.

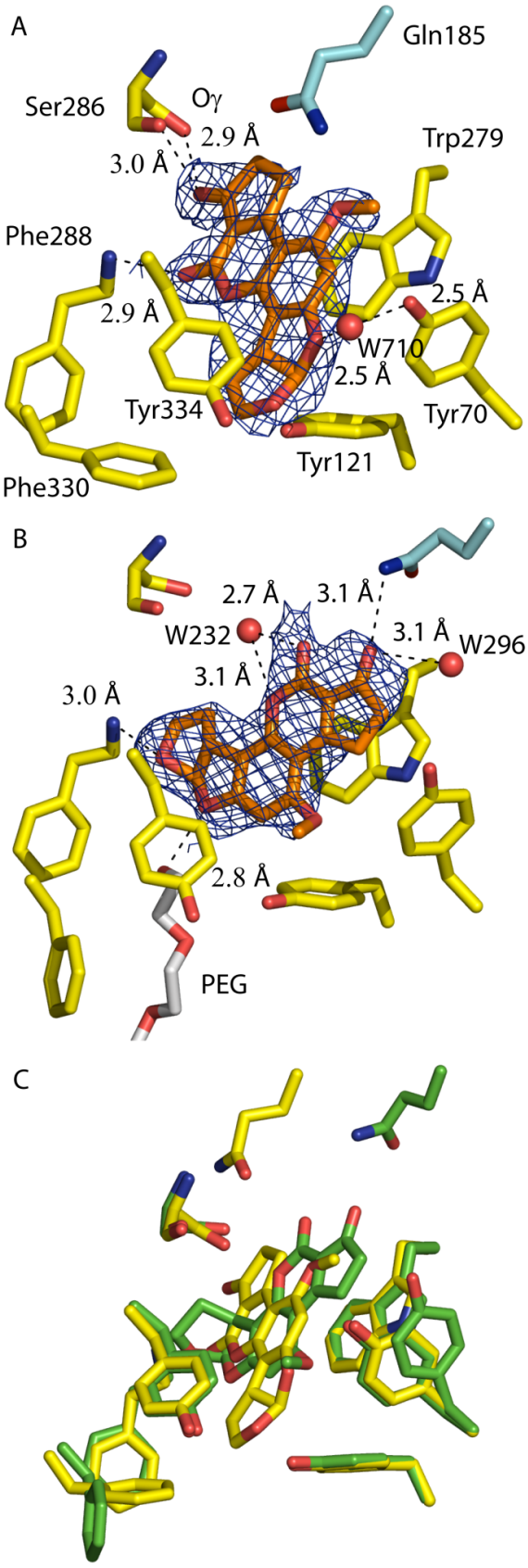

Figure 2. View of the PAS in the AB1/TcAChE complex obtained with the orthorhombic (A) and trigonal (B) crystals (AEO and AET, respectively), and superposition of those two views (C). The F_o-F_c maps are contoured at 3σ. AB1 is displayed as an orange stick model (A and B). Tyr70, Tyr121, Trp279, Ser286, Phe288, Phe330 and Tyr334 are represented as stick models, with carbon atoms colored yellow (A and B), oxygen atoms red and nitrogen atoms blue, as well as Gln185, from a symmetry-related copy of the enzyme, is represented as a stick model, with carbon atoms colored cyan, oxygen atoms red and nitrogens blue. Carbon atoms of residues and AB1 are in yellow and green in the orthorhombic and the trigonal complex, respectively, in the superposition view (C). Water molecules are represented as red balls. Hydrogen bonds are represented by black dashed lines. A PEG molecule is displayed as a stick model with carbon atoms colored gray, and oxygens blue. In the trigonal Tyr70 exhibits two alternative conformations.

Orthorhombic crystals of the AB1/TcAChE complex (AEO)

Orthorhombic crystals of *Tc*AChE were soaked for 14 h in a soaking solution containing 10% ethanol and a final AB1 concentration of ~100μM. A data set at 2.3 Å resolution revealed AB1 bound near the top of the active-site gorge (Fig. 1) at the PAS (Fig. 2A). The binding mode is identical in the two monomers, A and B. For all structures in the orthorhombic crystal form, figures and distances are of monomer A.

Interaction of AB1 with the enzyme is mainly through three hydrogen bonds, two of which involve the backbone. The cyclopentenone oxygen interacts with the carbonyl and Oγ oxygen atoms of Ser286*O* and Ser286*Oγ* (3.0 Å and 2.9 Å respectively), and the lactone oxygen O11 is within H-bond distance of Phe288*N* (2.9 Å). A strong H-bond links the water molecule 710 to the proximal furan oxygen O6A of AB1 (2.5 Å). AB1 is further stabilized by interaction with the indole of Trp279. This is not a stacking interaction, since only the distal edge of the six-membered ring of the indole is in contact with the coumarin moiety (distance of 3.5 Å between closest atoms); however the methoxy group of the AB1 moiety projects towards the pyrrole ring of Trp279 (distance of 3.7 Å between closest atoms). The distal furan carbon C8A of AB1 is only 2.8 Å from Phe330 Cε1, which has undergone a conformational change with respect to its position in native *Tc*AChE (PDB entry code: 1W75). Its χ_1 and χ_2 angles are rotated by 30 and 60º, respectively. AB1 makes additional hydrophobic interactions with Tyr70, Tyr121 and Tyr334 (3.3 Å, 3.2 Å and 3.4 Å, respectively).

A rotation of 40° and 160° in the χ_1 and χ_2 angles of His440 are observed, respectively, compared to the native *Tc*AChE structure; this results in an increase of 1.1 Å in the distance between His440Nε2 and Ser200Oγ (Fig. 3A and table 2), thus disrupting the hydrogen-bonding between these two components of the catalytic triad. Furthermore, the main chain of His440 is displaced by 0.4 Å. An ESDDM was calculated between AEO and the native structure (1W75) that is essentially empty (not shown), implying there are no major overall conformational changes.

The possible effect of the EtOH in which AB1 had been dissolved on the structure of the *Tc*AChE in the orthorhombic crystals, in the absence of AB1, was addressed by exposing orthorhombic crystals of *Tc*AChE to soaking solution containing 10% EtOH, and solving the structure (EO) at 2.20 Å resolution. His440 was seen to undergo a conformational change in EO similar to that observed in AEO. However, in EO, two alternative conformations were modeled, with similar occupancies, one being very similar to that

seen in the native enzyme (1W75), and the other to that seen in the AEO complex. Residual Fo-Fc density was seen within the active site, next to His440, but no EtOH molecule could be unambiguously modeled. An ESDDM calculated between EO and 1W75 was featureless, indicating that there was no large-scale effect of EtOH on the structure of *Tc*AChE in the orthorhombic crystals.

	Ser200-His440 (Å)	Glu327-His440 (Å)
1EA5	3.0	2.6
AET	3.3	2.8
ET	2.9	2.6
1W75	2.7	2.7
AEO	3.8	6.2
EO[1]	3.0/5.1	2.6/4.7
ADO	3.2	3.0
DO	3.1	2.8

[1]The two values correspond to the two alternative conformations of His440.

Table2: H-bond lengths in the catalytic triad in the crystal structures studied

Since ethanol is responsible, at least partially, for the conformational change undergone by His440 in AEO and EO, experiments were conducted in which EtOH was replaced by DMSO. Thus, AB1, at a concentration of ~8 mM in soaking solution containing 10% DMSO, was soaked into orthorhombic crystals of *Tc*AChE. A 2.7 Å resolution data set permitted solution of the structure of the complex so obtained (ADO). The structure reveals an AB1 molecule bound at the PAS in almost the same orientation as in the complex in which EtOH was present in the soaking solution (AEO) (not shown). A small movement of His440 is also observed in ADO, viz., a 0.3 Å translation of the main chain with respect to its position in the native structure (1W75), leading to an increase of 0.5 Å in the distance between Ser200 Oγ and His440 Nε2 (Fig. 3B; table 2). A DMSO molecule was modeled in the active site, with one of its oxygens at a distance of 3.4 Å from His440 Nε2. However, its orientation could not be unambiguously defined. In the chosen orientation there is an H-bond between the DMSO oxygen atom and a water

molecule (321; 2.7 Å), which also makes three other H-bonds: with Ser200Oγ (2.7 Å), Gly119N (3.2 Å) and with another water molecule (322; 3.0 Å).

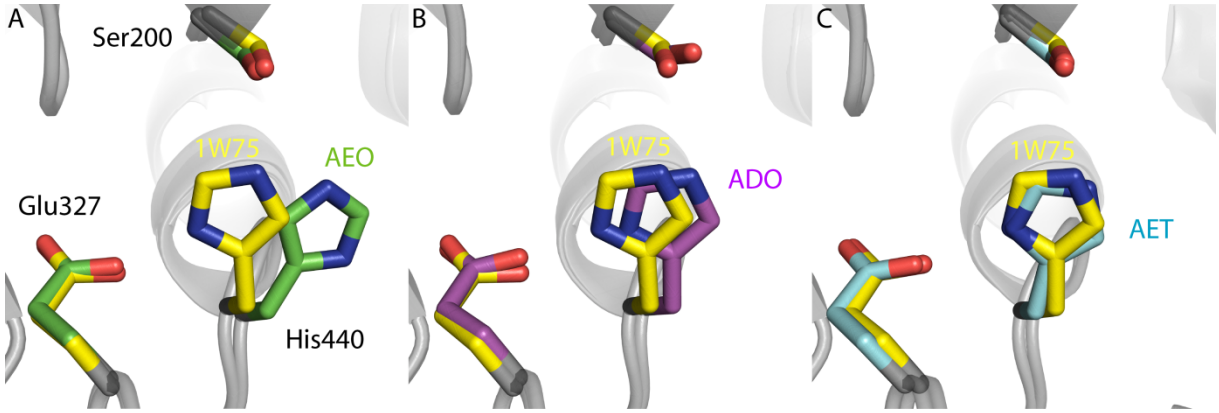

Figure 3. Movements of His440 caused by binding of AB1. The structures of orthorhombic (A and B) and trigonal (C) TcAChE crystals, in their native forms (PDB entry codes 1W75 and 1EA5, respectively), and complexed with AB1 (AEO, ADO and AET, respectively) in the presence of 10% EtOH (A and C) or 10% DMSO (B) are overlaid. The catalytic triad residues, Ser200, Glu327 and His440, are represented as sticks. The structures are presented as stick models, with carbon atoms coloured yellow in the native orthorhombic and trigonal TcAChE structures, green in the AEO, magenta in ADO and cyan in the AET. Oxygens are coloured red, and nitrogens blue in all six structures.

In order to assess the intrinsic effects of DMSO on the structure of *Tc*AChE, an orthorhombic crystal was soaked in soaking solution containing 10% DMSO. The structure (DO) was solved at 2.3 Å resolution, and revealed no conformational change relative to the native structure, as assessed by calculating an ESDDM between DO and the native structure, 1W75 (not shown). A DMSO molecule was modeled in DO at the same locus but not in the same orientation as in ADO.

Trigonal crystals of the AB1/TcAChE complex (AET)

Trigonal crystals of *Tc*AChE were soaked for 12 h in ~100 µM AB1 in soaking solution containing 10% EtOH, *i.e.,* the same conditions used to obtain the AEO structure. The structure of the AB1/*Tc*AChE complex in the trigonal space group (referred to as AET) was solved at 2.4 Å resolution. As in AEO, AB1 binds at the PAS, but in a different orientation (Fig. 2B). The AB1 molecules observed in AET (Fig. 2B) and in AEO (Fig. 2A) are both positioned within the same plane along the gorge axis, but one is rotated by 90° with respect to the other (Fig. 2C). Thus, the dihydrofurofuran group points towards

Phe288 in AET and towards the bottom of the gorge in AEO. As a consequence, AB1 penetrates deeper into the gorge in the orthorhombic than in the trigonal crystals.

In AET, the inhibitor is mainly stabilized through π-stacking of both the lactone ring of its coumarin moiety and its cyclopentenone ring against the indole of Trp279 (3.7 Å between closest non-hydrogen atoms). An H-bond between the distal furan oxygen O7 of AB1 and Phe288 *N* (2.7 Å) further contributes to stabilization. AB1 also forms H-bonds with two water molecules neither of which interacts directly with the protein: water 232 interacts with both the coumarin lactone oxygens, O11 and O10 (2.7 and 2.9 Å, respectively), and water 296 with the cyclopentenone oxygen O1 (3.0 Å). The latter also H-bonds with Gln185 Nε2 (3.0 Å) of a symmetry-related molecule. An overlay with the structure of native *Tc*AChE in the same trigonal crystal form (PDB entry code 1EA5) shows that the conformation of Gln185 is unchanged (not shown). The side chain of Tyr70 is rotated by 24º compared to the native structure in order to avoid a steric clash with the AB1. Finally, an H-bond is established between the proximal furan oxygen, O6A, and a PEG molecule spanning the gorge. This PEG molecule has been identified in several published crystal structures [Greenblatt 1999; Koellner 2000; Koellner 2002], yet is better defined in AET than in the structures previously described, most probably because of a stabilizing interaction with AB1.

Conformational changes in *Tc*AChE in the trigonal crystals upon binding of AB1 were investigated by the calculation of an ESDDM between AET and the native structure (1EA5) (Fig. 4A). The change in distance between each pair of Cα atoms is plotted according to their sign and their magnitude. The matrix shows that movements occur, which involve the two sub-domains of *Tc*AChE, *viz.,* residues 4-305 and 306-535, which face one another across the active site gorge [Morel 1999]. There are few movements relative to each other of pairs of amino-acids which belong to the same sub-domain; most of the movements involve pairs of amino-acids belonging to the two different sub-domains. Four regions within the C-terminal domain are affected. The most prominent movements involve residues 325-348 and residues 348-383. Region 325-348 moves towards AB1 and the 4-305 sub-domain, while the adjacent region 348-383 moves away (Fig. 4B). This movement occurs with residue 348 as a pivot. The maximum displacement is seen in the main chain carbonyl oxygen of Tyr334 O that rotates by 55° (not shown). Region 348-383 comprises one of the helices that form the four-helix bundle

connecting the two monomers in the *Tc*AChE dimer. The second helix involed is at the C-terminus, residues 517-535, which also displays a movement. Thus, binding of AB1 triggers a series of small movements, resulting in a small tilt within the four-helix bundle. A fourth region (425-438), is part of a loop at the rim of the gorge and moves towards the N-terminal domain.

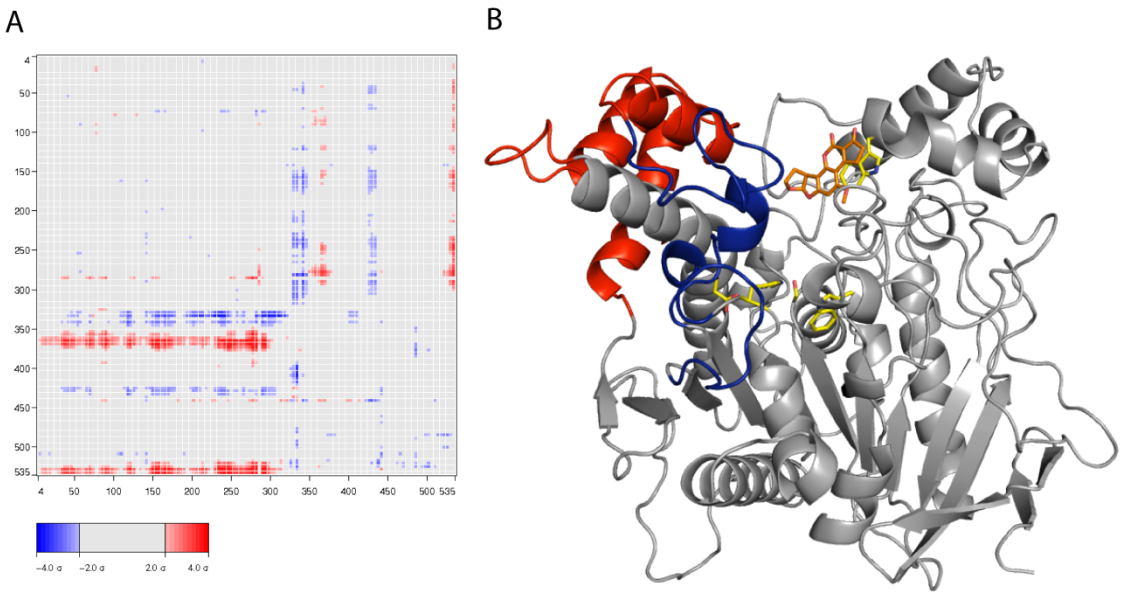

Figure 4. A/ Error-scaled difference-distance matrices of trigonal crystalline TcAChE, calculated using ESCET, between the structures of the enzyme in complex with AB1 (AET) and in the native form (PDB entry code 1EA5). The sigma cutoff for the calculation was set to 2σ-4σ. Blue and red indicate a decrease and an increase between pairs of Cα, respectively. B/ Overview of the structure of trigonal TcAChE binding aflatoxin at the PAS (AET). The structure of TcAChE is represented as a cartoon. Regions that approach (residues 325-348 and 425-438) and move away (residues 348-483 and 517-535) from the C-terminal domain of TcAChE are in red and blue, respectively. Residues of the catalytic triad (Ser200-Glu327-His440), the CAS residue Trp84 and the PAS residue Trp279 are represented as sticks. Aflatoxin is represented as orange sticks.

Variation in inter-Cα distances upon binding of AB1 in the trigonal crystals also involves residues within the catalytic triad. Small movements in the main and side chain atoms of His440 are comparable in magnitude to those observed in ADO (Fig. 3C and table 2). The His440 main chain is displaced by 0.3 Å, and the side chain is slightly displaced by a rotation of 10º in χ_1, resulting in an increased His440 Nε2 - Ser200 Oγ distance (3.3 Å) relative to the native structure (3.0 Å); in contrast, His440 Nδ1 is slightly closer to Glu327 Oε1 (2.6 Å) than in the native structure (2.7 Å).

In order to assess the effect of EtOH on the structure of *Tc*AChE in the trigonal crystals, they were exposed to soaking solution containing 10% ethanol, and the structure was solved at 2.20 Å resolution (ET). No EtOH molecule could be detected at either the CAS or the PAS. Furthermore, the structure showed no significant difference with respect to native *Tc*AChE as judged by a virtually empty ESDDM calculated between ET and 1EA5 (not shown). In particular, EtOH had no effect on the distance between His440 and Ser200 (not shown), in contrast to what had been observed for the orthorhombic crystals. A structure of *Tc*AChE determined after soaking trigonal crystals for 15 h in a solution of 8 mM AB1 in soaking solution containing in 10% DMSO did not reveal any bound AB1 (not shown).

DISCUSSION

The mode of interaction of AB1 with *Tc*AChE was addressed by use of X-ray crystallography, employing *Tc*AChE crystals of two different space groups, orthorhombic ($P2_12_12_1$) and trigonal ($P3_121$) In both crystal forms AB1 binds only at the PAS, but in different orientations. In the orthorhombic crystals, movement of His440 resulted in disruption of the catalytic triad, but a control experiment showed that this was due to the presence of 10% EtOH in the soaking solution. AB1 binding to *Tc*AChE in the trigonal crystal form involved a hydrogen bond to a symmetry-related copy of the enzyme and was accompanied by structural changes in the vicinity of the PAS involving movements of the two sub-domains of *Tc*AChE. Three aspects are discussed below: The modes of binding of AB1; the effect of EtOH on the structure of *Tc*AChE in the orthorhombic crystals, and pitfalls identified in our study that should be taken into account if X-ray crystallography is used to study ligand/protein interactions.

Binding of AB1 at the PAS

Structural insight into binding of inhibitors at the PAS is limited [Bourne 2003], and only one example involving *Tc*AChE has been published so far, that of its complex with Thioflavin T (PDB entry code 2J3Q; scheme 2) [Harel 2008]. This complex was obtained using crystals in the trigonal space group $P3_221$. For *Tc*AChE in the $P3_121$ crystal form, it has been suggested that steric hindrance at the opening of the gorge produced by contact with a symmetry-related copy of the enzyme might preclude the binding of bulky inhibitors at the PAS [Harel 2008]. In the present study we have, for the first time, obtained and solved the structures of complexes of AB1 bound at the PAS of *Tc*AChE in the $P3_121$ trigonal and the $P2_12_12_1$ orthorhombic crystal forms.

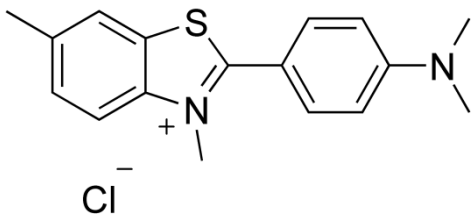

Scheme 2. Chemical formula of thioflavin T.

AB1 binds at the PAS in two very different orientations in the two crystal forms (Fig. 2C). In the trigonal form, the main stabilizing factors are a π-π stacking interaction of

AB1 with the indole moiety of Trp279, and an H-bond with Gln185 of a symmetry-related molecule (Fig. 2B). Gln185 is in the same orientation as in the native enzyme, and had previously been shown to form an H-bond with a bifunctional inhibitor bound in the gorge of *Tc*AChE crystallized in the $P3_121$ trigonal form [Haviv 2005]. In the orthorhombic crystals, AB1 binds slightly deeper within the gorge. The π-π stacking interaction of AB1 with the Trp279 indole moiety observed in the trigonal crystal form does not occur in the orthorhombic complex. Instead, it is stabilized mainly by four H-bonds with the protein, including one mediated by a water molecule, and by hydrophobic interactions with aromatic residues of the gorge wall (Fig. 2A). Unarguably, the binding mode of AB1 in the orthorhombic form is more relevant to the mode of binding in solution, since the ligand does not interact with a symmetry-related enzyme.

In order to identify subtle structural changes in the backbone of *Tc*AChE due to binding of AB1 that might hint at an allosteric effect on the active site, error-scaled distance-difference matrices (ESDDM) [Schneider 2000; Schneider 2002] were calculated between the complexes and the native structures. For the orthorhombic crystal form such a matrix was empty, thus clearly showing that AB1 had not caused any such allosteric changes. However, examination of the ESDDM for the trigonal form revealed that binding of AB1 produced movements of four small regions near the PAS (Fig. 4B). *Tc*AChE consists of two sub-domains facing one another across the active-site gorge [Morel 1999]. The movements observed all occur in the C-terminal domain of the enzyme and are with respect to the N-terminal domain. A normal mode analysis [Suhre & Sanejouand 2004] contained a strong Eigen mode producing an ESDDM with respect to the native structure similar to that shown in figure 4A (not shown). The movements induced upon binding of AB1 to the enzyme in the trigonal crystals, which are highlighted in figure 4B, might thus be related to breathing motions within the active site gorge of the native enzyme. One of the four regions that move upon binding of AB1 includes Glu327, the acid component of the catalytic triad. As a consequence, the H-bond between Glu327 and His440 is elongated by 0.2 Å (Table 2). Thus the movements displayed in figure 3 might reflect an allosteric mechanism by which ligand binding at the PAS affects substrate hydrolysis at the CAS, rather than producing inhibition of activity by steric hindrance of the entrance of substrate to the gorge.

In orthorhombic crystals, AB1 penetrates deeper into the gorge than in the trigonal crystals, since no H-bond is formed with a symmetry-related copy of the enzyme. In this binding mode, an ESDDM does not reveal any movements of the backbone. However, the side chains of two important residues, His440 and Phe330, undergo major conformational changes (Fig. 2C and 3). The movement of His440 could be clearly ascribed to the presence of 10% EtOH in the soaking solution, and is discussed below. The movement of Phe330 is directly caused by the binding of AB1, and its phenyl ring assumes a conformation similar to that observed when thiocholine or a non-hydrolysable substrate analogue is trapped within the CAS [Colletier 2006a]. This movement of Phe330 may be associated with the allosteric effect of binding of a ligand at the PAS on catalysis that has been observed in kinetic studies [Brochier 2001; Radic 2001; Rosenberry 2008; Stojan 2004].

The binding mode of AB1 in the orthorhombic crystal form can be compared to that of ThT, the only PAS inhibitor for which the crystal structure of a complex with *Tc*AChE has been reported so far, the crystals being trigonal with a $P3_221$ space group [Harel 2008]. ThT and aflatoxin both stack against Trp279, but the stacking is not strictly parallel, and in the case of AB1 the ligand does not completely lie over the indole ring. While both ligands share the same non-bonding interactions (with Tyr70, Tyr121, Phe330 and Tyr334), the corresponding distances are smaller for AB1 than for ThT. The latter penetrates deeper into the gorge than AB1. Thus ThT C16 and AB1 CAD are 5.3 and 7.3 Å, respectively, from Trp84Cβ. The rotation of Phe330 observed upon binding of AB1 in the orthorhombic crystals does not occur, for steric reasons, upon binding of ThT [Harel 2008]. It is worth noting that AB1 is fluorescent [Dall'asta 2003], and could thus be employed, similarly to ThT, as a fluorescent reporter of binding at the CAS [Harel 2008; Rosenberry 2008]. Furthermore, it could be employed for probing the dynamics of the PAS by fluorescence spectroscopy [Weik 2004].

Disruption of the catalytic triad by EtOH

The AB1/*Tc*AChE complex in the orthorhombic form (AEO), but not in the trigonal form (AET), undergoes a conformational change in the side chain of His440 that results in breakage of both hydrogen bonds (Ser200Oγ-His440Nε2, His440Nδ1-Glu327Oε1) within the catalytic triad (Fig. 3 and table 2). A control experiment, in which orthorhombic

crystals were soaked in crystallization medium with the same EtOH content (10%), but devoid of AB1 revealed an alternate position for His440 similar to that observed in the corresponding AB1/*Tc*AChE complex (AEO), although with a lower occupancy (80%). The disruption of the catalytic triad in the orthorhombic AB1/*Tc*AChE complex can thus clearly be ascribed to the presence the EtOH used to solubilize the inhibitor. The catalytic histidine in AChE has been observed earlier to adopt multiple conformations, *viz.* upon binding organophosphate compounds [Ekstrom 2006a; Millard 1999a], upon interaction with the anti-Alzheimer drug rivastigmine [Bar-On 2002] or as a result of X-ray radiation damage [Weik 2001b]. Movement of the catalytic Ser200 in a complex of *Tc*AChE with a bifunctional inhibitor also led to a broken H-bond within the catalytic triad [Paz 2009].

EtOH has been shown to inhibit AChE competitively (inhibition constant of 1M) [Fekonja 2007]. Inhibition by EtOH has been attributed to the lower ability of substrate to displace EtOH rather than water. Most of the water molecules in the active-site gorge of *Tc*AChE are crystallographically ordered [Koellner 2000], yet no EtOH molecules could be modeled in any of the four *Tc*AChE crystal structures obtained in the presence of 10% EtOH, *viz.,* AEO, EO, AET and ET. The observation of the disruption of the catalytic triad in the presence of EtOH in orthorhombic crystals thus offers an alternate explanation for inhibition by EtOH to that proposed by Fekonja and coworkers [Fekonja 2007].

Studies on the structure of subtilisin Carlsberg in anhydrous acetonitrile [Fitzpatrick 1993] and in anhydrous dioxane [Schmitke 1997] and of acyl-subtilisin in acetonitrile [Schmitke 1998] did not reveal any major conformational changes. Affected residues were located either in flexible loops or remote from the active site [Schmitke 1998]. In the case of *Tc*AChE, EtOH did cause structural changes in the active site, and DMSO did not. Even though a DMSO molecule could be identified in contact with His440 both in the structure of the AB1/*Tc*AChE complex (ADO), and in the absence of AB1 (DO), in both cases, the catalytic triad remained intact.

Crystallographic pitfalls on the way to determining a functionally relevant protein ligand complex

A total of six crystal structures had to be determined before the functionally most relevant mode of binding of AB1 to *Tc*AChE, and the concomitant structural changes in the enzyme could be identified. Three pitfalls became evident, two related to crystal packing, and one to the organic solvent used to solubilize the inhibitor.

The binding mode of AB1 differed in the two crystal forms employed, due to formation of a hydrogen bond of the inhibitor with a symmetry-related copy of the enzyme in the trigonal, but not in the orthorhombic form. A similar interaction with a symmetry-related copy was earlier shown to be responsible for the enantioselectivity of a bifunctional inhibitor interacting with the trigonal crystal form of *Tc*AChE [Haviv 2005]. An influence of crystal packing on ligand binding has also been reported for a pentamer of heat-labile enterotoxin [Minke 2000]. Another effect of crystal packing on ligand binding, and on resulting structural changes, is more difficult to assess structurally, namely the impact on protein flexibility, dynamics and conformational heterogeneity.

EtOH was able to disrupt the catalytic triad of *Tc*AChE in the orthorhombic but not in the trigonal crystal form. The crystallographically averaged structure of the enzyme is very similar in both crystal forms. Therefore, we conjecture that differences in crystal packing limit the flexibility of the active site more in the trigonal form than in the orthorhombic form. Similarly, different packing environments for monomers of an oligomeric protein have been put forward as an explanation for different intermediate states being trapped in structurally identical monomers of a dioxygenase [Kovaleva & Lipscomb 2007].

A third pitfall relates to solubilization of the ligand prior to crystallogenesis or crystal soaking. In the case of a water-insoluble ligand such as AB1, an organic solvent must be used. As a consequence, crystallographic conditions may differ greatly from conditions in solution. In the present study, EtOH, but not DMSO, disrupted the catalytic triad, producing a conformational change that could have been erroneously attributed to the binding of AB1. In conclusion, solvent effects should always be properly monitored in appropriate crystallographic control experiments, before assigning conformational changes to the interaction of the ligand, and more than one crystal form should be employed if available.

Acknowledgements**.** We warmly acknowledge fruitful discussions with Jacques-Philippe Colletier throughout the entire course of this study. We are grateful to him and to Colin Jackson for critically reading the manuscript. We are grateful to the ESRF for beam-time under long-term projects MX498, MX609 and MX722 (IBS BAG) and MX551 and MX 666 (radiation-damage BAG) and the ESRF staff for providing efficient help during data collection. Financial support by the CEA, the CNRS and the UJF is acknowledged, as well as a grant to MW from the Agence Nationale de la Recherche (ANR) (project number JC05_45685). This study was supported by the European Commission Sixth

Framework Research and Technological Development Program “SPINE2-COMPLEXES” Project, under contract no. 031220, by a gift from Mr. Erwin Pearl, and by grants from the Benoziyo Center for Neurosciences, the Nalvyco Foundation, the Bruce Rosen Foundation and the Neuman Foundation. J.L.S. is the Morton and Gladys Pickman Professor of Structural Biology.

Table 1: Crystallographic and refinement data.

	AET	*ET*	*AEO*	*EO*	*ADO*	*DO*
PDB entry code						
ESRF beamline	ID14-2	ID29	ID14-2	ID14-1	ID14-1	ID14-4
Temperature (K)	100	100	100	100	100	100
Number of frames	120	120	180	180	180	120
Exposure time (s/frame)	10	1 (transmission 10%)	8	10	3	1
Wavelength (Å)	0.933	1.24	0.933	0.934	0.934	0.940
Space group	$P3_121$	$P3_121$	$P2_12_12_1$	$P2_12_12_1$	$P2_12_12_1$	$P2_12_12_1$
Unit cell parameters (Å)						
a	113.14	112.14	91.75	91.76	91.72	91.16
b	a=b	a=b	107.06	106.67	106.64	105.77
c	137.18	137.89	150.76	150.91	150.63	149.90
Resolution range (Å)[1]	2.40 (2.50-2.40)	2.20 (2.30-2.20)	2.27 (2.35-2.27)	2.25 (2.30-2.25)	2.70 (2.90-2.70)	2.30 (2.40-2.30)
Completeness (%)[1]	99.0 (99.1)	99.2 (98.6)	97.9 (96.9)	99.3 (99.7)	99.4 (99.4)	99.6 (99.4)
R_{sym} (%)[1,2]	8.9 (51.2)	5.9 (52.7)	5.8 (50.8)	10.3 (60.3)	10.9 (53.8)	7.2 (42.6)
$I/\sigma(I)$[1]	17.3 (3.1)	20.9 (4.1)	24.4 (4.3)	15.2 (3.5)	15.9 (3.5)	19.7 (4.9)
Unique reflections[1]	39815 (4529)	51393 (6312)	67841 (6564)	75267 (4917)	41029 (4180)	64705 (7688)
Redundancy	5.5	7.1	7.2	7.4	6.1	7.9
$R_{cryst\ (\%)}$	18.78	20.14	19.61	20.5	19.08	21.01
$R_{free\ (\%)}$	24.58	21.84	24.67	24.1	25.82	24.54
R.m.s.d. bond length (Å)	0.013	0.011	0.011	0.012	0.015	0.013
R.m.s.d. bond angles (degree)	1.518	1.221	1.450	1.472	1.765	1.496
Number of atoms						
Total	4840	4818	9435	9066	8931	8943
Protein	4316	4290	4278	8393	8438	8425
Water	379	435	741	588	329	482
Carbohydrates	28	42	56	56	98	56
Aflatoxin	23		46		46	
B-factor ($Å^2$)						
Global	26.6	37.8	23.1	19.8	22.4	34.1
Protein	24.8	36.0	22.4	19.1	21.7	33.8

Water	28.7	48.1	27.8	22.8	20.0	37.0
Carbohydrates	61.0	75.3	56.2	49.8	61.2	59.0
Aflatoxin	48.0		53.4		74.1	

[1]: values in brackets refer to the highest resolution shell.

[2]: $$R_{sym} = \frac{\sum_{hkl} \sum_{i} \left| I_i(hkl) - \overline{I(hkl)} \right|}{\sum_{hkl} \sum_{i} I_i(hkl)}$$

6.3.3 Bilan

Il existe peu de structures d'AChE avec des inhibiteurs du PAS dans la PDB. Les structures que nous présentons sont les seuls exemples dans le cas de la *Tc*AChE dans les groupes d'espace $P3_121$ et $P2_12_12_1$. Au cours de cette thèse, nous avons ainsi pu explorer structuralement chacune des régions clés de l'AChE : la gorge aromatique, le site actif et le PAS.

Les propriétés de luminescence de l'AB1, et en particulier son caractère phosphorescent, nous ont permis de réaliser l'étude dynamique du PAS présentée ci-après. En réalisant les études structurale et dynamique d'un seul et même système, *i.e.* le couple PAS/AB1, des informations cruciales pour la mise en place d'une expérience de cristallographie cinétique contrôlée par la température peuvent être obtenues.

6.4 L'aflatoxine : un inhibiteur phosphorescent qui suggère un nouveau moyen d'étudier la dynamique des protéines

6.4.1 Présentation de l'article

L'AB1 est phosphorescente. Nous avons mesuré son temps de vie de phosphorescence en fonction de la température dans des complexes cristallins de *Tc*AChE et d'AB1 et dans la solution de trempage qui a permis de les préparer. L'évolution du temps de phosphorescence de l'AB1 diffère selon la nature de l'échantillon. Les fluorophores sont sensibles à leur environnement. Le temps de vie de phosphorescence doit donc dépendre de la nature et de la dynamique de celui-ci. Les résultats exposés dans cet article (en préparation) nous permettent de proposer une nouvelle approche pour étudier la dynamique locale des protéines : la mesure du temps de vie de phosphorescence d'un fluorophore lié à cette protéine. Le temps de vie de phosphorescence de l'AB1 à température cryogénique est de l'ordre de la seconde. Les mouvements de la protéine que nous pouvons sonder avec une telle méthode se produisent donc sur cette échelle de temps : ce sont des mouvements de grande amplitude tels que des mouvements de boucles

ou de domaines. Ainsi, la mesure du temps de vie de phosphorescence de l'AB1 nous a permis d'avoir accès à la dynamique lente du PAS. Nous avons pu mettre en évidence un couplage entre la dynamique du solvant et celle de la protéine, qui se produit à partir de ~170 K : à cette température, les échantillons subissent une transition. Nous suggérons que la transition vitreuse du solvant permet l'augmentation de la flexibilité de la protéine en autorisant des mouvements figés à plus basse température. La formation de glace cristalline massive au-delà de ~ 200 K rend impossible l'exploitation de cette putative transition dynamique de la protéine à ces températures. Toutefois, nos résultats suggèrent que l'intervalle de températures 170 – 200 K peut être utilisé dans des expériences de cristallographie cinétique nécessitant une flexibilité accrue du PAS. Les expériences de cristallographie cinétique auxquelles nous avons participé [Colletier, Royant, Specht, Sanson, Nachon, Masson, Zaccai, Sussman, Goeldner, Silman, Bourgeois & Weik 2007 ; Colletier, Bourgeois, Sanson, Fournier, Sussman, Silman & Weik 2008] (annexes 3 et 4) ont essentiellement permis de sonder la dynamique du site actif. L'expulsion de la choline a été suivie par cristallographie cinétique au moyen d'une choline en cage photoclivable, laquelle se lie à la fois au niveau du CAS et du PAS. Les cartes de densité électronique montrent en effet qu'une fraction des cholines en cage a été expulsée. Une brève excursion à température ambiante concomitamment à la photolyse a toutefois été nécessaire pour le succès de l'expérience. L'expulsion du produit enzymatique de l'AChE a également été l'objet d'une expérience de cristallographie cinétique basée sur la radiolyse d'un analogue de substrat par une intense irradiation X. La radiolyse a été observée lorsque le cristal de *Tc*AChE était soumis à une température de 150 K, mais non à 100 K. Cette expérience souligne ainsi l'importance de connaître une plage de températures à laquelle la protéine est suffisamment flexible pour étudier une réaction enzymatique par cristallographie cinétique. L'objectif principal de l'étude présentée ci-après est précisément de disposer d'un outil permettant de repérer cette température.

6.4.2 Article

Manuscrit en préparation.

Phosphorescence lifetime measurement as a probe for protein structural dynamics

ABSTRACT

Protein structures are animated by a multitude of motions that confer biological activity. Occurring on a broad time scale from femtoseconds to minutes, structural dynamics of proteins are studied by complementary biophysical techniques each sensitive to motions in a narrow time window. Here, we present phosphorescence-lifetime studies as a way to probe protein dynamics on the ms - s time scale. The phosphorescent molecule aflatoxin was employed to probe local dynamics of its binding site in crystals of the target enzyme acetylcholinesterase and in solution. Experiments as a function of temperature revealed changes in both the dynamics of the solvent and the crystalline enzyme at 165 - 170 K, suggesting that both are coupled. Phosphorescence lifetime studies further enlarge the spectroscopic toolbox that assists and complements kinetic crystallography studies by informing about protein motions on the ms - s time scale.

Manuscript in preparation.

INTRODUCTION

Structure, dynamics and activity of biological macromolecules are intimately linked. Functionally important motions occur between conformational substates, the ensemble of which form the conformational landscape of a protein [Frauenfelder 1991]. Studying the structural dynamics of a protein thus involves characterizing the conformational substates that a protein adopts during e.g. a catalytic process and the rates at which these substates are sampled. An ideal method to study structural protein dynamics should yield information both at atomic resolution and on the entire range of timescales relevant to protein dynamics, i.e. from the femtosecond to the second timescales. Laue diffraction of biological macromolecules is a valuable method in this context. It allows investigating structural dynamics from the nanosecond to the millisecond timescale [Bourgeois 2006]. However, it has several drawbacks. Indeed, this method is in most cases based on a pump-probe process and thus requires the studied catalytic process to be photoactivable. Furthermore, crystals employed rarely fulfill the quality criteria that lead to processable diffraction patterns. Another method, nuclear magnetic resonance (NMR), is a method that intrinsically provides both structural and dynamic information [Lindorff-Larsen 2005]. NMR is however often limited to molecules smaller than 30 kDa.

Structural dynamics can also be studied by combining x-ray crystallography with spectroscopic techniques. The trajectory of the catalytic pathway of adenylate kinase was unraveled by the combination of NMR, fluorescence resonance energy transfer (FRET), molecular dynamics and x-ray crystallography [Henzler-Wildman 2007b]. In such an approach, the structures are determined by crystallography and a spectroscopic method is used for probing the dynamics of the protein. The appropriate spectroscopic method is chosen depending on the timescale of the movements to be characterized [Henzler-Wildman 2007a; Henzler-Wildman 2007c]. Kinetic crystallography combined with *in crystallo* spectroscopy [Bourgeois 2005; Bourgeois 2009] can be employed to generate, trap and characterize intermediate-states in crystalline proteins.

Fluorescence lifetime spectroscopy is a technique that can quite easily be performed in order to study protein dynamics and complement kinetic crystallography experiments. If the protein is not intrinsically fluorescent, a fluorescent ligand may serve as a reporter of the protein motions that occur on the timescale of its fluorescence lifetime, i.e. typically

on the nanosecond timescale, which is that of side chain motions. Alternatively, it was proposed to use phosphorescence lifetime as a probe for studying protein dynamics at room temperature [Saviotti & Galley 1974; Vanderkooi 1987]. Measuring the phosphorescence lifetime permits to get insight into structural dynamics on the ms-s timescale, i.e. that of enzyme catalysis and large-scale conformational changes [Henzler-Wildman 2007a]. Information about the dynamics of a protein at such a timescale would thus be beneficial for kinetic crystallography experiments. Tryptophan phosphorescence lifetime was used for probing the dynamics of some proteins [D'Auria 2008]. However, proteins may have none or too many tryptophans. Furthermore, although phosphorescence lifetime spectroscopy is easy to be measured, it has not been used extensively on proteins because phosphorescence is quenched by oxygen at room temperature [Lakowicz 2006]. Nevertheless, at the cryo-temperatures used in temperature-controlled kinetic crystallography, oxygen does not diffuse. Thus, phosphorescence lifetime spectroscopy can be envisaged.

Acetylcholinesterase has been the subject of a great number of structural dynamics experiments [Boyd 2000; Epstein 1979; Rosenberry 2008; Taylor 1975]. It hydrolyzes the neurotransmitter acetylcholine at a rate of several thousand molecules per second [Silman 2005]. Hence, knowledge of its structural dynamics and insight into how Nature managed to fine-tune its molecular motions are of importance for understanding its functioning. AChE has its active site at the bottom of a deep and narrow gorge [Sussman 1991]. At the opening of the latter lies a so-called peripheral anionic site (PAS), which is believed to guide substrates *en route* to the active site [Colletier 2006a]. Even though its constitutive residues have been identified, the role of the PAS is not fully understood. Structures of AChE in complex with several PAS inhibitors have been solved recently [Bourne 2003; Colletier 2006b; Harel 2008; Rydberg 2006].

Aflatoxin B1 (AB1) is a reversible PAS inhibitor of AChE that not only hinders the traffic of substrates and products, but may also allosterically alter its catalytic efficiency [Hansmann 2009]. AB1 is phosphorescent, a property that has been used for its detection in culture media at room temperature [Rojas-Duran 2007]. AB1 is thus of particular interest for obtaining insight into the dynamics of the PAS. The structure of the complex of *Torpedo californica* (*Tc*) AChE with AB1 was solved in two crystal forms, revealing two distinct binding modes [Sanson]. The complex in the orthorhombic space group $P2_12_12_1$ is most likely the functionally relevant form, while the binding mode observed in

the trigonal space group $P3_121$ occurs through an interaction with a symmetry-related copy of the enzyme (Fig. 1).

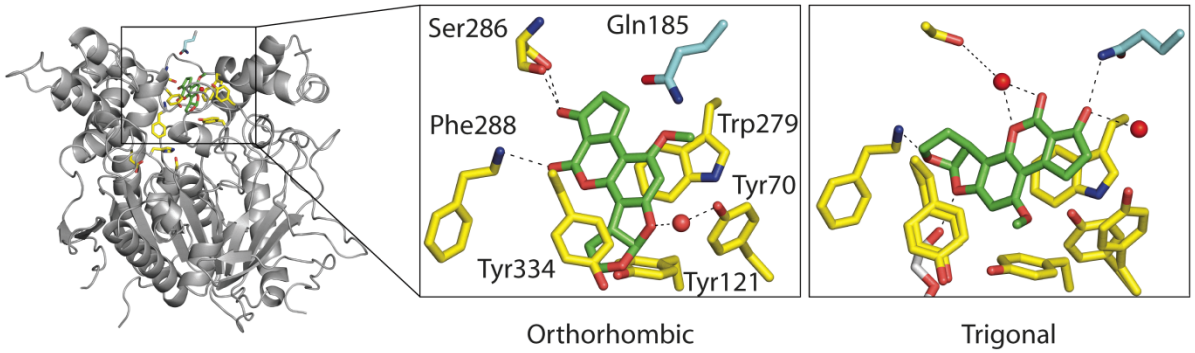

Figure 1. Overview of the TcAChE/AB1 complex and close-up view of the PAS in the orthorhombic space group (upper box) and trigonal space group (lower box). AB1, PAS residues Tyr70, Tyr121, Trp279, Ser286, Phe288 and Tyr334, the catalytic triad (Ser200, Glu327 and His440), Gln185 from a symmetry-related molecule and a PEG molecule are displayed as stick models. AB1, residues of the PAS and the catalytic triad, Gln185 and the PEG molecule have carbon atoms in green, yellow, cyan and gray respectively. Oxygen and nitrogen atoms are in red and blue, respectively. Water molecules are displayed as red balls. Hydrogen bonds are represented by black dashed lines.

In the present study, we have used AB1 as a spectroscopic probe and measured its phosphorescence lifetime as a function of temperature in complex with crystalline *Tc*AChE and in the corresponding soaking solution. The phosphorescence lifetime and its cryo-temperature dependence were found to depend on the environment. Solvent glass transitions and protein dynamical transition were observed through characteristic changes in the temperature-dependence of the phosphorescence lifetime. Our results lend expectations on the study of slow dynamics (ms-s timescale) in proteins.

MATERIALS AND METHODS

Chemicals.

Aflatoxin B1 (AB1, scheme 1), polyethyleneglycol (PEG) 200, morpholinoethylsulfonic acid (MES), ethanol (EtOH) and dimethysulfoxide (DMSO) were purchased from Sigma Chemical Co. (St Louis, MO, USA). AB1 was solubilized at its saturation concentration (estimated at approximately 1mM) in pure EtOH.

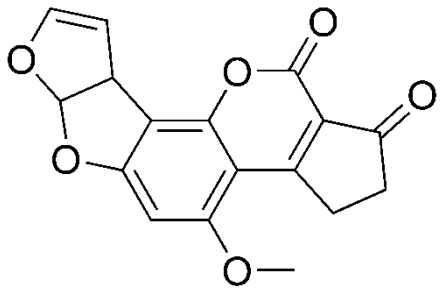

Scheme 1. Structure of AB1.

Sample preparation

*Tc*AChE enzyme (MW 65000) was purified as described previously [Sussman 1991]. Trigonal (space group $P3_121$) and orthorhombic (space group $P2_12_12_1$) crystals of *Tc*AChE were grown at 4°C in hanging drops using the vapor diffusion method in 32-34% (v/v) PEG200, 150 mM MES at pH 5.6-6.0. These crystals contain 68% and 59% (v/v) solvent, respectively. They were soaked for times ranging from 12 h to 6 months in 36% (v/v) PEG 200, 0.15 M MES pH 5.8, 10% ethanol, and 0.1 mM aflatoxin (referred to as *the soaking solution*). Subsequently, they were transferred for ~30 s into a drop (3 μl) of the soaking solution devoid of both ethanol and aflatoxin (referred to as *the wash solution*) and flash-cooled to 100 K using a cryoloop (Hampton Research, Laguna Niguel, CA) in the cryostream of a cooling device (Oxford Cryosystems, Oxford, UK). Transfer to the wash solution allowed removal of aflatoxin from the solvent surrounding crystals of *Tc*AChE.

Thin films of the soaking solution and of a solution of *Tc*AChE (11.5 mg.ml^{-1}, i.e. 175 μM) were flash-cooled to 100 K in 0.2 μm*0.3 μm cryoloops. The soaking solution was taken from drops from which crystals were fished.

Data Acquisiton

Data acquisition was performed at the Cryobench laboratory (ESRF, Grenoble, France) [Bourgeois 2002].

The phosphorescence decay of aflatoxin was recorded as a function of temperature from 100 up to 240 K. The temperature was adjusted through a Labview-based graphical interface (National Instruments, Austin, TX). The staircase temperature profile was set to alternate increases by 5 K at a rate of 360 K/h and plateaus, approximately 1 minute long, during which were recorded the phosphorescence decays. The duration of a temperature ramp experiment was approximately 75 minutes.

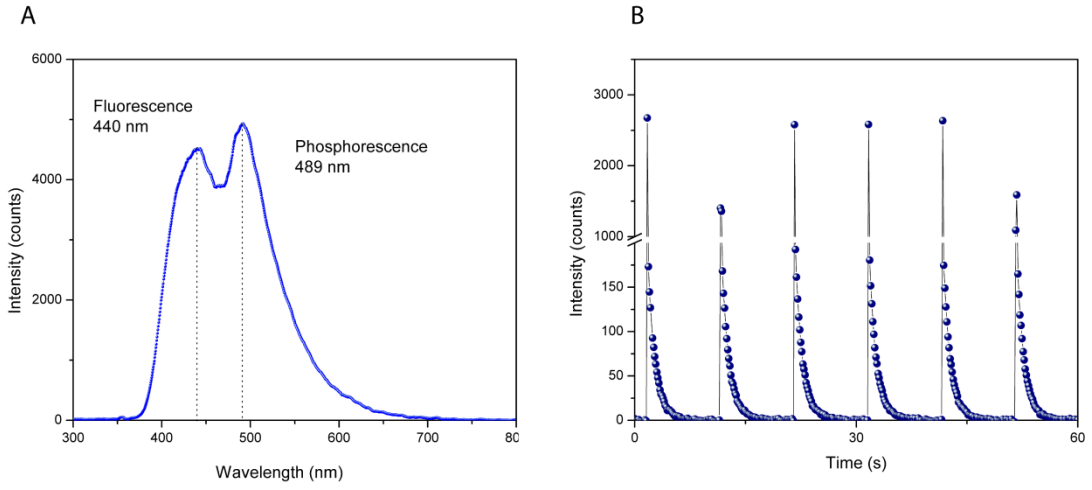

Figure 2. Emission spectrum of aflatoxin B1 bound to the peripheral site of orthorhombic TcAChE (a) and typical acquisition plot and fit of the phosphorescence data (b). After excitation of the sample by a 355 nm laser, the phosphorescence intensity is followed at 489 nm. Several (at least six) decays are measured. The decays are then fitted with a monoexponential function.

Phosphorescence excitation was provided by a 355 nm JDS Uniphase laser. The output power of the laser was measured to be ~2.5 mW. Short excitation pulses (10–30 ms) were

delivered at a frequency of 0.1 Hz. The duration of the pulses was chosen so as to minimize photobleaching. It is noteworthy that pulses longer than 30 ms did not yield greater intensities, thereby suggesting that the amount of excitable fluorophores is saturated within this timeframe. Phosphorescence emission spectra were collected at 90° with a CCD-based microspectrophotometer dedicated to the study of protein crystals at cryo-temperatures [Bourgeois 2002]. A 375 nm longpass filter was used so as to protect the CCD from repetitive exposure to the intense laser light. No significant shift in the phosphorescence emission spectrum was observed as a function of temperature. The phosphorescence was therefore followed at 489 nm (Fig. 2a) throughout the temperature ramp. At least 6 decays were collected at every temperature plateau (Fig. 2b). The spectrophotometer was set to record the phosphorescence intensity every 140 ms in most experiments. The choice of the acquisition time was a compromise between intensity and the number of data points.

The experiment was performed on soluble *Tc*AChE in complex with AB1 only once at 100 K.

Size of the samples

Soluble samples were approximately 1 nL in volume. Trigonal crystals were approximately 10 nL. Orthorhombic crystals were approximately 5 nL in volume and as they grow as thin plates it was rather difficult to estimate their thickness.

The size of the crystals did not have much effect on the intensity of the phosphorescence of AB1. The spot of the laser on the sample is approximately a circle of 50 μm in diameter. All dimensions of the crystalline samples, but the thickness of orthorhombic crystals, were bigger than 50 μm. Thus the volume illuminated depended only on the path length of the laser light through the crystal. No absorption of the exciting light and re-absorption of the emitted light (inner filter effect) were observed. The significantly weaker phosphorescence intensity in solution samples was due to their small volume.

Orientation of the samples

The orientation of crystalline samples is an important factor that can affect the intensity of the measured phosphorescence. The crystal orientation leading to the maximum

phosphorescence intensity was determined and then kept constant during the course of the temperature-derivative experiment.

Data processing

The data were automatically processed with an in-house python script. First, all decays were identified. At each temperature, the first decay was fitted by a monoexponential function using Gnuplot. All the decays were then superposed. Subsequently, the newly generated set of points was fitted and yielded both the lifetime and an estimate of the experimental error (chi2 test).

Phosphorescence data from six, three and three individual temperature ramps were averaged for experiments performed in orthorhombic crystals, trigonal crystals and in the soaking solution, respectively. Linear regression was then performed in order to determine the slopes of the linear temperature domains of the evolution of the phosphorescence lifetime. The sets of points used in the regression calculation were chosen so that they yielded the highest correlation coefficient.

RESULTS

The phosphorescence of AB1 at cryo-temperatures was serendipitously observed in a crystal of *Tc*AChE in complex with the inhibitor (Fig. 3). The phosphorescence lifetime of AB1 was in the ms-s timescale at temperatures between 100 and 240 K and could be easily measured at the Cryobench.

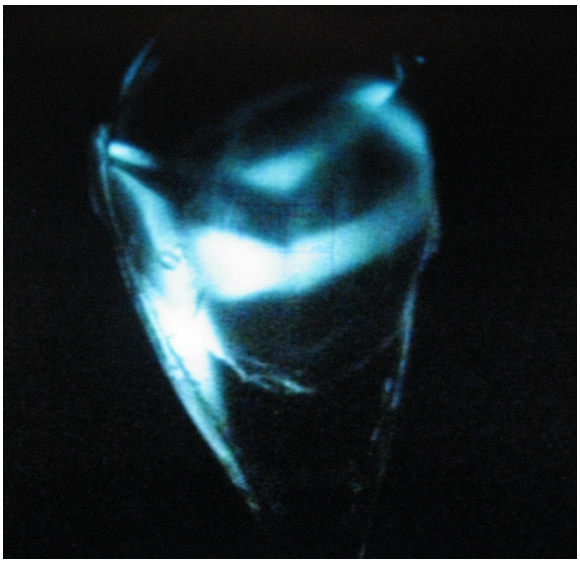

Figure 3. Photograph of a trigonal crystal of TcAChE in complex with AB1 during the phosphorescence decay (after excitation by a 355 nm laser).

Phosphorescence lifetime of AB1 at 100 K

The phosphorescence lifetime of AB1 was measured at 100 K in complexes of *Tc*AChE with AB1, in solution and *in crystallo* (in both the trigonal and orthorhombic space groups), and in the soaking solution from which the *Tc*AChE/AB1 complexes were formed. The values are reported in table 1.

The phosphorescence intensities of AB1 complexed to soluble *Tc*AChE were significantly weaker than those of AB1 complexed to crystalline *Tc*AChE. Thus, the statistical error was significantly higher in the former than in the latter.

Sample	Phosphorescence lifetime of AB1 (s)	Size of the sample (nL)	Concentration in AB1 (mM)	Phosphorescence intensity (counts per 140 ms)	Chi2 of the lifetime (%)
Soluble *Tc*AChE	1.32	<1	0.17	~50	8
Trigonal *Tc*AChE	0.94	10	6.7	80-350	<1
Orthorhombic *Tc*AChE	1.22	5	9.4	50-300	1
Soaking solution	1.07	<1	0.10	30-60	1-2

Table 1. Phosphorescence lifetime of AB1 at 100K.

The longest lifetime was measured in soluble *Tc*AChE (1.3 s). It was close to that measured in orthorhombic crystals (1.2 s). The shortest lifetime is that measured in trigonal crystals (0.9 s). The lifetime in the soaking solution was 1.1 s.

Phosphorescence lifetime of AB1 as a function of temperature

The phosphorescence lifetime of AB1 was measured as a function of temperature in two forms of crystalline *Tc*AChE, and in the soaking solution.

a) In orthorhombic *Tc*AChE.

Figure 4a shows three independent experiments performed on three orthorhombic crystals soaked in identical solutions of AB1. We note no large dispersion of the lifetime. Two linear temperature domains are identifiable. The high temperature domain (170 – 205 K) shows a higher rate of decrease in phosphorescence lifetime than the low temperature domain (100 – 170 K). Crystalline ice was visualized in samples above 205 K and was associated to lower intensities of phosphorescence, hence greater errors. Averaging the measurements of the phosphorescence of several repetitions of the experiment allowed estimating that the transition between the two domains occurs at ~170 K (Fig. 5). The 100-170 K domain may be composed of two domains with a transition at ~120 K.

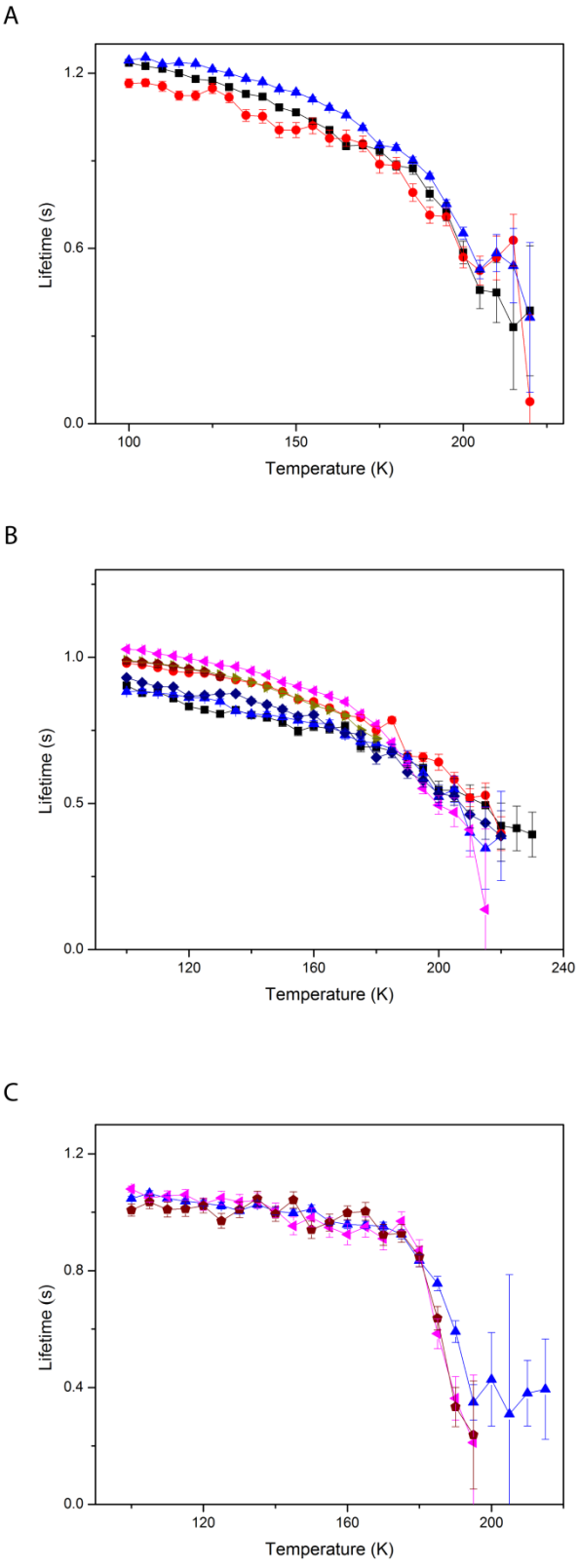

Figure 4. Evolution of the phosphorescence lifetime of AB1 as a function of temperature in complex with TcAChE in orthorhombic crystals (a), trigonal crystals (b) and in the soaking solution (c).

b) In trigonal *Tc*AChE.

The same measurements on trigonal crystals yielded a more disperse, yet similar, evolution (Fig. 4b). The transition is again estimated to occur at ~170 K (Fig. 5). However, we note major differences with respect to the evolution of the phosphorescence lifetime in orthorhombic crystals. The slopes of the linear temperature domains are smaller in trigonal than in orthorhombic crystals.

c) In the soaking solution.

The evolution of the phosphorescence lifetime in the soaking solution yields a sharper transition (Fig. 4c) that is estimated to occur at ~165 K (Fig. 5). Again, the evolution is linear below and above the transition temperature. Below the transition, the lifetime is less sensitive to temperature changes than in any crystalline sample. Above the transition, on the contrary, the slope of the curve is much accentuated, thereby indicating high sensitivity to temperature increase.

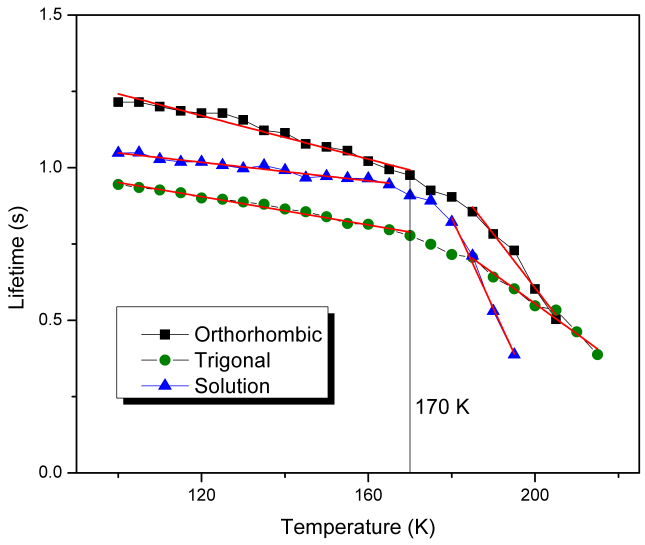

Figure 5. Average phosphorescence lifetime of AB1 as a function of temperature in the soaking solution (blue triangles) and in complex with TcAChE in trigonal (green circles) and orthorhombic (black squares) crystals. Calculation of averages was performed with at least three data sets. For each curve, two linear domains were identified and fitted to a line through a linear regression process. The slopes of the low-temperature domains in solution, and in trigonal and orthorhombic TcAChE were -0.0015, -0.0023 and -0.0036 s.K^{-1}, respectively. The slopes of the high-temperature domains in solution, and in trigonal and orthorhombic TcAChE were -0.0030, -0.0010 and -0.0018 s.K^{-1}, respectively.

Arrhenius plots of the averaged phosphorescence data were calculated (Fig. 6). The plots show that the decrease of the lifetime with temperature does not follow an Arrhenius law. Though two linear temperature domains can be identified, the transitions in the decrease of the lifetime is not as clear as in figure 4.

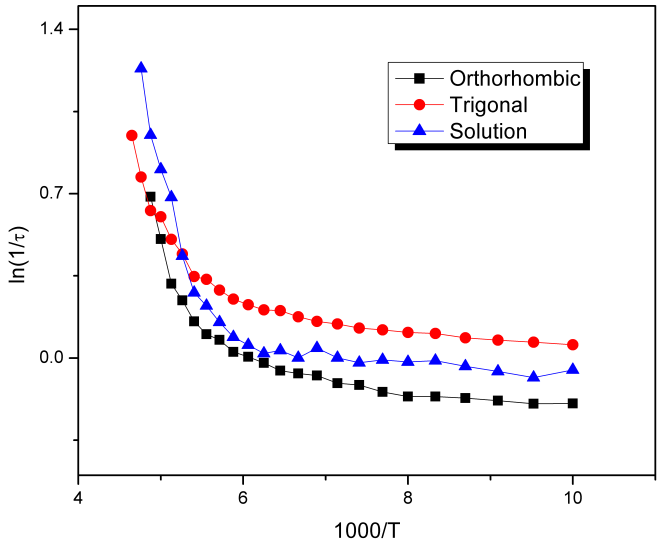

Figure 6. Arrhenius plot of the phosphorescence lifetime of AB1 as a function of temperature in solution (blue triangles) and bound to trigonal (red circles) and orthorhombic (black squares) TcAChE.

The temperature-derivative experiment was not performed in *Tc*AChE/AB1 complexes in solution because those samples yielded too weak phosphorescence intensities.

A great number of parameters are likely to affect the phosphorescence lifetime of AB1. Identifying them and examining their effect on the phosphorescence lifetime of AB1 was not the objective of our study. Hence we kept constant as many parameters as possible. We have performed measurements after various soaking times, which show no clear effect on the phosphorescence lifetime of AB1 and its evolution as a function of temperature (not shown).

DISCUSSION

The phosphorescence of AB1 was measured as a function of temperature in solution and in complex with *Tc*AChE in orthorhombic and trigonal crystal forms. In each type of sample, the phosphorescence lifetime was shown to decrease with increasing temperature. Transitions in the evolution of the lifetime were found in all types of samples. Although no significant differences in the transition temperatures were observed, the temperature domains so defined show differential rates of phosphorescence decrease with temperature. The phosphorescence lifetime of AB1 in complex with soluble *Tc*AChE was measured only at 100 K and was longer than in any other sample.

Localization of AB1 in TcAChE crystals

An important issue is to know whether the phosphorescence in crystalline samples was that of AB1 bound at the PAS of *Tc*AChE or in the solvent channels of the crystals. It is unlikely that the phosphorescence measured in crystalline samples originates from AB1 in the solvent channels because the concentration of AB1 in crystals (that of *Tc*AChE) is larger than that in solution by at least a factor of 100. Furthermore, the crystals were washed in solutions free of AB1 before every measurement. The concentration ratio of AB1 bound to *Tc*AChE and in the solvent channels was thus increased.

Effect of the environment on the phosphorescence lifetime of AB1

In all four samples at 100 K, the phosphorescence lifetime of AB1 is comprised between 0.9 and 1.3 s. These values are in agreement with those of a previous study, in which the phosphorescence lifetime of AB1 in complex with DNA and in solution (both in 50% ethylene glycol) was measured to be 1.27 s at 77 K in both cases [Neely 1970].

The phosphorescence lifetime at 100 K of AB1 in complex with soluble *Tc*AChE (1.3 s) is closer to that of AB1 in complex with *Tc*AChE in the orthorhombic crystal form (1.2 s) than that in complex with *Tc*AChE in the trigonal crystal form (0.9 s). The environment of AB1 may thus be similar in soluble *Tc*AChE and in the orthorhombic crystal form of the enzyme, which supports the hypothesis that the biologically relevant binding mode of

AB1 is that seen in the orthorhombic crystal form (Sanson *et al,* manuscript submitted). The smaller lifetime in the trigonal crystal form may be explained by partial quenching of the phosphorescence by the π-stacking interaction with Trp279.

Coupling of solvent and enzyme dynamics

Transitions in the evolution of the phosphorescence lifetime of AB1 as a function of temperature were identified in *Tc*AChE crystals and in the soaking solution. Not only are the transition temperatures close to each other, but also the overall behavior of the lifetime as a function of temperature is similar in all three samples. Therefore, the evolution of the lifetime in solution may be intrinsic to AB1 and may be modulated by the nature and dynamics of its environment. Differences in the slopes of the decrease of phosphorescence lifetime as a function of temperature were observed. The differences in the lifetime evolution *in crystallo* with respect to that in solution may yield information about the dynamics of the crystalline enzyme.

The lowest transition temperature of the phosphorescence lifetime of AB1 is in the soaking solution (165 K). The transitions in trigonal and orthorhombic crystals have both been estimated to occur at 170 K. If the 5 K shift in the transition is significant, it stems either from the crystalline nature of the sample or from binding to *Tc*AChE. The measurement of the phosphorescence lifetime of AB1 in soluble *Tc*AChE/AB1 complexes would help addressing the origin of the shift, which was hampered by the weak phosphorescence signal.

Transition temperatures define two linear temperature domains. Below the transition, slopes are small. In the soaking solution, it is almost zero. The smaller rate of decrease of the phosphorescence lifetime of AB1 in solution with regard to that in crystalline samples before the transition suggests that the environment of AB1 in the protein gains flexibility at a higher rate than in the solution. Indeed, at temperatures around 100 K, solutions are amorphous and thus rigid, whereas the PAS environment of AB1 in the crystalline enzyme may gain already flexibility upon raising the temperature.

Above the transition, the slope of the lifetime decrease in solution is larger than in any crystal form. The solution thus gains flexibility at a higher rate than *Tc*AChE in any crystal form above 170 K. As a consequence, the transition in the evolution of the lifetime

of AB1 in solution is likely to reflect the glass transition of the solution at ~170 K. Then, coupling between the dynamics of solvent and that of the protein may occur. The flexibility of the solution may induce a dynamic transition in the protein, which in turn could allow the release of certain protein motions. Molecular dynamics simulations on carboxy myoglobin showed that solvent mobility allows protein atomic fluctuations above 180 K and that below this temperature protein motions are decoupled from those of the solvent [Vitkup 2000].

The experiment performed in solution provides information about the phosphorescence lifetime of AB1 in bulk solvent. However, it is not obvious if the phosphorescence lifetime of AB1 behaves similarly in the solvent channels of *Tc*AChE crystals. Indeed, solvent channels may not be bulk-like, due to the confinement imposed by the crystal packing of *Tc*AChE crystals.

Differential flexibility of the PAS in trigonal and orthorhombic crystals

The slopes of the decrease of the phosphorescence lifetime of AB1 are larger in orthorhombic crystals than in trigonal crystals in both temperature domains. Thus, the PAS in the orthorhombic crystal form gains more flexibility than in the trigonal crystal form, below and above the transition.

Below the transition, the flexibility of the PAS in the orthorhombic form may be intrinsically larger than that in the trigonal form, thereby suggesting that the crystal packing modulates flexibility of the PAS at cryo-temperatures. The crystal packing may constrain *Tc*AChE so that the two domains constituting *Tc*AChE [Morel 1999] are more rigid in the trigonal enzyme than in the orthorhombic enzyme.

Above the transition, *i.e.* after the coupling of solvent and enzyme dynamics occurred, the rate of decrease of the phosphorescence lifetime of AB1 in orthorhombic crystals is again larger than that in trigonal crystals. The difference may originate from differential coupling of solvent and enzyme dynamics in the two crystal forms. With regard to the size of the solvent channels, which are larger in trigonal than in orthorhombic *Tc*AChE crystals, it could have been anticipated that the less congested packing of trigonal *Tc*AChE would have yielded the lifetime closest to that of AB1 complexed to *Tc*AChE in solution. However, the PAS is more solvent accessible in orthorhombic *Tc*AChE. The

crystal packing of trigonal *Tc*AChE brings a symmetry-related enzyme close to the PAS, one residue of which makes a hydrogen-bond with AB1 (Sanson *et al.*, manuscript submitted). Thus, AB1 is surrounded by more solvent in orthorhombic than in trigonal crystals. Collisional quenching of the phosphorescence of AB1 [Lakowicz 2006] is therefore likely to be more effective in orthorhombic crystals of *Tc*AChE than in trigonal ones. Furthermore, the binding mode of AB1 may be crucial. Indeed, AB1 is mainly linked through hydrogen bonds to the PAS in orthorhombic crystals, whereas in the trigonal form the interaction is essentially through a π-stacking with Trp279. Thus, hydrogen bonds may be a better medium for communicating the flexibility of the solvent to the enzyme.

Below 170 K, the lifetime in solution has intermediary values between that of AB1 in complex with *Tc*AChE in trigonal and orthorhombic crystals. Just below the transition temperature, the behavior of the lifetime in orthorhombic crystals approaches that in solution, which supports the hypothesis of a better coupling of solvent and enzyme dynamics in the orthorhombic than in the trigonal form.

Our results suggest that the PAS of *Tc*AChE in orthorhombic crystals is more flexible than that in trigonal *crystals*. The higher flexibility of orthorhombic crystals was observed already. Indeed, kinetic crystallography experiments were performed successfully on orthorhombic *Tc*AChE crystals [Colletier 2007; Colletier 2008]. The expulsion of the photolabile cage and of the arsenocholine from the gorge has been seen in orthorhombic [Colletier 2007] but not in trigonal *Tc*AChE crystals (J.P. Colletier, personal communication).

The omega loop is one of the most dynamic regions of *Tc*AChE and part of it belongs to the PAS [Boyd 2004; Bui 2008; Shi 2003]. Hence, the dynamics probed in our experiments on crystalline *Tc*AChE may be that of the omega loop. Performing phosphorescence lifetime spectroscopy on another enzyme featuring a mobile loop may support this hypothesis. Lactate dehydrogenase has a mobile gating loop [Abad-Zapatero 1987]. Provided that a phosphorescent ligand that binds to the loop is found, phosphorescence lifetime spectroscopy may provide insight into the dynamics of the loop, thereby supporting the validity of the method proposed in the present study.

Glass transition of the solvent and dynamic transition of crystalline TcAChE

We have found a transition at 170 K in both crystalline samples. However, a temperature of 155 K has been employed in crystallographic experiments involving *Tc*AChE, in order to increase protein flexibility at cryo-temperatures so that radicals produced by x-ray irradiation [Weik 2001b] and cleavage of a ligand [Colletier 2008] occur at these non-functional temperatures. It had indeed been shown that crystalline-ice formation starts in *Tc*AChE crystals at 155 K [Weik 2001a]. Hence, as we already pointed out, the glass transition of the solvent is expected to increase its flexibility. Also, it was suggested that the glass transition occurs in crystals having large solvent channels [Weik 2001a]. Therefore, as trigonal crystals of *Tc*AChE have larger solvent channels than orthorhombic ones, it was expected that the flexibility of the PAS is greater in the former. However, our results tend to confirm, on the contrary, that *Tc*AChE *is* more flexible in the orthorhombic crystal form than in the trigonal one at cryo-temperatures.

Neutron scattering revealed a dynamic transition in *Tc*AChE at 220 K [Gabel 2009]. The corresponding timescale probed is different (ps-ns) and the probed dynamics is global (averaged over the entire enzyme).

Experiments of temperature-derivative fluorescence microspectrophotometry (TDFM) on a trigonal *Tc*AChE/fluorescein complex and on a solution of fluorescein revealed transitions that occur at 151 K and 158 K, respectively [Weik 2004]. It had been proposed that the signal measured in the trigonal *Tc*AChE/fluorescein complex came from fluorescein in solvent channels. The authors also pointed out that the temperatures of the glass transition determined in all crystals used in the experiment varied between 151 K and 164 K. Hence, our results and TDFM experiments show that the glass transition occurs between 160 and 170 K on the ns and s timescales.

The discrepancy between repetitions of all temperature-derivative measurements may stem from the flash-cooling process. Not only crystals had variable sizes, but also the procedure of flash-cooling is manual. Hence, crystalline samples may have not vitrified identically.

A complementary tool for kinetic crystallography

A temperature-controlled kinetic crystallography experiment can be performed successfully only if the protein has enough flexibility to allow for the movements required by the studied dynamical event, e.g. the expulsion of an enzymatic product. At cryogenic temperatures, the adequate temperature range is expected to be that corresponding to the dynamic transition of the protein. Kinetic crystallography experiments on the PAS of crystalline *Tc*AChE should then be performed in temperature ranges where the protein has gained enough flexibility, i.e. between 170 K, the dynamic transition temperature of the PAS, and 200 K, the beginning of massive crystalline-ice formation in the solvent channels.

Determining the dynamic transition of a protein can be achieved by lifetime spectroscopy. The timescale of motions probed with lifetime spectroscopy is that of the lifetime of the fluorophore. The method presented here, performed with a luminescent ligand having the appropriate phosphorescence lifetime allows probing protein motions relevant in the dynamic transition. It could thus be complementary to kinetic crystallography. Furthermore, measurement of the phosphorescence lifetime extends the range of timescales offered by microspectrophotometric methods such as Raman, fluorescence and absorption spectroscopy towards longer timescales. Microspectrophotometry could be employed to explore the full range of functionally-relevant motions of enzymes. The combination of a fluorescent and a phosphorescent probe (which may be a unique molecule) may allow probing both slow (ms) and fast (ns) dynamics of a protein.

Acknowledgements**.** We are grateful to Joel L. Sussman for providing us with *Tc*AChE, Dominique Bourgeois and Philippe Carpentier for their experimental assistance and Jacques-Philippe Colletier for fruitful discussions.

6.4.3 Bilan

Cette approche spectroscopique constitue le pendant dynamique de l'article présenté dans la partie précédente, et le volet dynamique principal de la thèse. Sur la base des structures des complexes de *Tc*AChE, nous avions une connaissance précise de la sonde et de son environnement, c'est à dire quelle partie de l'enzyme nous avons sondée. Une fenêtre de températures à l'intérieur de laquelle les expériences de cristallographie cinétique sont possibles a pu être précisée. Nous avons également observé que le PAS est plus flexible dans les cristaux de *Tc*AChE orthorhombiques que dans la forme trigonale. Nous avons ainsi à notre disposition une méthode spectroscopique complémentaire à une expérience de cristallographie cinétique contrôlée par la température. Les perspectives envisagées pour faire suite à ces travaux seront présentées dans la partie suivante.

7. DISCUSSION GÉNÉRALE,

CONCLUSION & PERSPECTIVES

7. DISCUSSION GÉNÉRALE, CONCLUSION & PERSPECTIVES

Les structures de la *Tc*AChE en complexe avec des molécules putativement anti-Alzheimer ont été résolues. La liaison du NF595 et celle du NF766 s'accompagnent de changements conformationnels de grande ampleur au niveau du PAS. Or, la deuxième génération de médicaments anti-Alzheimer s'appuie, en sus d'un site de liaison dans le CAS qui vise à inhiber l'hydrolyse de l'acétylcholine, sur un site de fixation au niveau du PAS afin d'inhiber la formation de fibres Aβ. La flexibilité du PAS doit donc être prise en compte dans la conception d'un médicament remplissant efficacement ces deux rôles. Elle a été mise en évidence par dynamique moléculaire et par comparaison de différentes structures de *Tc*AChE en complexe avec différents ligands [Xu 2008b; Xu 2008c]. L'ensemble des conformations minoritaires constitue un répertoire de modes de liaison possibles pour un ligand. Parmi les méthodes utilisées en routine dans les étapes de la conception d'un médicament, l'amarrage moléculaire (*molecular docking*) permet de prédire le mode de liaison de molécules sélectionnées à partir d'une bibliothèque de molécules à tester. Il existe aujourd'hui des techniques dites de *flexible docking* qui tiennent compte de la flexibilité d'une protéine. Toutefois, les changements conformationnels d'une amplitude comparable à celle du Trp279 dans les structures de la *Tc*AChE avec le NF595 et le NF766 sont rarement pris en compte par les logiciels de *docking* et sont difficiles à prévoir [B-Rao 2009].

Les structures des complexes de *Tc*AChE avec le NF766 et le NF1056 ont révélé deux sites de liaison inédits : à mi-hauteur de la gorge et sur la surface de l'enzyme au pourtour du PAS, respectivement. Il est raisonnable d'imaginer que l'étendue de la surface d'interaction entre la *Tc*AChE et le NF1056 au niveau du PAS soit à même de permettre *in vivo* l'inhibition de la promotion de la fibrillation d'Aβ ; l'inhibition est effective *in vitro* (G. Campiani, communication personnelle). Bien que de nombreuses étapes restent à franchir avant une éventuelle mise sur le marché, cette molécule ou un dérivé pourrait bien devenir le nouveau fer de lance de la lutte contre la MA.

Les états réactionnels du vieillissement de la *Tc*AChE inhibée par le soman ont été caractérisés structuralement [Sanson 2009]. Alors qu'un mélange racémique des quatre stéréoisomères du soman ($P_{R/S}C_{R/S}$) a été utilisé lors de la procédure de trempage, il s'est avéré que la *Tc*AChE sélectionne uniquement la forme P_SC_R. Les études cinétiques avaient mis en évidence une faible discrimination en faveur des énantiomères P_SC_S. La sélection de l'énantiomère P_SC_R résulte soit de l'effet de l'empilement cristallin, soit d'un réarrangement de l'énantiomère P_SC_S en P_SC_R. Cette incertitude pourrait être aisément levée en résolvant la structure des conjugués de la *Tc*AChE avec les énantiomères purs.

Le meilleur modèle expliquant le mécanisme de vieillissement de l'AChE inhibée par le soman, le modèle *push-pull*, a été essentiellement confirmé. Dans ce modèle, Glu199 et Trp84 « poussent » les électrons du soman alors que l'His440 les « tire ». Cette double action aboutit à la déplétion en électrons puis à la rupture de la liaison O-C (qui lie le groupement phosphonyl du soman à son groupement pinacolyl). La structure du conjugué non-vieilli soutient cette vision du processus. Toutefois, les détails de ce modèle ont été nuancés. Nous avons mis en évidence la possibilité de l'intervention d'une molécule d'eau très conservée dans la polarisation de la liaison O-C. En outre, nous avons effectué un affinement alternatif de la structure non-vieillie dans lequel nous avons laissé plus de liberté géométrique au soman. Cet affinement montre un allongement de la liaison O-C de ~0.3 Å. Ainsi, la liaison O-C pourrait être fragilisée dès la première étape de l'inhibition de l'AChE par le soman. Pour expliquer l'allongement de la liaison, nous avons testé toutes les possibilités envisageables, c'est à dire un mélange des énantiomères $P_SC_{R/S}$, une superposition du soman non déalkylé et du soman déalkylé avec les différents produits du vieillissement retenus au niveau du Trp84. Compte tenu de la résolution de la structure (1.9 Å), nous pensons que l'allongement de cette liaison est réel. L'observation de cette liaison allongée illustre la grande efficacité catalytique de l'AChE, même si la machinerie aboutit dans ce cas à une inhibition irréversible. La rapidité du vieillissement de la *Tc*AChE inhibée par le soman est ainsi plus compréhensible. Le modèle *push-pull* est, de plus, parfaitement compatible avec cette observation dans la mesure où ce sont les résidus précédemment cités qui sont susceptibles d'occasionner l'allongement de la liaison O-C. Les structures des conjugués de la *Tc*AChE avec les énantiomères purs de soman seront utiles pour prouver l'allongement de la liaison O-C.

Des expériences de spectrométrie de masse ont récemment révélé l'existence d'un état réactionnel supplémentaire [Gilley 2009]. Une réaction de β-élimination convertit la

sérine catalytique en déhydroalanine et occasionne le départ concomitant de l'OP. Il n'a pas encore été définitivement établi si cette réaction est liée à la préparation des échantillons pour la spectrométrie de masse. Toutefois, un pH alcalin favorise la β-élimination, laquelle peut se produire à partir des formes âgée et non-vieillie (P. Masson, communication personnelle). Au cours de cette thèse, nous avons pu vérifier que les cristaux de *Tc*AChE supportent des pH élevés (au moins jusqu'à 10). Nous pourrions ainsi espérer caractériser structuralement cet état réactionnel de l'inhibition de l'AChE par un OP.

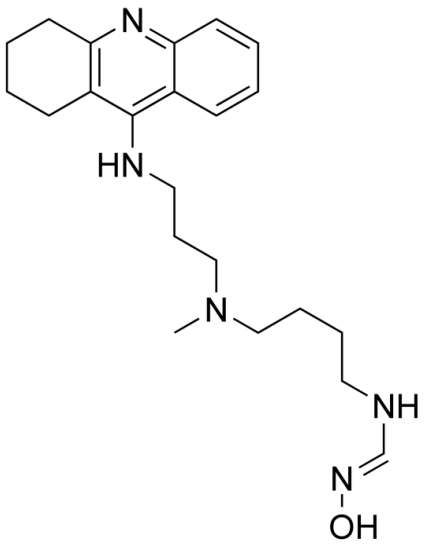

Figure 21. Structure d'un putatif réactivateur, hybride du composé anti-Alzheimer et d'une oxime.

Avec l'intention de comprendre l'inefficacité du 2-PAM à réactiver l'AChE inhibée par le soman, nous avons résolu la structure du conjugué *Tc*AChE/soman vieilli en complexe avec ce réactivateur. Cette dernière révèle une orientation non productive de la fonction oxime du 2-PAM. L'attaque nucléophile devrait idéalement s'effectuer « par le haut », c'est-à-dire que la fonction oxime doit pointer vers le bas de la gorge, au-dessus de l'atome de phosphore. Des réactivateurs plus efficaces se lient au niveau du PAS (HI-6 et HLö-7) [Worek 2007]. Pour mieux contrôler l'orientation de l'oxime, nous proposons d'utiliser non seulement un site de liaison au niveau du PAS, mais également le site de liaison à mi-hauteur de la gorge révélé par le complexe *Tc*AChE/NF766. La molécule la plus évidente à tester dans ce contexte est une chimère du NF766 et du 2-PAM : il serait certainement aisé de remplacer l'une des tacrines du NF766 par une fonction oxime (Fig. 21). En outre, la flexibilité du PAS devra être prise en compte pour optimiser la conception de nouveaux réactivateurs par *flexible docking* ou toute autre méthode

reposant sur la connaissance de la structure de la cible de l'antidote. L'étude dynamico-structurale menée sur les complexes *Tc*AChE/AB1 a apporté des informations quant aux relations dynamique-structure-fonction du PAS. Ces informations, utiles pour la mise au point d'une expérience de cristallographie cinétique, pourraient se révéler précieuses dans la conception de nouveaux médicaments (réactivateurs ou anti-Alzheimer) qui exploitent le PAS comme site de liaison.

Les structures de la *Tc*AChE avec un inhibiteur du site périphérique, l'AB1, ont été résolues. Nous avons observé que l'éthanol, utilisé pour solubiliser l'AB1, a un effet notoire sur la conformation de la triade catalytique de la *Tc*AChE (dans les cristaux orthorhombiques). Le changement conformationnel est plus marqué en présence d'AB1 (solubilisée dans l'éthanol). Il n'a toutefois pas pu être établi que cet effet soit d'ordre allostérique car celui-ci n'a pas été mis en évidence dans la structure du complexe de la *Tc*AChE avec l'AB1 solubilisée dans le DMSO. Les mécanismes structuraux de la communication entre le PAS et le CAS conservent donc leur mystère. Il est possible que le phénomène d'allostérie ne puisse pas être mis en évidence parce qu'il est transitoire, parce qu'il fait intervenir des changements conformationnels trop subtiles pour être observés dans une structure cristallographique, ou encore parce qu'il est purement d'ordre dynamique [Popovych 2006].

Les effets du solvant ne sont pas le seul biais découvert dans cette étude. Il est apparu que l'empilement cristallin influence le mode de liaison de l'AB1. En effet, dans les cristaux trigonaux, un résidu (Gln185) d'une molécule de *Tc*AChE liée par la symétrie interagit avec l'inhibiteur, lequel adopte une orientation différente de celle observée dans les cristaux orthorhombiques. Cette étude illustre les précautions qui doivent être prises avant de conclure quant à l'interprétation biologique d'une structure. Afin de supprimer les artefacts mis en évidence, nous proposons tout d'abord de rechercher un solvant dont les effets sont absolument neutres sur l'enzyme. Le DMSO ne correspond pas à ce critère : bien que petits par rapport à ceux déclenchés par l'éthanol, les effets du DMSO sur la triade catalytique ont été observés. L'effet allostérique, s'il existe, pourrait alors être incontestablement mis en évidence. Nous proposons également de résoudre la structure du complexe *Tc*AChE/AB1 à partir de l'enzyme mutée au niveau de la Gln185 (Q185A, par exemple). Nous avons postulé que le mode de liaison biologiquement pertinent est celui de la forme orthorhombique. Si cette hypothèse est exacte, la structure du complexe

du mutant de *Tc*AChE avec l'AB1, dans la forme trigonale, montrera le mode de liaison observé dans la forme orthorhombique.

L'AB1 a été une grande source d'idées et de résultats au cours de cette thèse. Nous avons tout d'abord participé à une étude visant à proposer l'AChE comme biosenseur capable de détecter des traces de la mycotoxine dans une culture contaminée [Hansmann, Sanson, Stojan, Weik, Marty & Fournier 2009]. C'est à cette occasion que nous avons cherché à résoudre la structure du complexe de la *Tc*AChE avec l'AB1. Lorsque nous avons découvert que l'AB1 est une molécule phosphorescente, nous avons utilisé cette propriété pour effectuer une étude de la dynamique du PAS.

A température cryogénique, le temps de vie de phosphorescence de l'AB1 est de l'ordre d'une seconde. Nous avons ainsi pu le mesurer aisément au Cryobench. Nous faisons l'hypothèse que le temps de vie de phosphorescence est lié à la flexibilité de son environnement : dans ce contexte l'AB1 pourrait être une sonde locale de la dynamique lente (à l'échelle de la ms-s) de la *Tc*AChE. Il faut toutefois rester prudent quant à la nature des mouvements sondés. Nous ne savons pas dans quelle mesure l'abaissement de la température et la viscosité du solvant qui baigne les cristaux affectent les mouvements de la protéine.

Le temps de vie de phosphorescence de l'AB1 a été mesuré entre 100 et 240 K dans des complexes de *Tc*AChE cristalline et d'AB1, et dans la solution de trempage associée. Une transition dans l'évolution du temps de vie a été mise en évidence dans les échantillons cristallins ainsi que dans la solution de trempage : nous suggérons qu'il s'agit de la transition vitreuse du solvant (dans l'expérience en solution) et de la transition dynamique du PAS (dans les expériences sur les cristaux). Nous suspectons un couplage entre la dynamique de l'enzyme et celle du solvant à partir de 170 K. Au-dessous de cette température, la dynamique de la protéine et celle du solvant seraient ainsi découplées ; nos résultats indiquent que la protéine possède une plus grande flexibilité que le solvant dans cette gamme de températures. Au-dessus de 170 K, le solvant est plus flexible que la protéine. Nous suggérons également que le PAS dans les cristaux orthorhombiques est plus flexible que dans les cristaux trigonaux, avant et après la transition. Nous espérons que cette méthode sera appliquée à d'autres couples protéine/ligand. Cela nous paraît pleinement envisageable. Parmi les ligands d'une protéine, les molécules aromatiques sont potentiellement des fluorophores. A température cryogénique, ces fluorophores sont susceptibles de phosphorescer ; nous avons notamment pu observer que le NF595

phosphoresce avec un temps de vie de l'ordre de 100 ms. Par ailleurs, un ligand phosphorescent se liant au CAS permettrait de sonder ce dernier par la méthode que nous proposons. Un dérivé de tacrine se liant uniquement au niveau du CAS pourrait probablement remplir ce rôle. Nous nous attendons à ce qu'une telle expérience révèle une transition dynamique de l'enzyme autour de 150 K, température ayant permis l'expulsion de la choline dans une expérience de cristallographie cinétique [Colletier, Bourgeois, Sanson, Fournier, Sussman, Silman & Weik 2008].

Les résultats de cette étude dynamique sont directement utilisables dans le cadre d'une expérience de cristallographie cinétique contrôlée par la température. Ils pourraient permettre de préciser la gamme de températures optimale pour la réaliser. Pour les cristaux de *Tc*AChE, nous proposons d'utiliser une température de 170 K pour profiter de l'augmentation substantielle de flexibilité tout en retardant au maximum la formation de glace cristalline dans l'échantillon.

L'utilisation d'une choline en cage photoclivable a permis de montrer par cristallographie cinétique l'expulsion de la choline (et de sa cage) [Colletier, Royant, Specht, Sanson, Nachon, Masson, Zaccai, Sussman, Goeldner, Silman, Bourgeois & Weik 2007]. Une excursion à température ambiante s'était avérée nécessaire pour y parvenir. La radiolyse à 150 K d'un analogue de substrat de l'AChE nous a permis de mettre en évidence certains changements conformationnels se produisant lors du clivage catalytique (mimé dans cette expérience) de la choline [Colletier, Bourgeois, Sanson, Fournier, Sussman, Silman & Weik 2008]. Nous avons appliqué cette dernière stratégie à des cristaux trigonaux de *Tc*AChE inhibée par le soman dans la forme non vieillie. Notre but était de déclencher la déalkylation du soman par radiolyse à 150 K. Comme la catalyse et le vieillissement de l'AChE utilisent les mêmes mécanismes [Millard 1999b], la radiolyse à une température proche de 150 K de la liaison O-C du soman nous paraît réalisable, d'autant plus que cette liaison est fragilisée dès la liaison du soman à l'AChE [Sanson 2009]. Toutefois, malgré de nombreux essais, le calcul de cartes Fo-Fo entre les jeux de données enregistrés sur des cristaux trigonaux après et avant une forte dose de rayons X indique que la radiolyse est au mieux partielle. Pour optimiser les conditions de l'expérience, l'utilisation de cristaux orthorhombiques est à envisager : la radiolyse de l'analogue de substrat a été réalisée sur des cristaux orthorhombiques [Colletier, Bourgeois, Sanson, Fournier, Sussman, Silman & Weik 2008]. Il reste néanmoins un obstacle à surmonter. En effet, la structure du conjugué *Tc*AChE/soman non vieilli dans la forme orthorhombique de l'enzyme est une

condition préalablement nécessaire à la réalisation de l'expérience de cristallographie cinétique proposée. Les données cristallographiques enregistrées sur de tels cristaux ne sont pas aussi claires que celles obtenues avec les cristaux trigonaux : le soman, et en particulier son groupement pinacolyl, n'est pas bien défini. Il est possible que le vieillissement soit plus rapide dans la forme orthorhombique en raison de la flexibilité plus importante de cette forme cristalline. Nous avons en outre pu constater que les cristaux orthorhombiques sont plus affectés que les cristaux trigonaux par les conditions de trempage avec la solution contenant le soman.

La spectroscopie Raman pourrait permettre de contrôler l'état de la liaison pendant l'expérience de cristallographie cinétique. La liaison P-O, adjacent à la liaison à cliver, est susceptible d'être à l'origine d'un signal Raman dont la fréquence et l'intensité pourraient être différents avant et après la rupture de la liaison. Il faut donc réussir à atténuer le fond du spectre Raman obtenu à partir de cristaux de *Tc*AChE dans les conditions cristallographiques que nous utilisons. C'est un véritable défi dans la mesure où les conditions permettant d'acquérir un spectre Raman exploitable doivent non seulement préserver l'activité de l'enzyme, mais également posséder un effet cryoprotectant.

Si l'expérience de cristallographie cinétique sur les cristaux de conjugués *Tc*AChE/soman devait porter ses fruits, le film du vieillissement de l'AChE inhibée par le soman, qui ne comporte que les images initiale et finale, pourrait être complété par l'instantané d'un éventuel état intermédiaire. Ces expériences représentent également une possibilité supplémentaire de mettre en évidence la *backdoor* de l'AChE, par laquelle les produits et les substrats pourraient sortir afin de faciliter leur trafic au sein de l'enzyme [Colletier, Royant, Specht, Sanson, Nachon, Masson, Zaccai, Sussman, Goeldner, Silman, Bourgeois & Weik 2007 ; Colletier, Bourgeois, Sanson, Fournier, Sussman, Silman & Weik 2008 ; Gilson 1994].

Avec ces travaux, une partie de la personnalité de l'AChE a été dévoilée. Notre démarche est potentiellement transposable à toute protéine pour laquelle des cristaux peuvent être obtenus. Nous espérons ainsi que les résultats obtenus trouveront un écho.

BIBLIOGRAPHIE

[1] http://upload.wikimedia.org

[2] http://micro.magnet.fsu.edu

[3 1984] Report of the specialists appointed by the Secretary-General to investigate allegations by the Islamic Republic of Iran concerning the use of chemical weapons, United Nations Security Council, New York, 1984.

[4 1986] Report of the mission dispatched by the Secretary-General to investigate allegations of the use of chemical weapons in the conflict between the Islamic Republic of Iran and Iraq, United Nations Security Council, New York, 1986.

[5 1987] Report of the mission dispatched by the Secretary-General to investigate allegations of the use of chemical weapons in the conflict between the Islamic Republic of Iran and Iraq, United Nations Security Council, New York, 1987.

[6 1993] IARC monographs on the evaluation of carcinogenic risks to humans. Some naturally occurring substances: food items and constituents, heterocyclic aromatic amines and mycotoxins, volume 56, International Agency for Research on Cancer, Lyon, 1993.

[7 1994] 7, The CCP4 suite: programs for protein crystallography. *Acta Crystallogr D Biol Crystallogr.* 1994, 50, 760-3.

[Abad-Zapatero 1987] C. Abad-Zapatero, J.P. Griffith, J.L. Sussman, and M.G. Rossmann, Refined crystal structure of dogfish M4 apo-lactate dehydrogenase. *J Mol Biol.* 1987, 198, 445-67.

[Alles 1940] G.A. Alles, and R.C. Hawes, Cholinesterases in the Blood of Man. *J Biol Chem.* 1940, 133, 375-390.

[Angell 1995] C.A. Angell, Formation of Glasses from Liquids and Biopolymers. *Science.* 1995, 267, 1924-1935.

[Anslyn 2006] E.V. Anslyn, and D.A. Dougherty, Modern physical organic chemistry, University Science, Sausalito, CA, 2006.

[Antonijevic 2007] B. Antonijevic, and M.P. Stojiljkovic, Unequal efficacy of pyridinium oximes in acute organophosphate poisoning. *Clin Med Res.* 2007, 5, 71-82.

[Antosiewicz 1995a] J. Antosiewicz, J.A. McCammon, S.T. Wlodek, and M.K. Gilson, Simulation of charge-mutant acetylcholinesterases. *Biochemistry.* 1995, 34, 4211-9.

[Antosiewicz 1995b] J. Antosiewicz, and J.A. McCammon, Electrostatic and hydrodynamic orientational steering effects in enzyme-substrate association. *Biophys J.* 1995, 69, 57-65.

[Antosiewicz 1995c] J. Antosiewicz, M.K. Gilson, I.H. Lee, and J.A. McCammon, Acetylcholinesterase: diffusional encounter rate constants for dumbbell models of ligand. *Biophys J.* 1995, 68, 62-8.

[Ashani 1982] Y. Ashani, and B.S. Green, Are the organophosphorus inhibitors of AChE transition state analogs? in: B.S. Green, Y. Ashani, and D. Chipman, (Eds.),

Chemical approaches to understanding enzyme catalysis : biometric chemistry and transition-state analogs., Elsevier Scientific, Amsterdam, 1982, pp. 169-188.

[Ashani 1995] Y. Ashani, Z. Radic, I. Tsigelny, D.C. Vellom, N.A. Pickering, D.M. Quinn, B.P. Doctor, and P. Taylor, Amino acid residues controlling reactivation of organophosphonyl conjugates of acetylcholinesterase by mono- and bisquaternary oximes. *J Biol Chem.* 1995, 270, 6370-80.

[Ashani 2003] Y. Ashani, A.K. Bhattacharjee, H. Leader, A. Saxena, and B.P. Doctor, Inhibition of cholinesterases with cationic phosphonyl oximes highlights distinctive properties of the charged pyridine groups of quaternary oxime reactivators. *Biochem Pharmacol.* 2003, 66, 191-202.

[Augustinsson 1949] K.B. Augustinsson, and D. Nachmansohn, Distinction between Acetylcholine-Esterase and Other Choline Ester-splitting Enzymes. *Science.* 1949, 110, 98-99.

[Aurbek 2006] N. Aurbek, H. Thiermann, L. Szinicz, P. Eyer, and F. Worek, Analysis of inhibition, reactivation and aging kinetics of highly toxic organophosphorus compounds with human and pig acetylcholinesterase. *Toxicology.* 2006, 224, 91-9.

[Austin 1975] R.H. Austin, K.W. Beeson, L. Eisenstein, H. Frauenfelder, and I.C. Gunsalus, Dynamics of ligand binding to myoglobin. *Biochemistry.* 1975, 14, 5355-73.

[Axelsen 1994] P.H. Axelsen, M. Harel, I. Silman, and J.L. Sussman, Structure and dynamics of the active site gorge of acetylcholinesterase: synergistic use of molecular dynamics simulation and X-ray crystallography. *Protein Sci.* 1994, 3, 188-97.

[B-Rao 2009] C. B-Rao, J. Subramanian, and S.D. Sharma, Managing protein flexibility in docking and its applications. *Drug Discov Today.* 2009, 14, 394-400.

[Bagjar 2006] J. Bagjar, J. Kassar, J. Fusek, K. Kuca, and D. Jun, Other toxic chemicals as potential chemical warfare agents. in: R.C. Gupta, (Ed.), Toxicology of organophosphate and carbamate compounds, Elsevier Academic Press, Amsterdam; London, 2006, pp. xvi, 763 p.

[Ball 2007] P. Ball, Water as an Active Constituent in Cell Biology. *Chemical Reviews.* 2007, 108, 74-108.

[Bar-On 2002] P. Bar-On, C.B. Millard, M. Harel, H. Dvir, A. Enz, J.L. Sussman, and I. Silman, Kinetic and structural studies on the interaction of cholinesterases with the anti-Alzheimer drug rivastigmine. *Biochemistry.* 2002, 41, 3555-64.

[Barak 1994] D. Barak, C. Kronman, A. Ordentlich, N. Ariel, A. Bromberg, D. Marcus, A. Lazar, B. Velan, and A. Shafferman, Acetylcholinesterase peripheral anionic site degeneracy conferred by amino acid arrays sharing a common core. *J Biol Chem.* 1994, 269, 6296-305.

[Barak 1995] D. Barak, A. Ordentlich, A. Bromberg, C. Kronman, D. Marcus, A. Lazar, N. Ariel, B. Velan, and A. Shafferman, Allosteric modulation of acetylcholinesterase activity by peripheral ligands involves a conformational transition of the anionic subsite. *Biochemistry.* 1995, 34, 15444-52.

[Bartolini 2003] M. Bartolini, C. Bertucci, V. Cavrini, and V. Andrisano, beta-Amyloid aggregation induced by human acetylcholinesterase: inhibition studies. *Biochem Pharmacol.* 2003, 65, 407-16.

[Bartolucci 2006] C. Bartolucci, M. Siotto, E. Ghidini, G. Amari, P.T. Bolzoni, M. Racchi, G. Villetti, M. Delcanale, and D. Lamba, Structural determinants of Torpedo californica acetylcholinesterase inhibition by the novel and orally active carbamate based anti-alzheimer drug ganstigmine (CHF-2819). *J Med Chem.* 2006, 49, 5051-8.

[Bartus 1982] R.T. Bartus, R.L. Dean, 3rd, B. Beer, and A.S. Lippa, The cholinergic hypothesis of geriatric memory dysfunction. *Science.* 1982, 217, 408-14.

[Behrman 1970a] E.J. Behrman, M.J. Biallas, H.J. Brass, J.O. Edwards, and M. Isaks, Reactions of phosphonic acid esters with nucleophiles. II. Survey of nucleophiles reacting with p-nitrophenyl methylphosphonate anion. *J Org Chem.* 1970, 35, 3069-3075.

[Behrman 1970b] E.J. Behrman, M.J. Biallas, H.J. Brass, J.O. Edwards, and M. Isaks, Reactions of phosphonic acid esters with nucleophiles. I. Hydrolysis. *J Org Chem.* 1970, 35, 3063-3069.

[Bencsura 1995] A. Bencsura, I. Enyedy, and I.M. Kovach, Origins and diversity of the aging reaction in phosphonate adducts of serine hydrolase enzymes: what characteristics of the active site do they probe? *Biochemistry.* 1995, 34, 8989-99.

[Benschop 1984] H.P. Benschop, C.A. Konings, J. Van Genderen, and L.P. De Jong, Isolation, anticholinesterase properties, and acute toxicity in mice of the four stereoisomers of the nerve agent soman. *Toxicol. Appl. Pharm.* 1984, 72, 61-74.

[Benschop 1988] H.P. Benschop, and L.P.A. De Jong, Nerve agent stereoisomers: analysis, isolation and toxicology. *Acc Chem Res.* 1988, 21, 368-374.

[Bergmann 1950] F. Bergmann, I.B. Wilson, and D. Nachmansohn, Acetylcholinesterase. IX. Structural features determining the inhibition by amino acids and related compounds. *J Biol Chem.* 1950, 186, 693-703.

[Berman 1981] H.A. Berman, W. Becktel, and P. Taylor, Spectroscopic studies on acetylcholinesterase: influence of peripheral-site occupation on active-center conformation. *Biochemistry.* 1981, 20, 4803-10.

[Berman 1989] H.A. Berman, and M.M. Decker, Chiral nature of covalent methylphosphonyl conjugates of acetylcholinesterase. *J Biol Chem.* 1989, 264, 3951-6.

[Bourgeois 2002]D. Bourgeois, X. Vernede, V. Adam, E. Fioravanti, and T. Ursby, A microspectrophotometer for UV-visible absorption and fluorescence studies of protein crystals, Journal of Applied Crystallography, 2002, pp. 319-326.

[Bourgeois 2005] D. Bourgeois, and A. Royant, Advances in kinetic protein crystallography. *Curr Opin Struct Biol.* 2005, 15, 538-47.

[Bourgeois 2006] D. Bourgeois, B. Vallone, A. Arcovito, G. Sciara, F. Schotte, P.A. Anfinrud, and M. Brunori, Extended subnanosecond structural dynamics of myoglobin revealed by Laue crystallography. *Proc Natl Acad Sci U S A.* 2006, 103, 4924-9.

[Bourgeois 2009] D. Bourgeois, and M. Weik, Kinetic protein crystallography: a tool to watch proteins in action. *Cryst Rev.* 2009, 15, 87 - 118.

[Bourne 1995]Y. Bourne, P. Taylor, and P. Marchot, Acetylcholinesterase inhibition by fasciculin: crystal structure of the complex. *Cell.* 1995, 83, 503-12.

[Bourne 2003]Y. Bourne, P. Taylor, Z. Radic, and P. Marchot, Structural insights into ligand interactions at the acetylcholinesterase peripheral anionic site. *Embo J.* 2003, 22, 1-12.

[Bourne 2004]Y. Bourne, H.C. Kolb, Z. Radic, K.B. Sharpless, P. Taylor, and P. Marchot, Freeze-frame inhibitor captures acetylcholinesterase in a unique conformation. *Proc Natl Acad Sci U S A.* 2004, 101, 1449-54.

[Bourne 2006]Y. Bourne, Z. Radic, G. Sulzenbacher, E. Kim, P. Taylor, and P. Marchot, Substrate and product trafficking through the active center gorge of acetylcholinesterase analyzed by crystallography and equilibrium binding. *J Biol Chem.* 2006, 281, 29256-67.

[Boyd 2000] A.E. Boyd, A.B. Marnett, L. Wong, and P. Taylor, Probing the active center gorge of acetylcholinesterase by fluorophores linked to substituted cysteines. *J Biol Chem.* 2000, 275, 22401-8.

[Boyd 2004] A.E. Boyd, C.S. Dunlop, L. Wong, Z. Radic, P. Taylor, and D.A. Johnson, Nanosecond dynamics of acetylcholinesterase near the active center gorge. *J Biol Chem.* 2004, 279, 26612-8.

[Brochier 2001] L. Brochier, Y. Pontie, M. Willson, S. Estrada-Mondaca, J. Czaplicki, A. Klaebe, and D. Fournier, Involvement of deacylation in activation of substrate hydrolysis by Drosophila acetylcholinesterase. *J Biol Chem.* 2001, 276, 18296-302.

[Broennimann 2006] C. Broennimann, E.F. Eikenberry, B. Henrich, R. Horisberger, G. Huelsen, E. Pohl, B. Schmitt, C. Schulze-Briese, M. Suzuki, T. Tomizaki, H. Toyokawa, and A. Wagner, The PILATUS 1M detector. *J Synchrotron Radiat.* 2006, 13, 120-30.

[Brovchenko 2008] I. Brovchenko, and A. Oleinikova, Which properties of a spanning network of hydration water enable biological functions? *Chemphyschem.* 2008, 9, 2695-702.

[Brunger 1992] A.T. Brunger, Free R value: a novel statistical quantity for assessing the accuracy of crystal structures. *Nature.* 1992, 355, 472-5.

[Brunger 2007] A.T. Brunger, Version 1.2 of the Crystallography and NMR system. *Nat. Protoc.* 2007, 2, 2728-33.

[Bui 2004] J.M. Bui, K. Tai, and J.A. McCammon, Acetylcholinesterase: enhanced fluctuations and alternative routes to the active site in the complex with fasciculin-2. *J Am Chem Soc.* 2004, 126, 7198-205.

[Bui 2005] J.M. Bui, and J.A. McCammon, Acetylcholinesterase: pivotal roles of its long omega loop (Cys69-Cys96) in regulating substrate binding. *Chem Biol Interact.* 2005, 157-158, 357-9.

[Bui 2008] J.M. Bui, and J. Andrew McCammon, Intrinsic conformational flexibility of acetylcholinesterase. *Chem Biol Interact.* 2008, 175, 303-4.

[Burmeister 2000] W.P. Burmeister, Structural changes in a cryo-cooled protein crystal owing to radiation damage. *Acta Crystallogr D Biol Crystallogr.* 2000, 56, 328-41.

[Butini 2008a]S. Butini, E. Guarino, G. Campiani, M. Brindisi, S.S. Coccone, I. Fiorini, E. Novellino, T. Belinskaya, A. Saxena, and S. Gemma, Tacrine based human cholinesterase inhibitors: synthesis of peptidic-tethered derivatives and their effect on potency and selectivity. *Bioorg Med Chem Lett.* 2008, 18, 5213-6.

[Butini 2008b] S. Butini, G. Campiani, M. Borriello, S. Gemma, A. Panico, M. Persico, B. Catalanotti, S. Ros, M. Brindisi, M. Agnusdei, I. Fiorini, V. Nacci, E. Novellino, T. Belinskaya, A. Saxena, and C. Fattorusso, Exploiting protein fluctuations at the active-site gorge of human cholinesterases: further optimization of the design strategy to develop extremely potent inhibitors. *J Med Chem.* 2008, 51, 3154-70.

[Cadogan 1969] J.I.G. Cadogan, D. Eastlick, F. Hampson, and R.K. Mackie, Reactivity of Organophosphorus Compounds .24. Acidic Hydrolysis of Dialkyl Methylphosphonates. *J Chem Soc B.* 1969, 144-6.

[Campiani 2005] G. Campiani, C. Fattorusso, S. Butini, A. Gaeta, M. Agnusdei, S. Gemma, M. Persico, B. Catalanotti, L. Savini, V. Nacci, E. Novellino, H.W. Holloway, N.H. Greig, T. Belinskaya, J.M. Fedorko, and A. Saxena, Development of molecular probes for the identification of extra interaction sites in the mid-gorge and peripheral sites of butyrylcholinesterase (BuChE). Rational design of

novel, selective, and highly potent BuChE inhibitors. *J Med Chem.* 2005, 48, 1919-29.

[Carletti 2008a] E. Carletti, H. Li, B. Li, F. Ekstrom, Y. Nicolet, M. Loiodice, E. Gillon, M.T. Froment, O. Lockridge, L.M. Schopfer, P. Masson, and F. Nachon, Aging of cholinesterases phosphylated by tabun proceeds through O-dealkylation. *J Am Chem Soc.* 2008, 130, 16011-20.

[Carletti 2008b] E. Carletti, N. Aurbek, E. Gillon, M. Loiodice, Y. Nicolet, J.C. Fontecilla-Camps, P. Masson, H. Thiermann, F. Nachon and F. Worek, Structure-analysis activity of aging and reactivation of human butyrylcholinesterase inhibited by analogues of tabun. *J Biochem.* 2009, 421, 97-106.

[Carpentier 2007] P. Carpentier, A. Royant, J. Ohana, and D. Bourgeois, Advances in spectroscopic methods for biological crystals. 2. Raman spectroscopy. *J Appl Cryst.* 2007, 40, 1113-1122.

[Carson 1991] K.A. Carson, C. Geula, and M.M. Mesulam, Electron microscopic localization of cholinesterase activity in Alzheimer brain tissue. *Brain Res.* 1991, 540, 204-8.

[Cavalli 2004] A. Cavalli, G. Bottegoni, C. Raco, M. De Vivo, and M. Recanatini, A computational study of the binding of propidium to the peripheral anionic site of human acetylcholinesterase. *J Med Chem.* 2004, 47, 3991-9.

[Chabriere 2001] E. Chabriere, X. Vernede, B. Guigliarelli, M.H. Charon, E.C. Hatchikian, and J.C. Fontecilla-Camps, Crystal structure of the free radical intermediate of pyruvate:ferredoxin oxidoreductase. *Science.* 2001, 294, 2559-63.

[Changeux 1966] J.P. Changeux, Responses of acetylcholinesterase from Torpedo marmorata to salts and curarizing drugs. *Mol Pharmacol.* 1966, 2, 369-92.

[Chen 1999] J.W. Chen, Y.L. Luo, M.J. Hwang, F.C. Peng, and K.H. Ling, Territrem B, a tremorgenic mycotoxin that inhibits acetylcholinesterase with a noncovalent yet irreversible binding mechanism. *J Biol Chem.* 1999, 274, 34916-23.

[Colletier 2006a] J.P. Colletier, D. Fournier, H.M. Greenblatt, J. Stojan, J.L. Sussman, G. Zaccai, I. Silman, and M. Weik, Structural insights into substrate traffic and inhibition in acetylcholinesterase. *Embo J.* 2006, 25, 2746-56.

[Colletier 2006b] J.P. Colletier, B. Sanson, F. Nachon, E. Gabellieri, C. Fattorusso, G. Campiani, and M. Weik, Conformational flexibility in the peripheral site of Torpedo californica acetylcholinesterase revealed by the complex structure with a bifunctional inhibitor. *J Am Chem Soc.* 2006, 128, 4526-7.

[Colletier 2007] J.P. Colletier, A. Royant, A. Specht, B. Sanson, F. Nachon, P. Masson, G. Zaccai, J.L. Sussman, M. Goeldner, I. Silman, D. Bourgeois, and M. Weik, Use of a 'caged' analogue to study the traffic of choline within acetylcholinesterase by kinetic crystallography. *Acta Crystallogr D Biol Crystallogr.* 2007, 63, 1115-28.

[Colletier 2008] J.P. Colletier, D. Bourgeois, B. Sanson, D. Fournier, J.L. Sussman, I. Silman, and M. Weik, Shoot-and-Trap: use of specific x-ray damage to study structural protein dynamics by temperature-controlled cryo-crystallography. *Proc Natl Acad Sci U S A.* 2008, 105, 11742-7.

[Costa 2006] L.G. Costa, Current issues in organophosphate toxicology. *Clin Chim Acta.* 2006, 366, 1-13.

[Crowther 1967] R.A. Crowther, and D.M. Blow, A method of positioning a known molecule in an unknown crystal structure. *Acta Crystallographica.* 1967, 23, 544-548.

[Cvetkovic 2005] A. Cvetkovic, C. Picioreanu, A.J. Straathof, R. Krishna, and L.A. van der Wielen, Relation between pore sizes of protein crystals and anisotropic solute diffusivities. *J Am Chem Soc.* 2005, 127, 875-9.

[Cygler 1994] M. Cygler, P. Grochulski, R.J. Kazlauskas, J.D. Schrag, F. Bouthillier, B. Rubin, A.N. Serreqi, and A.K. Gupta, A Structural Basis for the Chiral Preferences of Lipases. *J Am Chem Soc.* 1994, 116, 3180-3186.

[D'Auria 2008] S. D'Auria, M. Staiano, A. Varriale, M. Gonnelli, A. Marabotti, M. Rossi, and G.B. Strambini, The tryptophan phosphorescence of porcine and mutant bovine odorant-binding proteins: a probe for the local protein structure and dynamics. *J Proteome Res.* 2008, 7, 1151-8.

[Dale 1914]H.H. Dale, The Action of Certain Esters and Ethers of Choline, and their Relation to Muscarine, 1914, pp. 147-190.

[Dall'asta 2003] C. Dall'asta, G. Ingletto, R. Corradini, G. Galaverna, and R. Marchelli, Fluorescence Enhancement of Aflatoxins Using Native and Substituted Cyclodextrins. *J Incl Phenom Macrocycl Chem.* 2003, 45, 257-263.

[Davies 1976] P. Davies, and A.J. Maloney, Selective loss of central cholinergic neurons in Alzheimer's disease. *Lancet.* 1976, 2, 1403.

[Davis 2007] I.W. Davis, A. Leaver-Fay, V.B. Chen, J.N. Block, G.J. Kapral, X. Wang, L.W. Murray, W.B. Arendall, 3rd, J. Snoeyink, J.S. Richardson, and D.C. Richardson, MolProbity: all-atom contacts and structure validation for proteins and nucleic acids. *Nucleic Acids Res.* 2007, 35, W375-83.

[De Ferrari 2001a] G.V. De Ferrari, W.D. Mallender, N.C. Inestrosa, and T.L. Rosenberry, Thioflavin T Is a Fluorescent Probe of the Acetylcholinesterase Peripheral Site That Reveals Conformational Interactions between the Peripheral and Acylation Sites. *J Biol Chem.* 2001, 276, 23282-23287.

[De Ferrari 2001b] G.V. De Ferrari, M.A. Canales, I. Shin, L.M. Weiner, I. Silman, and N.C. Inestrosa, A structural motif of acetylcholinesterase that promotes amyloid beta-peptide fibril formation. *Biochemistry.* 2001, 40, 10447-57.

[de Jong 1985] L.P. de Jong, and G.Z. Wolring, Aging and stereospecific reactivation of mouse erythrocyte and brain acetylcholinesterases inhibited by soman. *Biochem Pharmacol.* 1985, 34, 142-5.

[DeLano 2002] W.L. DeLano, The PyMOL Molecular Graphics System, DeLano Scientific, San Carlos, CA, 2002.

[Diederichs 1997] K. Diederichs, and P.A. Karplus, Improved R-factors for diffraction data analysis in macromolecular crystallography. *Nat Struct Mol Biol.* 1997, 4, 269-275.

[Doster 1989] W. Doster, S. Cusack, and W. Petry, Dynamical transition of myoglobin revealed by inelastic neutron scattering. *Nature.* 1989, 337, 754-6.

[Drenth 2007] J. Drenth, and J. Mesters, Principles of protein X-ray crystallography, Springer, New York, 2007.

[Du 2004] D.M. Du, and P.R. Carlier, Development of bivalent acetylcholinesterase inhibitors as potential therapeutic drugs for Alzheimer's disease. *Curr Pharm Des.* 2004, 10, 3141-56.

[Dumas 1990] D.P. Dumas, H.D. Durst, W.G. Landis, F.M. Raushel, and J.R. Wild, Inactivation of organophosphorus nerve agents by the phosphotriesterase from Pseudomonas diminuta. *Arch Biochem Biophys.* 1990, 277, 155-9.

[Dundas 2006] J. Dundas, Z. Ouyang, J. Tseng, A. Binkowski, Y. Turpaz, and J. Liang, CASTp: computed atlas of surface topography of proteins with structural and topographical mapping of functionally annotated residues. *Nucleic Acids Res.* 2006, 34, W116-8.

[Eastman 1995] J. Eastman, E.J. Wilson, C. Cervenansky, and T.L. Rosenberry, Fasciculin 2 binds to the peripheral site on acetylcholinesterase and inhibits substrate hydrolysis by slowing a step involving proton transfer during enzyme acylation. *J Biol Chem.* 1995, 270, 19694-701.

[Ebbinghaus 2007] S. Ebbinghaus, S.J. Kim, M. Heyden, X. Yu, U. Heugen, M. Gruebele, D.M. Leitner, and M. Havenith, An extended dynamical hydration shell around proteins. *Proc Natl Acad Sci U S A.* 2007, 104, 20749-52.

[Eddleston 2008] M. Eddleston, E. Juszczak, N.A. Buckley, L. Senarathna, F. Mohamed, W. Dissanayake, A. Hittarage, S. Azher, K. Jeganathan, S. Jayamanne, M.R. Sheriff, and D.A. Warrell, Multiple-dose activated charcoal in acute self-poisoning: a randomised controlled trial. *Lancet.* 2008, 371, 579-87.

[Eichler 1994] J. Eichler, A. Anselment, J.L. Sussman, J. Massoulie, and I. Silman, Differential effects of "peripheral" site ligands on Torpedo and chicken acetylcholinesterase. *Mol Pharmacol.* 1994, 45, 335-40.

[Ekstrom 2006a] F. Ekstrom, C. Akfur, A.K. Tunemalm, and S. Lundberg, Structural changes of phenylalanine 338 and histidine 447 revealed by the crystal structures of tabun-inhibited murine acetylcholinesterase. *Biochemistry.* 2006, 45, 74-81.

[Ekstrom 2006b] F. Ekstrom, Y.P. Pang, M. Boman, E. Artursson, C. Akfur, and S. Borjegren, Crystal structures of acetylcholinesterase in complex with HI-6, Ortho-7 and obidoxime: structural basis for differences in the ability to reactivate tabun conjugates. *Biochem Pharmacol.* 2006, 72, 597-607.

[Ekstrom 2009] F. Ekstrom, A. Hornberg, E. Artursson, L.G. Hammarstrom, G. Schneider, and Y.P. Pang, Structure of HI-6*sarin-acetylcholinesterase determined by X-ray crystallography and molecular dynamics simulation: reactivator mechanism and design. *PLoS One.* 2009, 4, e5957.

[Ekström 2006a] F. Ekström, Y.P. Pang, M. Boman, E. Artursson, C. Akfur, and S. Borjegren, Crystal structures of acetylcholinesterase in complex with HI-6, Ortho-7 and obidoxime: structural basis for differences in the ability to reactivate tabun conjugates. *Biochem Pharmacol.* 2006, 72, 597-607.

[Ekström 2006b] F. Ekström, C. Akfur, A.K. Tunemalm, and S. Lundberg, Structural changes of phenylalanine 338 and histidine 447 revealed by the crystal structures of tabun-inhibited murine acetylcholinesterase. *Biochemistry.* 2006, 45, 74-81.

[Ekstrom 2007] F.J. Ekstrom, C. Astot, and Y.P. Pang, Novel nerve-agent antidote design based on crystallographic and mass spectrometric analyses of tabun-conjugated acetylcholinesterase in complex with antidotes. *Clin Pharmacol Ther.* 2007, 82, 282-93.

[Ekström 2007] F.J. Ekström, C. Astot, and Y.P. Pang, Novel nerve-agent antidote design based on crystallographic and mass spectrometric analyses of tabun-conjugated acetylcholinesterase in complex with antidotes. *Clin Pharmacol Ther.* 2007, 82, 282-93.

[Emsley 2004] P. Emsley, and K. Cowtan, Coot: model-building tools for molecular graphics. *Acta Crystallogr D Biol Crystallogr.* 2004, 60, 2126-32.

[Epstein 1979] D.J. Epstein, H.A. Berman, and P. Taylor, Ligand-induced conformational changes in acetylcholinesterase investigated with fluorescent phosphonates. *Biochemistry.* 1979, 18, 4749-54.

[Eyer 1992] P. Eyer, I. Hagedorn, R. Klimmek, P. Lippstreu, M. Loffler, H. Oldiges, U. Spohrer, I. Steidl, L. Szinicz, and F. Worek, HLo 7 dimethanesulfonate, a potent bispyridinium-dioxime against anticholinesterases. *Arch Toxicol.* 1992, 66, 603-21.

[Faerman 1996] C. Faerman, D. Ripoll, S. Bon, Y. Le Feuvre, N. Morel, J. Massoulie, J.L. Sussman, and I. Silman, Site-directed mutants designed to test back-door hypotheses of acetylcholinesterase function. *FEBS Lett.* 1996, 386, 65-71.

[Fang 2008] L. Fang, B. Kraus, J. Lehmann, J. Heilmann, Y. Zhang, and M. Decker, Design and synthesis of tacrine-ferulic acid hybrids as multi-potent anti-Alzheimer drug candidates. *Bioorg Med Chem Lett.* 2008, 18, 2905-9.

[Fekonja 2007] O. Fekonja, M. Zorec-Karlovsek, M. El Kharbili, D. Fournier, and J. Stojan, Inhibition and protection of cholinesterases by methanol and ethanol. *J Enzyme Inhib Med Chem.* 2007, 22, 407-15.

[Felder 2002] C.E. Felder, M. Harel, I. Silman, and J.L. Sussman, Structure of a complex of the potent and specific inhibitor BW284C51 with Torpedo californica acetylcholinesterase. *Acta Crystallogr D Biol Crystallogr.* 2002, 58, 1765-71.

[Fenimore 2002] P.W. Fenimore, H. Frauenfelder, B.H. McMahon, and F.G. Parak, Slaving: solvent fluctuations dominate protein dynamics and functions. *Proc Natl Acad Sci U S A.* 2002, 99, 16047-51.

[Fenimore 2004] P.W. Fenimore, H. Frauenfelder, B.H. McMahon, and R.D. Young, Bulk-solvent and hydration-shell fluctuations, similar to alpha- and beta-fluctuations in glasses, control protein motions and functions. *Proc Natl Acad Sci U S A.* 2004, 101, 14408-13.

[Fitzpatrick 1993] P.A. Fitzpatrick, A.C. Steinmetz, D. Ringe, and A.M. Klibanov, Enzyme crystal structure in a neat organic solvent. *Proc Natl Acad Sci U S A.* 1993, 90, 8653-7.

[Fleming 2007] C.D. Fleming, C.C. Edwards, S.D. Kirby, D.M. Maxwell, P.M. Potter, D.M. Cerasoli, and M.R. Redinbo, Crystal structures of human carboxylesterase 1 in covalent complexes with the chemical warfare agents soman and tabun. *Biochemistry.* 2007, 46, 5063-71.

[Frauenfelder 1991] H. Frauenfelder, S.G. Sligar, and P.G. Wolynes, The energy landscapes and motions of proteins. *Science.* 1991, 254, 1598-603.

[Frauenfelder 2009] H. Frauenfelder, G. Chen, J. Berendzen, P.W. Fenimore, H. Jansson, B.H. McMahon, I.R. Stroe, J. Swenson, and R.D. Young, A unified model of protein dynamics. *Proc Natl Acad Sci U S A.* 2009, 106, 5129-34.

[Gabel 2009] F. Gabel, P. Masson, M.T. Froment, B.P. Doctor, A. Saxena, I. Silman, G. Zaccai, and M. Weik, Direct correlation between molecular dynamics and enzymatic stability: a comparative neutron scattering study of native human butyrylcholinesterase and its "aged" soman conjugate. *Biophys J.* 2009, 96, 1489-94.

[Garman 1999] E. Garman, Cool data: quantity AND quality. *Acta Crystallogr D Biol Crystallogr.* 1999, 55, 1641-53.

[Garman 2003] E.F. Garman, and S. Doublie, Cryocooling of macromolecular crystals: optimization methods. *Methods Enzymol.* 2003, 368, 188-216.

[Gemma 2006] S. Gemma, E. Gabellieri, P. Huleatt, C. Fattorusso, M. Borriello, B. Catalanotti, S. Butini, M. De Angelis, E. Novellino, V. Nacci, T. Belinskaya, A. Saxena, and G. Campiani, Discovery of huperzine A-tacrine hybrids as potent inhibitors of human cholinesterases targeting their midgorge recognition sites. *J Med Chem.* 2006, 49, 3421-5.

[Gibney 1990]G. Gibney, S. Camp, M. Dionne, K. MacPhee-Quigley, and P. Taylor, Mutagenesis of essential functional residues in acetylcholinesterase. *Proc Natl Acad Sci U S A.* 1990, 87, 7546-50.

[Gilson 1994] M.K. Gilson, T.P. Straatsma, J.A. McCammon, D.R. Ripoll, C.H. Faerman, P.H. Axelsen, I. Silman, and J.L. Sussman, Open "back door" in a molecular dynamics simulation of acetylcholinesterase. *Science.* 1994, 263, 1276-8.

[Gilley 2009] C. Gilley, M. MacDonald, F. Nachon, L.M. Schopfer, J. Zhang, J.R. Cashman and O. Lockridge, Nerve agent analogues that produce soman, sarin,

tabun and cyclohexil methylphosphonate-modified human butyrylcholinesterase. *Chem Res Toxicol.* 2009, 22, 1680-1688.

[Gonzalez 1994] A. Gonzalez, and C. Nave, Radiation damage in protein crystals at low temperature. *Acta Crystallogr D Biol Crystallogr.* 1994, 50, 874-7.

[Greenblatt 1999] H.M. Greenblatt, G. Kryger, T. Lewis, I. Silman, and J.L. Sussman, Structure of acetylcholinesterase complexed with (-)-galanthamine at 2.3 A resolution. *FEBS Lett.* 1999, 463, 321-6.

[Greenblatt 2003] H.M. Greenblatt, H. Dvir, I. Silman, and J.L. Sussman, Acetylcholinesterase: a multifaceted target for structure-based drug design of anticholinesterase agents for the treatment of Alzheimer's disease. *J Mol Neurosci.* 2003, 20, 369-83.

[Greenblatt 2004] H.M. Greenblatt, C. Guillou, D. Guenard, A. Argaman, S. Botti, B. Badet, C. Thal, I. Silman, and J.L. Sussman, The complex of a bivalent derivative of galanthamine with torpedo acetylcholinesterase displays drastic deformation of the active-site gorge: implications for structure-based drug design. *J Am Chem Soc.* 2004, 126, 15405-11.

[Grubic 1995] Z. Grubic, A. Stalc, M. Sentjurc, S. Pecar, M.K. Gentry, and B.P. Doctor, Different effects of two peripheral anionic site-binding ligands on acetylcholinesterase active-site gorge topography revealed by electron paramagnetic resonance. *Biochim Biophys Acta.* 1995, 1249, 155-60.

[Hansmann 2009] T. Hansmann, B. Sanson, J. Stojan, M. Weik, J.L. Marty, and D. Fournier, Kinetic insight into the mechanism of cholinesterasterase inhibition by aflatoxin B1 to develop biosensors. *Biosens Bioelectron.* 2009, 24, 2119-24.

[Harel 1992] M. Harel, J.L. Sussman, E. Krejci, S. Bon, P. Chanal, J. Massoulie, and I. Silman, Conversion of acetylcholinesterase to butyrylcholinesterase: modeling and mutagenesis. *Proc Natl Acad Sci U S A.* 1992, 89, 10827-31.

[Harel 1993] M. Harel, I. Schalk, L. Ehret-Sabatier, F. Bouet, M. Goeldner, C. Hirth, P.H. Axelsen, I. Silman, and J.L. Sussman, Quaternary ligand binding to aromatic residues in the active-site gorge of acetylcholinesterase. *Proc Natl Acad Sci U S A.* 1993, 90, 9031-5.

[Harel 1995] M. Harel, G.J. Kleywegt, R.B. Ravelli, I. Silman, and J.L. Sussman, Crystal structure of an acetylcholinesterase-fasciculin complex: interaction of a three-fingered toxin from snake venom with its target. *Structure.* 1995, 3, 1355-66.

[Harel 1996] M. Harel, D.M. Quinn, H.K. Nair, I. Silman, and J.L. Sussman, The X-ray Structure of a Transition State Analog Complex Reveals the Molecular Origins of the Catalytic Power and Substrate Specificity of Acetylcholinesterase. *J Am Chem Soc.* 1996, 118, 2340-2346.

[Harel 2005] M. Harel, J.L. Hyatt, B. Brumshtein, C.L. Morton, R.M. Wadkins, I. Silman, J.L. Sussman, and P.M. Potter, The 3D structure of the anticancer prodrug CPT-11 with Torpedo californica acetylcholinesterase rationalizes its inhibitory action on AChE and its hydrolysis by butyrylcholinesterase and carboxylesterase. *Chem Biol Interact.* 2005, 157-158, 153-7.

[Harel 2008] M. Harel, L.K. Sonoda, I. Silman, J.L. Sussman, and T.L. Rosenberry, Crystal structure of thioflavin T bound to the peripheral site of Torpedo californica acetylcholinesterase reveals how thioflavin T acts as a sensitive fluorescent reporter of ligand binding to the acylation site. *J Am Chem Soc.* 2008, 130, 7856-61.

[Hasinoff 1982] B.B. Hasinoff, Kinetics of acetylthiocholine binding to electric eel acetylcholinesterase in glycerol/water solvents of increased viscosity. Evidence for a diffusion-controlled reaction. *Biochim Biophys Acta.* 1982, 704, 52-8.

[Haviv 2005] H. Haviv, D.M. Wong, H.M. Greenblatt, P.R. Carlier, Y.P. Pang, I. Silman, and J.L. Sussman, Crystal packing mediates enantioselective ligand recognition at the peripheral site of acetylcholinesterase. *J Am Chem Soc.* 2005, 127, 11029-36.

[Hebert 2003] L.E. Hebert, P.A. Scherr, J.L. Bienias, D.A. Bennett, and D.A. Evans, Alzheimer disease in the US population: prevalence estimates using the 2000 census. *Arch Neurol.* 2003, 60, 1119-22.

[Henderson 1990] R. Henderson, Cryo-Protection of Protein Crystals against Radiation Damage in Electron and X-Ray Diffraction. *Proc R Soc Lond B.* 1990, 241, 6-8.

[Henzler-Wildman 2007a] K. Henzler-Wildman, and D. Kern, Dynamic personalities of proteins. *Nature.* 2007, 450, 964-72.

[Henzler-Wildman 2007b] K.A. Henzler-Wildman, V. Thai, M. Lei, M. Ott, M. Wolf-Watz, T. Fenn, E. Pozharski, M.A. Wilson, G.A. Petsko, M. Karplus, C.G. Hubner, and D. Kern, Intrinsic motions along an enzymatic reaction trajectory. *Nature.* 2007, 450, 838-44.

[Henzler-Wildman 2007c] K.A. Henzler-Wildman, M. Lei, V. Thai, S.J. Kerns, M. Karplus, and D. Kern, A hierarchy of timescales in protein dynamics is linked to enzyme catalysis. *Nature.* 2007, 450, 913-6.

[Herkenhoff 2004] S. Herkenhoff, L. Szinicz, V.K. Rastogi, T.C. Cheng, J.J. DeFrank, and F. Worek, Effect of organophosphorus hydrolysing enzymes on obidoxime-induced reactivation of organophosphate-inhibited human acetylcholinesterase. *Arch Toxicol.* 2004, 78, 338-43.

[Hobbiger 1959] F. Hobbiger, and P.W. Sadler, Protection against lethal organophosphate poisoning by quaternary pyridine aldoximes. *Br J Pharmacol Chemother.* 1959, 14, 192-201.

[Holzgrabe 2007] U. Holzgrabe, P. Kapkova, V. Alptuzun, J. Scheiber, and E. Kugelmann, Targeting acetylcholinesterase to treat neurodegeneration. *Expert Opin Ther Targets.* 2007, 11, 161-79.

[Hooft 1996] R.W. Hooft, G. Vriend, C. Sander, and E.E. Abola, Errors in protein structures. *Nature.* 1996, 381, 272.

[Hope 1988] H. Hope, Cryocrystallography of biological macromolecules: a generally applicable method. *Acta Crystallogr B.* 1988, 44 (Pt 1), 22-6.

[Hope 1990] H. Hope, Crystallography of biological macromolecules at ultra-low temperature. *Annu Rev Biophys Biophys Chem.* 1990, 19, 107-26.

[Hornberg 2007a] A. Hornberg, A.K. Tunemalm, and F. Ekstrom, Crystal structures of acetylcholinesterase in complex with organophosphorus compounds suggest that the acyl pocket modulates the aging reaction by precluding the formation of the trigonal bipyramidal transition state. *Biochemistry.* 2007, 46, 4815-25.

[Hornberg 2007b] A. Hornberg, A.K. Tunemalm, and F. Ekström, Crystal structures of acetylcholinesterase in complex with organophosphorus compounds suggest that the acyl pocket modulates the aging reaction by precluding the formation of the trigonal bipyramidal transition state. *Biochemistry.* 2007, 46, 4815-25.

[Inestrosa 1996] N.C. Inestrosa, A. Alvarez, C.A. Perez, R.D. Moreno, M. Vicente, C. Linker, O.I. Casanueva, C. Soto, and J. Garrido, Acetylcholinesterase accelerates assembly of amyloid-beta-peptides into Alzheimer's fibrils: possible role of the peripheral site of the enzyme. *Neuron.* 1996, 16, 881-91.

[Juers 2001] D.H. Juers, and B.W. Matthews, Reversible lattice repacking illustrates the temperature dependence of macromolecular interactions. *J Mol Biol.* 2001, 311, 851-62.

[Kabsch 1993] W. Kabsch, Automatic processing of rotation diffraction data from crystals of initially unknown symmetry and cell constants. *J Appl Cryst.* 1993, 26, 795-800.

[Kaplan 2001] D. Kaplan, A. Ordentlich, D. Barak, N. Ariel, C. Kronman, B. Velan, and A. Shafferman, Does "butyrylization" of acetylcholinesterase through substitution of the six divergent aromatic amino acids in the active center gorge generate an enzyme mimic of butyrylcholinesterase? *Biochemistry.* 2001, 40, 7433-45.

[Keijer 1969] J.H. Keijer, and G.Z. Wolring, Stereospecific aging of phosphonylated cholinesterases. *Biochim Biophys Acta.* 1969, 185, 465-8.

[Kewitz 1956] H. Kewitz, and I.B. Wilson, A specific antidote against lethal alkylphosphate intoxication. *Arch Biochem Biophys.* 1956, 60, 261-3.

[Kim 2009] C.U. Kim, B. Barstow, M.W. Tate, and S.M. Gruner, Evidence for liquid water during the high-density to low-density amorphous ice transition. *Proc Natl Acad Sci U S A.* 2009, 106, 4596-600.

[Kitz 1970] R.J. Kitz, L.M. Braswell, and S. Ginsburg, On the question: is acetylcholinesterase an allosteric protein? *Mol Pharmacol.* 1970, 6, 108-21.

[Klebe 2008] G. Klebe, The foundations of protein-ligand interaction, Crystallography and drug design, Erice, 2008.

[Koellner 2000] G. Koellner, G. Kryger, C.B. Millard, I. Silman, J.L. Sussman, and T. Steiner, Active-site gorge and buried water molecules in crystal structures of acetylcholinesterase from Torpedo californica. *J Mol Biol.* 2000, 296, 713-35.

[Koellner 2002] G. Koellner, T. Steiner, C.B. Millard, I. Silman, and J.L. Sussman, A neutral molecule in a cation-binding site: specific binding of a PEG-SH to acetylcholinesterase from Torpedo californica. *J Mol Biol.* 2002, 320, 721-5.

[Kovach 1994] I.M. Kovach, N. Qian, and A. Bencsura, Efficient product clearance through exit channels in substrate hydrolysis by acetylcholinesterase. *FEBS Lett.* 1994, 349, 60-4.

[Kovach 2004] I.M. Kovach, Stereochemistry and secondary reactions in the irreversible inhibition of serine hydrolases by organophosphorus compounds. *J Phys Org Chem.* 2004, 17, 602-614.

[Kovaleva 2007] E.G. Kovaleva, and J.D. Lipscomb, Crystal structures of Fe2+ dioxygenase superoxo, alkylperoxo, and bound product intermediates. *Science.* 2007, 316, 453-7.

[Kovarik 2004] Z. Kovarik, Z. Radic, H.A. Berman, V. Simeon-Rudolf, E. Reiner, and P. Taylor, Mutant cholinesterases possessing enhanced capacity for reactivation of their phosphonylated conjugates. *Biochemistry.* 2004, 43, 3222-9.

[Kovarik 2006] Z. Kovarik, M. Calic, A.L. Vrdoljak, and B. Radic, Interaction of pyridinium oximes with acetylcholinesterase and their effect on organophosphate-poisoned mice. *J Mol Neurosci.* 2006, 30, 113-4.

[Kronman 1994] C. Kronman, A. Ordentlich, D. Barak, B. Velan, and A. Shafferman, The "back door" hypothesis for product clearance in acetylcholinesterase challenged by site-directed mutagenesis. *J Biol Chem.* 1994, 269, 27819-22.

[Kryger 1998] G. Kryger, I. Silman, and J.L. Sussman, Three-dimensional structure of a complex of E2020 with acetylcholinesterase from Torpedo californica. *J Physiol Paris.* 1998, 92, 191-4.

[Kryger 2000] G. Kryger, M. Harel, K. Giles, L. Toker, B. Velan, A. Lazar, C. Kronman, D. Barak, N. Ariel, A. Shafferman, I. Silman, and J.L. Sussman, Structures of recombinant native and E202Q mutant human acetylcholinesterase complexed with the snake-venom toxin fasciculin-II. *Acta Crystallogr D Biol Crystallogr.* 2000, 56, 1385-94.

[Lakowicz 2006] J.R. Lakowicz, Principles of fluorescence spectroscopy, Springer, New York, 2006.

[le Du 1996] M.H. le Du, D. Housset, P. Marchot, P.E. Bougis, J. Navaza, and J.C. Fontecilla-Camps, Structure of fasciculin 2 from green mamba snake venom: evidence for unusual loop flexibility. *Acta Crystallogr D Biol Crystallogr.* 1996, 52, 87-92.

[Leiros 2001] H.K. Leiros, S.M. McSweeney, and A.O. Smalas, Atomic resolution structures of trypsin provide insight into structural radiation damage. *Acta Crystallogr D Biol Crystallogr.* 2001, 57, 488-97.

[Leslie 2006] A.G. Leslie, The integration of macromolecular diffraction data. *Acta Crystallogr D Biol Crystallogr.* 2006, 62, 48-57.

[Li 2005] W. Li, R. Pi, H.H. Chan, H. Fu, N.T. Lee, H.W. Tsang, Y. Pu, D.C. Chang, C. Li, J. Luo, K. Xiong, Z. Li, H. Xue, P.R. Carlier, Y. Pang, K.W. Tsim, M. Li, and Y. Han, Novel dimeric acetylcholinesterase inhibitor bis7-tacrine, but not donepezil, prevents glutamate-induced neuronal apoptosis by blocking N-methyl-D-aspartate receptors. *J Biol Chem.* 2005, 280, 18179-88.

[Lindorff-Larsen 2005] K. Lindorff-Larsen, R.B. Best, M.A. Depristo, C.M. Dobson, and M. Vendruscolo, Simultaneous determination of protein structure and dynamics. *Nature.* 2005, 433, 128-32.

[Lobo 2000] A. Lobo, L.J. Launer, L. Fratiglioni, K. Andersen, A. Di Carlo, M.M. Breteler, J.R. Copeland, J.F. Dartigues, C. Jagger, J. Martinez-Lage, H. Soininen, and A. Hofman, Prevalence of dementia and major subtypes in Europe: A collaborative study of population-based cohorts. Neurologic Diseases in the Elderly Research Group. *Neurology.* 2000, 54, S4-9.

[Lockridge 1997] O. Lockridge, R.M. Blong, P. Masson, M.T. Froment, C.B. Millard, and C.A. Broomfield, A single amino acid substitution, Gly117His, confers phosphotriesterase (organophosphorus acid anhydride hydrolase) activity on human butyrylcholinesterase. *Biochemistry.* 1997, 36, 786-95.

[Luo 1999] C. Luo, A. Saxena, M. Smith, G. Garcia, Z. Radic, P. Taylor, and B.P. Doctor, Phosphoryl oxime inhibition of acetylcholinesterase during oxime reactivation is prevented by edrophonium. *Biochemistry.* 1999, 38, 9937-47.

[Luo 2003] C. Luo, H. Leader, Z. Radic, D.M. Maxwell, P. Taylor, B.P. Doctor, and A. Saxena, Two possible orientations of the HI-6 molecule in the reactivation of organophosphate-inhibited acetylcholinesterase. *Biochem Pharmacol.* 2003, 66, 387-92.

[Luo 2007] C. Luo, M. Tong, N. Chilukuri, K. Brecht, D.M. Maxwell, and A. Saxena, An in vitro comparative study on the reactivation of nerve agent-inhibited guinea pig and human acetylcholinesterases by oximes. *Biochemistry.* 2007, 46, 11771-9.

[Macilwain 1993] C. Macilwain, Study proves Iraq used nerve gas. *Nature.* 1993, 363, 3.

[Mallender 2000] W.D. Mallender, T. Szegletes, and T.L. Rosenberry, Acetylthiocholine binds to asp74 at the peripheral site of human acetylcholinesterase as the first step in the catalytic pathway. *Biochemistry.* 2000, 39, 7753-63.

[Marchot 1993] P. Marchot, A. Khelif, Y.H. Ji, P. Mansuelle, and P.E. Bougis, Binding of 125I-fasciculin to rat brain acetylcholinesterase. The complex still binds diisopropyl fluorophosphate. *J Biol Chem.* 1993, 268, 12458-67.

[Marrs 1993] T.C. Marrs, Organophosphate poisoning. *Pharmacol Ther.* 1993, 58, 51-66.

[Masson 1994] P. Masson, P. Gouet, and C. Clery, Pressure and propylene carbonate denaturation of native and "aged" phosphorylated cholinesterase. *J Mol Biol.* 1994, 238, 466-78.

[Masson 1996] P. Masson, M.T. Froment, C.F. Bartels and O. Lockridge, Asp70 in the peripheral anionic site of human butyrylcholinesterase. *Eur J Biochem.* 1996, 235, 36-48.

[Masson 1997] P. Masson, P. Legrand, C.F. Bartels, M.T. Froment, L.H. Schopfer and O. Lockridge, Role of aspartate 70 and tryptophan 82 in binding of succinyldithiocholine to human butyrylcholinesterase. *Biochem.* 1997, 36, 2266-77.

[Masson 1999] P. Masson, C. Clery, P. Guerra, A. Redslob, C. Albaret, and P.L. Fortier, Hydration change during the aging of phosphorylated human butyrylcholinesterase: importance of residues aspartate-70 and glutamate-197 in the water network as probed by hydrostatic and osmotic pressures. *Biochem J.* 1999, 343 Pt 2, 361-9.

[Masson 2008] P. Masson, F. Nachon, C.A. Broomfield, D.E. Lenz, L. Verdier, L.M. Schopfer, and O. Lockridge, A collaborative endeavor to design cholinesterase-based catalytic scavengers against toxic organophosphorus esters. *Chem Biol Interact.* 2008, 175, 273-80.

[Masson 2009] P. Masson, E. Carletti, and F. Nachon, Structure, Activities and Biomedical Applications of Human Butyrylcholinesterase. *Protein Pept Lett.* 2009, 16, 1215-24.

[Maxwell 2001] D.M. Maxwell, and K.M. Brecht, Carboxylesterase: specificity and spontaneous reactivation of an endogenous scavenger for organophosphorus compounds. *J Appl Toxicol.* 2001, 21 Suppl 1, S103-7.

[McPherson 2002] A. McPherson, Introduction to macromolecular crystallography, Wiley-Liss, Hoboken, N.J., 2002.

[McPherson 1976] A. McPherson, Jr., The growth and preliminary investigation of protein and nucleic acid crystals for X-ray diffraction analysis. *Methods Biochem Anal.* 1976, 23, 249-345.

[Mesulam 1992] M. Mesulam, K. Carson, B. Price, and C. Geula, Cholinesterases in the amyloid angiopathy of Alzheimer's disease. *Ann Neurol.* 1992, 31, 565-9.

[Mesulam 2002] M. Mesulam, A. Guillozet, P. Shaw, and B. Quinn, Widely spread butyrylcholinesterase can hydrolyze acetylcholine in the normal and Alzheimer brain. *Neurobiol Dis.* 2002, 9, 88-93.

[Michel 1967] H.O. Michel, B.E. Hackley, Jr., L. Berkowitz, G. List, E.B. Hackley, W. Gillilan, and M. Pankau, Ageing and dealkylation of Soman (pinacolylmethylphosphonofluoridate)-inactivated eel cholinesterase. *Arch Biochem Biophys.* 1967, 121, 29-34.

[Millard 1995] C.B. Millard, O. Lockridge, and C.A. Broomfield, Design and expression of organophosphorus acid anhydride hydrolase activity in human butyrylcholinesterase. *Biochemistry.* 1995, 34, 15925-33.

[Millard 1998] C.B. Millard, O. Lockridge, and C.A. Broomfield, Organophosphorus acid anhydride hydrolase activity in human butyrylcholinesterase: synergy results in a somanase. *Biochemistry.* 1998, 37, 237-47.

[Millard 1999a] C.B. Millard, G. Koellner, A. Ordentlich, A. Shafferman, I. Silman, and J.L. Sussman, Reaction Products of Acetylcholinesterase and VX Reveal a Mobile Histidine in the Catalytic Triad. *J Am Chem Soc.* 1999, 121, 9883-9884.

[Millard 1999b] C.B. Millard, G. Kryger, A. Ordentlich, H.M. Greenblatt, M. Harel, M.L. Raves, Y. Segall, D. Barak, A. Shafferman, I. Silman, and J.L. Sussman,

Crystal structures of aged phosphonylated acetylcholinesterase: nerve agent reaction products at the atomic level. *Biochemistry.* 1999, 38, 7032-9.

[Minke 2000] W.E. Minke, J. Pickens, E.A. Merritt, E. Fan, C.L. Verlinde, and W.G. Hol, Structure of m-carboxyphenyl-alpha-D-galactopyranoside complexed to heat-labile enterotoxin at 1.3 A resolution: surprising variations in ligand-binding modes. *Acta Crystallogr D Biol Crystallogr.* 2000, 56, 795-804.

[Mishima 1998] O. Mishima, and H.E. Stanley, The relationship between liquid, supercooled and glassy water. *Nature.* 1998, 396, 329-335.

[Mitchell 1999] E. Mitchell, P. Kuhn, and E. Garman, Demystifying the synchrotron trip: a first time user's guide. *Structure.* 1999, 7, R111-21.

[Moran 1993] M.A. Moran, E.J. Mufson, and P. Gomez-Ramos, Colocalization of cholinesterases with beta amyloid protein in aged and Alzheimer's brains. *Acta Neuropathol.* 1993, 85, 362-9.

[Morel 1999] N. Morel, S. Bon, H.M. Greenblatt, D. Van Belle, S.J. Wodak, J.L. Sussman, J. Massoulie, and I. Silman, Effect of mutations within the peripheral anionic site on the stability of acetylcholinesterase. *Mol Pharmacol.* 1999, 55, 982-92.

[Mozzarelli 1996] A. Mozzarelli, and G.L. Rossi, Protein function in the crystal. *Annu Rev Biophys Biomol Struct.* 1996, 25, 343-65.

[Murshudov 1997] G.N. Murshudov, A.A. Vagin, and E.J. Dodson, Refinement of macromolecular structures by the maximum-likelihood method. *Acta Crystallogr D Biol Crystallogr.* 1997, 53, 240-55.

[Nachmansohn 1945] D. Nachmansohn, and M.A. Rothenberg, Studies on Cholinesterase. I. On the Specificity of the Enzyme in Nerve Tissue. *J Biol Chem.* 1945, 158, 653-666.

[Nagao 1997] M. Nagao, T. Takatori, Y. Matsuda, M. Nakajima, H. Iwase, and K. Iwadate, Definitive evidence for the acute sarin poisoning diagnosis in the Tokyo subway. *Toxicol Appl Pharmacol.* 1997, 144, 198-203.

[Nanao 2005] M.H. Nanao, G.M. Sheldrick, and R.B. Ravelli, Improving radiation-damage substructures for RIP. *Acta Crystallogr D Biol Crystallogr.* 2005, 61, 1227-37.

[Nanao 2006] M.H. Nanao, and R.B. Ravelli, Phasing macromolecular structures with UV-induced structural changes. *Structure.* 2006, 14, 791-800.

[Nave 2005] C. Nave, and E.F. Garman, Towards an understanding of radiation damage in cryocooled macromolecular crystals. *J Synchrotron Radiat.* 2005, 12, 257-60.

[Neely 1970] W.C. Neely, J.A. Lansden, and J.R. McDuffie, Spectral studies on the deoxyribonucleic acid-aflatoxin B1 system. Binding interactions. *Biochemistry.* 1970, 9, 1862-6.

[Nicolet 2003] Y. Nicolet, O. Lockridge, P. Masson, J.C. Fontecilla-Camps, and F. Nachon, Crystal structure of human butyrylcholinesterase and of its complexes with substrate and products. *J Biol Chem.* 2003, 278, 41141-7.

[Nolte 1980] H.J. Nolte, T.L. Rosenberry, and E. Neumann, Effective charge on acetylcholinesterase active sites determined from the ionic strength dependence of association rate constants with cationic ligands. *Biochemistry.* 1980, 19, 3705-11.

[Oldiges 1970] H. Oldiges, and K. Schoene, [Pyridinium and imidazolium salts as antidotes for soman and paraoxon poisoning in mice]. *Arch Toxikol.* 1970, 26, 293-305.

[Ollis 1992] D.L. Ollis, E. Cheah, M. Cygler, B. Dijkstra, F. Frolow, S.M. Franken, M. Harel, S.J. Remington, I. Silman, J. Schrag, and et al., The alpha/beta hydrolase fold. *Protein Eng.* 1992, 5, 197-211.

[Ordentlich 1993a] A. Ordentlich, D. Barak, C. Kronman, Y. Flashner, M. Leitner, Y. Segall, N. Ariel, S. Cohen, B. Velan, and A. Shafferman, Dissection of the human acetylcholinesterase active center determinants of substrate specificity. Identification of residues constituting the anionic site, the hydrophobic site, and the acyl pocket. *J Biol Chem.* 1993, 268, 17083-95.

[Ordentlich 1993b] A. Ordentlich, C. Kronman, D. Barak, D. Stein, N. Ariel, D. Marcus, B. Velan, and A. Shafferman, Engineering resistance to 'aging' of phosphylated human acetylcholinesterase. Role of hydrogen bond network in the active center. *FEBS Lett.* 1993, 334, 215-20.

[Ordentlich 1995] A. Ordentlich, D. Barak, C. Kronman, N. Ariel, Y. Segall, B. Velan, and A. Shafferman, Contribution of aromatic moieties of tyrosine 133 and of the anionic subsite tryptophan 86 to catalytic efficiency and allosteric modulation of acetylcholinesterase. *J Biol Chem.* 1995, 270, 2082-91.

[Ordentlich 1999] A. Ordentlich, D. Barak, C. Kronman, H.P. Benschop, L.P. De Jong, N. Ariel, R. Barak, Y. Segall, B. Velan, and A. Shafferman, Exploring the active center of human acetylcholinesterase with stereomers of an organophosphorus inhibitor with two chiral centers. *Biochemistry.* 1999, 38, 3055-66.

[Otting 1991] G. Otting, E. Liepinsh, and K. Wuthrich, Protein hydration in aqueous solution. *Science.* 1991, 254, 974-80.

[Owen 2006] R.L. Owen, E. Rudino-Pinera, and E.F. Garman, Experimental determination of the radiation dose limit for cryocooled protein crystals. *Proc Natl Acad Sci U S A.* 2006, 103, 4912-7.

[Painter 2006] J. Painter, and E.A. Merritt, Optimal description of a protein structure in terms of multiple groups undergoing TLS motion. *Acta Crystallogr D Biol Crystallogr.* 2006, 62, 439-50.

[Pang 2003] Y.P. Pang, T.M. Kollmeyer, F. Hong, J.C. Lee, P.I. Hammond, S.P. Haugabouk, and S. Brimijoin, Rational design of alkylene-linked bis-pyridiniumaldoximes as improved acetylcholinesterase reactivators. *Chem Biol.* 2003, 10, 491-502.

[Parak 1982] F. Parak, E.W. Knapp, and D. Kucheida, Protein dynamics. Mossbauer spectroscopy on deoxymyoglobin crystals. *J Mol Biol.* 1982, 161, 177-94.

[Parak 2003a] F.G. Parak, Physical aspects of protein dynamics. *Rep Prog Phys.* 2003, 103.

[Parak 2003b] F.G. Parak, Proteins in action: the physics of structural fluctuations and conformational changes. *Curr Opin Struct Biol.* 2003, 13, 552-7.

[Paz 2009] A. Paz, Q. Xie, H.M. Greenblatt, W. Fu, Y. Tang, I. Silman, Z. Qiu, and J.L. Sussman, The crystal structure of a complex of acetylcholinesterase with a bis-(-)-nor-meptazinol derivative reveals disruption of the catalytic triad. *J Med Chem.* 2009, 52, 2543-9.

[Petsko 1984] G.A. Petsko, and D. Ringe, Fluctuations in protein structure from X-ray diffraction. *Annu Rev Biophys Bioeng.* 1984, 13, 331-71.

[Petsko 2004] G.A. Petsko, and D. Ringe, Protein structure and function, New Science, London, 2004.

[Popovych 2006] N. Popovych, S. Sun, R.H. Ebright, and C.G. Kalodimos, Dynamically driven protein allostery. *Nat Struct Mol Biol.* 2006, 13, 831-8.

[Poziomek 1958] E.J. Poziomek, B.E. Hackley, and G.M. Steinberg, Pyridinium Aldoximes1. *J Org Chem.* 1958, 23, 714-717.

[Quinn 1987] D.M. Quinn, Acetylcholinesterase: enzyme structure, reaction dynamics, and virtual transition states. *Chem Rev.* 1987, 87, 955-979.

[Radic 1991] Z. Radic, E. Reiner, and P. Taylor, Role of the peripheral anionic site on acetylcholinesterase: inhibition by substrates and coumarin derivatives. *Mol Pharmacol.* 1991, 39, 98-104.

[Radic 1994] Z. Radic, R. Duran, D.C. Vellom, Y. Li, C. Cervenansky, and P. Taylor, Site of fasciculin interaction with acetylcholinesterase. *J Biol Chem.* 1994, 269, 11233-9.

[Radic 1995] Z. Radic, D.M. Quinn, D.C. Vellom, S. Camp, and P. Taylor, Allosteric control of acetylcholinesterase catalysis by fasciculin. *J Biol Chem.* 1995, 270, 20391-9.

[Radic 1999] Z. Radic, and P. Taylor, The influence of peripheral site ligands on the reaction of symmetric and chiral organophosphates with wildtype and mutant acetylcholinesterases. *Chem Biol Interact.* 1999, 119-120, 111-7.

[Radic 2001] Z. Radic, and P. Taylor, Interaction kinetics of reversible inhibitors and substrates with acetylcholinesterase and its fasciculin 2 complex. *J Biol Chem.* 2001, 276, 4622-33.

[Ramaroson 2003] H. Ramaroson, C. Helmer, P. Barberger-Gateau, L. Letenneur, and J.F. Dartigues, [Prevalence of dementia and Alzheimer's disease among subjects aged 75 years or over: updated results of the PAQUID cohort]. *Rev Neurol (Paris).* 2003, 159, 405-11.

[Ravelli 2000] R.B. Ravelli, and S.M. McSweeney, The 'fingerprint' that X-rays can leave on structures. *Structure.* 2000, 8, 315-28.

[Ravelli 2002] R.B. Ravelli, P. Theveneau, S. McSweeney, and M. Caffrey, Unit-cell volume change as a metric of radiation damage in crystals of macromolecules. *J Synchrotron Radiat.* 2002, 9, 355-60.

[Ravelli 2005] R.B. Ravelli, M.H. Nanao, A. Lovering, S. White, and S. McSweeney, Phasing in the presence of radiation damage. *J Synchrotron Radiat.* 2005, 12, 276-84.

[Raves 1997] M.L. Raves, M. Harel, Y.P. Pang, I. Silman, A.P. Kozikowski, and J.L. Sussman, Structure of acetylcholinesterase complexed with the nootropic alkaloid, (-)-huperzine A. *Nat Struct Biol.* 1997, 4, 57-63.

[Recanatini 2004] M. Recanatini, and P. Valenti, Acetylcholinesterase inhibitors as a starting point towards improved Alzheimer's disease therapeutics. *Curr Pharm Des.* 2004, 10, 3157-66.

[Richard 2007] J.L. Richard, Some major mycotoxins and their mycotoxicoses--an overview. *Int J Food Microbiol.* 2007, 119, 3-10.

[Richter 1942] D. Richter, and P.G. Croft, Blood esterases. *Biochem J.* 1942, 36, 746-57.

[Ripoll 1993] D.R. Ripoll, C.H. Faerman, P.H. Axelsen, I. Silman, and J.L. Sussman, An electrostatic mechanism for substrate guidance down the aromatic gorge of acetylcholinesterase. *Proc Natl Acad Sci U S A.* 1993, 90, 5128-32.

[Rochu 2007] D. Rochu, E. Chabriere, and P. Masson, Human paraoxonase: a promising approach for pre-treatment and therapy of organophosphorus poisoning. *Toxicology.* 2007, 233, 47-59.

[Rojas-Duran 2007] T.R. Rojas-Duran, C.A. Fente, B.I. Vazquez, C.M. Franco, A. Sanz-Medel, and A. Cepeda, Study of a room temperature phosphorescence phenomenon to allow the detection of aflatoxigenic strains in culture media. *Int J Food Microbiol.* 2007, 115, 149-58.

[Rosenberry 1975] T.L. Rosenberry, Catalysis by acetylcholinesterase: evidence that the rate-limiting step for acylation with certain substrates precedes general acid-base catalysis. *Proc Natl Acad Sci U S A.* 1975, 72, 3834-8.

[Rosenberry 1996] T.L. Rosenberry, C.R. Rabl, and E. Neumann, Binding of the neurotoxin fasciculin 2 to the acetylcholinesterase peripheral site drastically

reduces the association and dissociation rate constants for N-methylacridinium binding to the active site. *Biochemistry.* 1996, 35, 685-90.

[Rosenberry 1999] T.L. Rosenberry, W.D. Mallender, P.J. Thomas, and T. Szegletes, A steric blockade model for inhibition of acetylcholinesterase by peripheral site ligands and substrate. *Chem Biol Interact.* 1999, 119-120, 85-97.

[Rosenberry 2005] T.L. Rosenberry, J.L. Johnson, B. Cusack, J.L. Thomas, S. Emani, and K.S. Venkatasubban, Interactions between the peripheral site and the acylation site in acetylcholinesterase. *Chem Biol Interact.* 2005, 157-158, 181-9.

[Rosenberry 2008] T.L. Rosenberry, L.K. Sonoda, S.E. Dekat, B. Cusack, and J.L. Johnson, Analysis of the Reaction of Carbachol with Acetylcholinesterase Using Thioflavin T As a Coupled Fluorescence Reporter. *Biochemistry.* 2008,

[Rossmann 1962] M.G. Rossmann, and D.M. Blow, The detection of sub-units within the crystallographic asymmetric unit. *Acta Crystallographica.* 1962, 15, 24-31.

[Royant 2007] A. Royant, P. Carpentier, J. Ohana, J. McGeehan, B. Paetzold, M. Noirclerc-Savoye, X. Vernede, V. Adam, and D. Bourgeois, Advances in spectroscopic methods for biological crystals. 1. Fluorescence lifetime measurements. *J Appl Cryst.* 2007, 40, 1105-1112.

[Rupley 1991] J.A. Rupley, and G. Careri, Protein hydration and function. *Adv Protein Chem.* 1991, 41, 37-172.

[Russel 2009] D. Russel, K. Lasker, J. Phillips, D. Schneidman-Duhovny, J.A. Velazquez-Muriel, and A. Sali, The structural dynamics of macromolecular processes. *Curr Opin Cell Biol.* 2009, 21, 97-108.

[Rydberg 2006] E.H. Rydberg, B. Brumshtein, H.M. Greenblatt, D.M. Wong, D. Shaya, L.D. Williams, P.R. Carlier, Y.P. Pang, I. Silman, and J.L. Sussman, Complexes of alkylene-linked tacrine dimers with Torpedo californica acetylcholinesterase: Binding of Bis5-tacrine produces a dramatic rearrangement in the active-site gorge. *J Med Chem.* 2006, 49, 5491-500.

[Sabbagh 2009] M.N. Sabbagh, Drug development for Alzheimer's disease: Where are we now and where are we headed? *Am J Geriatr Pharmacother.* 2009, 7, 167-85.

[Sanson] B. Sanson, D. Fournier, J.L. Sussman, I. Silman, and M. Weik, Torpedo californica Acetylcholinesterase in Complex with the Peripheral Site Ligand Aflatoxin B1. submitted.

[Sanson 2009] B. Sanson, F. Nachon, J.P. Colletier, M.T. Froment, L. Toker, H.M. Greenblatt, J.L. Sussman, Y. Ashani, P. Masson, I. Silman, and M. Weik, Crystallographic snapshots of nonaged and aged conjugates of soman with acetylcholinesterase, and of a ternary complex of the aged conjugate with pralidoxime. *J Med Chem.* 2009, published online,

[Savini 2003] L. Savini, A. Gaeta, C. Fattorusso, B. Catalanotti, G. Campiani, L. Chiasserini, C. Pellerano, E. Novellino, D. McKissic, and A. Saxena, Specific targeting of acetylcholinesterase and butyrylcholinesterase recognition sites. Rational design of novel, selective, and highly potent cholinesterase inhibitors. *J Med Chem.* 2003, 46, 1-4.

[Saviotti 1974] M.L. Saviotti, and W.C. Galley, Room temperature phosphorescence and the dynamic aspects of protein structure. *Proc Natl Acad Sci U S A.* 1974, 71, 4154-8.

[Saxena 1993] A. Saxena, B.P. Doctor, D.M. Maxwell, D.E. Lenz, Z. Radic, and P. Taylor, The role of glutamate-199 in the aging of cholinesterase. *Biochem Biophys Res Commun.* 1993, 197, 343-9.

[Saxena 1998] A. Saxena, C. Viragh, D.S. Frazier, I.M. Kovach, D.M. Maxwell, O. Lockridge, and B.P. Doctor, The pH dependence of dealkylation in soman-

inhibited cholinesterases and their mutants: further evidence for a push-pull mechanism. *Biochemistry.* 1998, 37, 15086-96.

[Schalk 1994] I. Schalk, L. Ehret-Sabatier, F. Bouet, M. Goeldner, and C. Hirth, Trp279 is involved in the binding of quaternary ammonium at the peripheral site of Torpedo marmorata acetylcholinesterase. *Eur J Biochem.* 1994, 219, 155-9.

[Schalk 1995] I. Schalk, L. Ehret-Sabatier, Y. Le Feuvre, S. Bon, J. Massoulie, and M. Goeldner, 6-Coumarin diazonium salt: a specific affinity label of the Torpedo acetylcholinesterase peripheral site. *Mol Pharmacol.* 1995, 48, 1063-7.

[Schmitke 1997] J.L. Schmitke, L.J. Stern, and A.M. Klibanov, The crystal structure of subtilisin Carlsberg in anhydrous dioxane and its comparison with those in water and acetonitrile. *Proc Natl Acad Sci U S A.* 1997, 94, 4250-5.

[Schmitke 1998] J.L. Schmitke, L.J. Stern, and A.M. Klibanov, Comparison of x-ray crystal structures of an acyl-enzyme intermediate of subtilisin Carlsberg formed in anhydrous acetonitrile and in water. *Proc Natl Acad Sci U S A.* 1998, 95, 12918-23.

[Schneider 2000] T.R. Schneider, Objective comparison of protein structures: error-scaled difference distance matrices. *Acta Crystallogr D Biol Crystallogr.* 2000, 56, 714-21.

[Schneider 2002] T.R. Schneider, A genetic algorithm for the identification of conformationally invariant regions in protein molecules. *Acta Crystallogr D Biol Crystallogr.* 2002, 58, 195-208.

[Schotte 2004] F. Schotte, J. Soman, J.S. Olson, M. Wulff, and P.A. Anfinrud, Picosecond time-resolved X-ray crystallography: probing protein function in real time. *J Struct Biol.* 2004, 147, 235-46.

[Schuttelkopf 2004] A.W. Schuttelkopf, and D.M. van Aalten, PRODRG: a tool for high-throughput crystallography of protein-ligand complexes. *Acta Crystallogr D Biol Crystallogr.* 2004, 60, 1355-63.

[Segall 1993] Y. Segall, D. Waysbort, D. Barak, N. Ariel, B.P. Doctor, J. Grunwald, and Y. Ashani, Direct observation and elucidation of the structures of aged and nonaged phosphorylated cholinesterases by 31P NMR spectroscopy. *Biochemistry.* 1993, 32, 13441-50.

[Shafferman 1992a] A. Shafferman, C. Kronman, Y. Flashner, M. Leitner, H. Grosfeld, A. Ordentlich, Y. Gozes, S. Cohen, N. Ariel, D. Barak, and et al., Mutagenesis of human acetylcholinesterase. Identification of residues involved in catalytic activity and in polypeptide folding. *J Biol Chem.* 1992, 267, 17640-8.

[Shafferman 1992b] A. Shafferman, B. Velan, A. Ordentlich, C. Kronman, H. Grosfeld, M. Leitner, Y. Flashner, S. Cohen, D. Barak, and N. Ariel, Substrate inhibition of acetylcholinesterase: residues affecting signal transduction from the surface to the catalytic center. *Embo J.* 1992, 11, 3561-8.

[Shafferman 1994] A. Shafferman, A. Ordentlich, D. Barak, C. Kronman, R. Ber, T. Bino, N. Ariel, R. Osman, and B. Velan, Electrostatic attraction by surface charge does not contribute to the catalytic efficiency of acetylcholinesterase. *Embo J.* 1994, 13, 3448-55.

[Shafferman 1996] A. Shafferman, A. Ordentlich, D. Barak, D. Stein, N. Ariel, and B. Velan, Aging of phosphylated human acetylcholinesterase: catalytic processes mediated by aromatic and polar residues of the active centre. *Biochem J.* 1996, 318 (Pt 3), 833-40.

[Shi 2001] J. Shi, A.E. Boyd, Z. Radic, and P. Taylor, Reversibly bound and covalently attached ligands induce conformational changes in the omega loop, Cys69-Cys96, of mouse acetylcholinesterase. *J Biol Chem.* 2001, 276, 42196-204.

[Shi 2003] J. Shi, K. Tai, J.A. McCammon, P. Taylor, and D.A. Johnson, Nanosecond dynamics of the mouse acetylcholinesterase cys69-cys96 omega loop. *J Biol Chem.* 2003, 278, 30905-11.

[Silman 2005] I. Silman, and J.L. Sussman, Acetylcholinesterase: 'classical' and 'non-classical' functions and pharmacology. *Curr Opin Pharmacol.* 2005, 5, 293-302.

[Smith 1986] J.L. Smith, W.A. Hendrickson, R.B. Honzatko, and S. Sheriff, Structural heterogeneity in protein crystals. *Biochemistry.* 1986, 25, 5018-27.

[Soreq 2001] H. Soreq, and S. Seidman, Acetylcholinesterase--new roles for an old actor. *Nat Rev Neurosci.* 2001, 2, 294-302.

[Stedman 1932] E. Stedman, E. Stedman, and L.H. Easson, Choline-esterase. An enzyme present in the blood-serum of the horse. *Biochem J.* 1932, 26, 2056-66.

[Stedman 1935] E. Stedman, and E. Stedman, The relative choline-esterase activities of serum and corpuscles from the blood of certain species. *Biochem J.* 1935, 29, 2107-0.

[Stojan 1998] J. Stojan, V. Marcel, S. Estrada-Mondaca, A. Klaebe, P. Masson and D. Fournier, A putative kinetic model for substrate metabolisation by drosophila acetylcholinesterase. *FEBS Lett.* 1998. 440, 85-8.

[Stojan 2004] J. Stojan, L. Brochier, C. Alies, J.P. Colletier, and D. Fournier, Inhibition of Drosophila melanogaster acetylcholinesterase by high concentrations of substrate. *Eur J Biochem.* 2004, 271, 1364-71.

[Stroppolo 2001] M.E. Stroppolo, M. Falconi, A.M. Caccuri, and A. Desideri, Superefficient enzymes. *Cell Mol Life Sci.* 2001, 58, 1451-60.

[Suhre 2004] K. Suhre, and Y.H. Sanejouand, ElNemo: a normal mode web server for protein movement analysis and the generation of templates for molecular replacement. *Nucleic Acids Res.* 2004, 32, W610-4.

[Sussman 1991] J.L. Sussman, M. Harel, F. Frolow, C. Oefner, A. Goldman, L. Toker, and I. Silman, Atomic structure of acetylcholinesterase from Torpedo californica: a prototypic acetylcholine-binding protein. *Science.* 1991, 253, 872-9.

[Szegletes 1998] T. Szegletes, W.D. Mallender, and T.L. Rosenberry, Nonequilibrium analysis alters the mechanistic interpretation of inhibition of acetylcholinesterase by peripheral site ligands. *Biochemistry.* 1998, 37, 4206-16.

[Tai 2001] K. Tai, T. Shen, U. Borjesson, M. Philippopoulos, and J.A. McCammon, Analysis of a 10-ns molecular dynamics simulation of mouse acetylcholinesterase. *Biophys J.* 2001, 81, 715-24.

[Tai 2002] K. Tai, T. Shen, R.H. Henchman, Y. Bourne, P. Marchot, and J.A. McCammon, Mechanism of acetylcholinesterase inhibition by fasciculin: a 5-ns molecular dynamics simulation. *J Am Chem Soc.* 2002, 124, 6153-61.

[Taylor 1975] P. Taylor, and S. Lappi, Interaction of fluorescence probes with acetylcholinesterase. The site and specificity of propidium binding. *Biochemistry.* 1975, 14, 1989-97.

[Teng 1990] T.Y. Teng, Mounting of crystals for macromolecular crystallography in a free-standing thin film. *J Appl Cryst.* 1990, 23, 387-391.

[Theobald 2006] D.L. Theobald, and D.S. Wuttke, THESEUS: maximum likelihood superpositioning and analysis of macromolecular structures. *Bioinformatics.* 2006, 22, 2171-2.

[Vanderkooi 1987] J.M. Vanderkooi, D.B. Calhoun, and S.W. Englander, On the prevalence of room-temperature protein phosphorescence. *Science.* 1987, 236, 568-9.

[Velan 1996] B. Velan, D. Barak, N. Ariel, M. Leitner, T. Bino, A. Ordentlich, and A. Shafferman, Structural modifications of the omega loop in human acetylcholinesterase. *FEBS Lett.* 1996, 395, 22-8.

[Vigny 1978] M. Vigny, S. Bon, J. Massoulie, and F. Leterrier, Active-site catalytic efficiency of acetylcholinesterase molecular forms in Electrophorus, torpedo, rat and chicken. *Eur J Biochem.* 1978, 85, 317-23.

[Viragh 1997] C. Viragh, R. Akhmetshin, I.M. Kovach, and C. Broomfield, Unique push-pull mechanism of dealkylation in soman-inhibited cholinesterases. *Biochemistry.* 1997, 36, 8243-52.

[Vitkup 2000] D. Vitkup, D. Ringe, G.A. Petsko, and M. Karplus, Solvent mobility and the protein 'glass' transition. *Nat Struct Biol.* 2000, 7, 34-8.

[Wang 1967] E.I. Wang, and P.E. Braid, Oxime reactivation of diethylphosphoryl human serum cholinesterase. *J. Biol. Chem.* 1967, 242, 2683-7.

[Weik 2000] M. Weik, R.B. Ravelli, G. Kryger, S. McSweeney, M.L. Raves, M. Harel, P. Gros, I. Silman, J. Kroon, and J.L. Sussman, Specific chemical and structural damage to proteins produced by synchrotron radiation. *Proc Natl Acad Sci U S A.* 2000, 97, 623-8.

[Weik 2001a] M. Weik, G. Kryger, A.M. Schreurs, B. Bouma, I. Silman, J.L. Sussman, P. Gros, and J. Kroon, Solvent behaviour in flash-cooled protein crystals at cryogenic temperatures. *Acta Crystallogr D Biol Crystallogr.* 2001, 57, 566-73.

[Weik 2001b] M. Weik, R.B. Ravelli, I. Silman, J.L. Sussman, P. Gros, and J. Kroon, Specific protein dynamics near the solvent glass transition assayed by radiation-induced structural changes. *Protein Sci.* 2001, 10, 1953-61.

[Weik 2002] M. Weik, J. Berges, M.L. Raves, P. Gros, S. McSweeney, I. Silman, J.L. Sussman, C. Houee-Levin, and R.B. Ravelli, Evidence for the formation of disulfide radicals in protein crystals upon X-ray irradiation. *J Synchrotron Radiat.* 2002, 9, 342-6.

[Weik 2004] M. Weik, X. Vernede, A. Royant, and D. Bourgeois, Temperature derivative fluorescence spectroscopy as a tool to study dynamical changes in protein crystals. *Biophys J.* 2004, 86, 3176-85.

[Weik 2005] M. Weik, U. Lehnert, and G. Zaccai, Liquid-like water confined in stacks of biological membranes at 200 k and its relation to protein dynamics. *Biophys J.* 2005, 89, 3639-46.

[Westbrook 1997] E.M. Westbrook, and I. Naday, Charge-coupled device-based area detectors. *Methods Enzymol.* 1997, 276, 244-68.

[Whitehouse 1982] P.J. Whitehouse, D.L. Price, R.G. Struble, A.W. Clark, J.T. Coyle, and M.R. Delon, Alzheimer's disease and senile dementia: loss of neurons in the basal forebrain. *Science.* 1982, 215, 1237-9.

[Wilson 1955] I.B. Wilson, and S. Ginsburg, Reactivation of acetylcholinesterase inhibited by alkylphosphates. *Arch Biochem.* 1955, 54, 569-71.

[Wilson 1971] I.B. Wilson, and H.C. Froede, The design of reactivators for irreversibly blocked acetylcholinesterase. in: E.J. Ariens, (Ed.), Drug Design, Vol. II, Academic Press, New-York, 1971, pp. 213-229.

[Wins 1974] P. Wins, and I.B. Wilson, The inhibition of acetylcholinesterase by organophosphorus compounds containing a P---Cl bond. *Biochim Biophys Acta.* 1974, 334, 137-145.

[Wong 2003] D.M. Wong, H.M. Greenblatt, H. Dvir, P.R. Carlier, Y.F. Han, Y.P. Pang, I. Silman, and J.L. Sussman, Acetylcholinesterase complexed with bivalent ligands related to huperzine a: experimental evidence for species-dependent protein-ligand complementarity. *J Am Chem Soc.* 2003, 125, 363-73.

[Wong 2000] L. Wong, Z. Radic, R.J. Bruggemann, N. Hosea, H.A. Berman, and P. Taylor, Mechanism of oxime reactivation of acetylcholinesterase analyzed by chirality and mutagenesis. *Biochemistry.* 2000, 39, 5750-7.

[Wood 2008] K. Wood, A. Frolich, A. Paciaroni, M. Moulin, M. Hartlein, G. Zaccai, D.J. Tobias, and M. Weik, Coincidence of dynamical transitions in a soluble protein and its hydration water: direct measurements by neutron scattering and MD simulations. *J Am Chem Soc.* 2008, 130, 4586-7.

[Worek 2002] F. Worek, G. Reiter, P. Eyer, and L. Szinicz, Reactivation kinetics of acetylcholinesterase from different species inhibited by highly toxic organophosphates. *Arch Toxicol.* 2002, 76, 523-9.

[Worek 2004] F. Worek, H. Thiermann, L. Szinicz, and P. Eyer, Kinetic analysis of interactions between human acetylcholinesterase, structurally different organophosphorus compounds and oximes. *Biochem Pharmacol.* 2004, 68, 2237-48.

[Worek 2005] F. Worek, L. Szinicz, and H. Thiermann, Estimation of oxime efficacy in nerve agent poisoning: a kinetic approach. *Chem Biol Interact.* 2005, 157-158, 349-52.

[Worek 2007] F. Worek, P. Eyer, N. Aurbek, L. Szinicz, and H. Thiermann, Recent advances in evaluation of oxime efficacy in nerve agent poisoning by in vitro analysis. *Toxicol. Appl. Pharm.* 2007, 219, 226-34.

[Xu 2008a] H. Xu, and C.M. Weeks, Rapid and automated substructure solution by Shake-and-Bake. *Acta Crystallogr D Biol Crystallogr.* 2008, 64, 172-7.

[Xu 2008b] Y. Xu, J.P. Colletier, H. Jiang, I. Silman, J.L. Sussman, and M. Weik, Induced-fit or preexisting equilibrium dynamics? Lessons from protein crystallography and MD simulations on acetylcholinesterase and implications for structure-based drug design. *Protein Sci.* 2008, 17, 601-5.

[Xu 2008c] Y. Xu, J.P. Colletier, M. Weik, H. Jiang, J. Moult, I. Silman, and J.L. Sussman, Flexibility of aromatic residues in the active-site gorge of acetylcholinesterase: X-ray versus molecular dynamics. *Biophys J.* 2008, 95, 2500-11.

[Yang 2007] G.Y. Yang, K.A. Oh, N.J. Park, and Y.S. Jung, New oxime reactivators connected with CH2O(CH2)nOCH2 linker and their reactivation potency for organophosphorus agents-inhibited acetylcholinesterase. *Bioorg Med Chem.* 2007, 15, 7704-10.

[Yusupov 2001] M.M. Yusupov, G.Z. Yusupova, A. Baucom, K. Lieberman, T.N. Earnest, J.H. Cate, and H.F. Noller, Crystal structure of the ribosome at 5.5 A resolution. *Science.* 2001, 292, 883-96.

[Zeller 1943] E.A. Zeller, and A. Bissegger, Über die Cholin-esterase des Gehirns und der Erythrocyten. zugleich 3. Mitteilung über die Beeinflussung von Fermentreaktionen durch Chemotherapeutica und Pharmaka. *Helvetica Chimica Acta.* 1943, 26, 1619-1630.

ANNEXES

ANNEXE 1: Conformationnal flexibility in the peripheral site of *Torpedo californica* acetylcholinesterase revealed by the complex structure with a bifunctional inhibitor [Colletier, Sanson, Nachon, Gabellieri, Fattorusso, Campiani & Weik 2006].

ANNEXE 2: Kinetic insight into the mechanism of cholinesterase inhibition by aflatoxin B1 to develop biosensors [Hansmann, Sanson, Stojan, Weik, Marty & Fournier 2009].

ANNEXE 3: Use of a 'caged' analogue to study the traffic of choline with acetylcholinesterase by kinetic crystallography [Colletier, Royant, Specht, Sanson, Nachon, Masson, Zaccai, Sussman, Goeldner, Silman, Bourgeois & Weik 2007].

ANNEXE 4: Shoot-and-Trap: use of specific x-ray damage to study structural protein dynamics by temperature-controlled cryo-crystallography [Colletier, Bourgeois, Sanson, Fournier, Sussman, Silman & Weik 2008].

ANNEXE 5: Script python pour le traitement des données de phosphorescence.

J|A|C|S
COMMUNICATIONS

Published on Web 03/21/2006

Conformational Flexibility in the Peripheral Site of *Torpedo californica* Acetylcholinesterase Revealed by the Complex Structure with a Bifunctional Inhibitor

Jacques Ph. Colletier,[†] Benoît Sanson,[†] Florian Nachon,[‡] Emanuele Gabellieri,[§,||] Caterina Fattorusso,[||,⊥] Giuseppe Campiani,[§,||] and Martin Weik*[,†]

Laboratoire de Biophysique Moléculaire, Institut de Biologie Structurale, 38027 Grenoble, France, Unité d'Enzymologie, Centre de Recherche du Service de Santé des Armées, BP87-38702 La Tronche, France, Dipartimento Farmaco Chimico Tecnologico, via Aldo Moro, Universitá di Siena, 53100 Siena, Italy, European Research Centre for Drug Discovery and Development, University of Siena, Italy, Dipartimento di Chimica delle Sostanze Naturali, Universita' di Napoli Federico II, via D. Montesano 49, 80131 Napoli, Italy

Received December 22, 2005; E-mail: martin.weik@ibs.fr

X-ray crystallography is a powerful tool that provides time-averaged pictures of biological macromolecules. These seemingly static structures are in reality animated by molecular motions stemming from transitions between substates in a conformational energy landscape.[1] This landscape is characterized by a very large number of conformational substates, the population of which depends on their free energy. A crystallographic structure represents only the predominant substate of a molecule, and minor populations can usually not be assessed. Yet, the understanding of biological function on a molecular level requires knowledge about both structural and dynamical aspects of, e.g., an enzyme. This is particularly obvious for acetylcholinesterase (AChE), the active site of which is accessed by a deep and narrow gorge[2] that makes "breathing" motions essential for traffic of substrates and products to occur.[3] Here, we report the X-ray crystallographic structure of AChE from *Torpedo californica* (*Tc*AChE) in complex with a gorge-spanning inhibitor, NF595[4] (Figure 1). NF595 has been synthesized with a view to developing a new generation of anti-Alzheimer drugs, interacting with both the active and peripheral binding sites of AChEs. Surprisingly, and for the first time in *Tc*AChE, a major conformational change is observed upon complexation in the peripheral substrate-binding site. We suggest that this conformational substate is part of the equilibrium dynamics of the native enzyme and that it has been selected by inhibitor binding.

AChE is one of nature's fastest enzymes. Essential in the process of signal transmission in cholinergic synapses, AChE is responsible for the breakdown of the neurotransmitter acetylcholine into acetate and choline.[5] It is the target of all currently approved anti-Alzheimer drugs, of insecticides, and of chemical warfare agents. The first structure of an AChE revealed the buried nature of the active site and a peripheral substrate-binding site at the entrance of the gorge near the enzyme's surface[2] (Figure 2a). Numerous structures of *Tc*AChE in complex with various inhibitors have been solved, providing insights into inhibitor-induced conformational changes.[5] The conformation of the active-site gorge appears to be highly conserved, and the observed structural changes are small, except for those of Phe330.

Trigonal crystals of *Tc*AChE[2] were soaked into the mother liquor solution containing 2 mM NF595, loop-mounted, and flash-cooled at 100 K; diffraction data were collected on beamline ID14-EH2 at the European Synchrotron Radiation Facility. Structure refinement to a resolution of 2.2 Å included rigid body refinement, simulated annealing, energy minimization, and individual B-factor refinement (PDB accession code 2CEK).

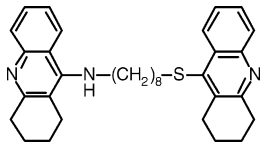

Figure 1. Structure of NF595 (referred to as compound 3h in ref 4). The heterodimer bears a tacrine moiety and a sulfur-containing tetrahydroacridine system connected by a 8-methylene linker.

NF595 spans the gorge, in agreement with previous docking studies,[4] and binds at the peripheral and the active sites (Figure 2b). Both heteroaromatic moieties are engaged in $\pi-\pi$ stacking interactions with two aromatic residues, i.e. with Trp84 and Phe330 in the lower part of the gorge, and with Trp279 and Tyr70 at the peripheral site. To make this parallel stacking mode possible, the side chains of both Phe330 and Trp279 rotate by about 90° with respect to their native positions. Whereas Phe330 is known to be a mobile residue, the conformational change of Trp279 has never been observed before in *Tc*AChE.

Bourne and collaborators recently determined the structure of mouse AChE (mAChE) in complex with a bifunctional inhibitor (*syn1* TZ2PA6) formed by in situ click chemistry.[6] This complex also revealed a 90° rotation of the mAChE Trp286, equivalent to *Tc*AChE Trp279, the key constituent of AChEs peripheral site. In the mAChE complex, Trp286 reorients in such a way that it is exposed to the solvent, whereas in the *Tc*AChE complex, Trp279 draws back toward the inside of the gorge. The two inhibitor-induced conformations of the peripheral-site tryptophan residues are thus 180° apart (Figure 2c). This conformational difference might be due either to the different inhibitors used or to the different packing patterns in crystals of *Tc*AChE and mAChE. The peripheral-site architecture in AChEs from different species, including mAChE, *Tc*AChE, and human AChE, is structurally conserved. Therefore, the inhibitor-induced conformations of Trp279 in *Tc*AChE and of Trp286 in mAChE are most probably part of a common energy landscape. They illustrate the wide range of conformations accessible to a functionally important residue. A smaller movement of Trp279 has also been observed in the crystal structure of *Tc*AChE in complex with DFP, in which a loop comprising this residue undergoes a conformational change.[7]

[†] Laboratoire de Biophysique Moléculaire, Institut de Biologie Structurale.
[‡] Unité d'Enzymologie, Centre de Recherche du Service de Santé des Armées.
[§] Dipartimento Farmaco Chimico Tecnologico, via Aldo Moro, Universitá di Siena.
[||] European Research Centre for Drug Discovery and Development, University of Siena.
[⊥] Dipartimento di Chimica delle Sostanze Naturali, Universita' di Napoli Federico II.

10.1021/ja058683b CCC: $33.50

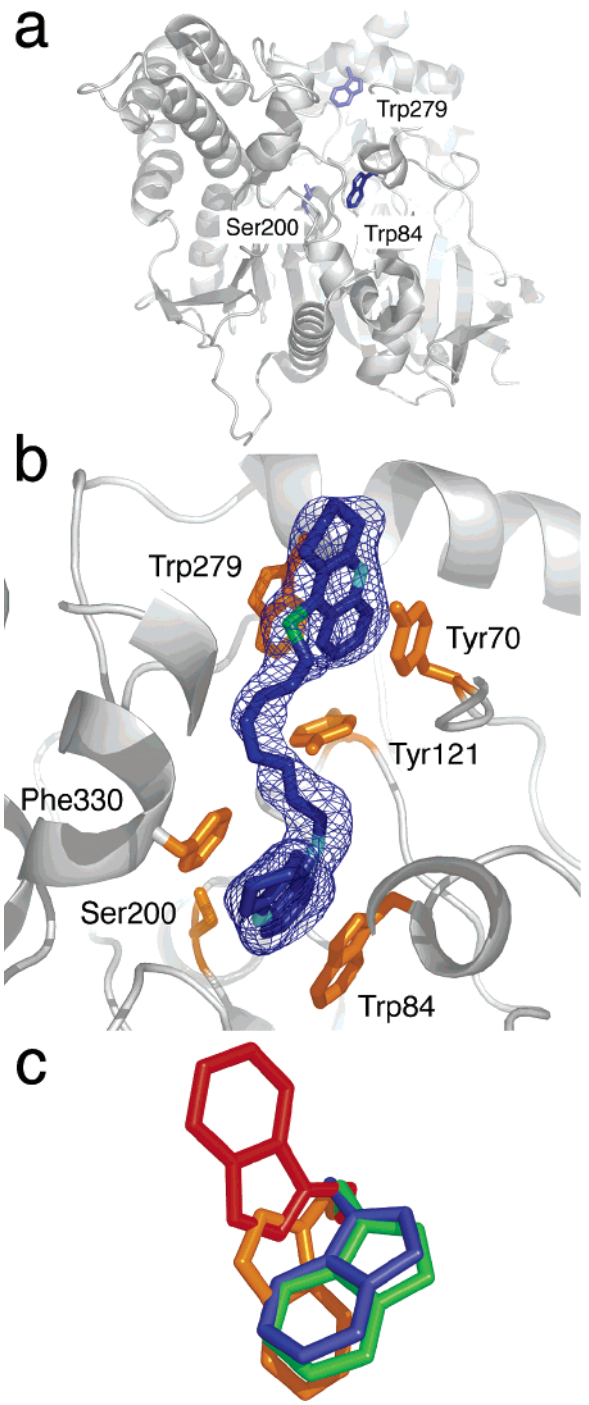

Figure 2. (a) 3D structure of native *Tc*AChE (PDB access code 1EA5), highlighting the catalytic Ser200 and Trp84 in the active and Trp279 at the peripheral substrate binding site. (b) The bifunctional inhibitor NF595 (S: green, N: light-blue, C: dark-blue) spans the gorge of *Tc*AChE. Its orientation was identified with the help of the strongly diffracting sulfur atom. Phe330 is present in two alternate conformations. Only the one close to NF595 is shown. The simulated-annealing omit map is contoured at 4.5 σ. (c) Conformational plasticity in the peripheral-site tryptophan (Trp279 of *Tc*AChE in the native (blue) and the NF595-bound (orange) structure and Trp286[6] of mAChE in the native (green) and an inhibitor-bound (red) structure. The χ values for the peripheral-site Trp side chains are: $\chi_1 = -61°$, $\chi_2 = 92°$ (Trp279 native), $\chi_1 = -116°$, $\chi_2 = -132°$ (Trp279 NF595), $\chi_1 = -60°$, $\chi_2 = 90°$ (Trp286 native) and $\chi_1 = -162°$, $\chi_2 = 52°$ (Trp286 *syn1* TZ2PA6). Panels a−c show the enzyme in very similar, yet not exactly identical orientations.

The AChE peripheral site has been shown to promote the growth and maturation of β-amyloid plates,[8] a process that is thought to be at the origin of neurodegeneration associated with Alzheimer disease. The observed mobility of the peripheral site should be of importance in the elaboration of models that aim at addressing the structural interaction between AChE and β-amyloid structures.

The observation of conformational flexibilities of the peripheral-site tryptophan, Phe330,[9] the catalytic His440,[10] and parts of the enzyme's wall near the acyl-binding pocket[11] draws a dynamic picture of the gorge and the active site in *Tc*AChE. Indeed, a delicate balance between rigidity and flexibility might resolve the apparent paradox between AChE catalytic efficiency and the reduced accessibility of its active site.

We suggest that the NF595 inhibitor selects a minor, yet already existing conformation of the complex energy landscape of the native enzyme. Indeed, experimental[12] and computational[13] evidence indicates that motions required for ligand binding or catalysis are already existing in the equilibrium dynamics of the native state of enzymes. Whether this holds true for Trp279 could be addressed by molecular dynamics simulations. The observed plasticity of functionally relevant structural elements is of importance for structure-based drug-design. Indeed, in the quest for tailor-made drugs, an enzyme should not be considered only as a rigid template, but conformational heterogeneity should be taken into account as well.[11] In this context, X-ray crystallography is a powerful tool that can address both structural and dynamical aspects of biological macromolecules.

Acknowledgment. We are grateful to Lilly Toker, Joel Sussman, and Israel Silman for providing us with purified *Tc*AChE and for a fruitful long-term collaboration, and to Martin Blackledge and Giuseppe Zaccai for critically reading the manuscript. We thank the ESRF staff for help during data collection. Financial support by the CEA to J.P.C. and M.W. is gratefully acknowledged.

Supporting Information Available: A movie, showing structural changes in the gorge upon binding of NF595, and X-ray data processing and structure refinement statistics. This material is available free of charge via the Internet at http://pubs.acs.org.

References

(1) Frauenfelder, H.; Sligar, S. G.; Wolynes, P. G. *Science* **1991**, *254*, 1598−1603.
(2) Sussman, J. L.; Harel, M.; Frolow, F.; Oefner, C.; Goldman, A.; Toker, L.; Silman, I. *Science* **1991**, *253*, 872−879.
(3) Shen, T.; Tai, K.; Henchman, R. H.; McCammon, J. A. *Acc. Chem. Res.* **2002**, *35*, 332−340.
(4) Savini, L.; Gaeta, A.; Fattorusso, C.; Catalanotti, B.; Campiani, G.; Chiasserini, L.; Pellerano, C.; Novellino, E.; McKissic, D.; Saxena, A. *J. Med. Chem.* **2003**, *46*, 1−4.
(5) Silman, I.; Sussman, J. L. *Curr. Opin. Pharmacol.* **2005**, *5*, 293−302.
(6) Bourne, Y.; Kolb, H. C.; Radic, Z.; Sharpless, K. B.; Taylor, P.; Marchot, P. *Proc. Natl. Acad. Sci. U.S.A.* **2004**, *101*, 1449−1454.
(7) Millard, C. B.; Kryger, G.; Ordentlich, A.; Greenblatt, H. M.; Harel, M.; Raves, M. L.; Segall, Y.; Barak, D.; Shafferman, A.; Silman, I.; Sussman, J. L. *Biochemistry* **1999**, *38*, 7032−7039.
(8) Inestrosa, N. C.; Alvarez, A.; Perez, C. A.; Moreno, R. D.; Vicente, M.; Linker, C.; Casanueva, O. I.; Soto, C.; Garrido, J. *Neuron* **1996**, *16*, 881−891.
(9) Kryger, G.; Silman, I.; Sussman, J. L. *Structure* **1999**, *7*, 297−307.
(10) Millard, C. B.; Koellner, G.; Ordentlich, A.; Shafferman, A.; Silman, I.; Sussman, J. L. *J. Am. Chem. Soc.* **1999**, *121*, 9883−9884.
(11) Greenblatt, H. M.; Guillou, C.; Guenard, D.; Argaman, A.; Botti, S.; Badet, B.; Thal, C.; Silman, I.; Sussman, J. L. *J. Am. Chem. Soc.* **2004**, *126*, 15405−15411.
(12) Eisenmesser, E. Z.; Millet, O.; Labeikovsky, W.; Korzhnev, D. M.; Wolf-Watz, M.; Bosco, D. A.; Skalicky, J. J.; Kay, L. E.; Kern, D. *Nature* **2005**, *438*, 117−121.
(13) Tobi, D.; Bahar, I. *Proc. Natl. Acad. Sci. U.S.A.* **2005**, *102*, 18908−18913.

JA058683B

Biosensors and Bioelectronics 24 (2009) 2119–2124

Contents lists available at ScienceDirect

Biosensors and Bioelectronics

journal homepage: www.elsevier.com/locate/bios

Kinetic insight into the mechanism of cholinesterasterase inhibition by aflatoxin B1 to develop biosensors

Tamara Hansmann[a,*], Benoît Sanson[b], Jure Stojan[c], Martin Weik[b], Jean-Louis Marty[d,*], Didier Fournier[a]

[a] Université de Toulouse, IPBS-CNRS 205 route de Narbonne, Toulouse, France
[b] Laboratoire de Biophysique Moléculaire, Institut de Biologie Structurale (CEA/CNRS/UJF), 41 rue Jules Horowitz, 38027 Grenoble Cedex 1, France
[c] Institute of Biochemistry, Medical Faculty, University of Ljubljana, Slovenia
[d] BIOMEM, Centre de Phytopharmacie, UPVD, 52 avenue Paul Alduy, 66860 Perpignan Cedex, France

ARTICLE INFO

Article history:
Received 15 August 2008
Received in revised form 13 October 2008
Accepted 5 November 2008
Available online 18 November 2008

Keywords:
Acetylcholinesterase
Aflatoxin B1
Enzyme
Inhibition
Biosensor
Peripheral site

ABSTRACT

In this paper, the inhibition effect of aflatoxin B1 on different species of cholinesterases was investigated to unravel action mechanism. The inhibition curves of several cholinesterase mutants (obtained by spectrophotometric measurements of enzyme activity, pS curves) were analyzed. They showed that this toxin reversibly inhibits cholinesterases by binding to a peripheral site located at the entrance of the active site gorge without entering inside the site. Electric eel enzyme revealed the highest inhibition extent with a binding constant estimated to 0.35 μM. This binding prevents the entrance of substrate en route to the catalytic site and also decreases chemical steps of the reaction at the catalytic site: acetylation is reduced to the half and deacetylation is reduced to the third. Electric eel acetylcholinesterase was used to settle an amperometric biosensor. The best detection was obtained by using 0.3 mU enzyme on the electrode and 0.5 mM ATCh in the solution. The limit of detection was 3 μM corresponding to 20% inhibition.

1. Introduction

Mycotoxins are fungal secondary products commonly present in contaminated food or animal feeds that can cause severe illnesses. The optimal growth temperature of moulds with mycotoxin production ranges between 24 and 35 °C and thus, affection of crops is mainly concerns humid and warm zones, principally subtropical and tropical countries (Williams et al., 2004) with important losses in terms of human health, animal health, and condemned agricultural products (Shane, 1994). Factors contributing to the presence or production of mycotoxins in food or feed include storage and environmental or ecological conditions. Aflatoxins, an especially aflatoxin B1 (AFB1), are one of the most toxic groups of mycotoxins. AFB1 is principally produced by *Aspergillus flavus* and *Aspergillus parasiticus* which afflict amylaceous semen like grains, maize, peanuts and pistachios. Aflatoxins structure was first time described in 1965 (Asao et al., 1965). Acute intoxication manifests as hepatotoxicity (Cullen and Newberne, 1994). Last severe outbreak of aflatoxicosis in humans took place between 2004 and 2005 in Kenya with over 150 deaths (Azziz-Baumgartner et al., 2005). Chronic subsymptomatic exposure provokes hepatic damage as well as nutritional and immunosuppressive effects like anorexia and decreased T-cell function (Williams et al., 2004; Azziz-Baumgartner et al., 2005; Hussein and Brasel, 2001). The known LD_{50} values for different animal species range between 0.3 and 10 mg/kg bodyweight (Wogan, 1966) and estimation of LD_{50} value for humans lies between 2 and 6 mg/kg bodyweight. Thus, a man with a weight of 70 kg would therefore die from an approximate single ingested dose of 140–420 mg with a probability of 50%.

Besides acute and chronic symptoms of aflatoxicosis, bioactivation of aflatoxin B1 by cytochrome P450 to its highly reactive aflatoxin-8-9-epoxide results in DNA adducts which induce mutagenic and carcinogenic effects in a dose-dependent manner. Most commonly aflatoxin B1 causes liver cancer especially in combination with other hepatic risk factors like hepatitis B virus infection (Croy et al., 1978; Muench et al., 1983; Bennett et al., 1981; Foster et al., 1983; Vinitketkumnuen et al., 1997). Consumption over a long time increases the risk of developing a hepatocarcinoma due to the accumulation of aflatoxin B1 in the liver during that life span. Thus, the WHO-International Agency for Research on Cancer described naturally occurring mixtures of aflatoxins in the environment to be

Abbreviations: AChE, acetylcholinesterase; BuChE, butyrylcholinesterase; ATCh, acetylthiocholine.

* Corresponding author. Fax: +33 4 68 66 22 23.
E-mail address: jlmarty@univ-perp.fr (J.-L. Marty).

0956-5663/$ – see front matter © 2008 Elsevier B.V. All rights reserved.
doi:10.1016/j.bios.2008.11.006

cancerogenic to humans and aflatoxin B1 was placed as a Class 1 carcinogen.

Due to its high toxicity, the U.S. Food and Drug Administration created a standard regulating the aflatoxins amount in food. It set the maximal value of overall aflatoxin B1 affliction at 20 ppb in grains and at 0.5 ppb in milk (U.S. Food and Drug Administration, 1995. Sec. 555.400) and European Union set limits of total aflatoxin concentration in groundnuts and cereals intended for direct human consumption to 4 ppb (commission regulation no 466/2001 of 8 March 2001).

In order to monitor and to regulate the food trade market in accordance to the established standards, routine analysis systems are required. Currently, qualitative and fast analysis of aflatoxin B1 traces is commonly carried out by ELISA immunoassays (Micheli et al., 2005; Piermarini et al., 2007; Zollner and Mayer-Helm, 2006). On the other hand, quantification is usually made using gas chromatography–mass spectrometry, thin-layer chromatography, liquid chromatography–mass spectrometry or high-performance liquid chromatography after extraction of aflatoxin B1 from contaminated food samples (Zollner and Mayer-Helm, 2006; Sugita-Konishi et al., 2006). However, sample analysis by these conventional methods is quite expensive and time consuming.

Recent reports suggest that biosensors using cholinesterase as biological component may be used to detect aflatoxin B1: aflatoxicosis has been correlated to a diminution of acetylcholine turnover in rat brain (Egbunike and Ikegwuonu, 1984), aflatoxin B1 inhibits acetylcholinesterase with a non-competitive inhibition pattern (Cometa et al., 2005) and further, a colorimetric biosensor using electric eel acetylcholinesterase was recently described (Arduini et al., 2007). The attempt of our study was to understand more about the mode of aflatoxin B1 action. We first wanted to establish if acetylcholinesterase (AChE) is inhibited by aflatoxin B1 at the same concentration range as it is known to induce acute toxic symptoms to humans. The second objective was to unravel the mechanism of AChE inhibition by steady state kinetic measurements and by using *in vitro* mutagenesis. The third attempt was to develop a field-compatible biosensor and to determine the detection limit.

2. Experimental procedures

2.1. Materials

Drosophila melanogaster AChE (Dm-AChE) were produced in baculovirus system and purified as already described (Chaabihi et al., 1994). Mutants were obtained as previously described (Boublik et al., 2002). Human AChE (Hu-AChE), human BuChE (Hu-BuChE) and *Electrophorus electricus* AChE (Ee-AChE) were purchased from Sigma Chemical Co. (St. Louis, MO, USA). *Torpedo californica* AChE (Tc-AChE) was kindly supplied for Lilly Toker and Israel Silman. Aflatoxin B1 (MW: 312) and acetylthiocholine (MW: 289) were from Sigma. Aflatoxin B1 was dissolved in ethanol (1 mM) and subsequent dilutions were made in water.

2.2. Kinetics

Hydrolysis of ATCh was measured using the Ellman method (Ellman et al., 1961). Briefly, the activity of the enzyme at 25 °C was evaluated by following the absorbance at 412 nm in 25 mM phosphate buffer, pH 7 for 1 min after the addition of the substrate to the mixture containing buffer, Ellman reagent, enzyme and AFB1. Chemical hydrolysis of substrate was subtracted. Substrate concentrations range was 10 μM to 300 mM, with a minimum of two repetitions per concentration value. The tested AFB1 concentrations were 1, 10, 50 and/or 100 μM, depending on the reaction. Data were analysed using the model and equation of Stojan et al. (2004a,b) for ATCh hydrolysis inhibition. Fittings were performed by multiple non-linear regressions using the program GOSA-fit (www.bio-log.biz).

2.3. Immobilization of Ee-AChE on electrodes and biosensor measurements

The electrodes were modified with cobalt-phthalocyanine as mediator (Gwent Electronic Materials, UK). 3 μL of a 1:1 mixture of polyvinylalcohol and the enzyme solution were automatically deposited on the working electrode surface with a micropipette and polymerized under neon light at 4 °C for 3 h. Sensors were then left in the dark at 4 °C for at least further 24 h.

The electrodes were then measured using a potentiostat in 10 ml of 100 mM phosphate buffer, pH 7 at 30 °C. ATCh was added to the buffer solution and it was hydrolysed by the immobilized enzymes. The mediator cobalt-phthalocyanine oxidised the product of the ATCh hydrolysis (thiocholine) and it was thus, reduced. The reoxidation of the mediator in the working electrode at +100 mV vs. Ag/AgCl pseudo-reference electrode generated a current that was linked to a flatbed recorder. In this work, the stability of the electrodes was checked by adding consecutively a fixed amount of substrate several times. Only when the current was the same after at least three measurements, the electrodes were considered stable and were incubated in phosphate buffer containing AFB1. The decrease in the substrate steady state current after addition of AFB1 was used to evaluate the inhibition extent. All measurements were accomplished with a minimum of two repetitions.

3. Results

3.1. Inhibition type and binding site

Regarding the literature, the kinetics of inhibition were analyzed using Dm-AChE because the pS curve displays activation and inhibition by substrate, allowing the estimation of some parameters describing substrate binding and hydrolysis (Stojan et al., 2004a,b; Colletier et al., 2006). It has been found that AFB1 inhibited cholinesterase activity in the μM range. However, no effect could be reported on the enzyme activity when pre-incubating acetylcholinesterase with AFB1 since it remained constant along the measurement time (5 min after addition of the last reaction component). Thus, AFB1 reversibly inhibits Dm-AChE, as it has been recently reported for Ee-AChE (Arduini et al., 2007). According to this result, the steady-state inhibition kinetics of AFB1 was analyzed by mixing enzyme, substrate and AFB1 and measuring the activity for 1 min.

The AFB1 binding model was analyzed using the model for acetylthiocholine (ATCh) hydrolysis with inhibitor involvement (Scheme 1). In this model, the substrate initially binds to the peripheral site (PAS), mainly consisting of Trp321 (Dm-AChE numbering), at the entrance of the active-site gorge, thereby resulting in the complex SpE. Gliding down the gorge to the catalytic site results in the formation of a Michaelis addition complex (ES), thus, setting free the peripheral site for another substrate molecule to give a ternary complex (SpES). At this point, the enzyme is acetylated (acetylated enzyme, EA, and SpEA) and choline is then released. In the next step, a water molecule approaches to the esteratic bond and induces deacetylation to regenerate the free enzyme (E). However, the binding of another substrate molecule to the peripheral site of the Michaelis complex, leading to SpES, may block the choline exit. Substrate binding at the peripheral site of the acetylated enzyme usually increases deacetylation ($a > 1$). However, the substrate molecule bound to the peripheral site can also enter deeper

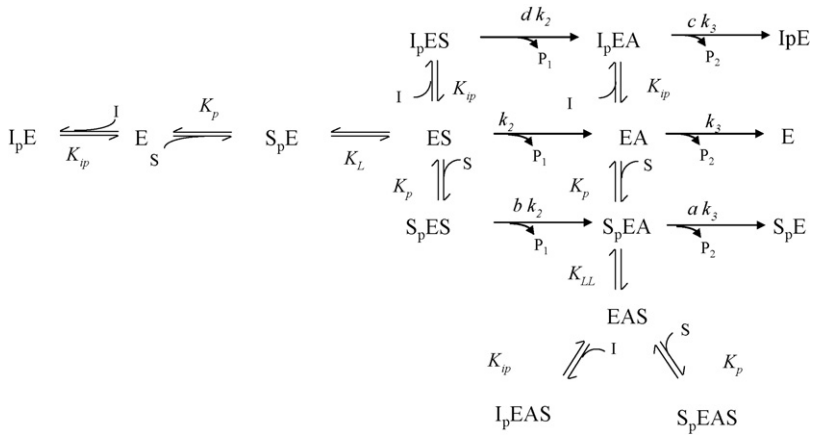

Scheme 1. Kinetic scheme used to analyse aflatoxin inhibition. 'E' represents the free AChE, 'EA' the acetylated enzyme, 'S' the substrate and 'I' the inhibitor. When a ligand is bound to the peripheral site, it is written on the left of 'E' with the subscript "p" added (SpE). When a ligand is bound at the catalytic site, the symbol is written on the right of 'E' (ES). Thus, SpEAS means that a substrate molecule is at the peripheral site and another substrate molecule at the catalytic site of acetylated enzyme. The general scheme for inhibitors was reduced for AFB1 by discarding the parts of the inhibitor binding at the catalytic site.

in the gorge of the acetylated enzyme (K_{LL}) thus, giving the EAS complex. At this stage, no water molecule can approach the ester bond and, as a consequence, the substrate molecule completely blocks deacetylation. Finally, if another substrate molecule binds to the peripheral site, a ternary complex between acetylated enzyme and two substrate molecules is formed (SpEAS). The derived initial rate equation for this model has been described in Stojan et al. (2004b).

Reversible inhibitors of AChE bind on the peripheral anionic site (PAS) and/or on the catalytic anionic site (CAS). Both binding positions prevents substrate hydrolysis either by corking the entrance to the active site (binding to PAS) or by the occupation of the choline binding site at the bottom of the gorge. The complete scheme corresponding to the binding to these two sites and its corresponding initial rate equation has been deeply detailed in Fekonja et al. (2007). Both binding sites can be distinguished with the fitting of the data by considering the presence of each complex: when the complexes IpE, IpES and IpEA are required for the fitting, the inhibitor binds to the peripheral site, but when the complexes EI, SEI are necessary, the inhibitor binds to the catalytic site. Whether all complexes are necessary, the inhibitor binds to both sites. The simplest model that fits on AFB1 inhibition data of substrate hydrolysis catalyzed by Dm-AChE was described as the binding of AFB1 to the peripheral site (Fig. 1A, Scheme 1, Eq. (1)) with an affinity estimated to 2.39 μM. Using an equation for the model of AFB1 binding in the catalytic site did not improve the fitting, showing that inhibition only results from the binding to the entrance of the active site, i.e. at the PAS. This binding impeded the entrance of substrate to the catalytic site, reduced deacetylation and increased the hindrance of choline exit thus, inhibiting the substrate hydrolysis. As substrate binds on the PAS before entering into the catalytic site, AFB1 behaved as a competitive inhibitor.

$$\frac{v}{[Et]} = \frac{k_3 \cdot k_2 \cdot [S]}{\frac{\left(k_3 \cdot K_p \cdot K_L \cdot \frac{1+[S]}{K_p} + \frac{[S]}{K_p \cdot K_L} + \frac{[S]^2}{K_p{}^2 \cdot K_L} + \frac{[S] \cdot [I]}{K_p \cdot K_{ip} \cdot K_L} + \frac{[I]}{K_{ip}}\right)}{\left(1 + \frac{b \cdot [S]}{K_p} + \frac{d \cdot [I]}{K_{ip}}\right)} + \frac{[S] \cdot k_2 \cdot \left(1 + \left(\frac{[S]}{K_p} + \frac{[S]}{K_p \cdot K_{LL}} + \frac{[S]^2}{K_p{}^2 \cdot K_{LL}} + \frac{[S]}{K_p} \cdot \frac{[I]}{K_{ip} \cdot K_{LL}} + \frac{[I]}{K_{ip}}\right)\right)}{1 + a \cdot \frac{[S]}{K_p} + c \cdot \frac{[I]}{K_{ip}}}} \quad (1)$$

Trp321, located at the entrance of the active site gorge is an essential residue of the PAS of Dm-AChE (corresponds to Trp279 in the Tc-AChE used for structural analysis). The binding of AFB1 to this site was verified by mutating this amino acid to alanine and the inhibition of the mutant by AFB1 was examined (Fig. 1B). Below 10 μM of AFB1 no inhibition could be observed, confirming that the binding of aflatoxin on the peripheral site was responsible for the inhibition observed with the wild type.

3.2. Sensitivity of cholinesterases to aflatoxin B1

Four species of AChE (beside Dm-AChE) were examined to find an acetylcholinesterase enzyme that reveals a high sensitivity towards AFB1. At AFB1 concentration ranging from 1 to 10 μM, inhibition was observed for all tested species except for Hu-BuChE (Fig. 1C–F). Hu-BuChE did not have a tryptophan in the PAS site, which was consistent with the lack of inhibition obtained even at 100 μM AFB1.

The affinity constants for the binding of AFB1 at the peripheral site (K_{ip} values) for Hu-AChE and Tc-AChE were in the same range than those obtained for Dm-AChE (~5 μM, Table 1). The lowest K_{ip} for the three inhibited enzyme species corresponded to Ee-AChE (0.5 μM). The effect of AFB1 on several *Drosophila* enzymes with mutations located at the entrance of the active site (R70V, Y71A, Y71D, Y71K, Y73A, W321L, W321N, W321del, L328F, Y370A) by fast screening of the hydrolysis of 1 mM ATCh at aflatoxin B1 concentrations of 1 and 10 μM was analyzed. However, anyone of these AChEs did not show more sensitive than Ee-AChE to AFB1.

3.3. Determination of the lowest aflatoxin B1 concentration detectable using an amperometric biosensor

Among all of examined AChEs, Ee-AChE was found to be inhibited by the lowest AFB1 concentrations and was used for developing the enzymatic biosensor. Initially, the optimal substrate concentration was established. The maximum inhibition was observed between 200 μM and 1 mM ATCh. At higher concentrations, reference and aflatoxin B1 curves converge as expected for a competitive inhibitor and further, substrate inhibition appears. Hence, no inhibition by the toxin could be observed at high substrate concentrations (Fig. 1). On the other hand, below 10 μM

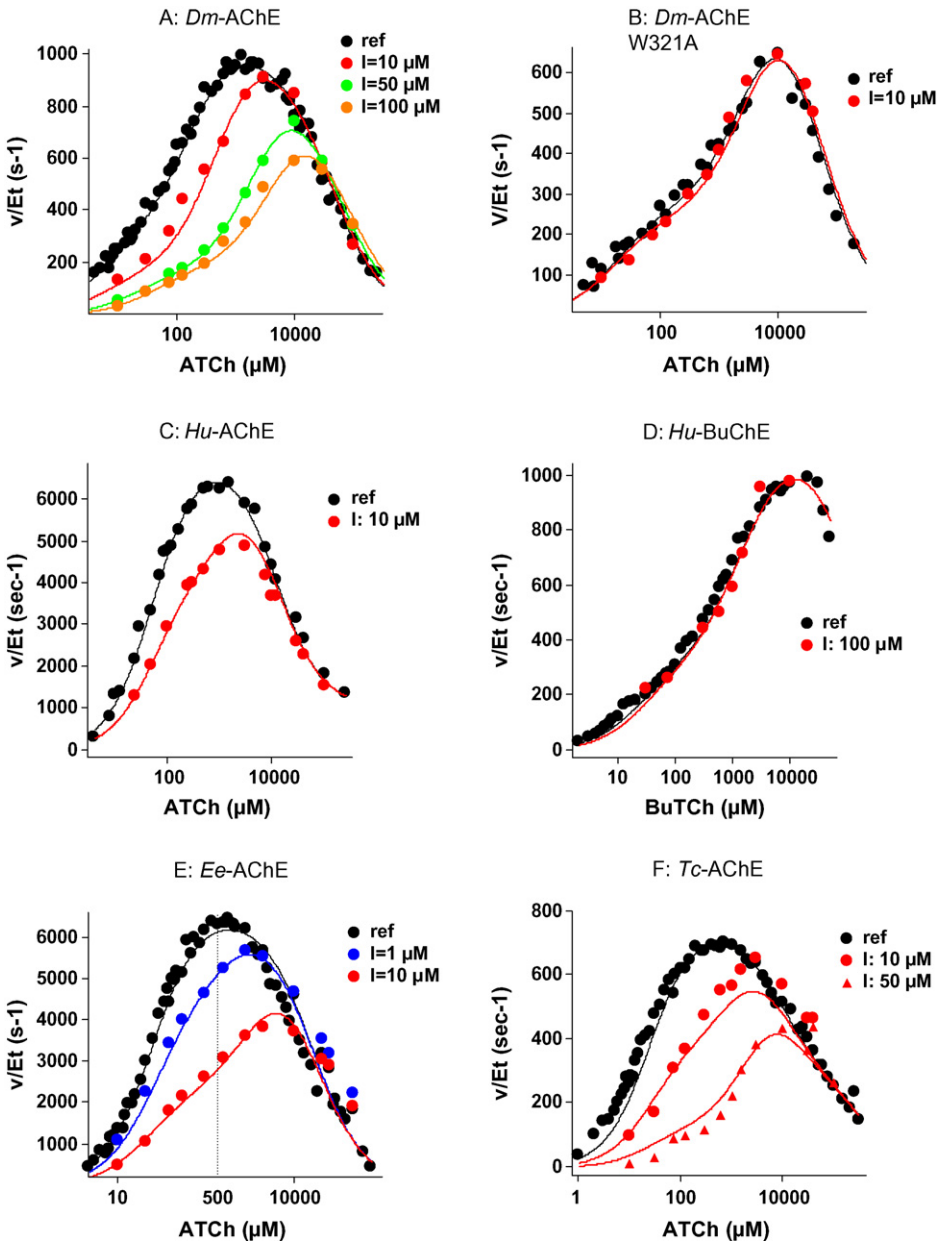

Fig. 1. Representation of the AFB1 inhibition curves for six AChE species. (A) *Drosophila melanogaster*-AChE. (B) *Drosophila melanogaster*-AChE peripheral site mutant. (C) *Human*-AChE. (D) *Human*-BuChE. (E) *Electric eel* AChE. (F) *Torpedo californica* AChE. ATCh concentration in µmol per litre; v/Et: substrate turnover, velocity/total enzyme concentration in s^{-1}.

measurements cannot be made because of the substrate depletion by enzyme hydrolysis during the experiment. Thus, a substrate concentration of 500 µM was chosen to obtain the maximum of inhibition (Fig. 2). Since detection values for inhibition by toxins can be quite variable, at least 20% inhibition is required to be sure of the authenticity of the results obtained which corresponds to a concentration of 3 µM AFB1.

4. Discussion

4.1. Binding site of aflatoxin B1

As previously discussed, AFB1 inhibits AChEs by binding at the peripheral site, located at the entrance of the active site gorge (at the tryptophan residue). It obstructs the entrance of the active site, substrate cannot enter to the catalytic site and choline cannot exit as proposed by the steric blockade model (Szegletes et al., 1998).

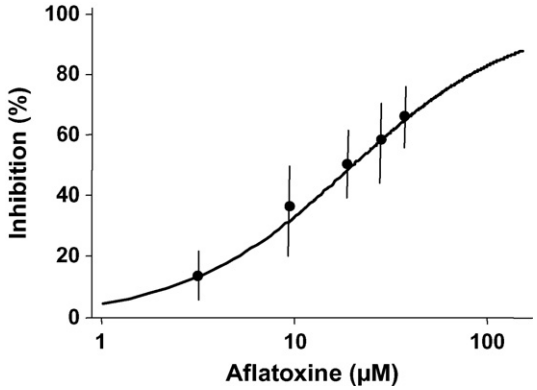

Fig. 2. Biosensor sensitivity. Inhibition of Ee-AChE immobilized on electrode as function of alfatoxin concentration and amount of enzyme immobilized on the electrode (1 mU corresponds to 1 fmol enzyme).

Table 1
Kinetic parameters estimated according to Scheme 1 for four AChE species (standard error).

	Substrate (ATCh)							Aflatoxin B1		
	K_p (μM)	K_i	K_{ii}	k_2 (s^{-1})	k_3 (s^{-1})	a	b	K_{ip} (μM)	c	d
Dm-AChE	159 (24)	4.06 (2.43)	190 (37)	44,563 (25,714)	347 (46)	3.82 (0.41)	0.078 (0.041)	2.39 (0.44)	1.1 (0.202)	0.023 (0.009)
Hu-AChE	543 (101)	0.018 (0.005)	9.23 (6.6)	14,375 (2,182)	13,471 (2,171)	1.6 (0.36)	0.01 (0.003)	5.1 (7.8)	3.28 (0.76)	0.155 (0.041)
Ee-AChE	319 (37)	1.29 (0.06)	66.4 (3.7)	73,957 (3,676)	7,165 (200)	1.52 (0.129)	0,077 (0.014)	0.35 (0.05)	0,34 (0.03)	0.53 (0.07)
Tc-AChE	449 (13)	1.7 (0.25)	269 (166)	24,000 (160)	836 (19)	0.93 (0.16)	0.017 (0.014)	9.8 (0.4)	0 (0.7)	0.017 (0.014)

These results emerged from the following observations: (1) Addition of a binding step of AFB1 inside the active site did not improve the description of inhibition, i.e. did not improve the fitting, which suggests that AFB1 does not slide to the catalytic site. (2) Mutation of Trp321 to alanine in Dm-AChE abolishes inhibition at 10 μM and 100 μM AFB1 does not inhibit Hu-BuChE. We may hypothesize that aflatoxin B1 does not enter into the active site because it is too big, especially when considering that its hydrophilic shell may further enlarge its size. Thus, aflatoxin is added to the list of ligands which bind on the peripheral site of cholinesterases such as propidium, gallanine or fasciculin (Bourne et al., 2003).

4.2. Comparison of binding constants with toxic doses to humans

One of the goals of this study was to address if cholinesterase inhibition plays a role in aflatoxicosis. Since no precise data of toxic amounts are available for humans, the of aflatoxin B1 for peripheral site (K_{ip}) of Hu-AChE (13 μmol/l) was compared to the known LD_{50} values for different animal species ranging between 1 and 32 μmol/kg bodyweight (Wogan, 1966). Actually, this value is in the same range, suggesting that acetylcholinesterase may be inhibited *in vivo* during aflatoxicosis. However, AFB1 is not homogeneously distributed in the body, but it accumulates in the liver, although neither reaches the muscles, nor the brain that contain the highest AChE density (Wogan, 1966). Aflatoxin B1 has been reported to inhibit other enzymes such as trypsin, amylase, lipase or cytochrome P450 (Guerre et al., 1997; Uwaifo, 1980) and aflatoxicosis has been associated with reduced activity levels of several enzymes (Osborne and Hamilton, 1981). Furthermore, some aflatoxin B1 metabolites are known to form adducts with proteins by conjugation with the ε-amino group of lysines. Thus, acetylcholinesterase represents one of few investigated enzymes whose activity is affected by AFB1 binding. Consequently, inhibition of acetylcholinesterase may not be significantly involved in aflatoxicosis etiopathology since hepatic, nutritional and immunologic symptoms are predominant.

4.3. Sensitivity of the biosensor

Attempting to create an AFB1 biosensor in the environment, the best conditions for a strong inhibition of Ee-AChE with small amounts of AFB1 were investigated.

Using the AChE biosensor, the minimum concentration of AFB1 detectable was 3 μM, corresponding to 1 mg/L. Regarding the fact that the European limit lays at 2 ppb (2 μg/kg) in grain and peanuts, it would be necessary to extract AFB1 from 0.5 kg of the crop sample and to concentrate the extract down to 1 mL or less. Thus, the sensitivity of Ee-AChE should be increased by mutagenesis to create an optimized biosensor able to facilitate the detection of AFB1 in the environment, compared to ELISA-immunoassays or chromatographic methods.

5. Conclusions

This paper confirms previous report claiming the inhibition of AChE by aflatoxin B1 (Cometa et al., 2005; Arduini et al., 2007). However, this inhibition does not seem to be involved in aflatoxicosis. The inhibition mechanisms of AFB1 were investigated using steady state kinetic measurements and *in vitro* mutagenesis. Experimental data suggests that inhibition comes from the binding of AFB1 on the peripheral site, located at the entrance of the active site. Binding constant has been found to depend on the enzyme source. Among studied enzymes, electric eel enzyme was the most sensitive with an affinity estimated to 0.35 μM. This enzyme was used for the development of a field-compatible biosensor. Its detection limit was estimated to 3 μM.

Acknowledgments

Financial support by the CEA, the CNRS and the UJF is acknowledged, as well as a grant to MW from the Agence Nationale de la Recherche (project number JC05-45685).

References

Arduini, F., Errico, I., Amine, A., Micheli, L., Palleschi, G., Moscone, D., 2007. Anal. Chem. 79, 3409–3415.
Asao, T., Buechi, G., Abdel-Kader, M.M., Chang, S.B., Wick, E.L., Wogan, G.N., 1965. J. Am. Chem. Soc. 87, 882–886.
Azziz-Baumgartner, E., Lindblade, K., Gieseker, K., Rogers, H.S., Kieszak, S., Njapau, H., Schleicher, R., McCoy, L.F., Misore, A., DeCock, K., Rubin, C., Slutsker, L., 2005. Environ. Health Perspect. 113, 1779–1783.
Bennett, R.A., Essigmann, J.M., Wogan, G.N., 1981. Cancer Res. 41, 650–654.
Boublik, Y., Saint-Aguet, P., Lougarre, A., Arnaud, M., Villatte, F., Estrada-Mondaca, S., Fournier, D., 2002. Protein Eng. 15, 43–50.
Bourne, Y., Taylor, P., Radic, Z., Marchot, P., 2003. EMBO J. 22, 1–12.
Chaabihi, H., Fournier, D., Fedon, Y., Bossy, J.P., Ravallec, M., Devauchelle, G., Cerutti, M., 1994. Biochem. Biophys. Res. Commun. 203, 734–742.
Colletier, J.P., Fournier, D., Greenblatt, H.M., Stojan, J., Sussman, J.L., Zaccai, G., Silman, I., Weik, M., 2006. EMBO J. 25, 2746–2756.
Cometa, M.F., Lorenzini, P., Fortuna, S., Volpe, M.T., Meneguz, A., Palmery, M., 2005. Toxicology 206, 125–135.
Croy, R.G., Essigmann, J.M., Reinhold, V.N., Wogan, G.N., 1978. Proc. Natl. Acad. Sci. U. S. A. 75, 1745–1749.
Cullen, J.M., Newberne, P.M., 1994. In: Eaton, D.L., Groopman, J.D. (Eds.), The Toxicology of Aflatoxins. Academic Press Inc., San Diego, pp. 3–21.
Egbunike, G.N., Ikegwuonu, F.I., 1984. Neurosci. Lett. 52, 171–174.
Ellman, G.L., Courtney, K.D., Andres Jr., V., Feather-Stone, R.M., 1961. Biochem. Pharmacol. 7, 88–95.
Fekonja, O., Zorec-Karlovsek, M., El Kharbili, M., Fournier, D., Stojan, J., 2007. J. Enzym. Inhib. Med. Chem. 22, 407–415.
Foster, P.L., Eisenstadt, E., Miller, J.H., 1983. Proc. Natl. Acad. Sci. U. S. A. 80, 2695–2698.
Guerre, P., Calleja, C., Burgat, V., Galtier, P., 1997. Chem. Biol. Interact. 107, 145–155.
Hussein, H.S., Brasel, J.M., 2001. Toxicology 167, 101–134.
Micheli, L., Grecco, R., Badea, M., Moscone, D., Palleschi, G., 2005. Biosens. Bioelectron. 21, 588–596.
Muench, K.F., Misra, R.P., Humayun, M.Z., 1983. Proc. Natl. Acad. Sci. U. S. A. 80, 6–10.
Osborne, D.J., Hamilton, P.B., 1981. Poult. Sci. 60, 1818–1821.
Piermarini, S., Micheli, L., Ammida, N.H., Palleschi, G., Moscone, D., 2007. Biosens. Bioelectron. 22, 1434–1440.
Shane, S.H., 1994. In: Eaton, D.L., Groopman, J.D. (Eds.), The Toxicology of Aflatoxins: Human Health, Veterinary, and Agricultural Significance. Academic Press, San Diego, pp. 513–527.
Stojan, J., Brochier, L., Alies, C., Colletier, J.P., Fournier, D., 2004a. Eur. J. Biochem. 271, 1364–1371.
Stojan, J., Golicnik, M., Fournier, D., 2004b. Biochim. Biophys. Acta 1703, 53–61.
Sugita-Konishi, Y., Nakajima, M., Tabata, S., Ishikuro, E., Tanaka, T., Norizuki, H., Itoh, Y., Aoyama, K., Fujita, K., Kai, S., Kumagai, S., 2006. J. Food Protect. 69, 1365–1370.
Szegletes, T., Mallender, W.D., Rosenberry, T.L., 1998. Biochemistry 37, 4206–4216.
Uwaifo, A.O., 1980. Toxicol. Lett. 7, 131–135.
Vinitketkumnuen, U., Chewonarin, T., Kongtawelert, P., Lertjanyarak, A., Peerakhom, S., Wild, C.P., 1997. Nat. Toxins 5, 168–171.
Williams, J.H., Phillips, T.D., Jolly, P.E., Stiles, J.K., Jolly, C.M., Aggarwal, D., 2004. Am. J. Clin. Nutr. 80, 1106–1122.
Wogan, G.N., 1966. Bacteriol. Rev. 30, 460–470.
Zollner, P., Mayer-Helm, B., 2006. J Chromatogr. A 1136, 123–169.

Acta Crystallographica Section D
Biological Crystallography
ISSN 0907-4449

Use of a 'caged' analogue to study the traffic of choline within acetylcholinesterase by kinetic crystallography

Jacques-Philippe Colletier,[a]‡ Antoine Royant,[b,c] Alexandre Specht,[d] Benoît Sanson,[a] Florian Nachon,[e] Patrick Masson,[e] Giuseppe Zaccai,[a,f] Joel L. Sussman,[g] Maurice Goeldner,[d] Israel Silman,[h] Dominique Bourgeois[b,c] and Martin Weik[a]*

[a]Laboratoire de Biophysique Moléculaire, Institut de Biologie Structurale 'Jean-Pierre EBEL', UMR 5075 CNRS-CEA-UJF, 38027 Grenoble, France, [b]Laboratoire de Cristallogenèse et de Cristallographie des Protéines, Institut de Biologie Structurale 'Jean-Pierre EBEL', UMR 5075 CNRS-CEA-UJF, 38027 Grenoble, France, [c]ESRF, 6 rue Jules Horowitz, BP 220, 38043 Grenoble Cedex, France, [d]Laboratoire de Chimie Bioorganique, UMR 7175–LC01 CNRS, Faculté de Pharmacie, Université Louis Pasteur, 74 Route du Rhin, 67400 Illkirch, France, [e]Unité d'Enzymologie, Centre de Recherches du Service de Santé des Armées, La Tronche, France, [f]Institut Laue-Langevin, 6 rue Jules Horowitz, BP 156, 38042 Grenoble, France, [g]Department of Structural Biology, Weizmann Institute of Science, 76100 Rehovot, Israel, and [h]Department of Neurobiology, Weizmann Institute of Science, 76100 Rehovot, Israel

‡ Present address: UCLA-DOE Institute of Genomics and Proteomics, University of California, Los Angeles, CA 90095-1570, USA.

Correspondence e-mail: weik@ibs.fr

Received 9 January 2007
Accepted 11 September 2007

PDB References: NPT-AsCh–*Tc*AChE complex, 2v96, r2v96sf; 2v97, r2v97sf; 2v98, r2v98sf; native *Tc*AChE, 2va9, r2va9sf.

Acetylcholinesterase plays a crucial role in nerve-impulse transmission at cholinergic synapses. The apparent paradox that it displays high turnover despite its active site being buried raises cogent questions as to how the traffic of substrates and products to and from the active site can occur so rapidly in such circumstances. Here, a kinetic crystallography strategy aimed at structurally addressing the issue of product traffic in acetylcholinesterase is presented, in which UV-laser-induced cleavage of a photolabile precursor of the enzymatic product analogue arsenocholine, 'caged' arsenocholine, is performed in a temperature-controlled X-ray crystallography regime. The 'caged' arsenocholine was shown to bind at both the active and peripheral sites of acetylcholinesterase. UV irradiation of a complex with acetylcholinesterase during a brief temperature excursion from 100 K to room temperature is most likely to have resulted in a decrease in occupancy by the caged compound. Microspectrophotometric experiments showed that the caged compound had indeed been photocleaved. It is proposed that a fraction of the arsenocholine molecules released within the crystal had been expelled from both the active and the peripheral sites. Partial q-weighted difference refinement revealed a relative movement of the two domains in acetylcholinesterase after photolysis and the room-temperature excursion, resulting in an increase in the active-site gorge volume of 30% and 35% in monomers A and B of the asymmetric unit, respectively. Moreover, an alternative route to the active-site gorge of the enzyme appeared to open. This structural characterization of acetylcholinesterase 'at work' is consistent with the idea that choline exits from the enzyme after catalysis either *via* the gorge or *via* an alternative 'backdoor' trajectory.

1. Introduction

Acetylcholinesterase (AChE) terminates nerve-impulse transmission at cholinergic synapses by rapid hydrolysis of the neurotransmitter acetylcholine (ACh; Rosenberry, 1975). This occurs in a two-step reaction: (i) the enzyme is acetylated with concomitant release of choline and (ii) a water molecule regenerates the free enzyme with concomitant release of acetic acid. In accordance with its crucial role, AChE is among the most efficient enzymes, with a turnover of 10^3–10^4 s^{-1} (Quinn, 1987; Silman & Sussman, 2005). It is also the target of a broad repertoire of poisons ranging from organophosphorus and carbamate insecticides (Casida & Quistad, 2005) and nerve agents (Millard & Broomfield, 1995) to natural toxins such as the alkaloid *d*-tubocurarine (Golicnik *et al.*, 2001) and fasciculin (FAS), a polypeptide toxin isolated from mamba

venom (Karlsson *et al.*, 1984). Furthermore, AChE is the target of the first generation of anti-Alzheimer drugs (Greenblatt *et al.*, 2003).

The crystal structure of *Torpedo californica* AChE (*Tc*AChE; Sussman *et al.*, 1991) unexpectedly revealed its active site to be deeply buried near the bottom of a narrow gorge. The enzyme is composed of two domains (Morel *et al.*, 1999) which face one another across the active-site gorge (Fig. 1). In addition to the active site, there is a second substrate-binding site, the peripheral anionic site (PAS), near the entrance to the gorge (Fig. 1; Colletier *et al.*, 2006). At the active site, the choline moiety of ACh is principally stabilized by a cation–π interaction with the indole ring of Trp84 (the residue numbering throughout the manuscript is that of *Tc*AChE), but also interacts with Glu199 and Phe330. The acetyl moiety also contributes to substrate stabilization in the active site by interactions of its carbonyl O atom and its methyl group with the 'oxyanion hole' (Gly117, Gly118 and Ala201) and the 'acyl pocket' (Trp233, Phe288, Phe290 and Phe331), respectively (Harel *et al.*, 1996; Colletier *et al.*, 2006). The catalytic triad, which is typical of a serine hydrolase, comprises Ser200, His440 and Glu327. The principal residues contributing to the PAS are Trp279, Tyr70, Tyr121 and Asp72. Site-directed mutagenesis, kinetic studies using PAS and catalytic anionic site (CAS) inhibitors (Radic *et al.*, 1991, 1994, 1995; Eichler *et al.*, 1994; Barak *et al.*, 1994; Golicnik *et al.*, 2001) and crystallographic studies of inhibitor–AChE complexes (Harel *et al.*, 1993; Bourne *et al.*, 1995; Harel *et al.*, 1995; Felder *et al.*, 2002) have produced a clear picture of the functional and structural architecture of the active-site gorge. Recently, X-ray crystallography has revealed structural details of substrate and product binding at both the CAS and the PAS (Colletier *et al.*, 2006; Bourne *et al.*, 2006).

The sequestration of its active site raises cogent questions as to how AChE achieves its high rate of substrate turnover. The narrowness of the gorge, which is only 5 Å wide at a bottleneck formed by the van der Waals surfaces of Phe330 and Tyr121, implies that AChE must undergo significant 'breathing' motions for traffic of substrates and products to occur *via* this route (Shen *et al.*, 2002; Xu *et al.*, 2003). Aligned with the gorge is a strong electrostatic gradient (Ripoll *et al.*, 1993; Felder *et al.*, 2002) that seems to be involved in guidance of the positively charged ACh towards the active site. However, this gradient should also impede the exit of the product choline (Ch). In this context, an alternative 'backdoor' exit for Ch was proposed (Ripoll *et al.*, 1993; see also Axelsen *et al.*, 1994), supporting evidence for which was obtained by molecular-dynamics (MD) simulations (Gilson *et al.*, 1994). This putative backdoor, which was not identified in the static X-ray structure, was reported to be adjacent to the Ch-binding locus of the CAS, Trp84. Likewise, an exit trajectory for the second product, acetate, was proposed just behind the 'acyl pocket' (Kovach *et al.*, 1994) and involves the 279–290 loop, which is seen to be disordered in the crystal structure of a *Tc*AChE–galanthamine derivative complex (Greenblatt *et al.*, 2004). Further experimental evidence for alternative access and exit routes to and from the active site comes from the absence of a bulky leaving group in the crystal structure of *Tc*AChE conjugated with a gorge-filling inhibitor covalently linked to Ser200 (Bartolucci *et al.*, 1999) and from the residual catalytic activity observed for AChE in complex with the gorge-capping polypeptide toxin fasciculin (FAS; Marchot *et al.*, 1993; Eastman *et al.*, 1995; Radic *et al.*, 1994, 1995). Subsequent MD studies have provided further evidence for a repertoire of 'backdoors' and 'side doors' (see, for example, Wlodek *et al.*, 1997; Enyedy *et al.*, 1998; Tai *et al.*, 2001; Bui *et al.*, 2004). However, mutagenesis studies have not yet provided any supporting evidence for a functional backdoor (Kronman *et al.*, 1994; Velan *et al.*, 1996; Faerman *et al.*, 1996). In this study, we used kinetic crystallography in an attempt to visualize the routes of product traffic within AChE.

In contrast to conventional X-ray crystallography, kinetic crystallography aims to describe the structural changes of crystalline proteins 'in action' (reviewed by Hajdu & Andersson, 1993; Bourgeois & Royant, 2005). It is important to note that many proteins are active in the crystalline state (Mozzarelli & Rossi, 1996), since a large amount of conformational freedom is preserved (Nienhaus *et al.*, 1998). Several kinetic crystallography approaches have been described based on real-time monitoring, steady-state accumulation or trapping of rate-limited intermediate states. Common to all these approaches is the requirement for reaction initiation in the crystal, *e.g.* by substrate delivery, pH jump or, in the case of photosensitive samples, by laser or flash-lamp irradiation. Reaction triggering by light is usually applied to proteins possessing endogenous photosensitivity such as haem proteins or photoreceptors. For proteins that are not innately photosensitive, use can be made of so-called 'caged compounds'; for example, photosensitive precursors of enzyme substrates or products (Schlichting *et al.*, 1990; Hajdu & Andersson, 1993;

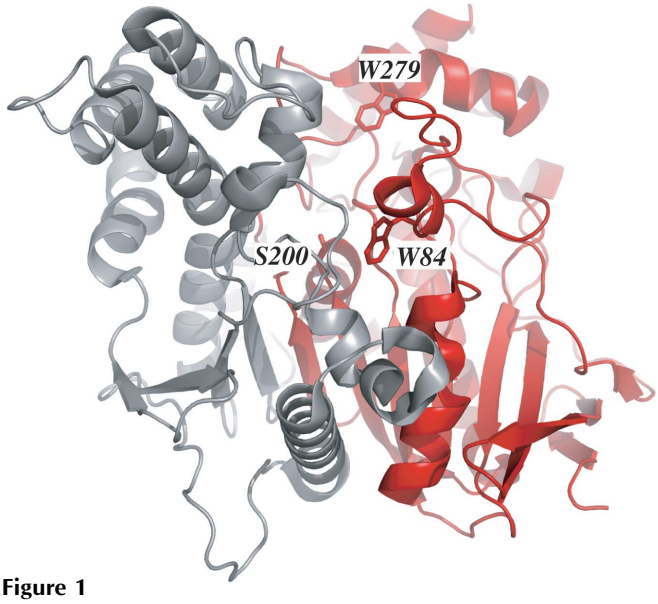

Figure 1
Three-dimensional structure of *Tc*AChE, highlighting the two domains on either side of the active-site gorge (residues 4–305 in red, residues 306–535 in grey). The catalytic Ser200 and Trp84 are shown at the bottom of the gorge (CAS) and the peripheral-site Trp279 at its rim (PAS).

Scheidig *et al.*, 1999; Ursby *et al.*, 2002; Bourgeois & Weik, 2005).

Here, we report kinetic crystallography studies on *Tc*AChE that combine temperature-controlled crystallography and the use of a 'caged' precursor of an analogue of the product Ch, arsenocholine (AsCh; Specht & Goeldner, 2004). Photolysis of the 'caged' compound was achieved by means of laser irradiation at room temperature (RT) during a brief temperature excursion from 100 K to RT. Partial *q*-weighted difference refinement (Fermi *et al.*, 1982; Terwilliger & Berendzen, 1995; Ursby & Bourgeois, 1997) was performed, which allowed the characterization of an activated state of the enzyme. The data suggest that the transient temperature increase to RT and photolysis resulted in reduced occupancy of AsCh at both the CAS and the PAS. Concomitantly, conformational changes were detected in the active-site gorge of the activated-state model of *Tc*AChE which resulted in the increase of the gorge volume and in the opening of an alternative route to and/or from the active site that may be involved in clearance of Ch from the active site.

2. Experimental procedures

2.1. Caged compound

The iodide salt of the caged compound [1-(2-nitrophenyl)-2,2,2-trifluoroethyl]-arsenocholine (NPT-AsCh; Fig. 2) was synthesized as described by Specht & Goeldner (2004). Its K_i for *Tc*AChE is 29 µ*M* in 25 m*M* sodium phosphate pH 7.0 at 293 K (J.-P. Colletier, unpublished results). When dissolved in water, NPT-AsCh displays an absorption maximum at 263 nm (not shown). The *o*-nitrosotrifluoromethylacetophenone released by UV irradiation has an absorption peak at 320 nm (not shown). Thus, photocleavage of NPT-AsCh can be monitored spectrophotometrically by following either its disappearance or the appearance of the byproduct. However, when it is complexed with crystalline *Tc*AChE the absorption of the latter at 280 nm prevents monitoring of the disappearance of NPT-AsCh and only the appearance of *o*-nitrosotrifluoromethylacetophenone can be monitored. The molar extinction coefficient of NPT-AsCh at 266 nm is 5160 M^{-1} cm^{-1} and that of the free cage is 4200 M^{-1} cm^{-1} at 320 nm.

2.2. Crystallization of *Tc*AChE, choice of crystal form and soaking procedure

*Tc*AChE was purified as described previously (Sussman *et al.*, 1988; Raves, 1998). Orthorhombic $P2_12_12_1$ (Greenblatt *et al.*, 2004) and trigonal $P3_121$ (Sussman *et al.*, 1991) crystals of native *Tc*AChE were obtained at 277 K by the hanging-drop vapour-diffusion method under the same crystallization conditions. The mother liquor was 32% PEG 200, 0.15 *M* MES pH 5.8–6.2 and a protein concentration of 11.5 mg ml^{-1} was employed. Orthorhombic *Tc*AChE crystals grew as thin plates (typically 150 × 150 × 50 µm) and were thus preferred over the more chunky trigonal crystals in order to maximize the penetration of UV light throughout the crystal. In order to obtain the crystalline NPT-AsCh–*Tc*AChE complex, orthorhombic crystals were soaked in the dark for 12 h at 277 K in mother liquor containing 5 m*M* NPT-AsCh pH 6.0. Crystals were washed for 10 s in mother liquor devoid of NPT-AsCh before flash-cooling to 100 K in a stream of gaseous N_2. Owing to the cryoprotective capacity of PEG 200, no additional cryoprotectant was necessary.

2.3. Cryophotolysis and microspectrophotometry

All microspectrophotometric characterization and preliminary experiments were conducted at the Cryobench Laboratory, which is jointly maintained by the European Synchrotron Radiation Facility (ESRF) and the Institut de Biologie Structurale (IBS) (Bourgeois *et al.*, 2002), and where a microspectrophotometer permits direct absorption measurements at 200–850 nm by protein crystals or by small solution volumes. The apparatus is composed of (i) a one-circle goniometer, (ii) three identical confocal mirror objectives focusing/collecting UV–visible light to/from the crystal, (iii) a CCD spectrophotometer (2.3 nm resolution in the 200–850 nm range, Ocean Optics), (iv) a microscope (Olympus) connected to a high-resolution camera (Olympus) permitting observation and centring of the crystal and (v) a cryocooling device (Oxford Cryosystems 600) that allows both flash-cooling and subsequent application of desired temperature profiles. Two of the objectives are aligned for transmission mode, while the third one is at 90° and is used to focus a 266 nm laser (2 mW passively *q*-switched YAG laser; Nanolase) onto the crystal. The laser and a deuterium/halogen lamp (Micropack deuterium/halogen lamp; Ocean Optics) are connected to the focusing objectives using optical fibres of 600 and 100 µm diameter (Spectraline), respectively, while an optical fibre of 200 µm diameter is used to guide the light from the receiving objective to the spectrophotometer. Spectra were recorded and analysed on a PC using the *OOIBase*32 software package (Ocean Optics). A detailed description of the Cryobench Laboratory can be found at http://www.esrf.fr/UsersAndScience/Experiments/MX/Cryobench/ (see also Bourgeois *et al.*, 2002; Royant *et al.*, 2007). To minimize ambient light exposure, which might produce small but unquantifiable photolysis of NPT-AsCh, the Cryobench Laboratory was only lit by a sodium lamp throughout all the experiments. Fig. 3(*a*) shows an experiment performed on an orthorhombic *Tc*AChE crystal soaked for 12 h in the dark at

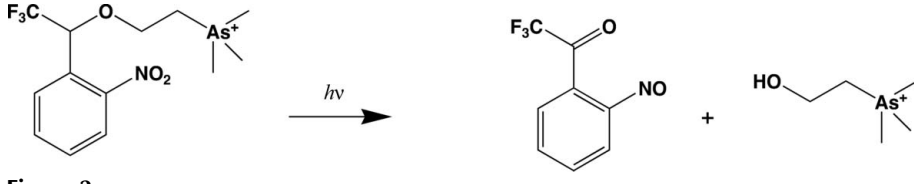

Figure 2
Photocleavage of NPT-AsCh into AsCh and *o*-nitrosotrifluoromethylacetophenone.

Table 1
Data-collection and refinement statistics.

Values in parentheses are for the highest resolution shells.

	Unphotolysed NPT-AsCh–*Tc*AChE complex (structure **1**)	Unphotolysed NPT-AsCh–*Tc*AChE complex after ART (structure **2**)	UV-damaged native *Tc*AChE (structure **3**)	NPT-AsCh–*Tc*AChE complex after photolysis and annealing to RT (structure **4**)
PDB code	2v96	2v97	2va9	2v98
ESRF beamline	BM30A	ID14-EH4	ID14-EH4	ID14-EH4
Data-collection temperature (K)	100	100	100	100
Oscillation step (°)	1	1	1	1
No. of frames	150	120	120	120
Exposure time per frame (s)	30	1	1	1
Wavelength (Å)	0.977	0.932	0.932	0.932
Space group	$P2_12_12_1$	$P2_12_12_1$	$P2_12_12_1$	$P2_12_12_1$
Unit-cell parameters (Å)				
a	91.42	91.20	91.42	91.62
b	103.64	104.46	106.55	104.47
c	147.31	148.05	150.15	148.80
Mosaicity† (°)	0.279	0.352	0.213	0.491
Resolution range (Å)	20.00–2.40 (2.50–2.40)	20.00–2.40 (2.50–2.40)	20.00–2.40 (2.50–2.40)	20.00–3.00 (3.10–3.00)
Completeness (%)	99.1 (99.7)	99.8 (100)	99.6 (97.7)	96.6 (94.6)
$R_{\rm merge}$‡ (%)	7.9 (34.7)	10.7 (46.7)	12.4 (45.0)	12.6 (49.8)
$I/\sigma(I)$	15.4 (4.4)	8.4 (2.8)	9.7 (3.1)	8.84 (2.5)
Unique reflections	54936	55871	58043	29073
Redundancy	5.9	3.8	6.1	3.3
$R_{\rm cryst}$ (%)	20.9	20.5§	20.4	20.3§
$R_{\rm free}$ (%)	24.4	26.7§	24.7	24.9§
R.m.s.d. bond lengths (Å)	0.009	0.007	0.006	0.009
R.m.s.d. bond angles (°)	1.501	1.535	1.326	1.415
No. of atoms in ASU				
Protein	8610	8455	8455	8455
Water	989	1083	855	1083
Carbohydrate	56	56	56	56
Ligands	84	84	0	84
Wilson *B* factor (Å^2)	36.35	41.82	31.13	47.81
Average *B* factor (Å^2)	34.39	38.82	21.40	42.36
Protein	33.39	36.03¶, 37.69††	29.02	41.83‡‡, 40.02§§
R.m.s.d. *B*				
Bonds				
Main-chain atoms	1.088	1.222	1.193	0.927
Side-chain atoms	1.706	1.908	1.879	1.142
Angles				
Main-chain atoms	1.815	1.979	1.924	1.585
Side-chain atoms	2.520	2.805	2.759	1.709
Water	41.38	51.85¶, 51.60††	38.27	52.86‡‡, 50.70§§
Carbohydrate	51.27	59.00¶, 58.61††	49.09	55.52‡‡, 58.94§§
Ligands	41.37	53.50¶, 56.22††	n/a	51.48‡‡, 55.65§§
Ramachandran statistics (%)				
Core	87.4	87.7¶, 80.4††	87.5	87.7‡‡, 76.7§§
Allowed regions	11.8	11.8¶, 18.4††	11.5	11.8‡‡, 21.9§§
Generously allowed regions	0.8	0.4¶, 1.0††	0.9	0.4‡‡, 1.1§§
Disallowed regions	0	0¶, 0††	0.1	0.0‡‡, 0.2§§

† Mosaicity as determined by *XDS* (Kabsch, 1993). ‡ $R_{\rm merge} = 100\sum_{hkl}\sum_i |I_i(hkl) - \langle I(hkl)\rangle|/\sum_{hkl}\sum_i I_i(hkl)$. § See Table 3 for details of *R* and $R_{\rm free}$ of structures **2** and **4**. ¶ Value for structure $\mathbf{2}^{\rm GS}$. †† Value for structure $\mathbf{2}^{\rm AS}$. ‡‡ Value for structure $\mathbf{4}^{\rm GS}$. §§ Value for structure $\mathbf{4}^{\rm AS}$.

277 K in 5 m*M* NPT-AsCh solution in mother liquor at pH 6.0. The crystal was then washed for 10 s in mother liquor devoid of NPT-AsCh before being loop-mounted and flash-cooled to 100 K. Fig. 3(*a*) shows the difference absorption spectra recorded at 100 K across the crystal after 300, 400, 500, 600, 700, 800 and 900 s exposure to the 266 nm laser. To maximize the efficiency of photolysis, the crystal was rotated during exposure to the laser beam, but all spectra were recorded at the same crystal orientation. Either a 355 nm laser or a flash-lamp could have been used to perform photolysis rather than the 266 nm laser that was actually employed (Specht *et al.*, 2001), but we did not have access to either of these light sources at the time of our experiments. Fig. 3(*b*) shows a simulation of the 266 nm light transmission across orthorhombic native *Tc*AChE and NPT-AsCh–*Tc*AChE crystals. The concentration of the enzyme in the orthorhombic crystals was calculated to be 9.4 m*M*. Values for the extinction coefficients of aromatic residues (Trp, Tyr and Phe) at 266 nm were taken from http://omlc.ogi.edu/spectra/PhotochemCAD/html/index.html and molar extinction coefficients of 87 339 and 97 659 M^{-1} cm^{-1} at 266 nm were calculated for a *Tc*AChE monomer and for a *Tc*AChE monomer in complex with two

NPT-AsCh molecules, respectively. Fig. 3 was produced using the software *PLOT* (http://plot.micw.eu/). To ensure efficient photolysis, illumination from two sides or rotation of the crystal during illumination should be performed and the crystal thickness should ideally not exceed ∼20 µm.

2.4. X-ray data collection

All X-ray data sets were collected at the ESRF after flash-cooling and maintaining the crystal in a stream of gaseous N_2 at 100 K. The data were indexed, merged and scaled using *XDS*/*XSCALE*. Structure-factor amplitudes were generated using *XDSCONV* (Kabsch, 1993). Data-collection statistics are given in Table 1.

2.4.1. Structure of the unphotolysed NPT-AsCh–*Tc*AChE complex (structure 1). Data were collected to 2.4 Å resolution on beamline BM30A (CRG FIP) from a 150 × 150 × 50 µm orthorhombic crystal.

2.4.2. Procedure for annealing to room temperature (ART). In order to evaluate the accessible time range for ART, preliminary experiments were conducted 'in-house' on a Rigaku R-AXIS IV diffractometer using native *Tc*AChE crystals. Typical dimensions of orthorhombic and trigonal crystals of *Tc*AChE are 150 × 150 × 50 and 150 × 150 × 150 µm, respectively. Crystals were mounted in a cryo-loop and flash-cooled to 100 K. After an initial diffraction image had been collected, ART was carried out by manually blocking the N_2-gas stream with a card for 1–60 s. After termination of ART, a second diffraction image was collected at 100 K and its diffraction limit was compared with that of the first image. Permissible time ranges for ART, *i.e.* the time during which no loss in the diffraction limit was observed, were ≤45 s for orthorhombic crystals and ≤30 s for trigonal crystals. The time spans required for crystals to reach RT were found to be 4 and 7 s for the orthorhombic and trigonal crystal forms, respectively, as evidenced by the absence of ice rings in the second diffraction pattern. Recovery of the diffraction power after the ART procedure is highly reproducible for crystals of either type (as assessed more than ten times on native *Tc*AChE crystals and more than 20 times on the complexes of various substrates, products or ligands with *Tc*AChE in both the orthorhombic and the trigonal crystal forms). However, trigonal crystals are more sensitive to multiple annealing cycles than orthorhombic crystals; while up to ten ART cycles of 5 s each can be undergone by a typical orthorhombic crystal without loss of more than 0.5 Å resolution, for trigonal crystals the second round of annealing is often already detrimental. The fact that the diffraction power of native orthorhombic crystals is occasionally increased upon ART is noteworthy.

2.4.3. Effect of ART on the structure of the unphotolysed NPT-AsCh–*Tc*AChE complex (structure 2). The effect of ART on the structure of the unphotolysed NPT-AsCh–*Tc*AChE complex was investigated using a 150 × 150 × 50 µm orthorhombic crystal. Subsequent to flash-cooling, the crystal underwent ART for 9 s before being flash-cooled back to 100 K for data collection (2.4 Å resolution) on beamline ID14-EH4.

2.4.4. UV damage at RT to a native *Tc*AChE crystal (structure 3). Since our experimental approach involves the use of a 266 nm laser to photocleave NPT-AsCh (see Fig. 4), a control was needed to discriminate between structural changes arising from UV damage at RT and those related to the exit of the NPT-AsCh photolysis products from the active site of *Tc*AChE. To ensure full penetration of the 266 nm light (see Fig. 3*b*), a rather thin orthorhombic crystal (∼250 × 100 × 30 µm) was employed. The 266 nm laser was connected by a 600 µm optic fibre to the focusing lens of an online microspectrophotometer (Nanao & Ravelli, 2006; Ravelli, Murray, McGeehan, Owen, Cipriani, Theveneau, Weik & Garman, manuscript in preparation) centred on the crystal (spot size on the crystal: 150 µm). The crystal was brought to RT for 9 s by blocking the cryostream manually with a card, during the first 5 s of which laser irradiation took place, before being flash-cooled back to 100 K for data collection (2.4 Å resolution); thus, a relaxation time of 4 s at RT was allowed after extinction of the laser. The crystal was rotated during the course of exposure to the laser beam.

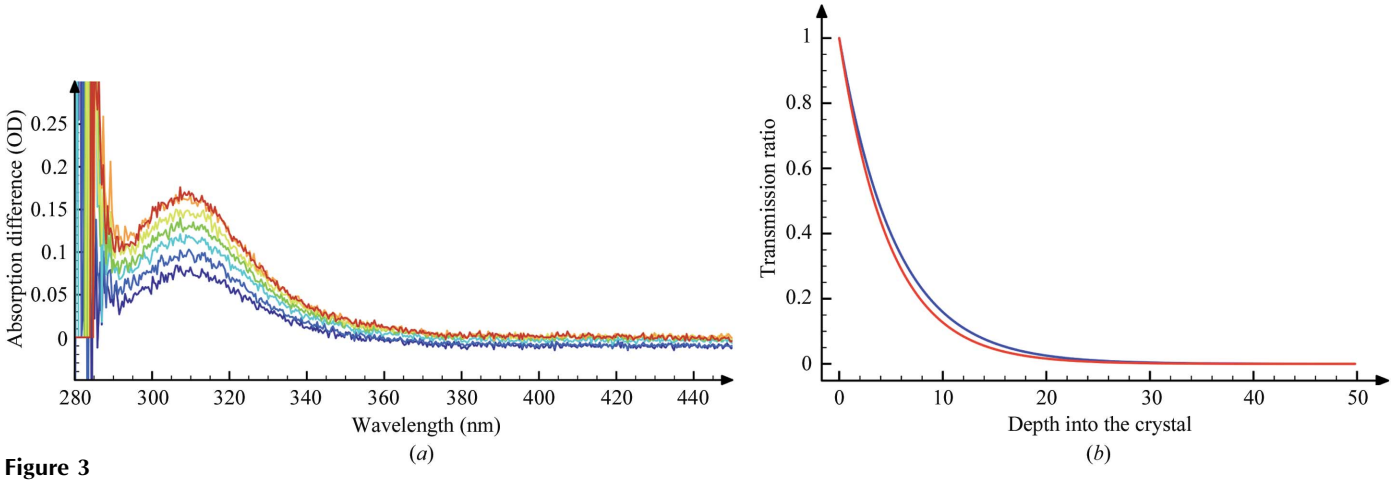

Figure 3
(*a*) *In cristallo* photolysis of NPT-AsCh. Difference OD spectra were recorded across orthorhombic *Tc*AChE–NPT-AsCh crystals at 100 K after 300, 400, 500, 600, 700, 800 and 900 s (blue to red colour) exposure to a 266 nm laser. (*b*) Simulated transmission of 266 nm light across orthorhombic native *Tc*AChE (blue) and NPT-AsCh–*Tc*AChE (red) crystals.

2.4.5. Structure of the photolysed NPT-AsCh–*Tc*AChE complex after ART (structure 4). Fig. 4 shows a schematic representation of the experimental procedure. The experiment was performed on beamline ID14-EH4. An orthorhombic crystal of the NPT-AsCh–*Tc*AChE complex of dimensions ~100 × 100 × 30 µm was employed. Photolysis of the NPT-AsCh was achieved using the experimental setup described in §2.4.4. The experimental procedure was identical to that described above for structure **3**.

2.5. Structure determination and refinement

2.5.1. NPT-AsCh–*Tc*AChE complexes. The native structure of *Tc*AChE in the orthorhombic space group (PDB code 1w75; Greenblatt *et al.*, 2004) without sugar and water molecules served as the starting model for rigid-body refinement of the two unphotolysed NPT-AsCh–*Tc*AChE complexes (structures **1** and **2**) in the resolution range 20–4 Å. Subsequently, both structures underwent simulated annealing to 2000 K, with slow-cooling steps of 10 K followed by 250 steps of conjugate-gradient minimization. Diffraction data from 20 to 2.4 Å were used for refinement and electron-density map calculations. For both structures, localization and attribution of the NPT-AsCh molecules was rather straightforward since the initial electron-density maps were of good quality. For each of the two monomers in the asymmetric unit (*A* and *B*) two NPT-AsCh molecules were assigned with full occupancies: one at the CAS and one at the PAS (Fig. 5). The strong anomalous signal of the As atom permitted unequivocal determination of the position of the AsCh moieties of the NPT-AsCh molecules (anomalous peaks of height >17σ at both binding loci in both structures **1** and **2**). *CNS* composite $2F_o - F_c$ OMIT maps were calculated, which provided the basis for the first step of manual rebuilding. Atoms lacking density at 1σ in this map were not included in the initial model and were reattributed afterwards only if subsequent $F_o - F_c$ electron-density maps displayed peaks of >3σ. Graphic operations and model building were performed with *Coot* (Emsley & Cowtan, 2004). Energy minimization and restrained individual *B*-factor refinement followed each stage of manual rebuilding. Refinement and map calculations were performed using *CNS* v.1.1 (Brünger *et al.*, 1998) and the *REFMAC* (Murshudov *et al.*, 1997) and *FFT* modules of the *CCP*4 suite (Collaborative Computational Project, Number 4, 1994).

In order to address the differences between structures **4** and **2**, the difference-refinement strategy was employed, *i.e.* refinement using $F_{diff} = F_c^2 + (F_o^4 - F_o^2)$ (Fermi *et al.*, 1982; Terwilliger & Berendzen, 1995). *q*-weights (Ursby & Bourgeois, 1997), which improve the estimate of the structure-factor amplitude differences, were used to ameliorate the signal-to-noise ratio [*i.e.* refinement using $F_{diff}^q = F_c^2 + q \times (F_o^4 - F_o^2)$; see Table 2]. The F_{diff} coefficients used in the refinement of structure **4** were generated using *DATAMAN* (Kleywegt & Jones, 1996) and the *SFTOOLS* module of the *CCP*4 suite. In addition, partial refinement was performed to gain further insight into the conformational changes undergone by the NPT-AsCh–*Tc*AChE complex upon UV irradiation and concomitant ART. Partial refinement involves

Table 2
R_{free} and R values for structure **4** after various refinement procedures.

	Complete independent refinement	Difference refinement†	*q*-weighted difference refinement	*q*-weighted partial (20%) difference refinement
R_{free} (%)	31.9	33.0	32.3	31.7
R‡ (%)	28.3	29.3	29.5	23.0
$R_{free,diff}$ (%)		28.6	25.3	24.9
R_{diff} (%)		23.9§	20.2¶	20.3¶

† Both sets of *R* factors are given here, *i.e.* the standard R/R_{free} factors and the difference $R_{diff}/R_{free,diff}$ factors. However, for assessing the accuracy of the difference refinement, only R_{diff} and $R_{free,diff}$ are relevant (Terwilliger & Berendzen, 1995). ‡ $R = 100\sum_{hkl} \big||F_{obs,4}(hkl)| - |F_{calc,4}(hkl)|\big| / \sum_{hkl} |F_{obs,4}(hkl)|$. § $R_{diff} = 100\sum_{hkl} \big||F_{calc,2}(hkl)| + \big||F_{obs,4}(hkl)| - |F_{obs,2}(hkl)|\big| - |F_{calc,4}(hkl)|\big| / \sum_{hkl} \big||F_{calc,2}(hkl)| + \big||F_{obs,4}(hkl)| - |F_{obs,2}(hkl)|\big|\big|$. ¶ $R_{diff} = 100\sum_{hkl} \big||F_{calc,2}(hkl)| + q\big||F_{obs,4}(hkl)| - |F_{obs,2}(hkl)|\big| - |F_{calc,4}(hkl)|\big| / \sum_{hkl} \big||F_{calc,2}(hkl)| + q\big||F_{obs,4}(hkl)| - |F_{obs,2}(hkl)|\big|\big|$.

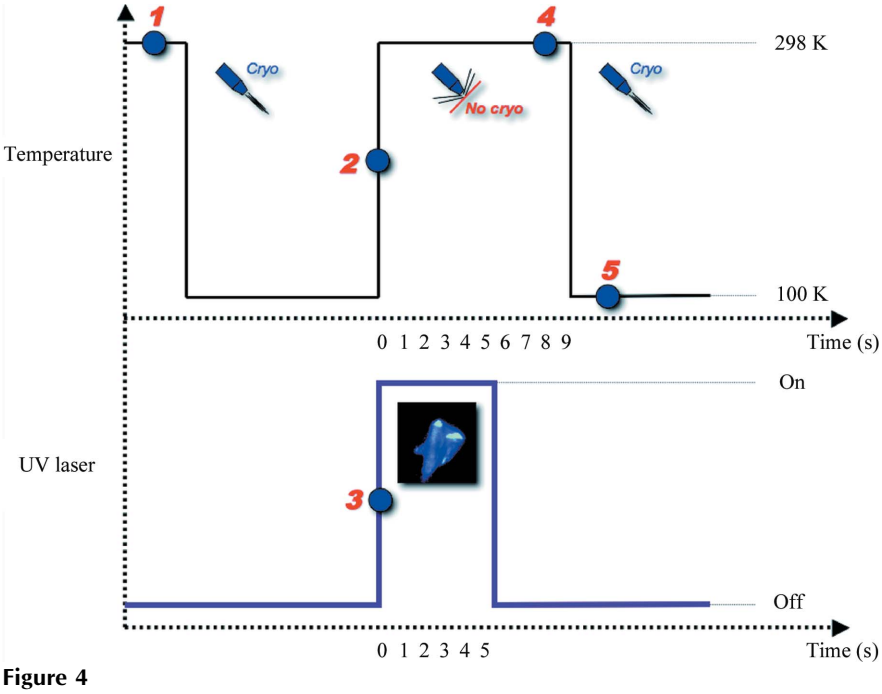

Figure 4
Temperature-controlled protein crystallography combined with photolysis of NPT-AsCh. The photolabile NPT-AsCh binds to the crystalline *Tc*AChE at room temperature (1) and the crystal is then flash-cooled to 100 K in a gaseous stream of N_2. The crystal is then subjected to ART (transient annealing to room temperature; 2), while photodissociation of NPT-AsCh to AsCh and *o*-nitrosotrifluoromethylacetophenone is concomitantly induced by a UV laser (3). Various relaxation times at room temperature are allowed after laser extinction (4). Structural changes of *Tc*AChE related to AsCh exit from the active site can then be trapped and characterized by X-ray data collection at 100 K (5).

refinement of an 'activated-state' (AS) conformation while the 'ground-state' (GS) model is held fixed. In practice, structure **2** was used as the starting model for rigid-body refinement using $F^{q}_{\rm diff}$. Subsequently, two identical models, $\mathbf{4}^{\rm GS}$ and $\mathbf{4}^{\rm AS}$, were generated. Structure $\mathbf{4}^{\rm GS}$ was held fixed by virtue of a strong harmonic force constant (418 kJ mol^{-1} Å^{-2}), whereas $\mathbf{4}^{\rm AS}$ was refined using $F^{q}_{\rm diff}$ by simulated annealing to 2000 K with cooling steps

Table 3
$R_{\rm free}$ and R values for structure **2** after partial refinement and for structure **4** after partial q-weighted difference refinement.

	Structure **2** before partial refinement	Structure **2** 20% AS/ 80% GS	Structure **4** 20% AS/ 80% GS	Structure **4** 40% AS/ 60% GS	Structure **4** 60% AS/ 40% GS	Structure **4** 80% AS/ 20% GS	Structure **4** 100% AS/ 0% GS
$R_{\rm free}$ (%)	27.2	26.7					
R† (%)	21.1	20.5					
$R_{\rm free,diff}$ (%)			24.9	25.2	25.6	25.4	25.3
$R_{\rm diff}$‡ (%)			20.3	20.1	20.0	20.1	20.2

† $R = 100\sum_{hkl}\big||F_{\rm obs,\mathbf{2}}(hkl)| - |F_{\rm calc,\mathbf{2}}(hkl)|\big|/\sum_{hkl}|F_{\rm obs,\mathbf{2}}(hkl)|$. ‡ $R_{\rm diff} = 100\sum_{hkl}\big||F_{\rm calc,\mathbf{2}}(hkl)| + q\big||F_{\rm obs,\mathbf{4}}(hkl)| - |F_{\rm obs,\mathbf{2}}(hkl)|\big| - |F_{\rm calc,\mathbf{4}}(hkl)|\big|/\sum_{hkl}\big||F_{\rm calc,\mathbf{2}}(hkl)| + q\big||F_{\rm obs,\mathbf{4}}(hkl)| - |F_{\rm obs,\mathbf{2}}(hkl)|\big|\big|$, with $F_{\rm calc,\ \mathbf{4}}(hkl) = aF_{\rm calc,\mathbf{4}^{GS}}(hkl) + bF_{\rm calc,\mathbf{4}^{AS}}(hkl)$, where a and b are the fractions of $\mathbf{4}^{\rm GS}$ and $\mathbf{4}^{\rm AS}$, respectively.

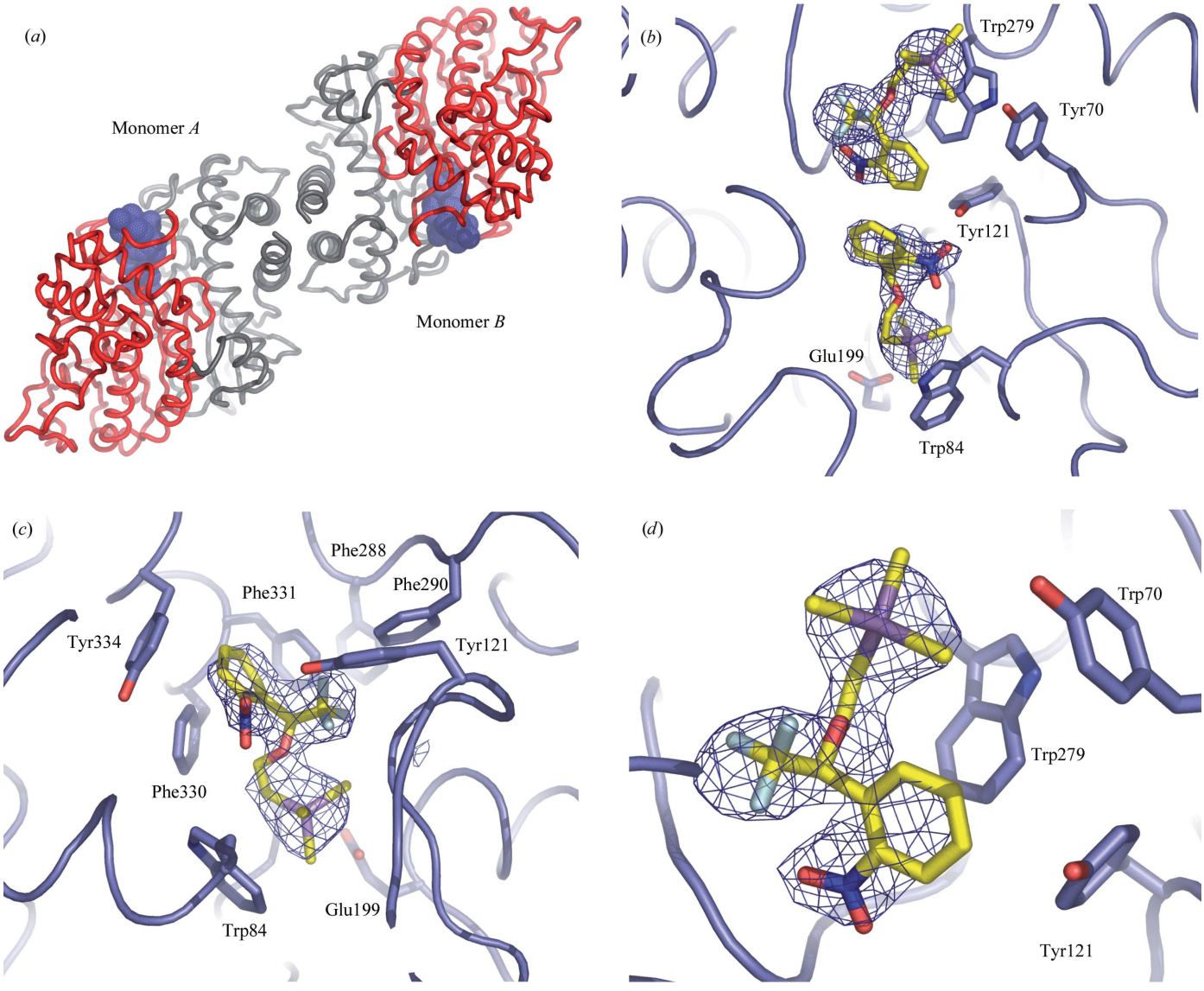

Figure 5
NPT-AsCh-binding sites in the unphotolysed NPT-AsCh–*Tc*AChE complex (structure **1**). (*a*) Overview of the dimer constituting the asymmetric unit. The C-terminal domains (in grey) of the two monomers interact with each other *via* a four-helix bundle. The caged compounds bound inside the gorge are shown as blue spheres; the N-terminal domains are shown in red. (*b*) Overview of the binding sites: Trp84 and Glu199 are shown in the CAS and Tyr70, Tyr121 and Trp279 at the PAS. (*c*) NPT-AsCh bound in the CAS. Trp84, Glu199 and Phe330 are shown in the CAS, as well as Phe288, Phe290 and Phe331 in the acyl pocket and Tyr334. (*d*) NPT-AsCh bound at the PAS. The principal PAS residues, Tyr70, Tyr121 and Trp279, are shown. The $F_{\rm o} - F_{\rm c}$ electron-density map (contour level 3.5σ) computed without the atomic coordinates of NPT-AsCh is superimposed on the model (monomer *B*) in (*b*)–(*d*).

Table 4
R.m.s.d. and maximum-likelihood σ values (Å) between structures.

The mean value is 0.3 Å.

	1w75	Structure **N**	Structure **1**	Structure $\mathbf{2}^{GS}$	Structure $\mathbf{2}^{AS}$	Structure **3**	Structure $\mathbf{4}^{GS}$	Structure $\mathbf{4}^{AS}$
1w75	0 (0)	0.22 (0.05)	0.35 (0.08)	0.34 (0.06)	0.46 (0.08)	0.19 (0.04)	0.36 (0.08)	0.65 (0.14)
Structure **N**	0.22 (0.05)	0 (0)	0.38 (0.07)	0.38 (0.09)	0.48 (0.11)	0.18 (0.04)	0.39 (0.09)	0.68 (0.15)
Structure **1**	0.35 (0.08)	0.38 (0.07)	0 (0)	0.23 (0.05)	0.41 (0.06)	0.35 (0.06)	0.29 (0.06)	0.63 (0.14)
Structure $\mathbf{2}^{GS}$	0.34 (0.06)	0.38 (0.08)	0.23 (0.05)	0 (0)	0.38 (0.06)	0.38 (0.09)	0.21 (0.04)	0.58 (0.13)
Structure $\mathbf{2}^{AS}$	0.46 (0.08)	0.48 (0.11)	0.41 (0.06)	0.38 (0.06)	0 (0)	0.46 (0.08)	0.40 (0.07)	0.66 (0.14)
Structure **3**	0.19 (0.04)	0.18 (0.04)	0.35 (0.06)	0.38 (0.09)	0.46 (0.08)	0 (0)	0.39 (0.09)	0.68 (0.15)
Structure $\mathbf{4}^{GS}$	0.36 (0.08)	0.39 (0.09)	0.29 (0.06)	0.21 (0.04)	0.40 (0.07)	0.39 (0.09)	0 (0)	0.58 (0.13)
Structure $\mathbf{4}^{AS}$	0.65 (0.14)	0.68 (0.15)	0.63 (0.14)	0.58 (0.13)	0.66 (0.14)	0.68 (0.15)	0.58 (0.13)	0 (0)

of 10 K, conjugate-gradient minimization and restrained individual *B*-factor refinement. This procedure was carried out five times, with the relative occupancies of $\mathbf{4}^{GS}$ and $\mathbf{4}^{AS}$ being varied from 0% to 100% in steps of 20%; the lowest R_{free} value was obtained for 20% AS and 80% GS (Tables 2 and 3). The resulting $F_o - F_c$ electron-density map is virtually featureless when displayed at $\pm 3\sigma$. As a control, the same partial refinement procedure was then applied to structure **2**, the final model of which obtained as described above was used to generate two conformers, $\mathbf{2}^{GS}$ and $\mathbf{2}^{AS}$, with relative occupancies of 80% and 20%, respectively. While structure $\mathbf{2}^{GS}$ was held fixed by virtue of a strong harmonic force constant (418 kJ mol^{-1} Å^{-2}), $\mathbf{2}^{AS}$ was subjected to simulated annealing to 2000 K with cooling steps of 10 K, conjugate-gradient minimization and restrained individual *B*-factor refinement. Structures $\mathbf{2}^{GS}$ and $\mathbf{2}^{AS}$ are virtually identical to structure **2**, yet structure $\mathbf{2}^{AS}$ displays small conformational changes that most probably reflect the conformational heterogeneity of the crystalline sample subsequent to ART. In the case of structure **2**, the partial refinement strategy also led to a significant decrease in the R_{free} and *R* values (Table 3).

Structural differences between structures **1**, $\mathbf{2}^{GS}$, $\mathbf{2}^{AS}$, $\mathbf{4}^{GS}$ and $\mathbf{4}^{AS}$ were evaluated on the basis of error-scaled difference distance matrices (ESDDM), which were produced using *ESCET* (Schneider, 2000; Fig. 6) after the maximum-likelihood superpositioning of all structures (**1**, $\mathbf{2}^{GS}$, $\mathbf{2}^{AS}$, $\mathbf{4}^{GS}$ and $\mathbf{4}^{AS}$; Table 4 and Fig. 7) using *THESEUS* (Theobald & Wuttke, 2006; http://www.theseus3d.org/). Owing to the limited resolution of structure **4** and the high correlation between occupancy and *B* factors, no attempt was made to determine the post-photolysis occupancies of the NPT-AsCh molecules in this structure. Instead, a qualitative assessment was obtained by computing $F_o^4 - F_o^2$ (not shown) and $q \times (F_o^4 - F_o^2)$ difference electron-density maps (Fig. 8; shown only

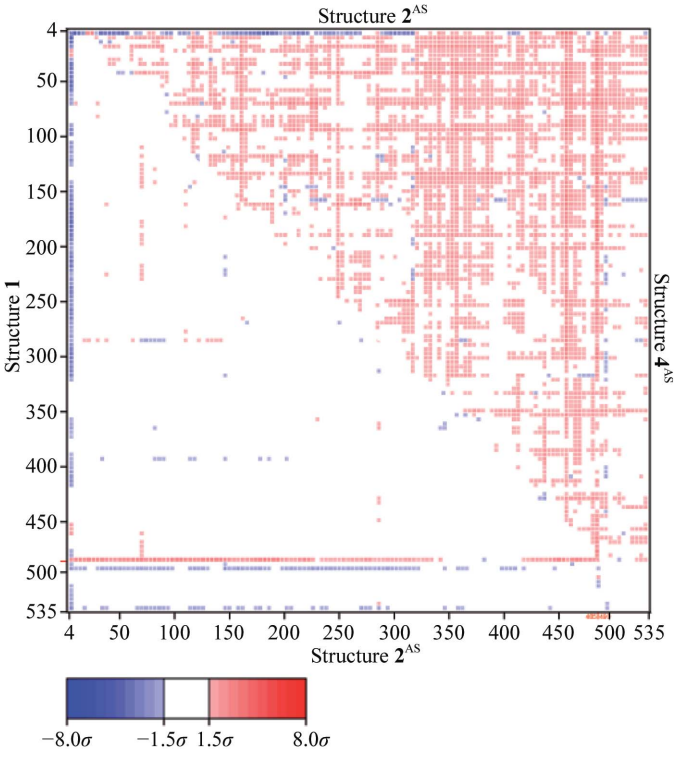

Figure 6
Error-scaled distance difference matrix (ESDDM) between the C^{α} atoms of structures **1** and $\mathbf{2}^{AS}$ (lower half) and between those of structures $\mathbf{2}^{AS}$ and $\mathbf{4}^{AS}$ (upper half). The ESDDM is shown for monomer *A*. Red and blue pixels indicate increases and decreases, respectively, in the distances between C^{α} atoms in structures **1** and $\mathbf{4}^{AS}$ with respect to structure $\mathbf{2}^{AS}$.

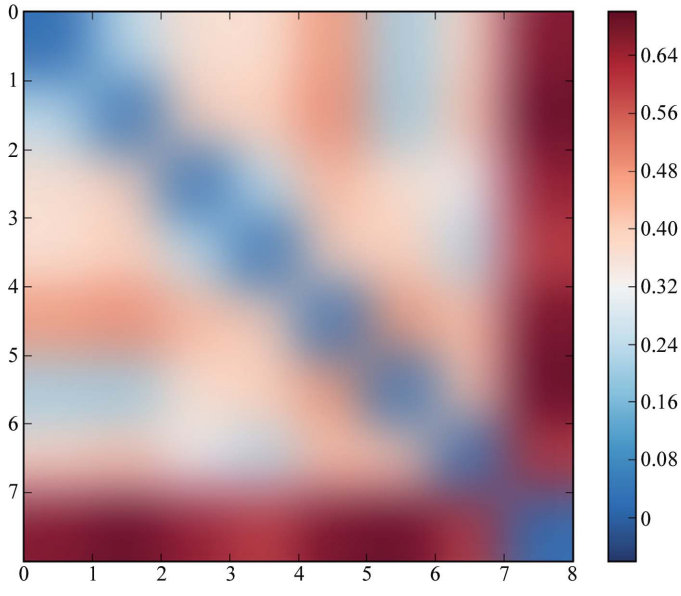

Figure 7
Matrix representation of the r.m.s.d. along the structures (monomers *A* and *B*) presented in the manuscript (as listed in Table 4). The blue-to-red scale varies from 0 to 0.70 Å. Structures are ordered as in Table 4.

Table 5
Molecular volume (Å^3) of the active-site gorge in native orthorhombic *Tc*AChE and in structures **N**, **1**, **2**^{GS}, **2**^{AS}, **3**, **4**^{GS} and **4**^{AS}.

Mean volume of the active-site gorge in native *Tc*AChE (structures 1w75, **N** and **3**): 915 Å^3 (monomer *A*) and 929 Å^3 (monomer *B*).

	1w75	Structure **N**	Structure **1**	Structure **2**^{GS}	Structure **2**^{AS}	Structure **3**	Structure **4**^{GS}	Structure **4**^{AS}
Monomer *A*	911	937	885	955	935	896	911	1177
Monomer *B*	904	963	925	977	1004	920	927	1247

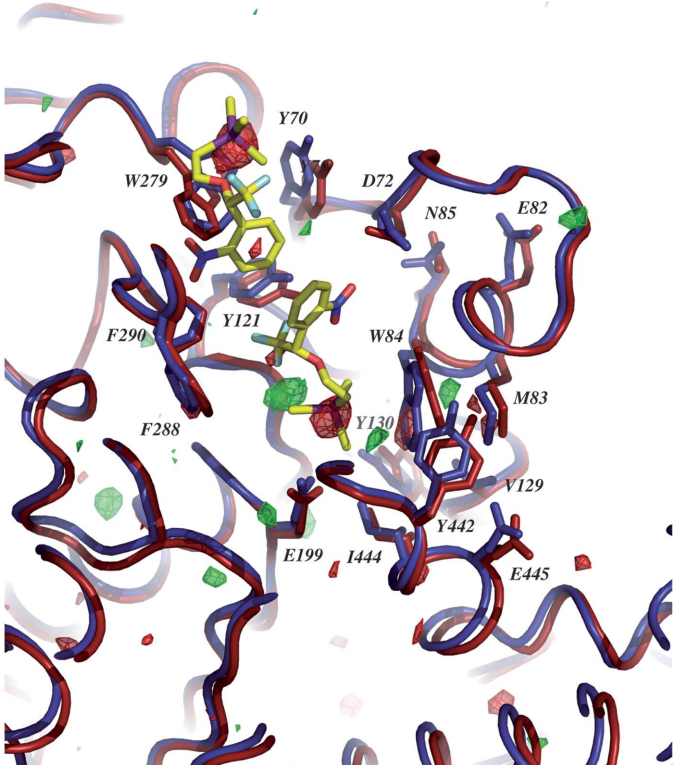

Figure 8
Relative decreases in the occupancies of NPT-AsCh in monomer *A* of structure **4** relative to structure **2**. The C$^\alpha$ traces of structures **2**^{GS} and **4**^{AS} are shown in dark blue and red, respectively. Residues Asp72, Trp84, Tyr130, Glu199 and Phe290 in the CAS and Tyr70, Tyr121 and Trp279 at the PAS are shown for both structures. Residues in the putative backdoor region (Met83, Val129, Tyr442, Ile444 and Glu445) are also shown. The $q \times (F_o^4 - F_o^2)$ difference electron-density map is superimposed on the model (contour levels -4σ, red; $+4\sigma$, green).

for monomer *A*) phased with the model of structure **2**. Both difference maps displayed strong negative ($<-5\sigma$) peaks for the As atoms of the two NPT-AsCh molecules bound to each of the two monomers of the asymmetric unit. The $q \times (F_o^4 - F_o^2)$ difference map yielded additional peaks on the protein moiety, which are consistent with the observed differences between structures **2**^{AS} and **4**^{AS}. Figs. 1, 5, 8 and 9 were produced using *PyMOL* (DeLano, 2002). Fig. 6 was produced using *ESCET* (Schneider, 2000) and Fig. 7, which is a matrix representation of the r.m.s.d. between the structures discussed throughout the manuscript, was produced using a Python script written by Chris Miller. Molecular topologies and parameters of NPT-AsCh were created using *XPLO2D* (Kleywegt, 1995). The qualities of the structures were checked and validated using *PROCHECK* (Laskowski *et al.*, 1993) from the *CCP*4 suite. The molecular volumes of the active-site gorge in the various structures were computed using *CASTp* (Dundas *et al.*, 2006) and are presented in Table 5. Refinement statistics are displayed in Table 1.

2.5.2. UV-damaged native *Tc*AChE. Structure determination and refinement (structure **3**) were carried out essentially as described above for structure **1**. Refinement statistics are given in Table 1. The quality of structure **3** was checked and validated using *PROCHECK*. The effect of UV irradiation on native *Tc*AChE was evaluated by computing an error-scaled difference distance matrix between this structure and that refined from a native crystal (**N**) annealed to RT for 9 s but without laser exposure (data not shown).

3. Results

3.1. Photolysis of the NPT-AsCh–*Tc*AChE complex

NPT-AsCh is a photolabile cholinergic ligand and can be photolysed by exposure to 266 nm laser light even at temperatures as low as 100 K (Specht *et al.*, 2001). Whether photolysis at 100 K leads to release of AsCh and the free *o*-nitrosotrifluoromethylacetophenone at that temperature or only to formation of an hemiacetal intermediate (Corrie *et al.*, 2003) with an absorption spectrum that closely resembles that of the free *o*-nitrosotrifluoromethylacetophenone remains to be clarified (Bourgeois & Weik, 2005). Photolysis of NPT-AsCh by means of 266 nm laser light can also be achieved in crystals of its complex with *Tc*AChE (Fig. 3*a*). However, owing to strong competitive absorption by aromatic residues, photolysis at this wavelength is only efficient if very thin crystals are used (<20 µm thickness; Fig. 3*b*).

3.2. Binding of NPT-AsCh within the active-site gorge of *Tc*AChE

The asymmetric unit of the orthorhombic crystal form of *Tc*AChE contains two copies of the protein that associate to form a dimer *via* a four-helix bundle (Greenblatt *et al.*, 2004; Fig. 5*a*), with the association being stabilized by an inter-subunit disulfide bridge that is not visible in the electron-density maps. The monomeric enzyme is composed of two domains, comprising residues 4–305 and 306–535, which face one another across the active-site gorge (Fig. 5*a*). In the following, the results referred to are valid for both monomers unless stated otherwise.

In structure **1** (the unphotolysed NPT-AsCh–*Tc*AChE complex), two NPT-AsCh molecules could be assigned with full occupancies to each monomer: one at the CAS and the other at the PAS (Fig. 5*b*). The use of NPT-AsCh instead of NPT-Ch permitted easy location of the As atoms owing to their clear anomalous signal (the *K*α absorption edge of As is

at 11.8 keV) at the wavelength employed (λ = 0.977 Å; *i.e.* 12.7 keV). The quaternary arsenium moiety of the NPT-AsCh bound at the CAS (Figs. 5*b* and 9) interacts mainly with Trp84, Phe330 and Glu199 (the distances between the two closest non-H atoms are 3.4, 3.3 and 3.0 Å, respectively), while its aromatic NPT moiety stacks between the side chains of Phe330, Phe331 and Tyr334 (Fig. 5; the distances between the two closest non-H atoms are 3.3, 3.5 and 3.2 Å, respectively). The CF_3 group of the NPT moiety of NPT-AsCh faces the acyl pocket, *i.e.* Trp233, Phe288 and Phe290, hence mimicking the methyl group of the acetyl moiety of ACh. A similar binding of a CF_3 group in the acyl pocket was observed in the crystal structure of the complex of *Tc*AChE with the transition-state analogue TMTFA (Harel *et al.*, 1996). Apart from the small rotations (<10°) undergone by the side chains of Phe330 and Phe331, no conformational changes are observed in the active site upon binding NPT-AsCh.

At the PAS, an NPT-AsCh is seen which is oriented 'upside-down' (Figs. 5*b* and 5*d*) relative to the NPT-AsCh bound at the CAS; hence, the two aromatic NPT moieties of the molecules bound at the PAS and at the CAS interact with each other *via* hydrophobic stacking (the distance between the two closest non-H atoms of their respective aromatic rings is 3.2 Å). The AsCh moiety of the NPT-AsCh molecule at the PAS points toward the bulk and is mainly stabilized by cation–π interactions with Tyr70 and Trp279 (the distances between the two closest non-H atoms are 3.5 and 3.4 Å, respectively). The aromatic NPT moiety binds within the gorge, with the CF_3 group in the vicinity of the main-chain atoms of Tyr334 and Gly335 (the distances between each F atom and the closest non-H atom are 3.0, 3.0 and 3.1 Å, respectively). The two O atoms of the nitro group are at a hydrogen-bonding distance from Phe288 N (distances of 2.6 and 2.9 Å). Upon binding of NPT-AsCh at the PAS, the side chain of Tyr70 undergoes a ∼20° rotation towards the bulk. The r.m.s.d. between this structure and the native structure (PDB code 1w75) is 0.35 Å (Table 4).

3.3. Control experiments: effects of ART and of UV irradiation at RT on *Tc*AChE crystals

Our experimental approach makes use of a 266 nm laser to photocleave NPT-AsCh and of ART to permit expulsion of the released AsCh from the active-site gorge (Fig. 4). Hence, two main controls were needed: (i) a control to address the issue of structural changes that might be induced by ART and (ii) a control to discriminate between conformational changes arising owing to UV damage and those related to NPT-AsCh photolysis and ART.

The effect of ART on the structure of the NPT-AsCh–*Tc*AChE complex was investigated by computing error-scaled difference distance matrices (ESDDMs; Schneider, 2000). In such a matrix, positive (red) and negative (blue) peaks indicate increased and reduced distances, respectively, between the C^{α} atoms of the structures being compared (*i.e.* expansion and contraction of given segments of the structure, respectively). ESDDMs were calculated between the unphotolysed structure obtained after flash-cooling to 100 K (structure **1**) and the two partial models refined using the data set collected after a 9 s ART (structures $\mathbf{2}^{GS}$ and $\mathbf{2}^{AS}$). The partial refinement procedure, carried out after a final model was independently refined and in which one conformer ($\mathbf{2}^{AS}$, with an occupancy of 20%) was allowed to change conformation while another one was held fixed ($\mathbf{2}^{GS}$, with an occupancy of 80%),

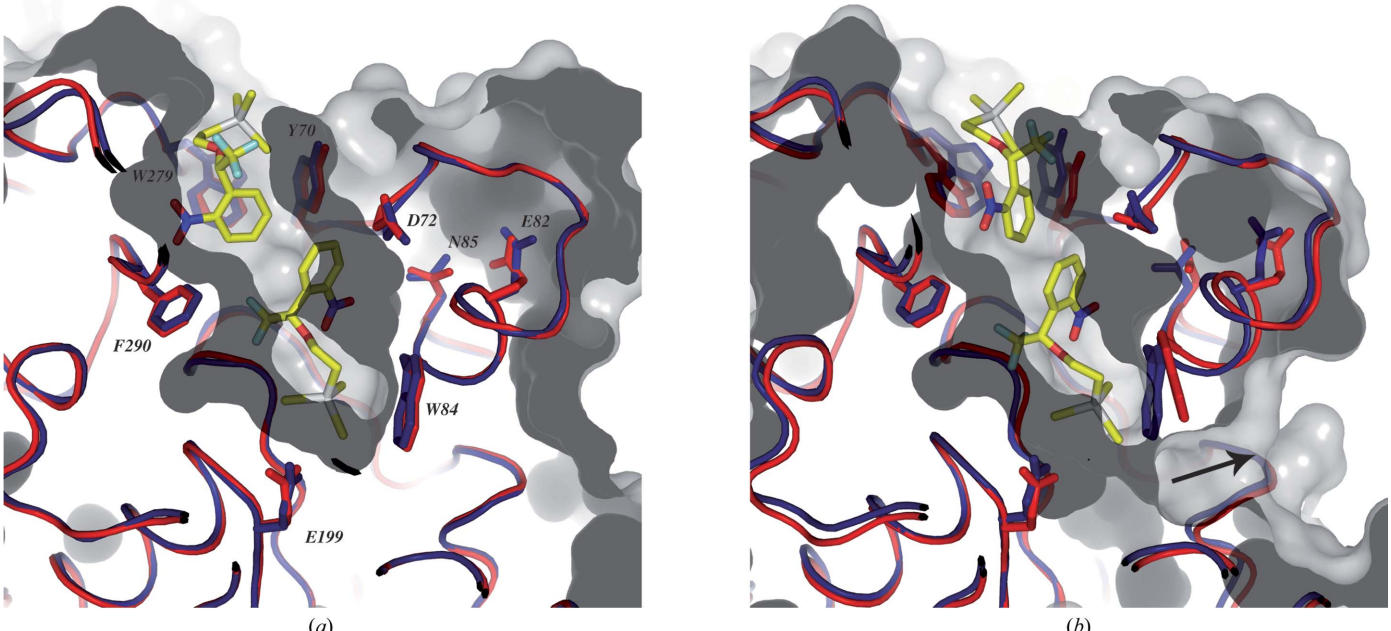

Figure 9
Opening of a backdoor across the gorge wall of the active-site in monomer *A*. (*a*) The Connolly surface of structure $\mathbf{2}^{AS}$ (red C^{α} trace and sticks), with structure $\mathbf{2}^{GS}$ (blue C^{α} trace and sticks) superimposed for comparison. (*b*) The Connolly surface of structure $\mathbf{4}^{AS}$ (red C^{α} trace and sticks), with structure $\mathbf{4}^{GS}$ being superimposed for comparison (blue C^{α} trace and sticks). Residues Tyr70, Asp72, Glu82, Met83, Trp84, Asn85, Trp279 and Phe290 are shown as sticks. The arrow indicates the opening of a channel owing to a conformational change of Trp84 in structure $\mathbf{4}^{AS}$.

clearly improved the accuracy of the model of structure **2** (Tables 1 and 2). The ESDDM computed between structures **1** and $\mathbf{2}^{AS}$ (Fig. 6, lower half) is essentially featureless, showing that no striking conformational changes are produced in the NPT-AsCh–*Tc*AChE complex by the ART procedure. Although refinement of structure **2** yielded a higher R_{free} value, only a small loss in diffraction quality was observed with respect to structure **1** (see Table 1), showing that the ART procedure does not damage the crystal. The two NPT-AsCh molecules are found at the same loci and both still display full occupancy. Peaks of $>17\sigma$ are seen for each As atom in the anomalous map of structure **2**, just as for structure **1**. The *B*-factor values of both the protein and the NPT-AsCh atoms are also very similar in structures **1** and **2**. The r.m.s.d. between structures **1** and $\mathbf{2}^{GS}$ is 0.23 Å, while that between structures **1** and $\mathbf{2}^{AS}$ is 0.41 Å (the r.m.s.d. between structures $\mathbf{2}^{GS}$ and $\mathbf{2}^{AS}$ is 0.38 Å, with the mean r.m.s.d. among the various structures discussed throughout the paper being 0.30 Å; Table 4).

In order to investigate the effect of UV exposure at RT on *Tc*AChE, a native orthorhombic *Tc*AChE crystal was flash-cooled to 100 K and then brought to RT for 9 s, during the first 5 s of which it was exposed to the 266 nm laser beam (structure **3**; see §2). An ESDDM was calculated between structures **3** and **N** (the native orthorhombic *Tc*AChE crystal annealed to RT for 9 s) and was virtually featureless, indicating that no significant structural changes occur during the 5 s UV irradiation at RT (not shown). It must be noted that no disulfide breakage was observed in structure **3** either in $F_o - F_c$ or in $F_o^{\mathbf{3}} - F_o^{\mathbf{N}}$ electron-density maps (the R_{merge} between the two data sets was 9%). The r.m.s.d. between structures **3** and **N** is 0.18 Å and that between structure **3** and the native structure is 0.19 Å (Table 4).

3.4. Structure of the NPT-AsCh–*Tc*AChE complex after photolysis of NPT-AsCh at RT

Data for this structure (structure **4**) were collected after flash-cooling to 100 K followed by 9 s ART, during the first 5 s of which the crystal was exposed to the 266 nm laser (see Fig. 4 and §2). This structure was refined using the 'difference-refinement' procedure (Fermi *et al.*, 1982; Terwilliger & Berendzen, 1995) to improve the estimates of structural differences with respect to structure **2**. Structure-factor difference amplitudes ($F_o^{\mathbf{4}} - F_o^{\mathbf{2}}$) were *q*-weighted (Ursby & Bourgeois, 1997) so as to improve their estimates and to reduce the noise level. Partial refinement was then carried out in which 20% of the structure was allowed to change conformation (structure $\mathbf{4}^{AS}$) while the remaining 80% was held fixed (structure $\mathbf{4}^{GS}$). The partial refinement strategy and the use of *q*-weighted structure-factor amplitude differences in the difference refinement improved the quality of structure **4** (Table 2). The results for monomers *A* and *B* are very similar and only those for monomer *A* are presented in the following unless stated otherwise.

The ESDDM between structures $\mathbf{2}^{AS}$ and $\mathbf{4}^{AS}$ (Fig. 6, upper half) reveals a clear tendency of the protein to expand upon photolysis of the bound ligand at RT, since most $C^{\alpha}-C^{\alpha}$ distances are larger (red pixels in Fig. 6) in structure $\mathbf{4}^{AS}$ than in structure $\mathbf{2}^{AS}$. In fact, the two domains of the enzyme, comprising residues 4–305 and 306–535, which face one another across the active-site gorge (Figs. 1 and 5*a*), move away from each other (Fig. 6, upper half), resulting in a large increase in the volume of the active-site gorge (30% and 35% for monomers *A* and *B*, respectively; Table 5).

The architecture of the active-site gorge is conserved in structure $\mathbf{4}^{GS}$ relative to structures **1**, $\mathbf{2}^{GS}$ and $\mathbf{2}^{AS}$. Structure $\mathbf{4}^{AS}$, however, displays a structure in which the conformation of the active-site gorge has been modified (Figs. 8 and 9). Most residues lining the gorge wall display small backbone movements (not more than a few tenths of an angstrom) with respect to structure $\mathbf{2}^{AS}$. The most important backbone deviations concern residues 114–120, 123–128, 336–348 and 437–448. Small side-chain deviations are observed for several residues on the surface. Inside the gorge, noteworthy movements are those of Tyr70, Asp72, Trp84, Tyr114, Tyr121, Leu127, Tyr130, Glu199, Phe288, Phe330 and Tyr442 in both monomers, Val129 and Glu445 in monomer *B* only and Trp279 in monomer *A* only (Figs. 8 and 9).

Difference electron-density maps were calculated between structures **2** and **4** using as Fourier coefficients either $F_o^{\mathbf{4}} - F_o^{\mathbf{2}}$ (not shown) or $q \times (F_o^{\mathbf{4}} - F_o^{\mathbf{2}})$ and the calculated phases of structure **2** (*i.e.* 20% $\mathbf{2}^{AS}$ and 80% $\mathbf{2}^{GS}$). The R_{merge} between the two data sets was 27%. Both yielded strong negative peaks (with only peaks of absolute value $>4\sigma$ being considered significant) for the As atoms of NPT-AsCh at both the CAS and the PAS (Fig. 8). These peaks suggest a decrease in the occupancy by As atoms at both sites. The putative decrease in the occupancies of the NPT-AsCh molecules in structure **4** was further confirmed by the weakness of the anomalous signal of their AsCh moiety. Indeed, only a very small peak is seen at the CAS of monomer *A* when the anomalous map is displayed at 4σ (not shown). A positive peak in the $q \times (F_o^{\mathbf{4}} - F_o^{\mathbf{2}})$ difference map is seen in the CAS next to the position of the arsenium moiety in structure **2** (Fig. 8), yet there is no concomitant anomalous signal at the same position or near it (not shown). This positive peak is thus unlikely to correspond to a repositioning of the photocleaved AsCh. Likewise, it seems improbable that it corresponds to a repositioning of the cage moiety, which appears to stay put based on the absence of a substantial negative density at the starting location of the cage. Rather, this positive peak might reveal the binding of a solvent molecule.

The $q \times (F_o^{\mathbf{4}} - F_o^{\mathbf{2}})$ difference electron-density map yielded significant peaks in the protein structure. Most importantly, a negative peak is seen at the side chain of Trp84 (-5.4σ) and a positive peak next to it (Fig. 8). A negative peak is seen at the PAS of monomer *B* at the side chain of Trp279 (-4.3σ; not shown). The main constituents of the PAS, Trp279, Tyr70, Tyr121 and Tyr334, undergo conformational changes in structure $\mathbf{4}^{AS}$. In the CAS of structure $\mathbf{4}^{AS}$, the side chain of Trp84 moves concertedly with Met83, Tyr130, Tyr442 and Glu445 (Figs. 8 and 9). As a consequence, an opening in the active-site wall is observed that is large enough to allow the passage of a water molecule. In monomer *B*, a channel is also

formed at the same position but is not large enough to allow the passage of a water molecule.

4. Discussion

4.1. Structural changes in the active site of *Tc*AChE after photolysis and annealing to RT

Our experimental approach was designed to address the issue of choline exit from the active site of AChE in structural terms and to examine the 'backdoor' hypothesis (Ripoll *et al.*, 1993; Gilson *et al.*, 1994). NPT-AsCh was bound within the active site of *Tc*AChE and AsCh was 'uncaged' by UV-induced photocleavage during a temperature excursion from 100 K to room temperature (RT). Difference electron-density maps suggested a decrease in the occupancy of the photo-freed AsCh at both the CAS and the PAS (Fig. 8). Our results suggest (but do not prove) that a proportion of the AsCh molecules had exited from the CAS after photolysis and annealing to room temperature. No intermediate binding sites for AsCh on its way out of the CAS were observed, despite the fact that use of caged AsCh instead of caged Ch increased the chance of identifying such sites owing to the strong anomalous scattering by the As atom (Peng *et al.*, 1998).

The partial difference refinement of structures **2** and **4** employed here assumes that the crystalline enzyme can adopt two states after photolysis and annealing to room temperature: a ground state and an activated state. Whereas the activated and ground states of structure **2** (control experiment) are similar, the activated state of structure **4** ($\mathbf{4}^{AS}$) differs from its ground state. Concomitant with the suggested decrease in the occupancy of the photo-freed AsCh, the two domains of the enzyme, which face one another across the active-site gorge (Morel *et al.*, 1999), moved away from each other in structure $\mathbf{4}^{AS}$ (Fig. 6), resulting in an increased volume of the active-site gorge (Table 5). The domain movements were not observed when a crystal of the NPT-AsCh–*Tc*AChE complex was annealed to RT under the same conditions but without UV irradiation or when a native *Tc*AChE crystal was subjected to UV irradiation at RT. These movements are therefore the result of NPT-AsCh photolysis and annealing to room temperature and may have been triggered by the exit of AsCh. This indicates that exit of AsCh occurs *via* the gorge, at least to some extent, at RT.

Most importantly, structure $\mathbf{4}^{AS}$ shows a deformation of the active-site gorge architecture. In particular, the rotation of the Trp84 side chain towards the bulk in monomer *A* of structure $\mathbf{4}^{AS}$, accompanied by side-chain movements of Met83, Val129, Tyr130, Tyr442, Ile444 and Glu445, opens a hole adjacent to the Ch-binding locus of the CAS that is large enough to allow the passage of a water molecule. Evidence for the opening of such a hole is reinforced by difference electron-density maps, in which a pair of positive and negative peaks substantiate the movement of Trp84. We suggest that the observed opening may be a residual trace of an even larger transient opening through which the photo-freed AsCh had escaped: the putative 'backdoor' (Gilson *et al.*, 1994). The negative peaks observed at the cage moieties of the NPT-AsCh molecules are of lower intensity than those observed for the side chain of Trp84 both at the CAS and the PAS. This is consistent with some AsCh molecules exiting the active site *via* a backdoor, leaving the cage still within the gorge.

Our results provide experimental evidence for the existence of a pathway other than the gorge through which at least a fraction of enzymatically generated choline may clear the active site after catalysis. In particular, the observed opening caused by a movement of Trp84 may serve as an alternative route to/from the active site for substrate/products when the principal access route *via* the gorge is obstructed, *e.g.* by binding of FAS (Marchot *et al.*, 1993; Radic *et al.*, 1994, 1995; Eastman *et al.*, 1995). The domain movements observed in our study probably reflect 'breathing motions' associated with choline exit *via* the gorge.

4.2. The caged-compound approach in kinetic crystallography of ChEs

X-ray protein crystallography is a very powerful technique for solving macromolecular structures. However, it suffers from the limitation that it displays the time-averaged structure of an ensemble of molecules present in the diffracting volume of the crystal. Consequently, dynamic information cannot usually be assessed. Exploration of the conformational energy landscape of a protein using X-ray crystallography requires the use of experimental tricks to overcome the inherently static nature of crystallographic structures. To date, most successful kinetic crystallography studies have exploited the use of lasers to synchronously and efficiently trigger photoswitchable reactions within light-sensitive proteins and of flash-cooling of the crystal to cryo-trap intermediate states (reviewed by Bourgeois & Royant, 2005). Here, photodissociation of a caged compound by a 266 nm laser was employed which in combination with a 'freeze–trigger–freeze' strategy allowed us to address the exit of AsCh from the active site of *Tc*AChE in structural terms.

Our approach suffers from at least three principal limitations. Firstly, we employed a 266 nm laser for the UV-induced photolytical reaction of the NPT-caged compound, which displays a maximal absorption cross-section at about this wavelength. However, owing to strong absorption by aromatic residues at 266 nm, less than 10% of the photons remained available for de-caging. Hence, rather thin crystals had to be used in order to maximize the efficiency of photolysis. It is likely that despite a tenfold lower absorption cross-section, the use of near-UV light at 355 nm (and at a similar power) would have allowed more homogeneous photolysis in thicker crystals while minimizing the specific UV damage to protein structures that has been described recently (Neves-Petersen *et al.*, 2002; Vernede *et al.*, 2006; Nanao & Ravelli, 2006). However, such a laser was not available at the time of our study. Further progress using this approach should benefit from the availability of tunable lasers and from the synthesis of caged compounds that dissociate most efficiently upon irradiation at

a wavelength remote from the absorption band of aromatic residues.

The second limitation of our approach relates to the annealing to room temperature (ART) procedure. ART of the crystals was performed to allow the occurrence of molecular motions of the protein, of the photolysis products and of the solvent that might be required for AsCh to exit the active-site gorge. ART procedures demand adequate robustness of the crystals and preliminary characterization of the accessible time range at RT. Other approaches have been used that avoid the need to freeze the sample before light-activation at RT, while preserving crystal integrity. For example, the loop-mounted crystal can be transiently embedded at 277 K in a capillary to avoid evaporation in the course of centring and illumination (Scheidig *et al.*, 1999). However, our approach has the advantage that sophisticated temperature profiles can be applied. In particular, transient annealing, following flash-cooling, to a cryotemperature window in which the solvent has acquired liquid-like properties (Weik, Kryger *et al.*, 2001; Weik, Ravelli *et al.*, 2001; Weik *et al.*, 2005) might unleash some of the motions of both protein and solvent required for a given enzymatic reaction to proceed a step further. Under such conditions and if a high photolysis efficiency of the given caged compound is achievable at cryogenic temperatures, higher resolution structures of intermediate states should be attainable (Ursby *et al.*, 2002).

Another limitation of the method concerns a possible discrepancy between the timescale on which experiments are performed (here seconds) and that on which most biologically relevant conformational changes occur (picoseconds to milliseconds). ART is thus best suited for very slow reactions, such as that referred to above (Scheidig *et al.*, 1999), that occur on the timescale of seconds or minutes. In the case of AChE, photolysis of the caged compound and enzymatic catalysis both occur on the microsecond timescale in solution. However, it is possible that the crystalline state and the presence of a highly viscous solvent slows the AChE catalytic turnover in our experimental conditions by several orders of magnitude (Raves, 1998).

5. Conclusions

We have described a kinetic crystallography approach based on a combination of the photolysis of rationally designed caged compounds with temperature-controlled protein crystallography. It can be used to trigger biologically relevant reactions within crystalline samples, hence allowing structural monitoring of the course of an enzymatic event. In the case of AChE, UV-induced photocleavage of NPT-caged AsCh during a brief annealing of the crystal at room temperature most probably resulted in a fraction of the AsCh molecules being expelled from the active-site gorge of the enzyme. Large-amplitude motions of the domains facing one another across the active-site gorge, as well as the increase in its volume occurring concomitantly with the expulsion of AsCh, suggest that product exit partially took place *via* the top of the gorge under the experimental conditions employed. Conformational changes were also observed in the putative backdoor region, suggesting that exit of Ch after catalysis may occur *via* routes alternative to the gorge.

We warmly thank Lilly Toker and Michal Cohen for purification of *Tc*AChE, and Elspeth Garman, Joanne McCarthy, John McGeehan, Jérémy Ohana, Raimond Ravelli and Xavier Vernede for fruitful discussions and help during data collection. We would like to thank one of the referees who advised us to employ the difference-refinement procedure. We gratefully acknowledge the ESRF for beamtime under long-term projects MX347 and MX438 (radiation damage BAG), and MX387 and MX498 (IBS BAG). We are grateful to Didier Fournier for fruitful discussions, to Mike Sawaya for critical reading of the manuscript and to Juan Fontecilla-Camps for regular access to the X-ray source in his laboratory. We thank James Murray for help in using *ESCET* and Chris Miller for providing us with a matrix-plotting Python script. Financial support by the CEA, the CNRS and the UJF is acknowledged, as well as a grant to MW from the Agence Nationale de la Recherche (project No. JC05_45685). JPC was supported by an EMBO short-term fellowship (ASTF230-2006). This study benefited from the US Army Medical and Material Command under Contract No. DAMD17-97-2-7022, the EC Fifth Framework Program on the Quality of Life and Management of Living Resources, the Kimmelman Center for Biomolecular Structure and Assembly (Rehovot, Israel), the Benoziyo Center for Neurosciences and the Kalman and Ida Wolens Foundation. JLS is the Pickman Professor of Structural Biology.

References

Axelsen, P. H., Harel, M., Silman, I. & Sussman, J. L. (1994). *Protein Sci.* **3**, 188–197.

Barak, D., Kronman, C., Ordentlich, A., Ariel, N., Bromberg, A., Marcus, D., Lazar, A., Velan, B. & Shafferman, A. (1994). *J. Biol. Chem.* **269**, 6296–6305.

Bartolucci, C., Perola, E., Cellai, L., Brufani, M. & Lamba, D. (1999). *Biochemistry*, **38**, 5714–5719.

Bourgeois, D. & Royant, A. (2005). *Curr. Opin. Struct. Biol.* **15**, 538–547.

Bourgeois, D., Vernede, X., Adam, V., Fioravanti, E. & Ursby, T. (2002). *J. Appl. Cryst.* **35**, 319–326.

Bourgeois, D. & Weik, M. (2005). *Dynamic Studies in Biology: Phototriggers, Photoswitches and Caged Biomolecules*, edited by M. Goeldner & R. Givens, pp. 410–435. Weinheim: Wiley-VCH.

Bourne, Y., Radic, Z., Sulzenbacher, G., Kim, E., Taylor, P. & Marchot, P. (2006). *J. Biol. Chem.* **281**, 29256–29267.

Bourne, Y., Taylor, P. & Marchot, P. (1995). *Cell*, **83**, 503–512.

Brünger, A. T., Adams, P. D., Clore, G. M., DeLano, W. L., Gros, P., Grosse-Kunstleve, R. W., Jiang, J.-S., Kuszewski, J., Nilges, M., Pannu, N. S., Read, R. J., Rice, L. M., Simonson, T. & Warren, G. L. (1998). *Acta Cryst.* D**54**, 905–921.

Bui, J. M., Tai, K. & McCammon, J. A. (2004). *J. Am. Chem. Soc.* **126**, 7198–7205.

Casida, J. E. & Quistad, G. B. (2005). *Chem. Biol. Interact.* **15**, 277–283.

Collaborative Computational Project, Number 4 (1994). *Acta Cryst.* D**50**, 760–763.

Colletier, J.-P., Fournier, D., Greenblatt, H., Sussman, J. L., Zaccai, G., Silman, I. & Weik, M. (2006). *EMBO J.* **25**, 2746–2756.

Corrie, J. E., Barth, A., Munasinghe, V. R., Trentham, D. R. & Hutter, M. C. (2003). *J. Am. Chem. Soc.* **125**, 8546–8554.

DeLano, W. L. (2002). *PyMOL.* DeLano Scientific, San Carlos, CA, USA.

Dundas, J., Ouyang, Z., Tseng, J., Binkowski, A., Turpaz, Y. & Liang, J. (2006). *Nucleic Acids Res.* **34**, W116–W118.

Eastman, J., Wilson, E. J., Cervenansky, C. & Rosenberry, T. L. (1995). *J. Biol. Chem.* **270**, 19694–19701.

Eichler, J., Anselmet, A., Sussman, J. L., Massoulie, J. & Silman, I. (1994). *Mol. Pharmacol.* **45**, 335–340.

Emsley, P. & Cowtan, K. (2004). *Acta Cryst.* D**60**, 2126–2132.

Enyedy, I. J., Kovach, I. M. & Brooks, B. R. (1998). *J. Am. Chem. Soc.* **120**, 8043–8050.

Faerman, C., Ripoll, D., Bon, S., Le Feuvre, Y., Morel, N., Massoulie, J., Sussman, J. L. & Silman, I. (1996). *FEBS Lett.* **386**, 65–71.

Felder, C. E., Harel, M., Silman, I. & Sussman, J. L. (2002). *Acta Cryst.* D**58**, 1765–1771.

Fermi, G., Perutz, M. F., Dickinson, L. C. & Chien, J. C. (1982). *J. Mol. Biol.* **155**, 495–505.

Gilson, M. K., Straatsma, T. P., McCammon, J. A., Ripoll, D. R., Faerman, C. H., Axelsen, P. H., Silman, I. & Sussman, J. L. (1994). *Science*, **263**, 1276–1278.

Golicnik, M., Fournier, D. & Stojan, J. (2001). *Biochemistry*, **40**, 1214–1219.

Greenblatt, H. M., Dvir, H., Silman, I. & Sussman, J. L. (2003). *J. Mol. Neurosci.* **20**, 369–383.

Greenblatt, H. M., Guillou, C., Guénard, D., Argaman, A., Botti, S., Badet, B., Thal, C., Silman, I. & Sussman, J. L. (2004). *J. Am. Chem. Soc.* **126**, 15405–15411.

Hajdu, J. & Andersson, I. (1993). *Annu. Rev. Biophys. Biomol. Struct.* **22**, 467–498.

Harel, M., Kleywegt, G. J., Ravelli, R. B., Silman, I. & Sussman, J. L. (1995). *Structure*, **3**, 1355–1366.

Harel, M., Quinn, D. M., Nair, H. K., Silman, I. & Sussman, J. L. (1996). *J. Am. Chem. Soc.* **118**, 2340–2346.

Harel, M., Schalk, I., Ehret-Sabatier, L., Bouet, F., Goeldner, M., Hirth, C., Axelsen, P. H., Silman, I. & Sussman, J. L. (1993). *Proc. Natl Acad. Sci. USA*, **90**, 9031–9035.

Kabsch, W. (1993). *J. Appl. Cryst.* **26**, 795–800.

Karlsson, E., Mbugua, P. M. & Rodriguez-Ithurralde, D. (1984). *J. Physiol. (Paris)*, **79**, 232–240.

Kleywegt, G. J. (1995). *Jnt CCP4/ESF–EACBM Newsl. Protein Crystallogr.* **31**, 45–50.

Kleywegt, G. J. & Jones, T. A. (1996). *Acta Cryst.* D**52**, 826–828.

Kovach, I. M., Qian, N. & Bencsura, A. (1994). *FEBS Lett.* **349**, 60–64.

Kronman, C., Ordentlich, A., Barak, D., Velan, B. & Shafferman, A. (1994). *J. Biol. Chem.* **269**, 27819–27822.

Laskowski, R. A., MacArthur, M. W., Moss, D. S. & Thornton, J. M. (1993). *J. Appl. Cryst.* **26**, 283–291.

Marchot, P., Khelif, A., Ji, Y. H., Mansuelle, P. & Bougis, P. E. (1993). *J. Biol. Chem.* **268**, 12458–12467.

Millard, C. B. & Broomfield, C. A. (1995). *J. Neurochem.* **64**, 1909–1918.

Morel, N., Bon, S., Greenblatt, H. M., Van Belle, D., Wodak, S. J., Sussman, J. L., Massoulie, J. & Silman, I. (1999). *Mol. Pharmacol.* **55**, 982–992.

Mozzarelli, A. & Rossi, G. L. (1996). *Annu. Rev. Biophys. Biomol. Struct.* **25**, 343–365.

Murshudov, G. N., Vagin, A. A. & Dodson, E. J. (1997). *Acta Cryst.* D**53**, 240–255.

Nanao, M. H. & Ravelli, R. B. (2006). *Structure*, **14**, 791–800.

Neves-Petersen, M. T., Gryczynski, Z., Lakowicz, J., Fojan, P., Pedersen, S., Petersen, E. & Petersen, S. B. (2002). *Protein Sci.* **11**, 588–600.

Nienhaus, G. U., Chu, K. & Jesse, K. (1998). *Biochemistry*, **37**, 6819–6823.

Peng, L., Nachon, F., Wirz, J. & Goeldner, M. (1998). *Angew. Chem. Int. Ed.* **37**, 2691–2693.

Quinn, D. M. (1987). *Chem. Rev.* **87**, 955–979.

Radic, Z., Duran, R., Vellom, D. C., Li, Y., Cervenansky, C. & Taylor, P. (1994). *J. Biol. Chem.* **269**, 11233–11239.

Radic, Z., Quinn, D. M., Vellom, D. C., Camp, S. & Taylor, P. (1995). *J. Biol. Chem.* **270**, 20391–20399.

Radic, Z., Reiner, E. & Taylor, P. (1991). *Mol. Pharmacol.* **39**, 98–104.

Raves, M. L. (1998). PhD thesis. Weizmann Institute of Science, Rehovot, Israel.

Ripoll, D. R., Faerman, C. H., Axelsen, P. H., Silman, I. & Sussman, J. L. (1993). *Proc. Natl Acad. Sci. USA*, **90**, 5128–5132.

Rosenberry, T. L. (1975). *Adv. Enzymol. Relat. Areas. Mol. Biol.* **43**, 103–218.

Royant, A., Carpentier, P., Ohana, J., McGeehan, J., Paetzold, B., Noirclerc-Savoye, M., Vernede, X., Adam, V. & Bourgeois, D. (2007). *J. Appl. Cryst.* In the press.

Scheidig, A. J., Burmester, C. & Goody, R. S. (1999). *Structure*, **7**, 1311–1324.

Schlichting, I., Almo, S. C., Rapp, G., Wilson, K., Petratos, K., Lentfer, A., Wittinghofer, A., Kabsch, W., Pai, E. F., Petsko, G. A. & Goody, R. S. (1990). *Nature (London)*, **345**, 309–315.

Schneider, T. R. (2000). *Acta Cryst.* D**56**, 714–721.

Shen, T., Tai, K., Henchman, R. H. & McCammon, J. A. (2002). *Acc. Chem. Res.* **35**, 332–340.

Silman, I. & Sussman, J. L. (2005). *Curr. Opin. Pharmacol.* **5**, 293–302.

Specht, A. & Goeldner, M. (2004). *Angew. Chem. Int. Ed. Engl.* **43**, 2008–2012.

Specht, A., Ursby, T., Weik, M., Peng, L., Kroon, J., Bourgeois, D. & Goeldner, M. (2001). *Chembiochem*, **2**, 845–848.

Sussman, J. L., Harel, M., Frolow, F., Oefner, C., Goldman, A., Toker, L. & Silman, I. (1991). *Science*, **253**, 872–879.

Sussman, J. L., Harel, M., Frolow, F., Varon, L., Toker, L., Futerman, A. H. & Silman, I. (1988). *J. Mol. Biol.* **203**, 821–823.

Tai, K., Shen, T., Borjesson, U., Philippopoulos, M. & McCammon, J. A. (2001). *Biophys. J.* **81**, 715–724.

Terwilliger, T. C. & Berendzen, J. (1995). *Acta Cryst.* D**51**, 609–618.

Theobald, D. L. & Wuttke, D. S. (2006). *Proc. Natl Acad. Sci. USA*, **103**, 18521–18527.

Ursby, T. & Bourgeois, D. (1997). *Acta Cryst.* A**53**, 564–575.

Ursby, T., Weik, M., Fioravanti, E., Delarue, M., Goeldner, M. & Bourgeois, D. (2002). *Acta Cryst.* D**58**, 607–614.

Velan, B., Barak, D., Ariel, N., Leitner, M., Bino, T., Ordentlich, A. & Shafferman, A. (1996). *FEBS Lett.* **395**, 22–28.

Vernede, X., Lavault, B., Ohana, J., Nurizzo, D., Joly, J., Jacquamet, L., Felisaz, F., Cipriani, F. & Bourgeois, D. (2006). *Acta Cryst.* D**62**, 253–261.

Weik, M., Kryger, G., Schreurs, A. M. M., Bouma, B., Silman, I., Sussman, J. L., Gros, P. & Kroon, J. (2001). *Acta Cryst.* D**57**, 566–573.

Weik, M., Ravelli, R. B., Silman, I., Sussman, J. L., Gros, P. & Kroon, J. (2001). *Protein Sci.* **10**, 1953–1961.

Weik, M., Schreurs, A. M. M., Leiros, H.-K. S., Zaccai, G., Ravelli, R. B. G. & Gros, P. (2005). *J. Synchrotron Rad.* **12**, 310–317.

Wlodek, S. T., Clark, T. W., Scott, L. R. & McCammon, J. A. (1997). *J. Am. Chem. Soc.* **119**, 9513–9522.

Xu, Y., Shen, J., Luo, X., Silman, I., Sussman, J. L., Chen, K. & Jiang, H. (2003). *J. Am. Chem. Soc.* **125**, 11340–11349.

Shoot-and-Trap: Use of specific x-ray damage to study structural protein dynamics by temperature-controlled cryo-crystallography

Jacques-Philippe Colletier*†‡, Dominique Bourgeois§¶, Benoît Sanson*, Didier Fournier‖, Joel L. Sussman**, Israel Silman††, and Martin Weik*‡

*Laboratoire de Biophysique Moléculaire and §Laboratoire de Cristallogenèse et de Cristallographie des Protéines, Institut de Biologie Structurale Jean Pierre Ebel, Commissariat à l'Énergie Atomique, Centre National de la Recherche Scientifique, Université Joseph Fourier, 41 rue Jules Horowitz, F-38027 Grenoble, France; ‖Groupe de Biotechnologie des Protéines, Institut de Pharmacologie et de Biologie Structurale, Centre National de la Recherche Scientifique, 205 route de Narbonne, 31077 Toulouse, France; Departments of **Structural Biology and ††Neurobiology, Weizmann Institute of Science, 76100 Rehovot, Israel; and ¶European Synchrotron Radiation Facility, 6 rue Jules Horowitz, 38000 Grenoble, France

Communicated by David Eisenberg, University of California, Los Angeles, CA, May 20, 2008 (received for review December 11, 2007)

Although x-ray crystallography is the most widely used method for macromolecular structure determination, it does not provide dynamical information, and either experimental tricks or complementary experiments must be used to overcome the inherently static nature of crystallographic structures. Here we used specific x-ray damage during temperature-controlled crystallographic experiments at a third-generation synchrotron source to trigger and monitor (Shoot-and-Trap) structural changes putatively involved in an enzymatic reaction. In particular, a nonhydrolyzable substrate analogue of acetylcholinesterase, the "off-switch" at cholinergic synapses, was radiocleaved within the buried enzymatic active site. Subsequent product clearance, observed at 150 K but not at 100 K, indicated exit from the active site possibly via a "backdoor." The simple strategy described here is, in principle, applicable to any enzyme whose structure in complex with a substrate analogue is available and, therefore, could serve as a standard procedure in kinetic crystallography studies.

acetylcholinesterase | kinetic crystallography | structure–dynamics–function relationships | energy landscape | synchrotron radiation

Protein function depends critically on the synergy of structure and dynamics. Structural dynamics, stemming from the interconversion of conformational states in the complex energy landscape of a protein (1, 2), are not readily accessible to conventional x-ray crystallography. The advent of third-generation synchrotron sources, producing highly brilliant x-ray beams, has opened up exciting possibilities for studying macromolecular structural dynamics by using an ensemble of techniques known as kinetic crystallography (3). Although specific radiation damage in the course of data collection is often an issue at highly intense insertion-device synchrotron beamlines (4–7), it has been used for certain aspects of macromolecular x-ray structure determination, such as for phasing purposes (8), to structurally follow the catalytic pathway of redox enzymes (9), and for monitoring the dynamical behavior of crystalline proteins at cryogenic temperatures (10, 11). Amino acid residues directly involved in protein function, including those at the active sites of enzymes, are among the most radiation-sensitive entities (4–6, 10, 12–16). This observation has been linked to the strain of residue conformations within active sites that is released upon specific radiation damage (17). In this study, temperature-controlled x-ray cryo-crystallography was shown to result in radiolytic cleavage of a substrate analogue bound at the active site of the enzyme *Torpedo californica* acetylcholinesterase (*Tc*AChE), and permitted monitoring of subsequent clearance of a radiolysis product from the active site.

AChE terminates transmission at cholinergic synapses by rapid hydrolysis of the neurotransmitter acetylcholine (ACh) (Fig. 1) to choline (Ch) and acetate (18). The reaction proceeds in two steps. First, the enzyme is acetylated and the Ch-product expelled. Then, a water molecule regenerates the free enzyme with concomitant release of acetic acid. AChE is one of fastest enzymes in nature, with a turnover of 10^3–10^4 s^{-1}, and is the target of most currently approved anti-Alzheimer drugs (19), of insecticides (20), and of chemical warfare agents (21). The crystal structure of *Tc*AChE revealed that its active site is buried at the bottom of a deep and narrow gorge (Fig. 2) (22), an unexpected architecture in view of its high catalytic efficiency. Significant molecular breathing motions are essential for traffic of substrate and products to occur along this gorge, and it has been suggested that products may exit the active site via a putative, transiently opened backdoor (23, 24). Structural snapshots of substrate and products bound within the gorge have been obtained recently (25, 26). Binding of a nonhydrolyzable substrate analogue [4-oxo-*N*,*N*,*N*-trimethylpentanaminium iodide (OTMA)] (Fig. 1) in the active site uncovered the structural features of the tetrahedral intermediate state, while the structure of the enzyme in the action of expelling a product analogue at room temperature provided evidence for a transient opening of the backdoor (27). Here, we report the radiolytic breakdown of OTMA in the OTMA/*Tc*AChE complex during collection of a series of crystallographic data sets at 100 and 150 K. Structural changes at 150 K indicate that the enzyme is flexible enough at that temperature to allow the exit of an analogue of the natural hydrolysis product, Ch, from the deeply buried active site. Radiolytic breakdown of substrate analogues, combined with temperature-controlled cryo-crystallography, is suggested as a methodology for studying product traffic and related structural dynamics in other crystalline enzymes.

Results

The substrate analogue OTMA differs from the natural substrate, ACh, only in the replacement of the ester oxygen by a carbon, thus being composed of acetyl (Ac) and pseudo-Ch (PsCh) moieties (Fig. 1); PsCh (*n*-propyltrimethylammonium) is

Author contributions: J.P.C. and M.W. designed research; J.P.C., B.S., and M.W. performed research; D.F. contributed new reagents/analytic tools; J.P.C., D.B., D.F., J.L.S., I.S., and M.W. analyzed data; and J.P.C., I.S., and M.W. wrote the paper.

The authors declare no conflict of interest.

Data deposition: The atomic coordinates have been deposited in the Protein Data Bank, www.pdb.org (PDB ID codes 2vja, 2vjb, 2vjc, 2vjd, 2vt6, and 2vt7).

†Present address: UCLA–DOE Institute for Genomics and Proteomics, University of California, Los Angeles, CA 90095.

‡To whom correspondence may be addressed. E-mail: jacques@colletier.com or weik@ibs.fr.

This article contains supporting information online at www.pnas.org/cgi/content/full/0804828105/DCSupplemental.

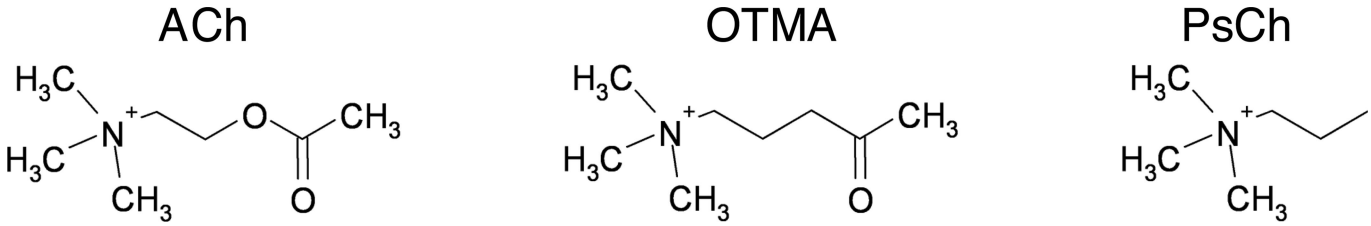

Fig. 1. Structures of ACh, OTMA, and PsCh.

an analogue of the enzymatic product Ch. OTMA binds, in orthorhombic crystals of *Tc*AChE, at the catalytic anionic subsite (CAS) of the active site and at the peripheral anionic site (PAS), in exactly the same manner as reported for trigonal *Tc*AChE crystals (25) (PDB ID code 2C5F). In the active site, its quaternary nitrogen makes cation-π interactions with Trp-84 and Phe-330, and an electrostatic interaction with the acidic side chain of Glu-199 (Fig. 3*A*). Its carbonyl oxygen hydrogen bonds to Gly-118N, Gly-119N, and Ala-201N in the oxyanion hole, and its carbonyl carbon is modeled at a covalent-bonding distance from the catalytic Ser-200 Oγ. At the PAS, a second OTMA molecule is bound, with its CH_3CO moiety pointing toward the active site. Its quaternary group makes cation-π interactions with the aromatic rings of Trp-279 (see Fig. 4*a*) and Tyr-70, whereas its carbonyl oxygen is weakly H-bonded to Tyr-121 Oζ.

Four consecutive data sets (I–IV) were collected from the same volume of a single crystal of an OTMA/*Tc*AChE complex at 100 K. The crystal was then translated, and a second series of four data sets was collected at another spot on the crystal at 150 K [see supporting information (SI) Table S1]. Thus, the two series reveal the x-ray dose-dependent evolution of the OTMA/*Tc*AChE complex at these two temperatures. From the first to the last data set, the resolution deteriorated from 2.3 to 2.4 Å at both temperatures. The cumulative doses absorbed after collection of data sets IV at 100 K and III at 150 K are nearly identical, 0.92 and 0.95 $\times$ 10^7 Gy, respectively. They correspond to approximately one-third of the experimentally determined Garman limit (3 $\times$ 10^7 Gy), above which the biological information extracted from a macromolecular structure is likely to be compromised (28).

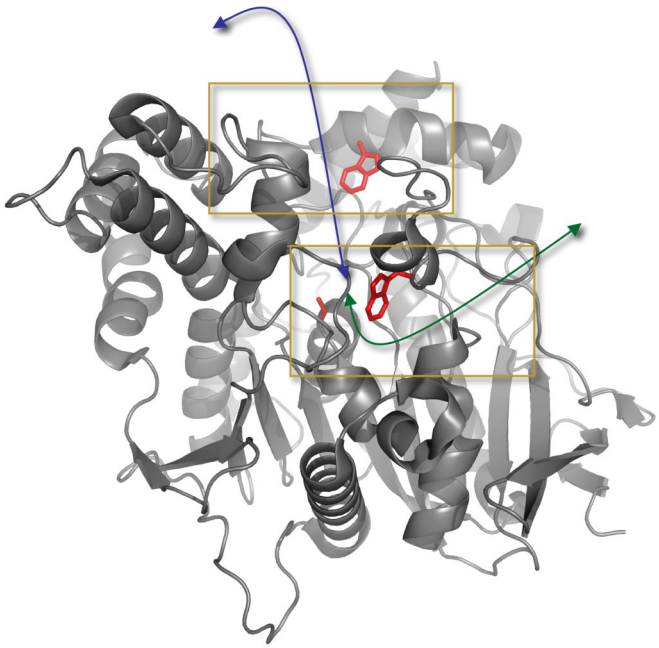

Fig. 2. Ribbon diagram of the three-dimensional structure of *Tc*AChE. The two main contributors to the stabilization of the substrate within the active-site (CAS), W84, and at the peripheral site (PAS), W279, are highlighted. The catalytic Ser-200 is shown at the bottom of the gorge. The blue arrow indicates the active-site gorge, and the green arrow highlights the putative backdoor. *Lower* and *Upper Insets*. indicate the parts that are expanded in Figs. 3 and 4, respectively.

Radiolytic Breakdown of OTMA in the Active Site of *Tc*AChE at 100 K. The OTMA in the CAS of the structure corresponding to data set I at 100 K (PDB ID code 2VJA) is well defined, as judged from $2F_o - F_c$ composite-omit electron density maps (Fig. S1*a*), reproducing the structural features reported previously (25). Electron density observed around OTMA is still continuous in data set IV at 100 K (PDB ID code 2VJB) while noticeably thinner (Fig. S1*b*). A strong negative peak is observed on OTMA in the Fourier difference map (Fig. 3*A*) computed with observed structure factor amplitudes of data sets I and IV and with calculated phases from model I [$(F_{o100K\text{-}IV} - F_{o100K\text{-}I})\cdot e^{-i\varphi_{100K\text{-}I}}$]. Inspection of B factors revealed a higher loss of definition of the PsCh moiety of OTMA, but not of the Ac group on Ser-200, compared with the loss of definition averaged over all protein and solvent atoms (see *Materials and Methods*). Radiation-induced cleavage of OTMA into PsCh and an Ac group is thus the most likely scenario. The strong positive peak (1 in Fig. 3*A*) below Phe-330 indicates that repositioning of the radio-released PsCh occurs within the active site. As a consequence, a water molecule interacting with the PsCh moiety of OTMA changes its position concomitantly, as suggested by a pair of positive and negative peaks (2 and 3 in Fig. 3*A*). The repositioning of the PsCh moiety occurs just below Phe-330, which, together with Tyr-121 (residue not shown in Fig. 3), forms a bottleneck in the middle of the gorge (22). A negative peak is seen on the Phe-330 phenyl ring in the Fourier difference map (Fig. 3*A*), as well as on the adjacent Tyr-334 (not shown), suggesting that both residues become partially disordered upon repositioning of the radiation-freed PsCh. The binding locus indicated for PsCh by the positive peak in the Fourier difference map is different from that reported earlier for the steady-state complex of *Tc*AChE with thiocholine (TCh) (25). The positive peak (4 in Fig. 3*A*) observed behind the acetate moiety of the OTMA molecule in the Fourier difference map had been attributed earlier to a radiation-induced movement of the catalytic His-440 (10).

Negative and positive peaks indicative of well documented damage to acidic residues and disulfide bonds (4–7) are also seen in the difference Fourier map (data not shown).

Radiolytic Breakdown of OTMA in the Active Site of *Tc*AChE at 150 K. The $2F_o - F_c$ composite-omit electron density for the OTMA in the CAS of the structure corresponding to data set I at 150 K (PDB ID code 2VJC) is as well defined (Fig. S1*c*) as the one corresponding to data set I at 100 K (Fig. S1*a*). However, as the x-ray dose increases, much greater structural changes occur in the active site at 150 K than at 100 K. At a cumulative absorbed dose similar to that for data set IV at 100 K, the $2F_o - F_c$ composite-omit map of data set III at 150 K (PDB ID code

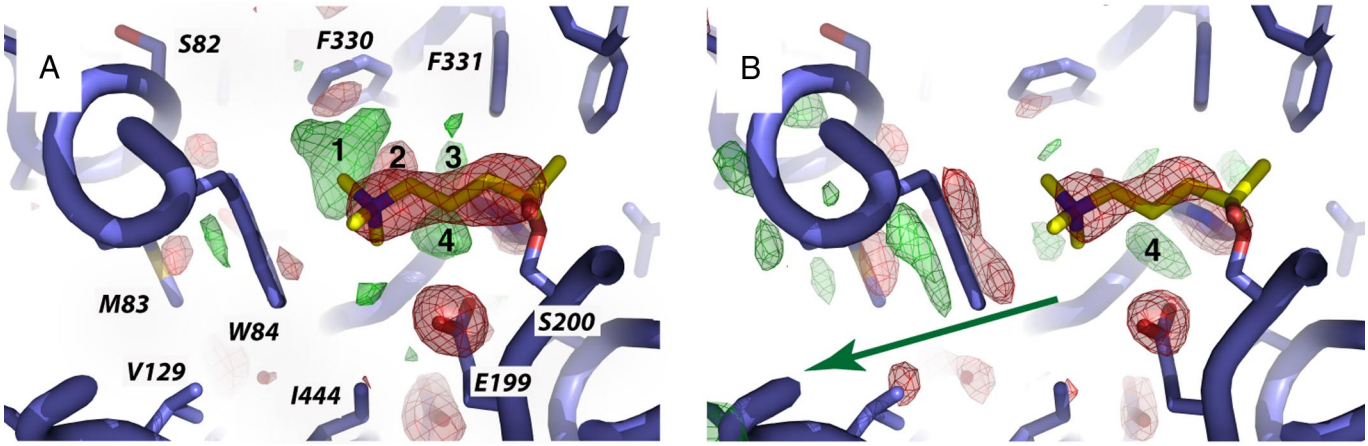

Fig. 3. OTMA in the CAS of *Tc*AChE at 100 K (*A*) and 150 K (*B*). Protein residues are shown in blue, and the OTMA molecule is shown in yellow. The Fourier difference maps (contour level 4σ) computed for data sets IV − I at 100 K (*A*) and for data sets III − I at 150 K (*B*), are shown superimposed on the model. Positive and negative peaks are shown in green and red, respectively. Peaks 1–4 are referred to in the text. The arrow in *B* indicates a putative backdoor exit of PsCh that is also indicated by a green arrow in Fig. 2. The orientation in Fig. 3 is the same as in Fig. S1 but slightly zoomed out. A version for the colorblind is given in Fig. S2.

2VJD) shows poorly defined and discontinuous electron density for the OTMA molecule bound at the CAS (Fig. S1*d*); only residual density is observed for the PsCh moiety next to Trp-84. The absence of electron-density around the Phe-330 phenyl group in the $2F_o - F_c$ composite-omit maps (Fig. S1 *c* and *d*) indicates that it is more disordered in data sets I and III at 150 K than at 100 K. Analogously, the water molecule interacting with the PsCh moiety of the OTMA molecule in the CAS at 100 K (Fig. S1*a*) has no discernable electron density in the $2F_o - F_c$ composite-omit maps calculated for data sets I and III at 150 K (Fig. S1 *c* and *d*). Thus, the crystalline enzyme is more flexible at 150 K than at 100 K. The Fourier difference map, calculated with the structure factor amplitudes of data sets I and III at 150 K, and with the calculated phases from model I [$(F_{o150K\text{-}III} - F_{o150K\text{-}I})\cdot e^{-i\varphi_{150K\text{-}I}}$], reveals an elongated negative peak on OTMA in the CAS (Fig. 3*B*), indicating radiolysis of the substrate analogue. No strong positive peak is seen adjacent to this negative peak, suggesting that the radiolytically generated PsCh does not reposition below Phe-330 at 150 K, as it does at 100 K. In the putative backdoor region, strong positive and negative peaks are observed on the side chains of Met-83, Trp-84, Val-129 (Fig. 3*B*), and on both the main and side chains of Tyr-442, Ser-79, and Gly-81 (data not shown). Again, the positive peak attributed earlier to a radiation-induced movement of the catalytic His-440 (10) is visible in the CAS (4 in Fig. 3*B*).

To address the effect of x-ray irradiation on native orthorhombic *Tc*AChE crystals at 150 K, a control experiment was performed, in which a similar cumulative x-ray dose was administered (i.e., 0.94×10^7 Gy, distributed over five consecutive data sets; see *SI Materials and Methods*). A Fourier difference map was then calculated between the first (control-I) and last (control-V) data set (Fig. S4 and Table S2). Peaks on Trp-84, Met-83, Glu-199 and His-440 are observed (Fig. S4) that are qualitatively similar to those in Fig. 3*B*.

Radiation-Induced Changes at the Peripheral Substrate-Binding Site (PAS). At 100 K, two positive peaks are observed in the Fourier difference map next to a negative one on the carboxyl group of Glu-278, the residue adjacent to Trp279 at the PAS (Fig. 4*A*). No significant negative peak is observed on the OTMA molecule bound at the PAS (Fig. 4 *A* and *B*), indicating that it is not affected by x-ray irradiation at 100 and 150 K, and that it does not move from its original position. Unlike at 100 K, no positive peaks are observed at 150 K next to the negative peak on the carboxyl group of Glu-278 (Fig. 4*B*).

Discussion

Build-Up of an Intermediate at 100 K and Exit of PsCh from the Active Site at 150 K. Two series of structures were collected, at 100 K and at 150 K, on two separate regions of a single crystal of a complex of *Tc*AChE with the nonhydrolyzable substrate analogue OTMA. At both temperatures, difference Fourier maps indicate loss of definition of the PsCh moiety of OTMA at increased absorbed x-ray doses, which we ascribe to radiolytic cleavage of the substrate analogue into an Ac group on the catalytic Ser-200 and PsCh, an analogue of the enzymatic product, Ch. The series of structures determined at 100 K is interpreted as illustrating the cleavage of the tetrahedral intermediate that forms subse-

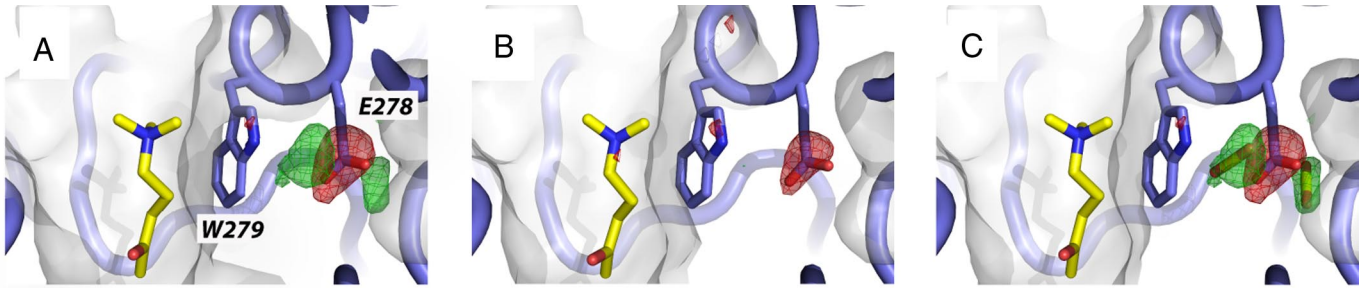

Fig. 4. OTMA at the PAS of *Tc*AChE. (*A* and *B*) The Fourier difference maps (contour level 4σ) computed for data sets IV − I at 100 K (*A*) and for data sets III − I at 150 K (*B*) are shown superimposed on the model. Positive and negative peaks are shown in green and red, respectively. (*C*) Two partially occupied CO_2 molecules are fitted in the positive peaks shown in the Fourier difference map at 100 K in *A*. A version for the colorblind is given in Fig. S3.

quent to binding of ACh in the CAS (Fig. 3*A*). PsCh repositions below Phe-330, a residue that is part of a bottleneck at midway down the active-site gorge. Phe-330 is a very mobile residue, and it has been suggested that it is involved in gating of traffic of substrate and products within the gorge (18, 25). The repositioning of PsCh, evidenced by the strong positive peak observed in the Fourier difference map calculated at 100 K, does not overlap with the position of TCh in complex with *Tc*AChE (PDB ID code 2C5G) (25), nor with that observed for TCh or Ch in complex with mouse AChE (PDB ID codes 2HA2 and 2HA3, respectively) (26). This difference might be ascribed either to the more hydrophobic character of PsCh, relative to TCh or Ch, leading to a different binding mode, or to the fact that the structures presented in refs. 25 and 26, although collected at cryo-temperatures, reflect equilibrium states obtained by soaking at room temperature that were trapped upon cryo-cooling.

At 150 K, no signs of reorientation of PsCh are observed after OTMA radiolysis. However, strong negative and positive features in the Fourier difference map (Fig. 3*B*) indicate a small shift in the equilibrium position of the indole ring of Trp-84 that suggests an exit trajectory (indicated by green arrows in Figs. 2 and 3*B*) for PsCh and, by analogy, for the natural enzymatic hydrolysis product, Ch, via the putative backdoor (23, 24, 27). A similar, but less pronounced displacement of the indole ring of Trp-84 was observed in a radiation-damage control on native orthorhombic *Tc*AChE crystals at 150 K (Fig. S4 and *SI Materials and Methods*). Thus, the Trp-84 movement shown in Fig. 3*B* is partially due to a relaxation at 150 K that might be a local response to radiation-induced changes elsewhere in the enzyme. In any case, the backdoor region is intrinsically more flexible at 150 than at 100 K. Together with the fact that the Fourier difference map is almost featureless at the top of the gorge (Fig. 4*B*), the observed Trp-84 movement argues that at 150 K PsCh exits predominantly via the backdoor. In a second control experiment, the absence of peaks on Trp-84 in a difference Fourier map computed between data set $I^{100\ K}$ and a data set of the native enzyme collected at 100 K (R_{merge} of structure factor amplitudes, 18%; data not shown) excluded the possibility that the movement of Trp-84 observed at 150 K (Fig. 3*B*) is due to unbinding of PsCh from Trp-84.

Our experiments do not allow to determine conclusively the radiochemical mechanism responsible for the cleavage of OTMA (Fig. 1). Secondary electrons or electron holes (7), mobile at both 100 and 150 K, most likely trigger the event by targeting the C–C bond between the Ac group and the PsCh moiety. In the natural substrate, ACh, the equivalent C–O bond between the Ac group and the Ch moiety is weakened by partial electron withdrawal in the tetrahedral intermediate and subsequently cleaved during substrate hydrolysis. OTMA binding in the active site mimics the tetrahedral intermediate that forms during enzymatic hydrolysis of ACh. Consequently, electrons might also be partially withdrawn from the C–C bond between the Ac group and the PsCh moiety in OTMA when it binds to the catalytic Ser-200, thus rendering the Ac carbon electrophilic. An increased radiation-sensitivity of the C–C bond might be the consequence, resulting in the observed OTMA cleavage. Indeed, x-ray irradiation has no significant effect on OTMA bound at the PAS, where ACh binds only transiently en route to the active site, and does not adopt a conformation resembling the transition state. This observation is in agreement with the early proposed "rack-and-strain" theory for enzymatic action, in which strain on the reactive bond is a consequence of the binding of the substrate within the active site of the enzyme (29).

Putative Trapping of Radio-Generated CO_2 Molecules at 100 K. Apart from the structural changes described above that are directly related to the radiolytic breakdown of the substrate analogue OTMA within the active site, most of the radiation damage features observed in the Fourier difference maps have already been reported for the native protein, namely the breakage of disulfide bridges and loss of definition of the carboxyl groups of acidic residues (4, 5, 10). The latter has been interpreted as resulting from the release of a CO_2 molecule by decarboxylation (5, 30). However, a previously undescribed feature was observed here for Glu-278, the residue adjacent to Trp-279 whose indole ring is the principal component of the PAS. For Glu-278 at 100 K, not only is a negative peak seen, but also two strong positive peaks on either side of it (Fig. 4*A*). A partially occupied CO_2 molecule could be fitted by real space refinement into each of the two positive peaks (Fig. 4*C*), and occupancies were estimated to be 5% and 13% (see *Materials and Methods* for details). Likewise, the occupancy of the Glu-278 carboxyl group was estimated to have been reduced to 79%. We thus suggest that either one or both of these positive peaks might reflect partial occupancy by a CO_2 molecule generated by decarboxylation. We conjecture that the Trp-279 indole ring, which blocks access to the active-site gorge, allows trapping of CO_2 at 100 K. Indeed, none of the other decarboxylated residues of the enzyme displays such clear and strong positive peaks next to the negative one. The fact that these peaks are absent from the Fourier map at 150 K (Fig. 4*B*) suggests that, at this temperature, the active-site gorge residues as a whole display sufficient flexibility for the CO_2 molecule to escape. Based on IR spectroscopic experiments, it has been reported that migration of photogenerated CO_2 in GFP occurs in a similar temperature range (31).

Conclusion and Perspectives

A close interdependency exists between the dynamics of a protein and of its immediate environment (32). Therefore, it is likely that dynamical changes in the hydration-water at the protein surface are involved in the observed change in protein flexibility with temperature (11, 33). Similar results were observed (at both 100 and 150 K) when analogous experimental protocols were conducted on a complex of *Tc*AChE (crystallized in the same space group under the same conditions) with a photolabile precursor of the enzymatic product analogue, arsenocholine, namely "caged arsenocholine" (27) (data not shown), and on a "pro-aged" complex of human butyrylcholinesterase (34) with the organophosphate nerve agent soman (J.-P.C., F. Nachon, B.S., P. Masson, and M.W., unpublished results). These findings indicate that the results described here are neither protein- nor ligand-dependent, and that the Shoot-and-Trap strategy is applicable to other crystalline protein systems. Synchrotron-radiation-induced cleavage at 100 K of a N–S bond in an inhibitor complexed with a liver X receptor has indeed been reported (35).

The use of specific radiation damage, in combination with temperature-controlled cryo-crystallography, is a simple experimental approach capable of providing valuable insight into functional aspects of the structural dynamics of enzymes. Whereas most kinetic crystallography techniques are highly time consuming, and require the use of dedicated equipment and materials (3, 27), the Shoot-and-Trap strategy has the advantages of being fast and accessible, in principle, to any synchrotron user. The experiments described here were indeed performed in less than 2 h, including the temperature ramping from 100 to 150 K, at a typical third-generation insertion-device beamline. Moreover, using only a single crystal throughout the experiment permitted conservation of very high isomorphism between the data sets, which is critical for the calculation of accurate Fourier difference maps (3, 27, 36). Although this method obviously requires predetermination of the radiation damage characteristics of a given native enzyme, it is, nevertheless, theoretically applicable to any crystalline enzyme for which a substrate analogue is available. We propose the Shoot-and-Trap strategy

as a simple technique that could allow the standardization of kinetic crystallography studies.

Materials and Methods

Chemicals. The nonhydrolyzable substrate analogue, OTMA (Fig. 1*B*), was synthesized according to Thanei-Wyss and Waser (37).

Crystallization of *Tc*AChE and Soaking Procedure. *Tc*AChE was purified and crystallized as described (22, 38). To obtain the *Tc*AChE/OTMA complex, a large orthorhombic ($P2_12_12_1$) crystal ($300 \times 300 \times 50$ μm^3) was soaked for 2 h at 4°C in a mother liquor solution [30% polyethylene glycol (PEG)200/150 μM morpholinoethanesulfonic acid (Mes), pH 6.0] containing 500 μM OTMA.

Data Collection. Because of the cryoprotective capacity of PEG200, the crystal was directly flash-cooled in the cryostream of a cooling device (700 series, Oxford Cryosystems) at 100 K. X-ray diffraction data were collected on beamline ID14-EH4 at the European Synchrotron Radiation Facility (ESRF) by using the unattenuated beam at a wavelength of 0.932 Å. A first series of four data sets (I–IV) was collected at 100 K on one area of the crystal by using an x-ray beam of dimensions 100×100 μm^2. Subsequently, the crystal was translated by 200 μm along the spindle axis, and the temperature of the cooling device was increased to 150 K at 360 K/h. A second series of four data sets (I–IV) was then collected at 150 K without changing the beam size. For each of the eight data sets, 180 frames were collected, with an oscillation range of 1° and an exposure time of 1 s per frame. The collection time of each series of four data sets was ≈45 min. The ramping time between 100 and 150 K was ≈10 min. Data sets were indexed, merged, and scaled by using XDS/XSCALE, and structure factor amplitudes were generated by using XDSCONV (39). The resolution limits were 2.3, 2.3, 2.3, and 2.4 Å for the four data sets I^{100K}–IV^{100K}, respectively, and 2.3, 2.3, 2.4, and 2.4 Å for the four data sets I^{150K}–IV^{150K}, respectively. The absorbed x-ray doses after collection of each data set, calculated by using the program RADDOSE (40), were 0.24, 0.23, 0.23, and 0.22×10^7 Gy for I^{100K}–IV^{100K}, respectively, and 0.33, 0.32, 0.30, and 0.30×10^7 Gy for I^{150K}–IV^{150K}, respectively. A refill of the synchrotron storage ring (operating in 16-bunch mode) between data sets IV^{100K} and I^{150K}, resulting in a 35% increase of the ring current, was at the origin of the differences in absorbed doses of the two series. The cumulative x-ray doses after collection of data sets IV^{100K} and III^{150K} were nearly identical (i.e., 0.92×10^7 and 0.95×10^7 Gy, respectively), each corresponding to approximately one-third of the experimentally determined Garman limit of 3×10^7 Gy (28). Statistics and other information concerning data collection are shown in Table S1.

Structure Determination and Refinement. The native structure of *Tc*AChE in the orthorhombic space group (PDB ID code 1W75) (41) served as the starting model for the rigid body refinement of data set I^{100K} in the resolution range 50–4 Å. Subsequently, the structure underwent simulated annealing to 2,000 K, with slow-cooling steps of 10 K, followed by 250 steps of conjugate-gradient minimization and 20 steps of individual B-factor refinement. The two monomers in the asymmetric unit (A and B) were manually rebuilt and refined independently. Here, all results and figures refer to monomer B; the results for monomer A are very similar and, thus, are not presented. Diffraction data from 50 Å to the resolution limits were used for refinement and electron-density map calculations. The final model for structure I^{100K} (with waters, sugars, OTMA, and ions) served as the starting model for the refinement of the three other structures (IV^{100K}, I^{150K}, and III^{150K}). They underwent rigid-body refinement, simulated annealing to 2,000 K with cooling steps of 10 K, and then 250 steps of conjugate-gradient minimization, followed by 20 steps of individual B-factor refinement. At the end of the refinements, the $F_o - F_c$ maps were virtually featureless at $\pm 3\sigma$. Unbiased initial electron density maps (Fig. S1) were obtained by calculation of composite-omit $2F_o - F_c$ maps after the rigid-body refinement step. Graphic operations and model building were performed with COOT (42). Refinement and map calculations were performed by using CNS, version 1.1 (43). Fourier difference maps were computed with observed structure factor amplitudes of data sets I^{100K} and IV^{100K} and calculated phases from model I^{100K} [$(F_{o100K\text{-}IV} - F_{o100K\text{-}I})\cdot e^{-i\varphi_{100K\text{-}I}}$], and with observed structure factor amplitudes of data sets I^{150K} and III^{150K} and calculated phases from model I^{150K} [$(F_{o150K\text{-}III} - F_{o150K\text{-}I})\cdot e^{-i\varphi_{150K\text{-}I}}$]. Structure factor amplitude differences were Q weighted to improve the signal-to-noise ratios of the Fourier difference maps (27, 36). R_{merge} values of structure factor amplitudes between data sets I^{100K} and IV^{100K}, and between data sets I^{150K} and III^{150K} were 8.2% and 10.7%, respectively. The figures were produced by using PyMOL (44). Molecular topologies and parameters of OTMA were created by using the PRODRG server at the University of Dundee (Dundee, Scotland) (45). Qualities of the structures were checked and validated by using PROCHECK (46). Refinement statistics are shown in Table S1.

Occupancies of OTMA atoms were set to 1 and not refined. Inspection of B factors in IV^{100K} (III^{150K}) with respect to I^{100K} (I^{150K}) revealed mean increases of 11% (24%) and 27% (44%), respectively, for the Ac and PsCh atoms in the CAS. At the PAS, the increases in B factors for the Ac and PsCh atoms were nearly identical, namely 4% (5%). The average B factor for all protein and solvent atoms increased by 8% (17%) between I^{100K} (I^{150K}) and IV^{100K} (III^{150K}) (Table S1).

To estimate the occupancies of the carboxyl group of Glu-278 and nearby putative CO_2 molecules in structure IV^{100K}, CO_2 molecules were included in the model and fitted by real-space refinement into the two positive difference-density features shown in Fig. 4*A*. B factors of CO_2 molecules were set to the average B factor of Trp-279 side and main chain atoms in structure IV^{100K} (38 $Å^2$), and their occupancies were refined. The occupancies of the two putative CO_2 molecules and of the Glu-278 carboxyl group were refined to 0.13, 0.05, and 0.78, respectively. Because of their low occupancies, CO_2 molecules were not included in the final model of IV^{100K} (PDB ID code 2VJB), and the occupancy of the Glu-278 carboxyl group was set to 1.

ACKNOWLEDGMENTS. We thank Lilly Toker and Michal Cohen for purification of *Tc*AChE; Raimond Ravelli, Joanne McCarthy, and Elspeth Garman for continuous discussions and help during data collection; Ian Carmichael, Chantal Houée-Levin, and David Milstein for fruitful discussions; David Eisenberg, Richard Dickerson, Duilio Cascio, Michael Sawaya, and Arthur Laganowsky for critically reading the manuscript; and the European Synchrotron Radiation Facility for beamtime under long-term projects MX551 and MX666 (radiation-damage BAG) and MX498 (IBS BAG). This work was supported by the Commissariat à l'Énergie Atomique, the Centre National de la Recherche Scientifique, the Université Joseph Fourier, Agence Nationale de la Recherche Grant JC05_45685 (to M.W.); the National Institutes of Health CounterACT Program; the U.S. Army Defense Threat Reduction Agency; the Nalvyco Foundation, the Kimmelman Center for Biomolecular Structure and Assembly (Rehovot, Israel); the Minerva Foundation (J.L.S.); the Benoziyo Center for Neuroscience (I.S.); the Israel Ministry of Science, Culture, and Sport (the Israel Structural Proteomics Center); the Divadol Foundation; and the European Commission VIth Framework ''SPINE2-COMPLEXES'' Project (LSHG-CT-2006-031220). J.-P.C. was supported by a Université Joseph Fourier grant and European Molecular Biology Organization Short-Term Fellowship ASTF230-2006. J.L.S. is the Pickman Professor of Structural Biology.

1. Frauenfelder H, Sligar SG, Wolynes PG (1991) The energy landscapes and motions of proteins. *Science* 254:1598–1603.
2. Henzler-Wildman KA, *et al.* (2007) A hierarchy of timescales in protein dynamics is linked to enzyme catalysis. *Nature* 450:913–916.
3. Bourgeois D, Royant A (2005) Advances in kinetic protein crystallography. *Curr Opin Struct Biol* 15:538–547.
4. Weik M, *et al.* (2000) Specific chemical and structural damage to proteins produced by synchrotron radiation. *Proc Natl Acad Sci USA* 97:623–628.
5. Ravelli RB, McSweeney SM (2000) The 'fingerprint' that x-rays can leave on structures. *Structure Fold Des* 8:315–328.
6. Burmeister WP (2000) Structural changes in a cryo-cooled protein crystal owing to radiation damage. *Acta Crystallogr D* 56:328–341.
7. Ravelli RB, Garman EF (2006) Radiation damage in macromolecular cryocrystallography. *Curr Opin Struct Biol* 16:624–629.
8. Ravelli RB, Leiros HK, Pan B, Caffrey M, McSweeney S (2003) Specific radiation damage can be used to solve macromolecular crystal structures. *Structure* 11:217–224.
9. Schlichting I, *et al.* (2000) The catalytic pathway of cytochrome p450cam at atomic resolution. *Science* 287:1615–1622.
10. Weik M, *et al.* (2001) Specific protein dynamics near the solvent glass transition assayed by radiation-induced structural changes. *Protein Sci* 10:1953–1961.
11. Weik M, *et al.* (2005) Supercooled liquid-like solvent in trypsin crystals: Implications for crystal annealing and temperature-controlled X-ray radiation damage studies. *J Synchrotron Radiat* 12:310–317.
12. Fioravanti E, Vellieux FM, Amara P, Madern D, Weik M (2007) Specific radiation damage to acidic residues and its relation to their chemical and structural environment. *J Synchrotron Radiat* 14:84–91.
13. Matsui Y, *et al.* (2002) Specific damage induced by X-ray radiatioin and structural changes in the primary photoreaction of bacteriorhodopsin. *J Mol Biol* 324:469–481.
14. Baxter RH, Seagle BL, Ponomarenko N, Norris JR (2004) Specific radiation damage illustrates light-induced structural changes in the photosynthetic reaction center. *J Am Chem Soc* 126:16728–16729.
15. Roberts BR, Wood ZA, Jonsson TJ, Poole LB, Karplus PA (2005) Oxidized and synchrotron cleaved structures of the disulfide redox center in the N-terminal domain of *Salmonella typhimurium* AhpF. *Protein Sci* 14:2414–2420.
16. Leiros HK, Timmins J, Ravelli RB, McSweeney SM (2006) Is radiation damage dependent on the dose rate used during macromolecular crystallography data collection? *Acta Crystallogr D* 62:125–132.
17. Dubnovitsky AP, Ravelli RB, Popov AN, Papageorgiou AC (2005) Strain relief at the active site of phosphoserine aminotransferase induced by radiation damage. *Protein Sci* 14:1498–1507.

18. Silman I, Sussman JL (2005) Acetylcholinesterase: 'Classical' and 'non-classical' functions and pharmacology. *Curr Opin Pharmacol* 5:293–302.
19. Greenblatt HM, Dvir H, Silman I, Sussman JL (2003) Acetylcholinesterase: a multifaceted target for structure-based drug design of anticholinesterase agents for the treatment of Alzheimer's disease. *J Mol Neurosci* 20:369–383.
20. Casida JE, Quistad GB (1998) Golden age of insecticide research: Past, present, or future? *Annu Rev Entomol* 43:1–16.
21. Millard CB, Broomfield CA (1995) Anticholinesterases: Medical applications of neurochemical principles. *J Neurochem* 64:1909–1918.
22. Sussman JL, *et al.* (1991) Atomic structure of acetylcholinesterase from *Torpedo californica*: A prototypic acetylcholine-binding protein. *Science* 253:872–879.
23. Ripoll DR, Faerman CH, Axelsen PH, Silman I, Sussman JL (1993) An electrostatic mechanism for substrate guidance down the aromatic gorge of acetylcholinesterase. *Proc Natl Acad Sci USA* 90:5128–5132.
24. Gilson MK, *et al.* (1994) Open ''back door'' in a molecular dynamics simulation of acethylcholinesterase. *Science* 263:1276–1278.
25. Colletier JP, *et al.* (2006) Structural insights into substrate traffic and inhibition in acetylcholinesterase. *EMBO J* 25:2746–2756.
26. Bourne Y, *et el.* (2006) Substrate and product trafficking through the active center gorge of acetylcholinesterase analyzed by crystallography and equilibrium binding. *J Biol Chem* 281:29256–29267.
27. Colletier JP, *et al.* (2007) Use of a 'caged' analogue to study the traffic of choline within acetylcholinesterase by kinetic crystallography. *Acta Crystallogr D* 63:1115–1128.
28. Owen RL, Rudino-Pinera E, Garman EF (2006) Experimental determination of the radiation dose limit for cryocooled protein crystals. *Proc Natl Acad Sci USA* 103:4912–4917.
29. Koshland DE, Jr, Neet KE (1968) The catalytic and regulatory properties of enzymes. *Annu Rev Biochem* 37:359–410.
30. Sevilla MD, D'Arcy JB, Morehouse KM (1979) An electron spin resonance study of .gamma.-irradiated frozen aqueous solutions containing N-acetylamino acids. *J Phys Chem* 83:2893–2897.
31. Van Thor JJ, Georgiev GY, Towrie M, Sage JT (2005) Ultrafast and low barrier motions in the photoreactions of the green fluorescent protein. *J Biol Chem* 280:33652–33659.
32. Fenimore PW, Frauenfelder H, McMahon BH, Young RD (2004) Bulk-solvent and hydration-shell fluctuations, similar to α- and β-fluctuations in glasses, control protein motions and functions. *Proc Natl Acad Sci USA* 101:14408–14413.
33. Wood K, *et al.* (2008) Coincidence of dynamical transitions in a soluble protein and its hydration water: Direct measurements by neutron scattering and MD simulations. *J Am Chem Soc* 130:4586–4587.
34. Nicolet Y, Lockridge O, Masson P, Fontecilla-Camps JC, Nachon F (2003) Crystal structure of human butyrylcholinesterase and of its complexes with substrate and products. *J Biol Chem* 278:41141–41147.
35. Farnegardh M, *et al.* (2003) The three-dimensional structure of the liver X receptor beta reveals a flexible ligand-binding pocket that can accommodate fundamentally different ligands. *J Biol Chem* 278:38821–38828.
36. Ursby T, Bourgeois D (1997) Improved estimation of structure-factor difference amplitudes from poorly accurate data. *Acta Crystallogr A* 53:564–575.
37. Thanei-Wyss P, Waser PG (1989) Interaction of quaternary ammonium compounds with acetylcholinesterase: Characterization of the active site. *Eur J Pharmacol* 172:165–173.
38. Sussman JL, *et al.* (1988) Purification and crystallization of a dimeric form of acetylcholinesterase from *Torpedo californica* subsequent to solubilization with phosphatidylinositol-specific phospholipase C. *J Mol Biol* 203:821–823.
39. Kabsch W (1993) Automatic processing of rotation diffraction data from crystals of initially unknown symmetry and cell constants. *J Appl Crystallogr* 26:795–800.
40. Murray JW, Garman EF, Ravelli RBG (2004) X-ray absorption by macromolecular crystals: The effects of wavelength and crystal composition on absorbed dose. *J Appl Crystallogr* 37:513–522.
41. Greenblatt HM, *et al.* (2004) The complex of a bivalent derivative of galanthamine with *Torpedo* acetylcholinesterase displays drastic deformation of the active-site gorge: Implications for structure-based drug design. *J Am Chem Soc* 126:15405–15411.
42. Emsley P, Cowtan K (2004) COOT: Model-building tools for molecular graphics. *Acta Crystallogr D* 60:2126–2132.
43. Brunger AT, *et al.* (1998) Crystallography & NMR system: A new software suite for macromolecular structure determination. *Acta Crystallogr D* 54:905–921.
44. DeLano WL (2002) *The PyMOL Molecular Graphics System*. (DeLano Scientific, San Carlos, CA).
45. Schuttelkopf AW, van Aalten DM (2004) PRODRG: A tool for high-throughput crystallography of protein-ligand complexes. *Acta Crystallogr D* 60:1355–1363.
46. Laskowski RA, MacArthur MW, Moss DS, Thornton JM (1993) PROCHECK: A program to check the stereochemical quality of protein structures. *J Appl Crystallogr* 26:283–291.

```
########################################
#         PHOSPHO v0.71                #
#           B. Sanson                  #
#           March 2009                 #
########################################

#Modules
import os, time
import Gnuplot
from math import exp

#Empty the log file produced by gnuplot
os.popen('rm fit.log')

# g is a variable for using Gnuplot
g = Gnuplot.Gnuplot(debug=1)

# Define the classes which contains the parameters and the choice
class Params:
      "List of parameters"
class What:
      "Choice"
class ListTemp:
      "List of temperatures and iterations "

# This function reads raw data, detects decays and then suitably
slices the raw data file
# so it produces a file for every detected decay.
# Sometimes it includes points that should be chopped off (points
that belong to the fluorescence peak)
def Prep_Data(temp):
      temp=mintemp
      Tfiles=[]
      NumSpecL=[]
      NumSpecList=[]
      TzeroL=[]
      TzeroList=[]
      while temp<=maxtemp:
            print 'Temperature %sK'%temp
            f=''.join([str(pref),str(temp),'K.time'])
            Tfiles.append(f)
            for Tfile in Tfiles:
                  Tempfile=open(Tfile,'r')
                  compteur=0
                  out=open('thrash','w')
                  diff=0
                  NumSpecL.append(temp)
                  TzeroL.append(temp)
                  imax2=imax
                  for line in Tempfile:
                        d=line.split()
                        try :
                              diff=float(d[1])-float(imax2)
                              if diff > 8 and float(imax2) < 8. :
                                    compteur+=1

      out=open(''.join([str(temp),'K_',str(compteur),'.time']),'w')
                                    NumSpecL.append(compteur)
```

```
                                    TzeroL.append(float(d[0]))
                                    tref=d[0]
                        except : print "Mmmmmvoyeeeeez"
                        try :
                              if float(d[1]) < float(imax) and
float(d[1]) < float(imax2) and float(d[0])-float(tref)<10: print >>
out, d[0],'\t',d[1]
                        except : print "Mmmmmvoyeeeeez"
                        imax2=d[1]
                  NumSpecList.append(NumSpecL)
                  NumSpecL=[]
                  TzeroList.append(TzeroL)
                  TzeroL=[]
            temp+=5
            Tfiles=[]
      Params.NumSpecList=NumSpecList
      Params.TzeroList=TzeroList
      return Params

## This function fits the first decay, samples the fit to get more
precise reference values.
## Then, for every decay, it finds the closest value as a starting
point to align the data points.
## It sums data points. It fits the sum and outputs the lifetime.

def Fit_First(a1=40):
      filein=open(''.join([str(temp),'K_1.time']),'r')
      dat=open('data.temp','w')
      ccc=0
      for j in filein :
            dat.write(j)
            if ccc == 0 :
                  a1=float(j.split()[1])
                  ccc+=1
      dat.close()
      print 'a1'
      print a1
      g('a(x) = a1*exp((a0-x)/a2)')
      o=open('fit.par','w')
      print >> o, 'a1 =',a1,'\na2 = 1\na0 =9' #write params
      o.close()
      g('fit a(x) "data.temp" using 1:2 via "fit.par" ')
      g('plot "data.temp" using 1:2, a(x)')
      if temp<180 : time.sleep(0.15)
      else : time.sleep(0.2)
      fit=open('fit.log')
      for line in fit :
            try :
                  l=line.split()
                  if l[0] == "a2" and l[2] != "1.000" and l[3] ==
"+/-":
                        firstl.append(l[2])
                  if l[0] == "a1" and l[1] != "1.000" and l[3] ==
"+/-":
                        firstl.append(l[2])
```

```
                  if l[0] == "a0" and l[3] != "1.000" and l[3] ==
"+/-":
                        firstl.append(l[2])
            except : print "Bah, non"
      os.popen('rm fit.log')

def Sample_First():
      sampletime=[]
      sampleintens=[]
      for p in firstl:
            a0=0
            a1=firstl[1]
            a2=firstl[0]
      print firstl
      temps=float(a0)
      while temps<=9:
            intensity=float(a2)*exp((float(a0)-temps)/float(a1))
            temps+=0.001
            sampletime.append(temps)
            sampleintens.append(intensity)
      Params.sampletime=sampletime
      Params.sampleintens=sampleintens
      return Params

def Find_Start(n):
      print 'n',n
      listetime=[]
      listeintens=[]
      filein=open(''.join([str(temp),'K_',str(n),'.time']))
      debut=1
      ccc=0
      LineElem=[]
      LineTime=[]
      for line in filein:
            lig=line.split()
            if ccc==0 : idebut=float(lig[1])
            ccc+=1
            LineElem.append(lig[1])
            LineTime.append(lig[0])
      filein.close()
      compt=0
      for pas in Params.sampleintens :
            if idebut>=float(Params.sampleintens[compt]) and
idebut<=float(Params.sampleintens[(compt-1)]) :
                  debut=compt
            compt+=1
      tzero=Params.sampletime[debut]
      tz=tzero
      tsuperzero=LineTime[0]
      incr=0
      for elem in LineElem:
            tzero=tz+float(LineTime[incr])-float(tsuperzero)
            listetime.append(tzero)
            listeintens.append(elem)
            incr+=1
      #print listetime
      Params.listetime=listetime
      Params.listeintens=listeintens
```

```
      return Params

def Sum_After_Find():
      listetime=[]
      listeintens=[]
      findout=open('findout.dat','w')
      sumtime=[]
      sumintens=[]
      last=Params.last
      for numero in range(1,last):
            print numero
            print 'numero'
            Find_Start(numero)
            for e in Params.listetime :
                  sumtime.append(e)
            for f in Params.listeintens :
                  sumintens.append(f)
      count=0
      for i in sumtime :
            print >> findout, sumtime[count],'\t',sumintens[count]
            count+=1
      findout.close()
      return Params

def Sort_Sum():
      print 'Sort_Sum here'
      d={}
      resu=[]
      filein=open('findout.dat','r')
      fileout=open('findout2.dat','w')
      for l in filein:
            d[l.split()[0]]=l.split()[1]
      SortedList=d.keys()
      SortedList.sort()
      for i in SortedList:
            fileout.write('%s\t%s\n'%(i,d[i]))
      fileout.close()

def Fit_After_Sort():
      a1=Params.imax
      g('a(x) = a1*exp((a0-x)/a2)')
      o=open('fit.par','w')
      print >> o, 'a1 =',a1,'\na2 = 1\na0 =9' #write params
      o.close()
      g('fit a(x) "findout.dat" using 1:2 via "fit.par" ')
      g('plot "findout.dat" using 1:2, a(x)')
      if temp<175 : time.sleep(0.25)
      else : time.sleep(0.35)
      fit=open('fit.log')
      for l in fit:
            try:
                  elem=l.split()
                  if elem[0] == "a2" and elem[3] != "1.000":
                        Params.lifetime.append(elem[2])
                        try:
                              err=elem[5].split('(')
```

```
                              err=''.join(err)
                              err=err.split('%')
                              err=''.join(err)
                              err=err.split(')')
                              err=''.join(err)
                              err=float(err)/100
                        except: print 'TIGHTROPE'
                        Params.error.append(err)
            except : print "AAAA"
      os.popen('rm fit.log')
      return Params

def Plot_After_Fit():
      resfit2=open('resfit2.dat','w')
      r=0
      temp=mintemp
      while temp<=(maxtemp):
            print >> resfit2, temp, Params.lifetime[r],
Params.error[r]
            temp+=5
            r+=1
      resfit2.close()
      g('plot "resfit2.dat" using 1:2:3 with yerrorbars')

#########################################################################
#########################
# This function reads the first lign of every "prepared" file for
one given temperature.
# It calculates the average and write it in a new file.

def Sum_Data(first=1,last=1):
      last=Params.last
      somme=[]
      for nombre in range(0,100):
            som=0
            compt=0
            for numspec in range(first,last):
                  compti=0

      filein=open(''.join([str(temp),'K_',str(numspec),'.time']))
                  for j in filein :
                        d=j.split()
                        if float(compti) == float(nombre) :
som=som+float(d[1])
                              compti+=1
                  compt=compt+1
            som=som/compt
            somme.append(som)
      print >> res2, somme
      fileout=open(''.join([str(temp),'K_average.time']),'w')
      time=1
      for intensity in somme :
            if float(intensity) > 0 :print >> fileout,
time,'\t',intensity
            time=time+0.143
      fileout.close()
```

```
# This function reads every decay file and calls gnuplot for fitting
data.
# It generates a file res.dat which contains lifetimes exctrated
from fits.
# The lifetimes are sorted by temperature.
def Fit_Data(first=1,last=1,a1=40,a2=1,a0=0) :
      last=Params.last
      a1=Params.imax
      try :
            for i in range(first,last):
                  h=Params.TzeroList[(i+1)]
                  f=open(''.join([str(temp),'K_',str(i),'.time']))
                  dat=open('data.temp','w')
                  for j in f:
                        dat.write(j)
                  dat.close()
                  g('a(x) = a1*exp((a0-x)/a2)')
                  o=open('fit.par','w')
                  print >> o, 'a1 =',a1,'\na2 = 1\na0 =',h #write
params
                  o.close()
                  g('fit a(x) "data.temp" using 1:2 via "fit.par" ')
                  g('plot "data.temp" using 1:2, a(x)')
                  time.sleep(0.15)
                  fit=open('fit.log')
                  for k in fit:
                        try :
                              l=k.split()
                              if l[0] == "a2" and l[3] != "1.000":
                                    print >> res, i, l[2], l[5]
                        except : print "Bah, non"
                  os.popen('rm fit.log')
            print >> res, temp
      except : print >> res, temp

### This module is a modification of Fit_Data. It is used when
averaging is performed before fitting.
def Fit_Data2(a1=40,a2=1,a0=1) :
      last=Params.last
      a1=Params.imax
      s=open(''.join([str(temp),'K_average.time']))
      dat=open('data.temp','w')
      for j in s :
            dat.write(j)
      dat.close()
      g('a(x) = a1*exp((a0-x)/a2)')
      o=open('fit.par','w')
      print >> o, 'a1 =',a1,'\na2 = 1\na0 =1' #write params
      o.close()
      g('fit a(x) "data.temp" using 1:2 via "fit.par" ')
      g('plot "data.temp" using 1:2, a(x)')
      time.sleep(0.5)
      fit=open('fit.log')
      for k in fit:
            try:
                  l=k.split()
```

```
                if l[0] == "a2" and l[3] != "1.000":
                        print >> resfit, l[2], l[5]
            except : print "AAAA"
      os.popen('rm fit.log')
      print >> resfit, temp

# This function calculates an average (stored in average.dat) of all
the lifetimes at a given temperature.
# It then plots the lifetime as a function of the temperature.
def Treat_Data(temp):
      r=open('res.dat')
      g=open('treated.dat','w')
      h=open('average.dat','w')
      print >> g, temp,
      av=0
      compteur=0
      for i in r :
            try:
                  a=i.split()
                  error=a[2]
                  error=error.split('(')
                  error=''.join(error)
                  error=error.split('%')
                  error=''.join(error)
                  error=error.split(')')
                  error=''.join(error)
            except: print 1000
            if float (a[0]) >= 100  :
                  if compteur!=0 :
                        av=av/compteur
                        print >> h, temp, av
                        av=0
                        compteur=0
                        print >> g, '\n', temp,
                  temp+=5
            if float(a[0]) < 100 and float(error) < 25 :
                  print >> g, a[1],
                  av=av+float(a[1])
                  compteur+=1
      print temp

### Modification of Treat_Data when averaging before fitting
def Treat_Data2(temp):
      filein=open('resfit.dat','r')
      fileout=open('treated.dat','w')
      for line in filein :
            try:
                  error=line.split()[1]
                  error=error.split('(')
                  error=''.join(error)
                  error=error.split('%')
                  error=''.join(error)
                  error=error.split(')')
                  error=''.join(error)
            except: print 1000
            if float (line[0]) >= 100  :
                  temp+=5
            if float(line[0]) < 100 and float(error) < 25 :
```

```
                print >> fileout, temp, line[0]

#########################################################################
#############
### Main part of the program
# Define main variables (NB: they belong to the Params class)

lchoice=[0,1,2,3,4,5,6]
What.ch=9

def Ask_Var():
      Params.pref=raw_input("Enter the prefix of the filenames :")
      Params.newpref=raw_input("Enter a new prefix for the filenames
(optional) :")
      if Params.newpref : Params.newpref=Params.pref
      Params.mintemp=int(raw_input("Enter the minimum temperature
:"))
      Params.maxtemp=int(raw_input("Enter the maximum temperature
:"))
      Params.imax=int(raw_input("Enter an approximation of the
maximum intensity :"))
      return Params

def Ask_What():
      print "What do you want to do?"
      print "0: Prepare, Fit and Average"
      print "1: Prepare data"
      print "2: Fit data"
      print "3: Finalize"
      print "4: Prepare and Fit"
      print "5: Prepare, Average and Fit"
      print "6: Test the New Method"
      while What.ch not in lchoice :
            What.ch=raw_input("Chose what you want to do :
0,1,2,3,4,5 or 6 (0 is default)")
            if What.ch=='' : What.ch=0
            What.ch=int(What.ch)

## Main routine
abc=0
Ask_Var()

# This is not mandatory: here simpler aliases of the previously
defined variables are created
pref=Params.pref
mintemp=Params.mintemp
maxtemp=Params.maxtemp
imax=Params.imax

while abc==0:
      Ask_What()
      if What.ch==0 or What.ch==1 or What.ch==4 or What.ch==5 or
What.ch==6: Prep_Data(mintemp)

      if What.ch==0 or What.ch==2 or What.ch==4 :
            res=open('res.dat','w')
```

```
            for u in Params.ltemper :
                  temp=max(u)
                  Params.last=max(u[1:])
                  Fit_Data()
            res.close()

      if What.ch==0 or What.ch==3 or What.ch==4  :
            Treat_Data(temp)
            g('plot "average.dat" using 1:2')
      if What.ch==5:
            res2=open('somme.dat','w')
            resfit=open('resfit.dat','w')
            for u in Params.ltemper :
                  temp=max(u)
                  Params.last=max(u[1:])
                  Sum_Data()
            for u in Params.ltemper :
                  temp=max(u)
                  Params.last=max(u[1:])
                  Fit_Data2()
            res2.close()
            resfit.close()
            Treat_Data2(temp)
            g('plot "treated.dat" using 1:2')

      if What.ch==6:
            Params.lifetime=[]
            Params.error=[]
            firstl=[]
            lastlist=[]
            for u in Params.NumSpecList :
                  temp=u[0]
                  Params.last=max(u[1:])
                  Fit_First()
                  Sample_First()
                  Sum_After_Find()
                  #Sort_Sum()
                  Fit_After_Sort()
            Plot_After_Fit()

# Transform filenames so the results of several experiments can be
stored
            #os.system('mv average.dat average_%s.dat' %
str(Params.newpref))
            #os.system('mv res.dat res_%s.dat' % str(Params.newpref))
# Remove temporary files
            os.system('rm thrash')
            #os.system('rm data.temp')
            os.system('rm *K_*.time')
# Return to the beginning
      What.ch=9
      abd=raw_input("Do you want to do something else? (type yes)")
      if abd == 'yes' : abc = 0
      else :
            print "Bye"
            break
```

Résumé

L'objectif de la thèse était de regarder l'acétylcholinestérase (AChE) en mouvement. L'AChE est une enzyme très rapide qui met fin à la transmission de l'influx nerveux au sein des synapses cholinergiques.
À l'aide de la cristallographie aux rayons X, des sous-états conformationnels de l'AChE de *Torpedo californica* (*Tc*) ont été piégés par sa liaison à des drogues anti-Alzheimer putatives. Les formes, non vieillie et vieillie, de la *Tc*AChE conjuguée au soman ont été caractérisées structuralement, éclairant ainsi le mécanisme de vieillissement de la *Tc*AChE inhibée par les organophosphorés (OP). La structure du complexe ternaire du conjugué vieilli avec un réactivateur a également été résolue. Toutes ces structures guideront l'élaboration de médicaments (drogues anti-Alzheimer ou antidotes contre l'empoisonnement par des OP) en prenant en compte la flexibilité de l'enzyme et ses conformations minoritaires.
La structure du complexe de la *Tc*AChE avec un inhibiteur de son site périphérique (PAS), l'aflatoxine B1 (AB1), a été résolue dans deux formes cristallines. Ce travail a mis en évidence des artefacts de la cristallographie nuisibles à l'interprétation biologique des structures. La mesure du temps de vie de phosphorescence de l'AB1 a permis de sonder les mouvements du PAS à l'échelle de la seconde et de révéler des différences de flexibilité liées à l'empilement cristallin de la *Tc*AChE. Cette méthode spectroscopique est complémentaire à la cristallographie cinétique. La gamme de températures cryogéniques identifiée pourrait en effet faciliter l'exploration du mécanisme réactionnel de l'AChE, en ralentissant l'enzyme sans pour autant la figer.

Summary

This work aimed at watching acetylcholinesterase (AChE) 'at work'. AChE is a very rapid enzyme and terminates the transmission of the nervous influx at cholinergic synapses.
Conformational substates of *Torpedo californica* (*Tc*) AChE were trapped in x-ray crystallography structures of the enzyme in complex with putative anti-Alzheimer drugs. Structures of both nonaged and aged conjugates of *Tc*AChE and soman were solved, which allowed to shed light on the mechanism of aging in organophosphate (OP) - inhibited AChE. The structure of the ternary complex of the nonaged conjugate and a reactivator was solved. All those structures will help designing new AChE-targeted drugs (anti-Alzheimer drugs or antidotes against OP poisoning) by taking into account flexibility and minor conformations of the enzyme.
The structure of *Tc*AChE in complex with the peripheral site (PAS) inhibitor aflatoxin B1 was solved in two crystal forms. This work revealed crystallography artifacts that should be avoided for correct biological interpretation. Measurement of the phosphorescence lifetime of AB1 allowed probing PAS dynamics on the timescale of seconds, thereby highlighting differential flexibility in two distinct crystal packing environments of *Tc*AChE. This spectroscopic method is proposed as a complementary tool for kinetic crystallography experiments. An optimal cryogenic temperature range was identified, which could help exploring the reaction mechanisms of AChE by slowing down the enzyme motions without freezing them.